Progress towards fluorescence microscopy imaging of a Strontium quantum gas

Romaric Journet

université
PARIS-SACLAY

Progress towards fluorescence microscopy of a quantum gas of strontium

Progrès vers l'imagerie par microscopie de fluorescence d'un gaz quantique de strontium

Thèse de doctorat de l'université Paris-Saclay

École doctorale n° 572 Ondes et Matières (EDOM)
Spécialité de doctorat : Physique
Graduate School : Physique. Référent : Institut d'Optique

Thèse préparée dans l'unité de recherche **Université Paris Saclay, Institut d'Optique Graduate School, CNRS, Laboratoire Charles Fabry**, 91127, Palaiseau, France, sous la direction de **Thomas BOURDEL**, chargé de recherche CNRS, le co-encadrement de **Marc CHENEAU**, chargé de recherche CNRS

Thèse soutenue à Paris-Saclay, le 16 mars 2023, par

Romaric JOURNET

Composition du jury

Membres du jury avec voix délibérative

Michel BRUNE Directeur de recherche CNRS, Laboratoire Kastler Brossel, Collège de France	Rapporteur
Florian SCHRECK Professeur, Institut of Physics, University of Amsterdam	Rapporteur
Marion DELEHAYE Chargée de recherche CNRS, Institut FEMTO-ST, Université Bourgogne Franche-Comté	Examinatrice
Christine GUERLIN Maître de conférence, Laboratoire Kastler Brossel - Laboratoire SYRTE, Observatoire de Paris	Examinatrice
Thierry LAHAYE Directeur de recherche CNRS, Laboratoire CHarles Fabry, Institut d'Optique Graduate School, Université Paris Saclay	Président

Membres du jury sans voix délibérative

Thomas BOURDEL Chargé de recherche CNRS, Laboratoire CHarles Fabry, Institut d'Optique Graduate School, Université Paris Saclay	Directeur de thèse
Marc CHENEAU Chargé de recherche CNRS, Laboratoire CHarles Fabry, Institut d'Optique Graduate School, Université Paris Saclay	Co-encadrant

THESE DE DOCTORAT
NNT : 2023UPASP022

université PARIS-SACLAY

ÉCOLE DOCTORALE
Ondes et matière (EDOM)

Titre : Progrès vers l'imagerie par microscopie de fluorescence d'un gaz quantique de strontium
Mots clés : strontium, gaz quantiques, microscopie de fluorescence

Résumé : Dans cette thèse, nous discutons des progrès réalisés dans le développement d'un microscope à gaz quantique pour l'étude de la dynamique hors équilibre dans des systèmes quantiques isolés après un quench. La perspective de ce travail est d'étudier la dynamique de relaxation des atomes de strontium dans un réseau optique 2D, décrit par le modèle de Bose-Hubbard.

Nous présentons le dispositif expérimental développé pour le refroidissement et le piégeage du strontium par laser. En particulier, nous décrivons la simulation et la mise en œuvre d'un nouveau dispositif de collimation du faisceau atomique. Les différentes étapes du refroidissement laser jusqu'au microkelvin sont présentées. Enfin, nous décrivons les implémentations du piège dipôle optique utilisé pour transporter le nuage atomique entre nos deux chambres à vide et piéger les atomes dans un réseau optique 2D.

Nous présentons également en détail le travail effectué pour préparer l'étape d'imagerie de fluorescence de l'expérience. Nous décrivons un nouvel algorithme pour analyser les futures images du microscope et le comparons aux méthodes standards. Avec cet algorithme, nous explorons les limites de résolution et de rapport signal à bruit nécessaires pour reconstruire la distribution des atomes avec des sensibilités au site unique et à l'atome unique. Nous avons également effectué des calculs de light-shifts pour le strontium à 1064nm pour l'état fondamental et excité (3P1) afin d'évaluer les paramètres du piège pendant l'imagerie. Enfin, nous calculons la dynamique d'un atome piégé dans le réseau optique. Nous calculons le nombre de photons diffusés et la durée de vie de l'atome dans le piège et discutons des mécanismes de refroidissement mis en jeu.

Title : Progress towards fluorescence microscopy of a quantum gas of strontium
Keywords : strontium, quantum gases, fluorescence microscopy

Abstract : In this thesis, we discuss the progress made in developing a quantum gas microscope for the study of out-of-equilibrium dynamics in isolated quantum systems after a quench. The prospect of this work is to study the relaxation dynamics of strontium atoms in a 2D optical lattice, described by the Bose-Hubbard model.

We present the experimental apparatus developed for the laser cooling and trapping of strontium. In particular, we describe the simulation and implementation of a new collimation setup for the atomic beam. The different stages of laser cooling down to the microkelvin are presented. Finally, we describe the optical dipole trap implementations used to transport the atomic cloud between our two vacuum chambers and trap the atoms in a 2D optical lattice.

We also present in detail the work done to prepare the fluorescence imaging stage of the experiment. We describe a new algorithm to analyze the future microscope images and compare it to standard methods. With this algorithm, we explore the resolution and signal-to-noise ratio limits required to reconstruct the atom distribution with single-site and single-atom sensitivities. We also performed computations of the AC-Stark shifts for strontium at 1064nm for the ground and excited state (3P1) to evaluate the trap parameters during the imaging. Finally, we compute the dynamics of a trapped atom in the optical lattice. We calculate the number of scattered photons and the lifetime of the atom in the trap and discuss the cooling mechanisms at play.

Résumé

Ce manuscrit de thèse résume les travaux réalisés durant ma thèse de physique au laboratoire Charles Fabry, au sein du groupe Gaz Quantiques, sous la direction de Marc Cheneau. L'objectif de ma thèse était de participer au dévelopement d'une nouvelle expérience d'atomes ultrafroids, et plus particulièrement, la construction d'un microscope à gaz quantiques utilisant des atomes de strontium 84. La construction de cette expérience a été commencée en 2016 avec l'arrivée d'Anaïs Molineri, la première doctorante de l'équipe, suivie en 2017 par Clémence Briosne–Fréjaville. Mon implication dans le projet a commencé en mars 2019, date de mon arrivée en stage au sein de l'"équipe strontium", puis s'est poursuivie durant ma thèse d'octobre 2019 à mars 2023. L'équipe a ensuite bénéficié de la participation de Sayali Shevate, post-doc dans l'équipe durant une année (2021-2022) et de Félix Faisant, doctorant dans l'équipe depuis octobre 2021.

La structure de ce manuscrit est la suivante. Dans le chapitre d'introduction, nous récapitulons les objectifs motivant la construction de cette nouvelle expérience, à savoir, l'étude de la dynamique quantique hors équilibre d'un système à N-corps décrit par le modèle de Bose-Hubbard. L'expérience dans son ensemble est ensuite présentée brièvement à travers la présentation d'un cycle expérimental "type".

Le chapitre 1 s'attache à la description de l'état d'avancement de l'expérience au moment de la soutenance de la thèse de Clémence Briosne–Fréjaville, en octobre 2020. Ce chapitre décrit l'implémentation des différents dispositifs nécessaires pour la réalisation de notre expérience par exemple : le four, l'obtention des différents pièges magnéto-optiques (MOT) et le design des différents pièges dipolaires.

Le chapitre 2 s'attache à la description de simulations ayant mené à un nouveau montage pour la collimation du jet atomique présentant un gain d'environ 60 en terme d'atomes au niveau du MOT.

Le chapitre 3 récapitule les avancées expérimentales obtenues durant ma thèse, tels que l'obtention des premiers MOT avec l'isotope le moins abondant ^{84}Sr et leur caractérisation en nombre d'atome et température, environ 10 millions d'atomes à 1 µK en fin de "MOT rouge", ou encore le transport du nuage d'atomes dans un piège dipolaire mobile sur 30 cm en quelques secondes.

Dans le chapitre 4, nous détaillons trois méthodes pour reconstruire l'occupation des sites du réseau optique à partir des (futures) images de microscopes : un algorithme de moindres carrés itératifs, une déconvolution utilisant le filtre de Wiener, et un réseau de neurone convolutif. Nous procédons à des caractérisations des performances de ces algorithmes en fonction de la taille de la réponse percutionnelle, du rapport signal à bruit

et de la pixelisation de l'image. Nous concluons que pour notre dispositif 200 photo-électrons par atomes sont suffisants pour obtenir des "taux d'erreur" inférieurs à 1%, correspondant à environ 2100 photons émis par atomes.

Le chapitre 5 s'attache au calcul des polarisabilités dynamiques pour les états $5s^2\ {}^1\mathrm{S}_0$ et $5s5p\ {}^3\mathrm{P}_1$, pertinents pour le piègeage et l'imagerie. On y discute également l'influence du choix d'un "axe de quantification", en imposant un champ magnétique de biais, sur le piégeage et l'émission de lumière lors de la phase d'imagerie.

Finalement, dans le sixième chapitre, nous présentons des résultats de simulation de la dynamique d'un atome de strontium piégé sur un site du réseau optique et excité par un champ laser à 689 nm à fréquence et intensité fixées. Nous détaillons le modèle utilisé ainsi que son implémentation numérique. Les résultats sont donnés à une dimension pour l'axe le mon confinant (vertical) après une résolution soit par une méthode *Monte Carlo Wavefunction* soit par l'intégration numérique d'équations de taux. Nous mettons en évidence que dans un piège à 1064 nm l'atome s'échappe en un temps fini. Cependant, nous mettons en évidence qu'il est possible d'obtenir des temps de vie de l'atome dans le piège de l'ordre de plusieurs secondes compatibles avec la diffusion d'environ 1000 photons. Enfin nous présentons des pistes d'amélioration de notre schéma d'excitation.

Remerciements

"Maintenant que mon temps décroît comme un flambeau,
Que mes tâches sont terminées ;
Maintenant que voici que je touche au tombeau
Par les deuils et par les années,

Et qu'au fond de ce ciel que mon essor rêva,
Je vois fuir, vers l'ombre entraînées,
Comme le tourbillon du passé qui s'en va,
Tant de belles heures sonnées ;"

Paroles sur la dune, Les Contemplations
Victor Hugo

Sur ces quelques vers mélancoliques, le moment de commencer cette ultime section de mon manuscrit arrive. Comment en quelques pages résumer tant d'aventures, de rencontres, d'échanges, de creusages de méninges ; tant d'émotions partagées, d'excitations, d'incertitudes, de frustrations, de joies, de rires, "tant de belles heures sonnées" ?

Les premières personnes que je souhaite remercier sont les membres de l'équipe strontium : Marc, Florence, Anaïs, Clémence, Sayali et Félix, avec qui j'ai eu le plaisir de collaborer pendant ces quatres années. Merci à toi Marc pour m'avoir choisi pour faire cette thèse avec toi, pour ta disponibilité de tous les instants, et les discussions passionantes que nous avons eu au fil des années. Merci à toi Florence pour toutes ces petites et grandes conversations qui m'ont beaucoup apportées sur les plans scientifique et humain. Anaïs, Clémence, mes grandes sœurs de manip, c'est avec vous que la plupart de ces aventures scientifiques ce sont déroulées. Vous m'avez tant appris qu'entamer une liste serait vain. Quelques souvenirs me reviennent toutefois, les longues soirées à guetter la première ombre d'un MOT rouge, les visios de soutient moral pendant le confinement, la visite de l'expérience à ses débuts en 2016 à mon arrivée à l'institut... Merci Clémence pour m'avoir formé à mon arrivé en stage, pour les cappuccinos, les phrases qui n'avaient pas besoin d'être terminées. Merci Anaïs pour ton énergie inépuisable et ta bonne humeur. Thanks Sayali for that year we spent working together, I really enjoyed exchanging ideas with you while fighting with the transport trap. Et finalement, merci Félix pour avoir repris les rênes de l'expérience quand j'ai dû m'en éloigner pour rédiger. Les discussions avec toi ont toujours été passionnantes.

Au-delà de l'équipe, j'ai partagé cette aventure avec le groupe Gaz Quantiques dans

son ensemble. Un grands merci aux différents permanents du groupe qui tour à tour m'ont apporté leur aide : Denis, Thomas, Chris, Isabelle, Vincent, David, et Alain. J'adresse aussi ces remerciements aux doctorants du groupe qui ce sont succédés au fil des années : Max, Guillaume, Cécile, Ziyad, Batiste, Antoine, Quentin, Gaétan, Lucas, Yukun, Alfred, Xudong, Léa, JP,... Merci au bureau du swag pour tous ces bons moments, ces discussions de physique et pour les dramas aussi.

J'ai eu la chance de pouvoir échanger avec des membres de plusieurs qroupes de recherche durant ma thèse que ce soit pour des échange de matériel ou pour des conseils, mais aussi durant les enseignements. Merci aux équipes pédagogiques d'optique physique, de mécanique quantique, de photométrie et de polarisation, ainsi qu'au service des TP dans son ensemble. J'ai aussi eu le plaisir d'interagir à plusieurs reprise avec Jean-René et Sophie des ateliers de mécanique et d'optique, qui m'ont toujours accueilli avec le sourire et bienveillance même quand mon cahier des charges n'était... pas très clairs. La plupart de ces interactions se sont toutefois faites autour d'un repas au Magnan, et je tiens à remercier tous les membres du groupe Imagerie et Information qui m'ont accueilli à leur table pour des conversations toujours drôles ou intéressantes, souvent les deux. Merci Matthieu, Caroline, François, Henri-François, Alice, Olivier, Lucas, Joana et aux autres satellites du groupe Aliénor, Hector pour tous ces bons moments en votre compagnie.

A mes amis merci pour le soutien les échanges et les bons moments, notamment pour les jeux de sociétés en visio pendant les confinements. Viviane, Benjamin, Elham et Estelle merci pour tous les bons moments mais aussi pour les difficultés traversées ensemble au fil des années.

Enfin un grand merci à ma famille qui m'a soutenu durant ces nombreuses années et sans qui rien de toute cela n'aurait été possible. Merci de m'avoir soutenu dans mes choix et durant les épreuves que j'ai dû surmonté. Finalmente, obrigado Yuri por todo o apoio ao longo destes últimos meses, quase um ano, que foram um pouco caóticos mas também de crescimento e aprendizado.

A tous merci !

Contents

Introduction

It might be noted here [...] that there is an alternative formulation of the many-body problem, i.e.*, how many bodies are required before we have a problem. [...] In the eighteenth-century Newtonian mechanics, the three-body problem was insoluble. With the birth of general relativity around 1910 and quantum electrodynamics in 1930, the two- and one-body problems became insoluble. And within modern quantum field theory, the problem of zero bodies (vacuum) is insoluble.*

Richard D. Mattuck,
A guide to Feynman diagrams in the many-body problem

I A new ultracold-atom experiment to study out-of-equilibrium dynamics

I.1 Correlation function in out-of-equilibrium dynamics

The properties of a quantum isolated system composed of many particles, when driven far from equilibrium by a change of an external parameter, a "quantum quench", are typically studied through the measurement of correlators of observables measured at (*a priori*) distinct locations and times. For instance, one can be interested in the spin-spin correlations in an Ising 1D chain of spin-1/2 particles. Such correlations can be written as the expectation value of products of operators. The case of 2-point correlators reads:

$$\langle \sigma_z(t,i)\sigma_z(t',j)\rangle = \langle \sigma_z(t-t',i-j)\sigma_z(0,0)\rangle = C(t-t',|i-j|), \tag{1}$$

where we used the hypothesis of invariance by translation in time and (discrete) translation in space, $\sigma_z(t,i)$ is the Pauli matrix acting on the spin at site i, at time t (in the Heisenberg picture). The angular brackets denote the quantum average on the state of the system. Such correlation functions give insights concerning the properties of the system, such as the existence of a long-range order, and thus show in what phase the system stands. For instance, if the correlator decays to 0 with the distance, we are in the unordered phase, while in the reverse case, we have an ordered phase [1]. The time evolution of the correlators gives information about the excitation of the system [2].

The question of the dynamics of such correlators, that is, their time dependence after a quench, is difficult to investigate in general. In 1D there are a few systems that can be described analytically, for instance, the Lieb-Liniger model using Bethe ansatz [3]. For the other 1D systems there exist efficient numerical methods such as the matrix-product-state method. In 2D the situation is even worse as there are even fewer analytical models and the efficient numerical methods in 1D are not applicable. The experimental study of those systems is therefore interesting to build some understanding of the phenomenon occurring when a many-body system is driven out of equilibrium. There are not many general results about many-body problems that can be stated; one such result describes the appearance of a "limit velocity for the spread of information" in the system, this result is known as the Lieb-Robinson bound [4] and is described in the following.

I.2 Propagation of the correlations: the Lieb-Robinson bound

In 1972, Lieb and Robinson studied the commutator of two arbitrary observables A_X and B_Y acting on two disjoint parts of the system X and Y, respectively, and evaluated at distinct times for a quantum spin system with finite-range interactions. They showed that the operator norm[1] of the commutator was exponentially suppressed outside of a "light-cone", spanned by some velocity v. This means that the observables on two distant regions will commute unless the two regions have had time to "communicate", that is, if the distance d between them is smaller than vt. The Lieb-Robinson bound reads:

$$\|[A_X(t), B_Y(0)]\|_{\text{op}} \leq c\|A_X\|_{\text{op}}\|B_Y\|_{\text{op}} \min(|X|, |Y|) \exp\left(\frac{v|t| - d}{\xi}\right). \tag{2}$$

In the above, $\|\cdot\|_{\text{op}}$ is the operator norm. $|X(Y)|$ denotes the number of sites inside the region $X(Y)$, and c, v, and ξ are positive constants. Another bound was derived thirty-four years after the publication of this result, but this time for the connected correlators[2] instead of the commutators, making the problem more amenable to experimental tests. This new bound derive by Bravyi *et al.* [5], and Nachtergaele *et al.* [6] reads:

$$|\langle A_X(t)B_Y(0)\rangle_c| \leq c'\|A_X\|_{\text{op}}\|B_Y\|_{\text{op}}(|X| + |Y|) \exp\left(\frac{2v|t| - d}{\xi'}\right), \tag{3}$$

with the same notations as before and $c', \xi' > 0$.

In measuring the correlations between two sites distant of d, we expect that the correlations are vanishing (exponential suppression) until a time $t = d/2v$ when the correlation front arrives. This situation is depicted in Figure 1 and gives rise to an effective light cone by analogy with special relativity, where an event can only affect the points in space-time that lie within a cone of slope c (the speed of light in vacuum).

These spin systems with finite range interactions have been studied both theoretically and experimentally in a variety of one-dimensional systems; see, for instance, in spin systems [7–9], or in cold atom systems described by the Bose-Hubbard model [10].[3] In principle, the Bose-Hubbard model violates one assumption of the derivations of (2) and (3), which is that the Hilbert space attached to each site of the lattice must be

[1] The operator norm is defined as the maximum magnitude of the operator's eigenvalues.

[2] The connected correlator $\langle AB\rangle_c$ is given by the relation $\langle AB\rangle_c = \langle AB\rangle - \langle A\rangle\langle B\rangle$

[3] The Bose-Hubbard model is described in the following section.

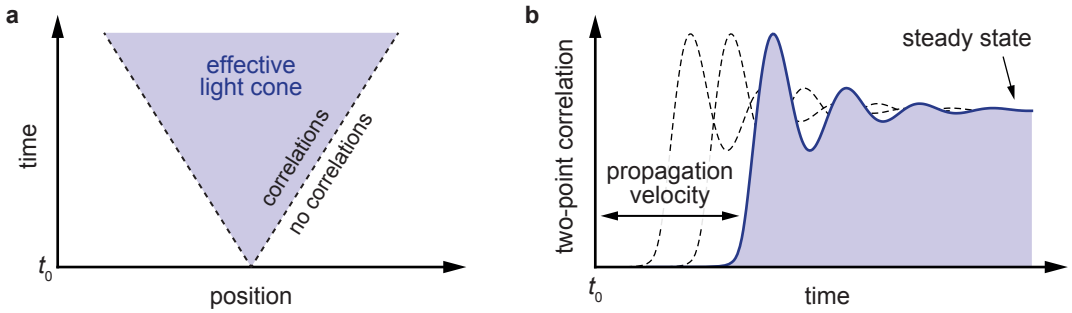

Figure 1: Schematic view of the propagation of the correlations and associated effective light-cone. According to equation (3), the correlations are exponentially suppressed outside a cone in a space-time representation (left). Equivalently, the correlations take some time to travel a given distance, as depicted on the right panel, where the correlations are plotted as a function of time for different distances.

finite-dimensional. Indeed, for an infinite system of bosons able to tunnel between the sites nothing prevents an arbitrary number of particles from accumulating on a site.

The numerical results on those systems in two or more dimensions to this day are still elusive. This situation results from the difficulty of simulating these configurations in more than 1D. This motivated the start of a new experiment aiming at observing the propagation of correlation in a two-dimensional lattice, using the technology of so-called *quantum-gas microscopes* [11]. Such microscopes give access to the occupation of each site enabling the measurements of density-density correlations as done in the article of Cheneau *et al.* [10].

I.3 Our experimental goals

Our experiment will be used at first to study the out-of-equilibrium dynamics in a 2D Bose-Hubbard system with ultracold ^{84}Sr. We will load a strontium Bose-Einstein condensate (BEC) in a 2D dimensional square lattice. There the Hamiltonian governing the dynamics can be written as follows:

$$\hat{H} = -J \sum_{\langle i,j \rangle} \hat{b}_j^\dagger \hat{b}_i + \frac{U}{2} \sum_i \hat{n}_i(\hat{n}_i - 1) - \sum_i \mu_i \hat{n}_i, \tag{4}$$

where the indices i, j label the lattice site in 2D ($i, j \in \mathbb{Z}^2$). We have introduced the bosonic operators on the site i, $\hat{b}_i$ and $\hat{b}_i^\dagger$, which are the usual annihilation and creation operators. The operators $\hat{n}_i = \hat{b}_i^\dagger \hat{b}_i$ are the number operators at the site i. Finally, J, U, and μ_i are the coefficient corresponding to the tunneling between neighboring sites ($\langle i, j \rangle$ denotes summation on nearest neighbors), the strength of the on-site interactions, and the chemical potential [12].

The phase diagram at low temperatures of the 2D Bose-Hubbard model depicted in Figure 2. At integer fillings, there are two phases in that model at low temperatures: the Mott insulator phase where the sites are all occupied by a fixed integer number of atoms, and a superfluid phase. Near the phase transition point, we observe that there is a "quantum critical region"; that region is an additional interest of our system. Indeed, the Lieb-Robinson velocity v is often interpreted as arising from the maximal group velocity

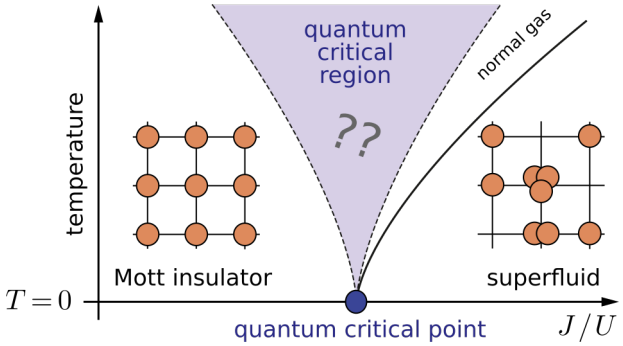

Figure 2: Phase diagram of the Bose-Hubbard model adapted from Witczak *et al.* [13].

of the quasi-particles in the system. The quasi-particles are viewed as the carrier of the correlations throughout the system; however, in the quantum critical region the quasi-particle picture breaks down and there are no "good" (*i.e.*, long-lived) quasi-particles [13]. The question of the existence of a light-cone-like propagation of the correlations in the quantum critical region remains to this day open.

Another direction our experiment could explore is the impact of the range of the interactions on the light-cone's shape or existence, see, for instance, Schneider *et al.* [14]. Exploiting the possibility of doing a Rydberg dressing on the alkaline-earth atoms while keeping them trapped using the polarizability of their ionic core [15,16], we could go from contact interaction to Van der Waals interaction ($\sim 1/R^6$) or a resonant dipole-dipole interaction ($\sim 1/R^3$), exploiting a Förster resonance [17].

II Our quantum gas microscope with strontium atoms

The building of our experiment began in 2016. It was started at the obtention of an ERC grant[4] in 2015 by Marc Cheneau. The experiment was first developed by Marc Cheneau, Florence Nogrette, and Anaïs Molineri (Ph.D. student). They were then joined by Clémence Briosne–Fréjaville (Ph.D. student) in 2017 and then myself in 2019. We give here a brief overview of strontium properties and interests for quantum gas microscopes. Then, we present the outline of a typical experimental cycle.

II.1 Our microscope

Our setup for the quantum gas microscopy consist of an aspheric lens with a high numerical aperture (0.64) inside the vacuum chamber and about one centimeter away from the atoms. This scheme is directly inspired by experiments of the Quantum Optics groupd at Laboratoire Charles Fabry. This lens is used as the first optical element of our microscope and aims at collecting the fluorescence from the atoms, collimate the flux and send it to the other optics outside the vacuum chamber. This approach is different than the standard one, where in general a microscope objective outside the chamber (or glass cell) is used.

[4](Grant agreement No. 679408–DYNAMIQS)

II.2 The choice of strontium

As an alkaline-earth element, strontium features properties that differ widely from the alkali elements, which have been widely used in the cold atom and quantum gases community. The presence of two cycling[5] optical transitions with very different linewidth allow performing multi-stage Doppler cooling, usual broad-line laser cooling on the broad ($461\,\mathrm{nm}$, $\Gamma_b = 2\pi \cdot 31\,\mathrm{MHz}$) transition and, subsequently, laser cooling on the narrow red transition ($\lambda_r = 689\,\mathrm{nm}, \Gamma_r = 2\pi \cdot 7.4\,\mathrm{kHz}$) reaching temperatures in the range of the microkelvin.

The presence of the narrow transition also allows performing laser cooling in an optical lattice [18] with a single laser beam, in contrast with the case of alkali elements, which require two beams of different frequencies to perform Raman sideband cooling with a tailored effective narrow transition [19].

An additional interest of strontium is the presence of both bosonic and fermionic isotopes, allowing to study the propagation of the correlations in fermionic systems. The natural abundancies presented in Table 1, along with the scattering lengths [20]:

Table 1: Natural abundancies of strontium and scattering lengths in units of Bohr radius ($a_0 = 53\,\mathrm{pm}$), [20]

Isotope	Abundancy	Scattering length (a_0)
^{88}Sr (boson)	82.58%	-1
^{87}Sr (fermion)	7.00%	97
^{86}Sr (boson)	9.86%	830
^{84}Sr (boson)	0.56%	124

Divalent atoms are also expected to allow optical trapping of Rydberg atoms, where one electron is in a state of high principal quantum number while the rest of the atom behaves like an ionic core with a single active electron (the second valence electron) [16].

Finally, the presence of "ultra-narrow" transitions allows in principle to have single-site addressability for strontium atoms trapped in an optical lattice. For instance, the electric quadrupole transition $^1\mathrm{S}_0 \leftrightarrow {}^3\mathrm{P}_2$ can be used in the presence of a magnetic-field, as was recently reported by Trautmann *et al.* [21].

II.3 Outline of the experimental cycle

The main steps of the experimental cycle are summarized in the following:

1. An oven and transverse molasses are used to produce a collimated beam of atoms. The atoms are subsequently slowed down using a Zeeman slower.
2. The atoms are then trapped and cooled down by multi-step laser cooling exploiting both the broad and narrow transitions of strontium. This results in a cloud of a few million atoms at about $1\,\mu\mathrm{K}$.
3. The atoms are then loaded in an optical dipole trap (at $1064\,\mathrm{nm}$) formed by a pair of crossed interfering beams that will be called "crossed optical tweezer" or simply "transport trap". This second name is prompted by the fact that this optical

[5] The broad transition is in fact almost closed, see Figure 1.2.

tweezer is used to transport our atoms from a first chamber to a second chamber, respectively called the MOT/science chamber.
4. In the science chamber, the atoms are loaded in a second optical trap (vertical lattice trap) confining them in a horizontal planar configuration. There the cloud undergoes Bose-Einstein condensation. Then we turn on the horizontal lattice beams to transfer the condensate into a 2D square optical lattice.
5. From a known initial configuration, we abruptly change the lattice depth, and let the system evolve for a determined time.
6. When we want to stop the evolution of the system, the lattice depth is increased to its maximum value to suppress the tunneling between the sites.
7. The freezing of the dynamics marks the beginning of the "imaging phase". We shine a laser beam nearly resonant with the narrow transition so that the atoms scatter photons that are collected by a lens inside the vacuum chamber and sent to a camera, realizing an *in situ* image of the atoms in the square lattice.

The details of the implementation are described in chapters 1 to 3 and in the Ph.D. theses of my predecessors [22, 23]. Applying this protocol, we will be able to measure observables such as the atom number on each site and extract from that measurement correlators of the form $\langle s_i(t)s_j(t)\rangle$, where s_i is the parity of the atom number on site i.

III Outline of the manuscript

This thesis is organized into six chapters, which can be grouped into two parts. The first three chapters expose the results obtained on the experiment, albeit preliminary ones, at the time we are writing these words. Chapters 4 to 6 are concerned with the imaging with the microscope.

The first chapter is dedicated to presenting the experimental apparatus as it was in October, 2020, when the last Ph.D. student, Clémence Briosne–Fréjaville defended her thesis. Chapter 2 exposes modifications that were made on the transverse molasses to improve the collimation of the atomic beam. It includes simulations of the fluxes of atoms at the level of the MOT chamber as a function of the laser beams' shape and power. We also expose the experimental tests of the impact of the modifications on the setup that were guided by the simulated performances. Chapter 3 presents the advances that were made on the laser cooling sequence and the first successful transports of the atoms in the crossed optical tweezers between the two chambers.

In chapter 4, we present a new algorithm for the analysis of the microscope images based on an iterative least-square approach. We compare that model to a Wiener filter deconvolution which is often used in microscope experiments. We present the optical characteristic of our system, and we show that satisfying performances for the detection of atoms are expected even in the regime where the individual atoms are not optically resolved.[6] Apart from the case study of our system, we explored the performances of the reconstruction algorithms in other experimental configurations to identify the minimal requirements to obtain single-site and single-atom sensitivity in a quantum gas microscope experiment. We will see that our approach lead to high fidelity, and is fast and robust.

In chapter 5, we compute the dynamical polarizabilities of strontium atoms at 1064 nm.

[6] In the sense of the Rayleigh criterion

These calculations are performed both for the ground state ($5s^2\,{}^1\mathrm{S}_0$) and the excited state ($5s5p\,{}^3\mathrm{P}_1$). The knowledge of the gound-state polarizability is required for the trapping in the different optical dipole traps on the experiment (transport crossed optical tweezers and optical lattice). As exposed in chapter 6, the value of the excited-state polarizability is crucial for the imaging phase of the experiment; in particular, we show that the magnitude of the excited polarizability compared to that of the ground state changes the range of parameters that one can use for the laser beam exciting the fluorescence. In this last chapter, we describe simulations that were performed to simulate the dynamics of a single trapped atom in the presence of near resonant light. Specifically, we discuss the number of fluorescence photons that can be extracted from such an atom, and its lifetime in the trap as a function of the laser intensity and detuning.

To this day, the cooling and trapping of ^{84}Sr (and ^{88}Sr) are routinely obtained in our experiment. The transport of the cloud with the crossed optical tweezers is under investigation and gives promising results. The optical setup for the vertical confinement for the lattice is already built and the beams producing the periodic potential of the lattice will be added in the coming months. The imaging setup for the microscope is almost finished too, and the reconstruction algorithms for the microscope images are waiting for real images to process.

Chapter 1

Pre-existing experimental setup

In this chapter, we present the experimental setup for our experiment not as it is but as it was at the moment of the defense of Clémence Briosne–Fréjaville [23]. The experimental apparatus's different components and stages are described. The aim is to give an overview of the experiment. We summarize the main characteristics of each subsystem and their specificities. We will also describe the status and performances of the different parts of the experiment, which will motivate the changes and progress made since then. The experimental apparatus is represented schematically in Figure 1.1.

The different stages of an experimental cycle, which is still prospective for the last steps, go as follows. We start with a hot vapor of strontium exiting the enclosure of an oven in the form of a pre-collimated atomic beam. This atomic beam goes through a collimation stage, performed by transverse molasses. The beam is slowed down using a Zeeman slower. Those atoms enter a first vacuum chamber, referred to as "the MOT chamber", where they are trapped and cooled using sequentially two magneto-optical

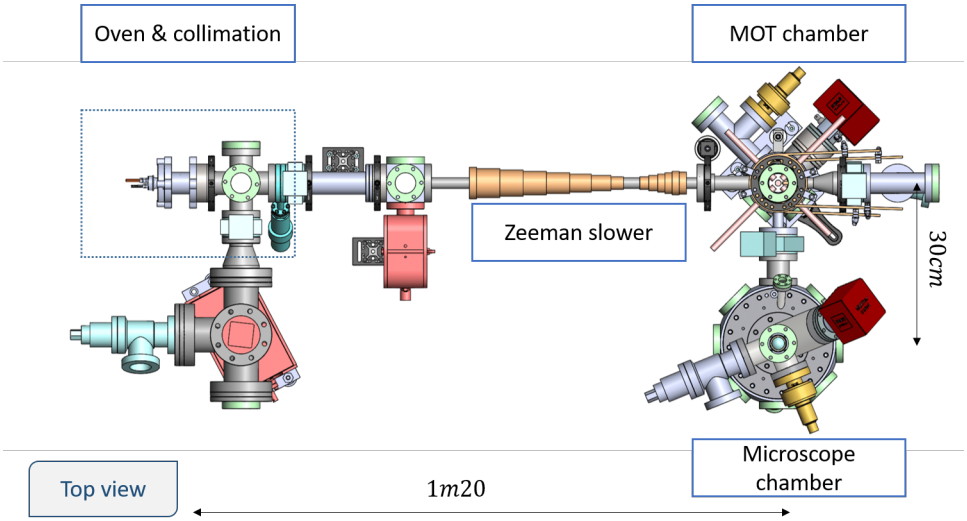

Figure 1.1: Top view of the vacuum system obtain with SOLIDWORKS©. The red components represents ionic+getter pumps or vacuum gauges.

traps (MOT) on two different transitions. At the end of the cooling in the MOTs, we load the cold cloud ($T \sim 1\,\mu K$) into an optical tweezer. This tweezer is then used to transport the atoms from the MOT chamber to a second chamber, which will be called "the science chamber". In that chamber, we transfer the atoms into an optical lattice, in a 2D configuration. The atoms trapped in this lattice will be in the focal plane of an aspheric lens under a vacuum which will serve as the first optics of a microscope objective to image *in situ* the atoms.

At the end of this chapter, we summarized where the design of the different subsystems are described in detail in the thesis of Anaïs Molineri [22] and Clémence Briosne–Fréjaville [23].

1.1 Laser system for cooling of strontium

The relevant levels for our experiment are summarized in Figure 1.2. In strontium, like in the other alkaline-earth-like atoms, two transitions are available for laser cooling. The transition at 461 nm will be called "the broad transition" ($\Gamma_b = 2\pi \cdot 31\,\text{MHz}$) or , alternatively, "the blue transition"; while the transition at 689 nm will be referred to as "narrow" ($\Gamma_r = 2\pi \cdot 7.4\,\text{kHz}$) or "red".
We will start by describing our experiment's laser system used for laser cooling.

1.1.1 Blue laser system

The primary laser source at 461 nm is an extended cavity diode laser (ECDL) from *Toptica*.[1] This laser produces about 60 mW of laser power at 461 nm.

[1] DL Pro HP

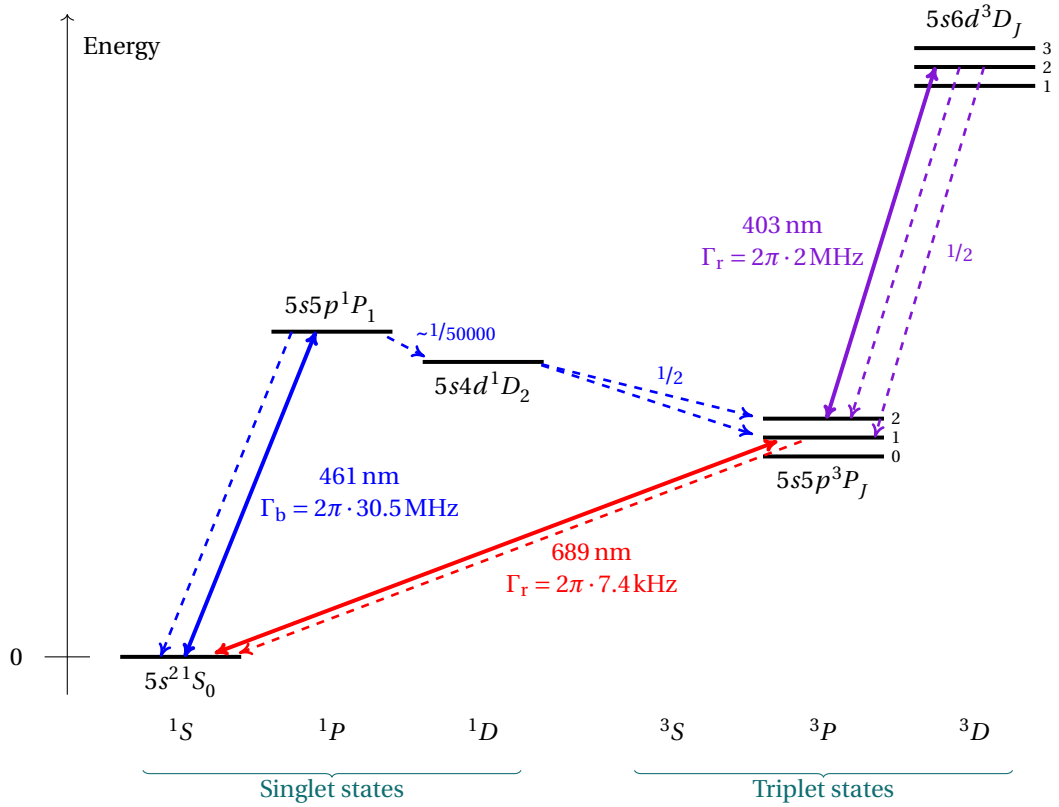

Figure 1.2: Level diagram with the relevant transitions for our experiment. The solid lines represent the transitions that are driven by our lasers. The dashed lines represent spontaneous decays. The fractions on the dashed line indicate the branching ratios of the different decay channels. As discussed later, the branching ratio of 1/50000 is not sometimes evaluated to be 1/21000 [18, 20, 24]. *Figure adapted from Clémence Briosne-Fréjaville* [23], itself adapted from S. Stellmer thesis [20].

1.1.1.1 Stabilization of the laser's frequency

The frequency stability of that laser is ensured by locking the laser on a spectroscopic signal from a hollow-cathode lamp.[2] More precisely, the spectroscopy scheme that is implemented is a modulation-transfer spectroscopy. This scheme, as described in [22, 25], produces a Doppler-free absorption signal at the resonance frequency for ^{88}Sr.[3] From this, we obtain an error signal with a dispersive shape of width on the order of the natural linewidth of the blue transition. We use this error signal and the PID module of the DLC controller to lock the laser's frequency on resonance with the blue transition of ^{88}Sr, via a retroaction on the piezo actuator controlling the external cavity's length.

Since we want to use ^{84}Sr, in our experiment, we introduce a frequency shift on the laser beam sent to the spectroscopy cell in order to compensate for the isotopic shift between ^{88}Sr and ^{84}Sr on the blue transition ($-270.8\,\mathrm{MHz}$). This frequency shift is introduced by a double-pass AOM that is used to switch from one isotope to the other.

1.1.1.2 Amplification using master/slave-injection locking

The output power of our Toptica laser ($\sim 60\,\mathrm{mW}$) is insufficient to cool our atoms efficiently. We use the injection-lock technique with "slave" laser diodes,[4] to amplify the output of the Toptica laser, which will be referred to as the "master laser", in the following.

The idea behind the injection-locking amplification is described in [26] and goes as follow. The master beam with a narrow spectrum ($\sim 100\,\mathrm{kHz}$) but low power is injected into a laser diode with higher output power but a spectrum that is neither narrow nor stabilized. The master beam will use the gain from the laser diode, giving rise to lasing at powers similar to the output power of the laser diode but with the master laser's spectrum. We use this procedure with three laser diodes. Resulting in three independent lasers with output powers of about 100 mW at the output of the diodes and 24, 20, and 39 mW on the atoms.[5] The implementation is summarized in Figure 1.3.

1.1.2 Red laser system

The laser system at 689 nm is very similar to the one in the blue. The primary source is again an ECDL from *Toptica*[6] with an output power of 25 mW.

1.1.2.1 Stabilization of the laser's frequency

The stabilization of the red laser is done using the Pound-Drever-Hall (PDH) technique on a high-finesse ($\mathcal{F} \sim 19\,000$) cavity from *Stable Laser System*, as described in the thesis of C. Briosne-Fréjaville or in E. Black's *Notes on PDH technique* [27]. This scheme

[2] ref: L2783-38NE-SR, from *Hamamatsu*

[3] ^{88}Sr is the most abundant isotope in natural strontium. It thus has the strongest absorption signals. A deformation of the spectroscopy signal can be observed on the side of the dispersive signal. The contribution of ^{86}Sr (natural abundancy of about 10%) to the spectroscopy signal can explain this distortion.

[4] ref: NDB4216E (100 mW) from *Nichia*

[5] Injection losses of the acousto-optic modulators and of the optical fibers used to transport and split the different beams.

[6] DLC Pro HD

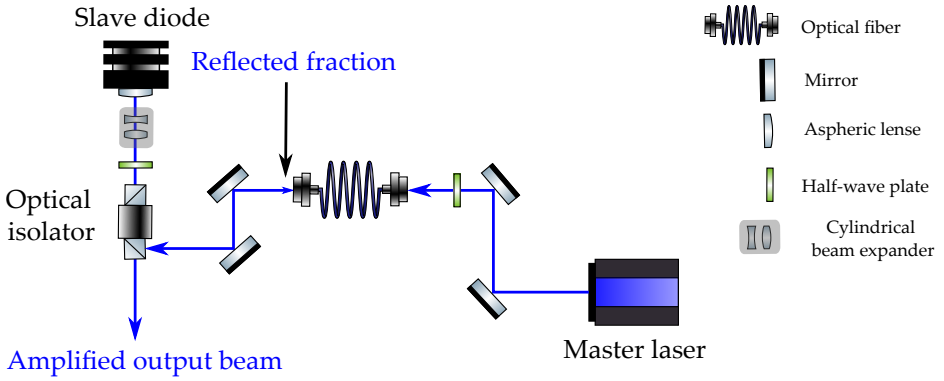

Figure 1.3: Injection lock amplification scheme. The beam from the master laser is sent into the slave diode that will amplify the incoming light. An optical isolator is used to reduce optical feedback from the following elements on the path of the output beam. It allows the separation of the incoming injection beam and output amplified beam. The optical fiber enables control of the mode matching between the injection beam and the output of the slave diode by maximizing the injection of the reflected fraction into the fiber. *Figure adapted from A. Molineri* [22].

produces a narrow spectrum,[7] compared to the natural linewidth of the red transition, and a frequency that is stable on short-time scales with a slow linear drift ($\sim 500\,\mathrm{Hz/s}$) [23,28].

1.1.2.2 Amplification using master-slave injection locking

We inject a slave diode[8] with the master red laser to obtain an output power of 100 mW via the same injection-locking protocol as for the blue laser. Figure 1.4 shows the spectrum of a beat note between the master beam and the amplified beam. This spectrum shows that the amplification process does not degrade the spectrum of the master laser significantly.

1.1.3 Purple laser system

A third ECDL laser from *Toptica*[9] is used in the experiment (the use of that laser is described in section 1.3.2). Its frequency is not stabilized and must currently be monitored on a wavelength meter and adjusted manually at least every hour. The output power is about 30 mW.

[7] Without an independent narrow laser to perform a proper measurement, the estimation of the linewidth is not very reliable. We estimate the linewidth to be in the kilohertz range.

[8] ref: HL6750MG from *Thorlabs*

[9] ref: DLC Pro HD

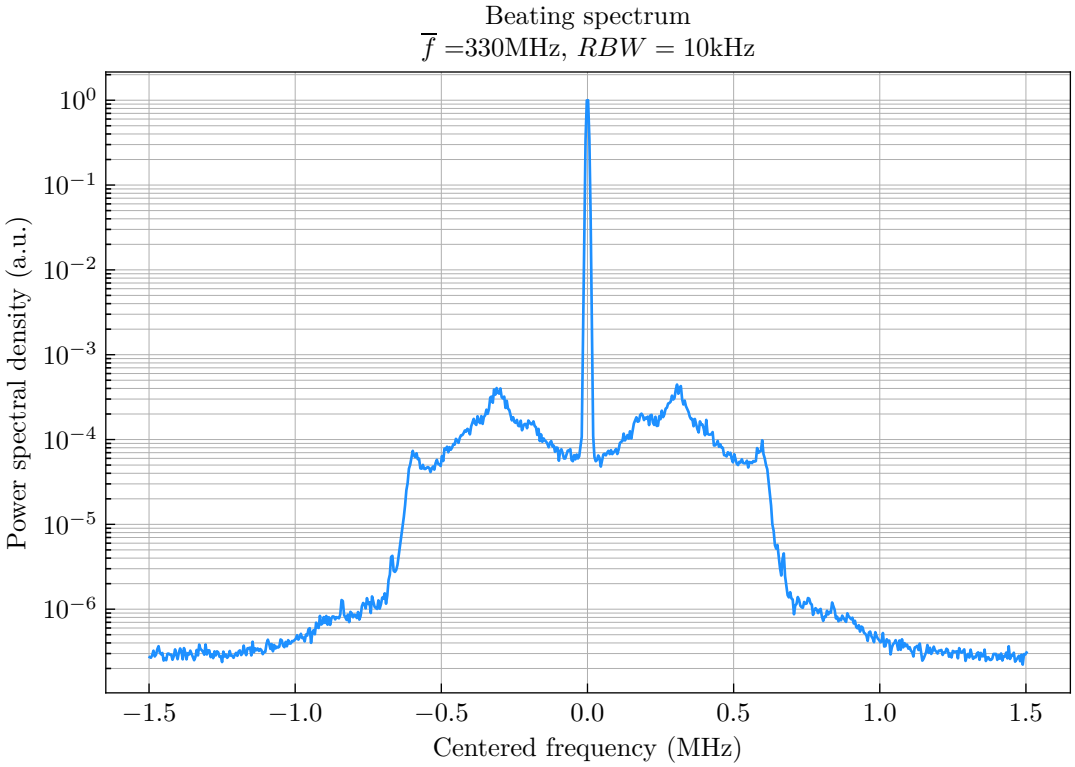

Figure 1.4: Beat note between the master and the slave red lasers. This signal is obtained by overlapping the two beams on a photodiode, monitored on a spectrum analyzer. The central frequency $\overline{f}$ of the spectrum is at 300 MHz; this shift is due to the AOMs on the beam paths. The resolution bandwidth (RBW) is set to 10 kHz, which is on the order of Γ_r. We observe a peak with a width limited by the RBW on top of a pedestal that is three decades lower than the main peak.

1.2 Production of a slow collimated beam of strontium

1.2.1 Strontium oven

We produce an atomic beam of strontium by creating a hot vapor inside an oven. Our oven was design and manufactered by SYRTE laboratory from Observatoire de Paris, the design is based on the one described in Schioppo *et al.* [29]. The oven consists of a reservoir containing about 10 g of metallic strontium. The reservoir is heated at about 500 °C. The heating is done under vacuum. Ceramic spacers and a copper thermal shield provide thermal insulation of the vacuum system, reducing heat conduction and radiative transfer. The hot atomic vapor escapes the reservoir through an aperture filled with micro-tubes. The micro-tubes are there to ensure a pre-collimation of the vapor so that we obtain an atomic beam that is not too divergent (see section 2.2.3.3). At the time of the thesis of C. Briosne-Fréjaville, the oven had recently been changed. The characterization of its divergence had not been performed yet. We will describe this measurement in section 2.3.1. A transverse cut is represented in Figure 1.5.

1.2.2 2D transverse molasses

At the oven's output (about 2 cm from it), we have a second collimation stage of the atomic beam using transverse molasses. The idea of transverse molasses is to use two pairs of retro-reflected beams to cool the atoms in the plane transverse to the propagation axis. The molasses dampen the initial transverse velocity, aligning it with the propagation axis.

We use the broad $^1S_0 \leftrightarrow {}^1P_1$ transition for that stage to obtain high radiation pressure forces. The available laser power was 12 mW (70 mW nowadays) per direction.[10] The beam's waist radii were 5 mm. The effects of the molasses were not noticeable at the time. This absence of effect might have been caused by the difficulty to align the molasses. Three main issues were identified:

- the intensities were too low to saturate the transition,
- the interaction time limited by the size of the beams was too short,
- the output of the oven was too far away, allowing the atomic beam to expand before it could be collimated.

The first two issues point toward increasing the beam sizes and laser power. The last one was the motivation for changing our old oven to the one from SYRTE. We will discuss in depth the optimization and performances of the transverse molasses setup in chapter 2.

1.2.3 Zeeman slower

After the collimation, the atomic beam propagates for 28 cm through a differential vacuum hole and arrives at the Zeeman slower. The details of the design and principle of the Zeeman slower are available in [22]. We will only summarize the main characteristics of our slower.

[10] This is the power in one of the two axes for a single pass through the atomic beam. Since the beams are retroreflected, we have about twice that power per axis.

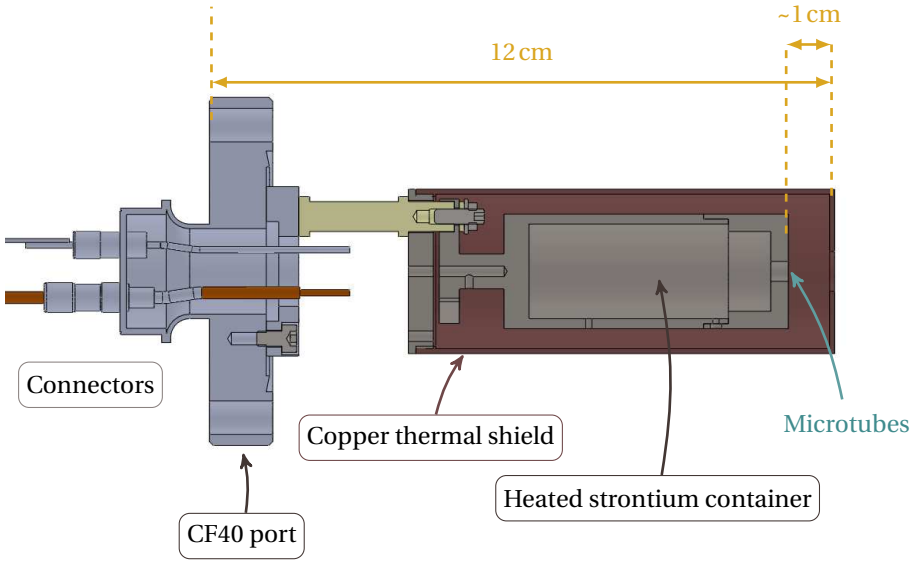

Figure 1.5: Cut of the strontium oven (side view). The connectors are used to supply electrical power to the tantalum cable heating the container, and to measure the oven's temperature. The thermal shield made of copper protects the nearby vacuum elements from the black-body radiation of the oven. *SolidWorks* file provided by SYRTE Laboratory.

Our Zeeman slower is 30 cm long. Like the transverse molasses, it operates on the ${}^1S_0 \leftrightarrow {}^1P_1$ transition. The internal diameter of the Zeeman slower's tube is 6 mm, granting further differential vacuum between the atomic source and the rest of the experiment. This small diameter also requires relatively good collimation of the atoms. The laser beam used for the Zeeman slower has a power of ~ 20 mW, a waist radius of a few millimeters, circular polarization, and a detuning of -435 MHz. The coils were chosen so that they can slow atoms with velocities under $420\,\mathrm{m \cdot s^{-1}}$, using a magnetic field difference of 600 G.

1.3 Magneto-optical Traps

In this section, we present the cooling sequence of strontium. This is a multi-stage cooling procedure, with the following steps defined in the subsequent sections:

1. Capture and pre-cooling in a magneto-optical trap (MOT) on the broad transition.
2. Accumulation of pre-cooled atoms in a metastable state trapped in the MOT's quadrupole magnetic field.
3. Repumping to the ground state and broadband MOT on the narrow transition.
4. Narrow-line MOT on the narrow transition.

1.3.1 Blue MOT

The atoms exiting the Zeeman slower are captured in a magneto-optical trap on the broad transition.We use three pairs of retro-reflected beams with circular polarizations. The laser beams have diameters of around 10 mm, giving rise to intensities on the order

of $13\,\mathrm{mW/cm^2}$ (for each of the 6 beams), that is, $I = 0.3 I_{\mathrm{sat}}$. The magnetic field gradient of around $64\,\mathrm{G/cm^2}$ is generated by a pair of coils close to an anti-Helmotz configuration. The detuning is set to $\Delta_{\mathrm{MOT}} = -2\pi \cdot 30\,\mathrm{MHz}$.

At the time of Clémence's thesis, the characterization of the blue MOT in terms of the number of atoms and temperature had not been performed yet. We present results on these characterizations in section 3.1.

1.3.2 Reservoir of metastable atoms and repumping

The $^1\mathrm{S}_0 \leftrightarrow {}^1\mathrm{P}_1$ transition on which the blue MOT is operated is not perfectly closed. From the $^1\mathrm{P}_1$ state, an atom can decay to the $5s4d\,{}^1\mathrm{D}_2$ state with a small branching ratio of 1:50 000 [20, 24] (or 1:21 000, according to [18]). The atom in that state can then decay to $5s5p\,{}^3\mathrm{P}_1$, in which case it returns to the ground state in 22 µs, or it can decay to $5s5p\,{}^3\mathrm{P}_2$. The latter is a metastable state with a lifetime on the order of 100 s [30] in a vacuum chamber at ambient temperature.[11] The atoms in $^3\mathrm{P}_2$ with $m_J = +1, +2$ are trapped in the quadrupolar magnetic field of the MOT.

Those trapped atoms will accumulate as long as the blue MOT is operated. The lifetime of atoms in the magnetic trap is limited by the collisions with the background gas. It was measured previously at 16 s [22]. Given the small branching ratio from the MOT to the metastable state, the atoms falling in the magnetic trap typically had time to go over multiple cycles on the cooling transition, leading to temperatures in the magnetic trap that should be comparable to the temperature of the blue MOT ($\sim$ mK).

Once enough atoms have accumulated in the magnetic trap, we turn off the blue MOT beams and close the atomic shutter positioned at the oven's output. We can then turn on the repumper laser at 403 nm on the $5\,\mathrm{s}^2\,{}^1\mathrm{S}_0 \leftrightarrow 5s6d\,{}^3\mathrm{D}_2$ transition. The purpose of the repumping stage is to transfer atoms from the metastable $^3\mathrm{P}_2$ state to the $^3\mathrm{P}_1$ state. Simultaneously, the experiment's parameters are switched to those used for the broadband red MOT described in the next section. The frequency of the 403-nm laser is not locked. The repumping was done by scanning the frequency over about 100 MHz. The repumping beams are overlapped with the three blue MOT beams using a fibered cluster from *Schäfter&Kirchoff* that features one input fiber per wavelength and has three outputs.

1.3.3 Broadband red MOT

1.3.3.1 The problem of recapture by the red MOT

While the repumper laser is acting, the magnetic field gradient is ramped down from 64 G/cm to about 1 G/cm.

Given the difference in the natural linewidths between the broad and narrow transition ($2\pi \cdot 31$ MHz and $2\pi \cdot 7.4$ kHz), the pre-cooled atoms are still too hot to be captured directly in a MOT on the red transition. More precisely, the temperature at the end of the blue MOT, which we expect to be conserved in the magnetic trap and, after repumping, is on the order of the Doppler temperature, 1 mK. Thus, the velocity distribution of the atoms

[11] The lifetime of that state is limited by the background black-body radiation [30].

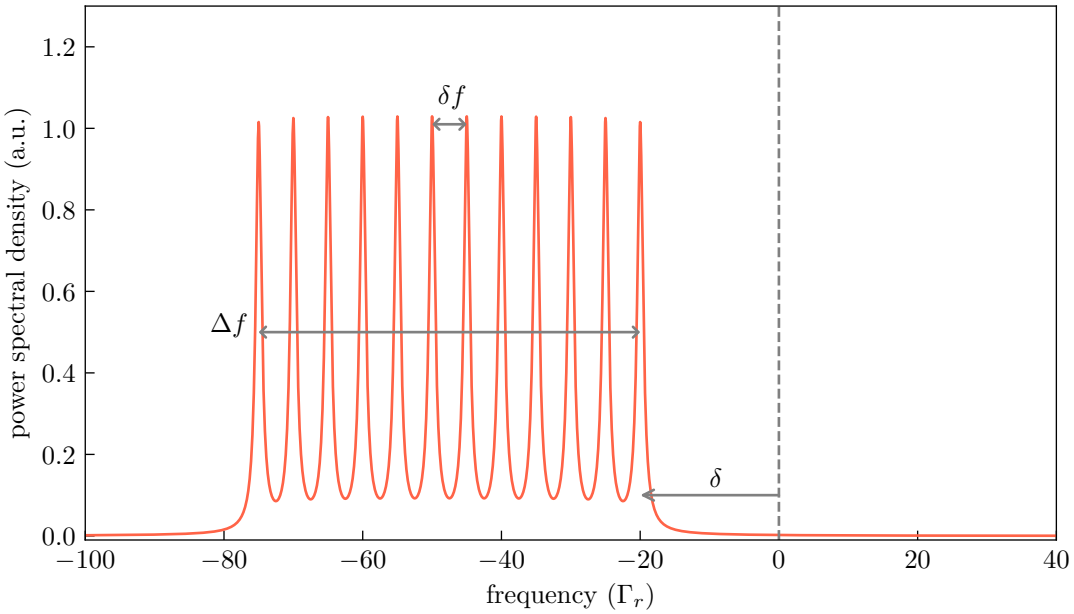

Figure 1.6: Qualitative picture of the frequency comb's spectrum generated by frequency modulation. The comb spacing has been increased for readability and the variation of the peaks heights has been neglected. A realistic comb is displayed in Figure 1.7. The power spectral density is plotted in arbitrary units.

goes well beyond the capture velocity of the red MOT. The thermal velocity (RMS) for strontium 88 at 1 mK is

$$v_{\text{th}}(T = 1\,\text{mK}) = \sqrt{\frac{3k_B T}{m}} = 0.5\,\text{m}\cdot\text{s}^{-1}\,, \tag{1.1}$$

while the capture velocity [31] is

$$v_{\text{capt}} \sim \frac{\Gamma_r}{k_r} = 5\,\text{mm/s}\,, \tag{1.2}$$

where k_r is the norm of the wavevector of the red laser $k_r = 2\pi/\lambda_r$.

1.3.3.2 Qualitative description of the broadband red MOT

To increase the capture velocity of the red MOT, we broaden the spectrum of the laser via frequency modulation. This gives rise to a comb-like structure where we set a comb spacing on the order of the natural linewidth of the red transition Γ_r. The comb is parametrized by its width Δf, the peak spacing δf, the saturation parameter for each peak, and the detuning from the resonance δ. δ is the detuning for the peak closest to resonance. These parameters are summarized in the qualitative picture in Figure 1.6.

The idea behind that technique is that the different frequencies in the laser's spectrum will interact with atoms of different velocity (or position) classes and cool each atom down to a velocity that will be on resonance with the next peak in the comb.

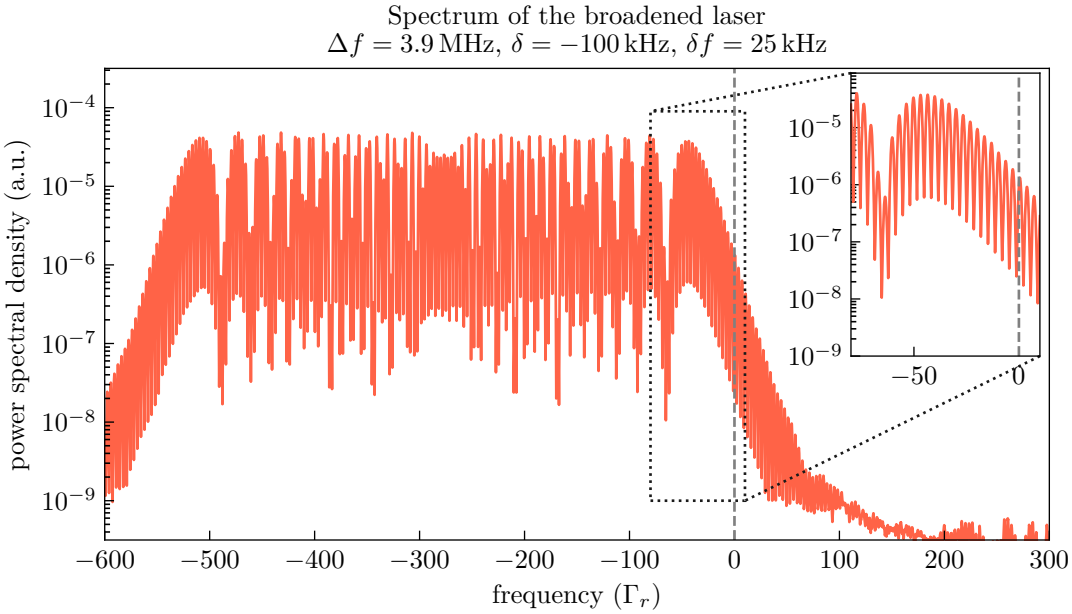

Figure 1.7: Spectrum of the beating between the (unmodulated) master red laser and the frequency-modulated beam after amplification by the slave diode. The frequency offset of the beating has been removed. The waveform used for that modulation is a symmetric triangular signal of amplitude corresponding to $\Delta f = 3.9\,\mathrm{MHz}$ peak-to-peak and a frequency of $\delta f = 25\,\mathrm{kHz}$. The final detuning δ is set to $-100\,\mathrm{kHz}$. We see that the envelope of the comb is not the ideal rectangle described in the qualitative picture above. The comb is not perfectly flat, and the edges are not infinitely sharp. This last effect places a fraction of the laser power to be on resonance or even on the blue of the atomic transition. However, this does not prevent the formation of the broadband red MOT. The resolution bandwidth for that acquisition was 10 kHz.

1.3.3.3 Implementation of the broadband red MOT

The frequency broadening of the laser at 689 nm is implemented by a frequency modulation on a double-pass acousto-optic modulator (AOM). The waveform of the modulation is a triangle signal at a frequency of 25 kHz with an amplitude such that the peak-to-peak modulation of the frequency is about 2 MHz. This generates a comb-like structure on the spectrum of the 689-nm laser, with a peak spacing of 25 kHz and width of 3.9 MHz (see Figure 1.7). An offset can also tune the detuning of the center-of-mass of the comb on the RF signal generator; this allows controlling the detuning δ of the peak closest to resonance, which sets the final temperature of the cloud for a given intensity [31].

The saturation parameter for each frequency component is controlled via the diffraction efficiency of the double-pass AOM. The intensity of the laser beam is chosen so that the saturation parameter is on the order of 1.

1.3.4 Narrow-line red MOT

Once the broadband MOT has slowed down all the atoms, we can stop the modulation to get a “monochromatic” laser field. From there, temperatures on the order of the µK (or a

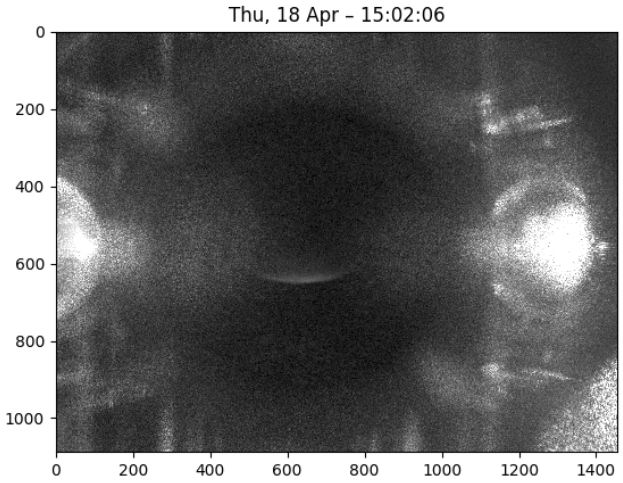

Figure 1.8: Raw picture of the first MOT on the narrow transition obtained by the team in 2019. The atoms are at the center of the picture with a crescent shape; the rest is stray light from the MOT beams. This configuration was obtained for a detuning of around $-3\,\mathrm{MHz}$, magnetic field gradient of a few G/cm and a saturation parameter of about 1. The estimated temperature is of about $70\,\mu\mathrm{K}$, significantly above the minimum temperature.

fraction of a microkelvin can be achieved). For instance, 400 nK was achieved by Katori *et al.* [32]). Which is off by only a factor of two from the simple[12] Doppler theory with a limit temperature of 175 nK, on the order of the recoil limit $\hbar^2k^2/2mk_B = 240\,\mathrm{nK}$ [31].

It is to be noted that the typical detunings in strontium experiments are usually far from the usual values on the order of Γ on a broad transition. Detunings of a few tens to a hundred of Γ_r are not uncommon (see, for instance, [20,32]).Given the low temperatures that are attained when the laser is detuned sufficiently from the resonance, the atomic cloud takes the form of a shell, as can be seen in Figure 1.8. This shape arises because the atoms are resonant with the laser only on a surface of constant magnetic field (ellipsoid in our case) and are cold enough that they fall under gravity and accumulate at the bottom of the trap.

1.4 Optical dipole traps system

In our experiment, we plan to use optical dipole traps (ODT) at two satges of our experiment:[13]

- The first one is to transport the atoms from the MOT chamber to the science chamber. This is implemented with an interfering crossed optical tweezer.
- The second ODT setup is the optical lattice. It is formed by three pairs of beams. The first pair is formed of two beamscrossing at an angle of 6° to produce horizontlae interference fringes, the atoms are trapped in a single fringe which prrovides a confinement in a 2D plane. The other two pairs are used to produce a periodic potential in the horizontal plane; they are formed by to retro-reflected beams along $\vec{X}$ and $\vec{Y}$ (see Figure 1.11), creating a square lattice.

In the following, we will describe the laser system used to generate those traps and give the details of each trap's beam configuration.

[12] "Simple" here means standard Doppler theory which is only valid for a broad transition.

[13] The principle of optical dipole traps is described in Chapter 5 and appendix B, where the calculations of the lightshifts for the relevant states are described in detail.

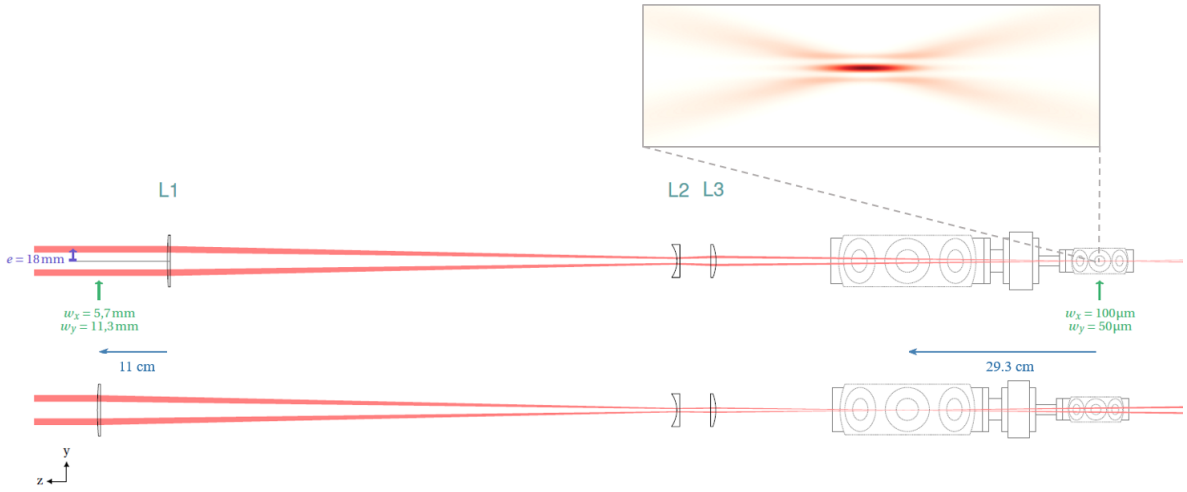

Figure 1.9: Schematic side view of the transport setup between the two vacuum chambers. The inset at the top represents a zoom of the crossing of the two beams with a single bright fringe at the center. The angle has been magnified for better visualization. *Adapted from [23].*

1.4.1 Laser system

To produce our optical dipole traps, we use to laser from ALS[14] at 1064 nm with nominal output powers of 50 W. That wavelength was chosen to ensure low scattering rates,[15] while keeping reasonable polarizability of the atoms. The low scattering rate ensures that the trapping potential is conservative and, in particular, that the heating from the scattering of trap photons will be negligible. Another advantage of that wavelength is that high-power lasers are readily available at 1064 nm. Since it is a standard wavelength, it reduces the needs for custom designs of optics or coatings.

1.4.2 Transport

The transport from the MOT chamber to the science chamber is done using an interfering crossed optical tweezer. The design of this trap was done by Clémence Briosne-Fréjaville and is presented in great detail in her thesis [23]. At the end of her thesis, this subsystem had been implemented, but not tested on the atoms. We will briefly summarize the general implementation and the expected key features in the following.

1.4.2.1 Principle of the interfering crossed optical tweezer

The transport method that was chosen relies on a moving optical dipole trap. The optical dipole trap is localized in the focal plane of a moving lens. The movement of the trap is

[14] ref: ALS-IR-1064-50-1-SF

[15] For instance, the scattering rate for a strontium atom in the ground state is on the order of $3\,s^{-1}$ for an intensity of $100\,kW/cm^2$, which is the order of magnitude of the intensities in the optical lattice at its maximal depth.

done by a translation stage[16] that moves the lens and hence the trapping laser's focus.

In our scheme, the ODT is generated by a pair of laser beams crossing at their waist at an angle of 1.2°. This scheme benefits from increased confinement along the transport's axis compared to the transport at the focus of a single beam (see Figure 1.9). A peculiarity of our system is that we chose to have interfering beams, which means that an interference pattern forms at the crossing of the beams with fringes modulating the intensity along the vertical direction. This configuration results in increased peak intensity at the center of the trap,[17] and a stronger gradient of intensity in the vertical direction, providing steeper trapping in the vertical direction, transport direction, and a deeper trap.

1.4.2.2 Overview of the optical setup

The optical setup to generate the transport ODT comprises two critical parts. The first one is the separation of the initial laser into two beams that will form the arms of the crossed trap. The second one is the optical system that does the translation of the focal point of the crossed laser beams.

The separation of the beam into two is depicted in Figure 1.10; it is done using a polarization beam splitter (TFP: thin film polarizer). The first one splits the incoming beam into two beams of equal intensities, the power balance being tuned with a half-wave plate. One beam is transmitted directly, while the reflected one is sent to a retroreflection stage containing a rotating phase plate, a quarter-wave plate, and a mirror for retroreflection. The rotating phase plate enables control of the relative phase of the two arms of the trap. The quarter-wave plate in double-pass ensures transmission through the second TFP. Since the two beams have different paths in this region of the setup, the stability of the setup is critical because we need interferometric stability of the optical phase, to have a steady ODT on the atoms.

After the separation of the two beams are sent to the moving lens. This lens is followed by a pair of lenses mounted in an afocal configuration. This system produces a transverse magnification $g_y = 1.6$, giving rise to a longitudinal magnification of $g_x = g_y^2 = 2.56$. It is used to magnify the displacement of the moving lens. A displacement of 12 cm of the lens resulting in a movement of 30 cm of the trap.

1.4.2.3 Expected characteristics

The beam profile characteristics at the trap position are planned to be the following. The estimated power is 35 W, and the waist radii of each beam are 50 µm in the vertical direction and 100 µm in the horizontal direction transverse to the transport axis. The angle between the beams is 1.2°, resulting in fringes of period 50.8 µm in the vertical direction.

This would result in a trap depth of about 500 µK = 10 MHz, which is well above the expected temperature of the cloud after the cooling on the narrow transition, allowing, in

[16] ref Newport XMS 160

[17] The contrast of the interference pattern will not be perfect because the polarization of our beams is contained in the vertical plain containing the beam (xz-plane of Figure 1.10). Thus, the two beams' polarizations will be "almost" vertical with an angle between the polarization of 1.2°. Thus, the interferences' contrast is given by $\cos(1.2°) = 0.9998$. The impact of this small angle on the intensity pattern will be neglected in the following.

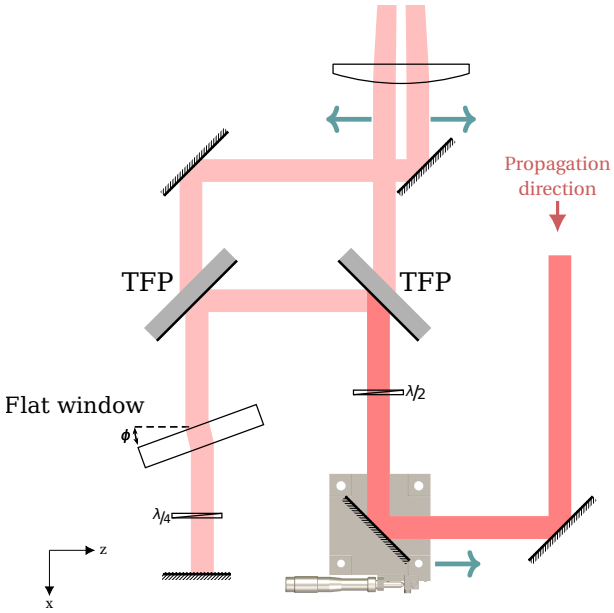

Figure 1.10: Separation of the laser beam generating the transport trap into two arms. The TFP (thin film polarizers) act as polarizing beam splitters. A phase plate (flat window) is introduced on the path of the retro-reflected arm to introduce a controllable phase shift. One mirror is mounted on a translation stage, enabling control over the spacing between the two arms ("optical accordion" with movements represented by the green arrows) and thus controlling the angle between the transport beams. *Figure adapted from [23]*

principle, the transfer of almost all the atoms from the red MOT to the transport trap. The trap frequency[18] along the transport axis is expected to be of 16 Hz. These parameters should permit the transport of the atoms from the MOT chamber to the science chamber in 1.5 s. For more details on the protocol of transport, characteristics of the trap, and constraints of the design, we refer the reader to the thesis of C. Briosne-Fréjaville [23].

1.4.3 Optical lattice

Once the atoms have been transported to the science chamber, we need to transfer them from the transport trap to the 2D optical lattice. In this section, we describe the expected characteristics of the lattice setup. A top view of the two chambers displays the different axes for the optical lattices is represented in Figure 1.11. The two axes are identical. In order to avoid interferences between the axes of the horizontal lattice, the different beams are shifted in frequency by AOMs; Table 1.1 summarizes the shifts for each axis. The confinement in the vertical direction is provided by an independent laser, it should be naturally at a frequency different from the horizontal beams.

Trap	Shift (MHz)
Horizontal trap (X)	80
Horizontal trap (Y)	90

Table 1.1: List of the frequency shifts for the different trapping beams for the optical lattice.

[18] extracted from the harmonic approximation at the minimum of the trap potential

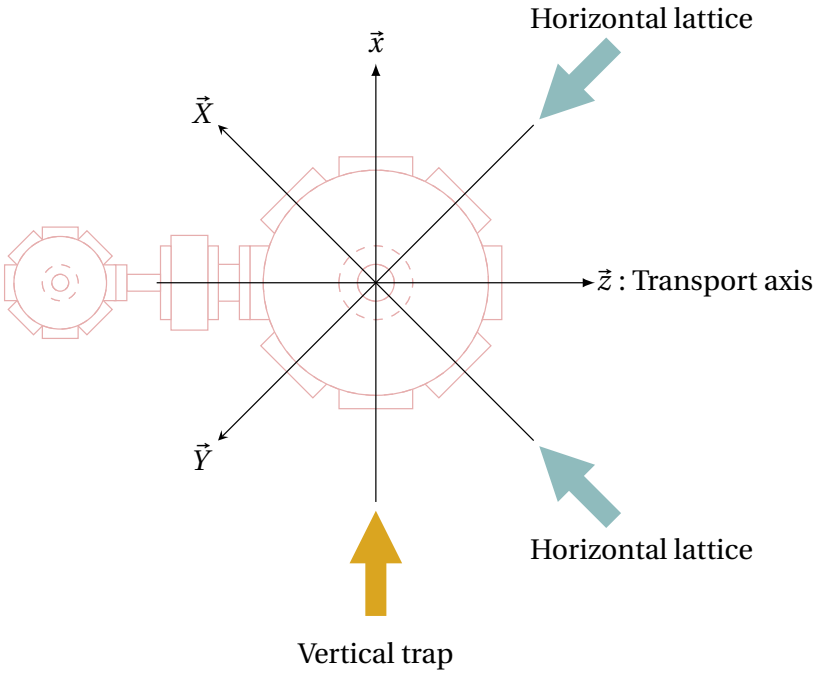

Figure 1.11: Top view of the two chambers, MOT on the left and science on the right, with the definition of the different axes. The axes of the optical lattice setup will be capitalized, and those of the transport and the MOT chamber will be lower case letters.

1.4.3.1 Vertical confinement

The confinement in a 2-dimensional geometry is done by a pair of interfering beams crossing at an angle of 6°, with waist radii of 60 µm along the vertical direction and 500 µm in the horizontal direction. The configuration is similar to that of the transport trap, and the optical setup is almost identical in its principles. To keep the system relatively simple, we use the TFP in transmission resulting in almost vertical polarizations (z-direction in Figure 1.10) of the two beams. This causes a minor loss of contrast in the interference pattern. Since the angle between the beams is small (6°), the loss of contrast is $1 - \cos(6°) = 1\%$.

This trap is generated from a second ALS laser at 1064 nm and 50 W of the same model as the one used for the transport trap. The available power on the atoms was estimated to be 35 W. The period of the interference pattern is 5.1 µm. From these parameters, we expect a trap depth of 80 µK = 1.7 MHz with a trap frequency of 12.6 kHz in the vertical direction.

1.4.3.2 Horizontal lattice

For our experiment, we will implement a 2D square lattice. The 2D confinement is provided by the vertical trap described above. The periodic potential is created by two pairs of retro-reflected beams (one along $\vec{X}$ and the other along $\vec{Y}$ see Figure 1.11), each beam is polarized vertically.

Those two pairs of beams will be generated from the same laser as the transport trap. This is possible since horizontal lattice and transport will not need to operate simultaneously. The commutation from one setup to the other is done using an acousto-optic modulator. The estimated available power is 17.5 W per axis, and the lattice period will be $\lambda/2 = 532$ nm. The trapping frequencies on one site in the horizontal plane will be

identical and equal to 76 kHz for a trap depth of about 33 µK = 0.7 MHz, at full power.

1.4.3.3 Status of the optical lattice by the end of 2020

The design of the optical lattice setup was completed during the thesis of Clémence, and most of the optics had been purchased. The implementation had not been started at that time.

1.4.4 Imaging of the atoms in the 2D optical lattice

For our experiments, we want to study our atomic sample in real space by direct imaging. For that, we need two ingredients, photons emitted by the atoms trapped in the optical lattice and an optical system to collect those photons and image the sample onto a camera. The imaging onto the camera will be discussed in chapter 4, while the fluorescence of the trapped atoms will be presented in chapter 6. This part will present the optical system inside the vacuum chamber and the general strategy for imaging the atoms.

1.4.4.1 Imaging configuration

At the end of an experiment, we want to freeze the dynamics of the atoms in the lattice by suppressing their ability to tunnel from site to site. For that purpose, we will ramp up rapidly the power of the optical lattice beams to their maximum value. We will then send a laser beam nearly resonant with the narrow transition and let the atoms fluoresce. The scattering of photons from this beam should heat the atoms trapped on a single site of the lattice, eventually leading to their loss before the end of the imaging. We will see in chapter 6, that by choosing the parameters adequately for that beam, we can introduce laser cooling(s) that partially balances this heating. This laser beam is oriented so that its wavevector has similar projections on all the axes of the optical lattice, which is a requirement imposed by the single-beam laser-cooling scheme (see chapter 6). Due to mechanical constraints in the design of the vacuum chamber, the projections on the lattice axes will not be equal. Instead, the wavevector will have projections of 0.61 for the vertical axis (normal to the plane of atoms), 0.53 for one horizontal axis, and 0.59 for the other.[19] We will see in chapter 6 that this should not have a substantial impact.

1.4.4.2 Optical system for the microscope

The first lens of the microscope objective is placed within the enclosure of the vacuum chamber.[20] This lens is an aspherical lens from *Edmund Optics*;[21] the focal lens is 18.75 mm, and the unmounted numerical aperture is 0.66. Once mounted, this lens has a numerical aperture of 0.64, which is the relevant value for our system. The role of this lens is to ensure efficient collection (hence the high numerical aperture) and collimation before crossing the viewport of the chamber. The presentation of the rest of the optical system will be postponed until chapter 4.

[19] The angles are 52.5° from the vertical axis instead of 54.75°, and 45° ± 3.2° for the horizontal axes.

[20] This setup is directly inspired by the design of two experiments in the Quantum Optics group at Laboratoire Charles Fabry.

[21] ref: 69-141 from *Edmund Optics*

This setup presents the advantage of long working distance and, thus, easier optical accesses. It also does not require the design of a custom high-performance microscope objective. As we will see in chapter 4, one drawback is that our setup is not expected to be diffraction-limited, requiring more elaborate image processing algorithm to analyze the images.

1.5 Conclusion

We presented an overview of the design of the experiment and its implementations or expected results. The details of the designs are present in the theses of Anaïs Molineri [22]:

- First version of the oven and optical molasses,
- Zeeman slower,
- Magneto-optical traps setups,
- Laser systems (first version) at 403 nm, 461 nm, and 689 nm,

and Clémence Briosne-Fréjaville [23]:

- Transport setup,
- Optical lattice,
- Science chamber,

where the above lists are not exhaustive but are meant to be used as guidelines to find details on what has been discussed in this chapter.

We will build upon those descriptions in the subsequent chapters. In chapter 2, we will present how we improved the transverse collimation of the atomic beam. In chapter 3, we describe the advances and characterizations that were performed on the magneto-optical traps, and on the transport of the cold atomic cloud. In chapters 4 to 6, we will present in detail the analysis of future images, the evaluation of the optical lattice parameters and the imaging protocol.

Chapter 2

Improvements in the collimation of the atomic beam

In our experiment, we are interested in making a BEC of strontium, which is then loaded into a 2-dimensional optical lattice. For that purpose, we use ^{84}Sr, which is more amenable to Bose-Einstein condensation but has a natural abundance of only 0.56% [20]. This low abundance compared to the 82.58% ([20]) of ^{88}Sr requires work on the brightness of our atomic beam, more precisely it requires to optimize the transverse collimation stage.

This chapter and the next one present the modifications, progresses, and restructurations performed during the past years. This chapter focuses on the changes made to increase the efficiency of the collimation of the atomic beam. We present the simulation of the transverse molasses (TM) setup. From that simulation, we identified the most relevant parameters to increase the atomic flux in the chamber of the magneto-optical trap: the distance the oven's output from the TM beams, the interaction time of an atom with those beams, and the laser intensity. At the end of this chapter, we compare three different configurations: our previous oven with low power, the new oven with higher power circular beams, and the "new oven" with high power elongated beams. We will

then compare the model to an actual measurement performed after redesigning the TM molasses setup.

2.1 Limitations of the previous setup

2.1.1 Access to the oven output

The initial oven that was in the experiment was inspired by an oven developed at Laboratoire de Physique des Lasers (Université Sorbonne Paris Nord). The main drawback of that oven was that its output was hidden inside a vacuum tube, 16 cm away from the viewports of the transverse molasses. During the 16 cm-propagation, the beam had time to expand before entering the collimation stage.

The transverse molasses align the atoms velocities with the ideal axis of propagation without affecting its position. Thus, any atom which traveled too far away from the axis will be lost due to collision with a wall, for instance, at the differential vacuum level.

Thus, bringing the oven's output closer to the molasses beams should increase the atomic flux. That is the reasoning behind our change of oven for the oven from SYRTE that has an access just 1 cm away from its output (see section 1.2.1).

2.1.2 Small interaction time and low available laser power

The duration for which an atom will interact with transverse molasses beams is set by the velocity of the atom along the axis of propagation of the atomic beam (perpendicular to the laser beams), and the size of the intensity profile along that same direction. In our case, we have typical velocities[1] of $400\,\mathrm{m}\cdot\mathrm{s}^{-1}$ and a beam diameter of 1 cm. This situation results in an interaction time of 25 µs.

As described in section 1.1.1, the available power before we changed the TM setup was 24 mW. This power was to be split into two since we use two directions for the transverse cooling. The beams had a circular shape and waist diameter of 1 cm, resulting in intensities of $I = 0.4 I_{\mathrm{sat}}$. The friction force resulting from radiation pressure will be on the order of $\Gamma_b P_e\, \hbar k$, corresponding to the scattering rate times the recoil from the absorption of one photon, with the population in the excited state P_e:

$$P_e = \frac{1}{2}\frac{s}{1+s}. \tag{2.1}$$

From this force using ($\Delta = -\gamma_b/2$, $s = 0.4$) we can extract a characteristic time $\tau = 21\,\mu\mathrm{s}$ (inverse of the friction coefficient α in [31]) for the damping of the transverse velocity. This reasoning is valid in the low saturation limit; we are in fact already close to the saturation, increasing further the saturation parameter will not improve much the performances. Instead, we would like to increase the interaction time to make it at least a few times larger than τ.We thus want to increase the beam's size along the propagation axis of the atomic beam. To prevent reduction of the saturation parameter, we will want to increase the laser power to compensate for the increased surface area of the beam.[2]

[1] Thermal velocity for a strontium atom at 500 K.

[2] The detuning was kept constant at $-\Gamma/2$ for the optimizations.

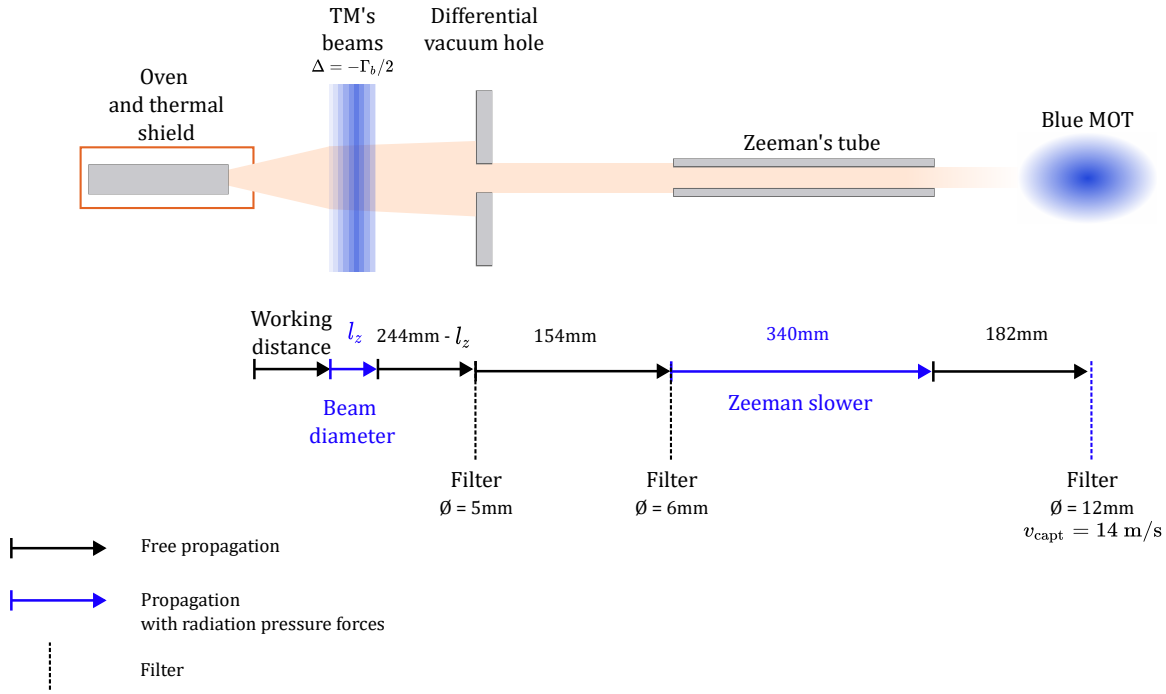

Figure 2.1: Schematic view of the different steps of the simulations for the transverse molasses. Note that the distance from the output of the oven to the differential vacuum hole is independent of the beam's diameter l_z.

2.2 Simulation of the impact of the different factors

The simulations presented in this section were developed during the first lockdown in 2020. They were motivated by the disappointing efficiencies of the initial transverse molasses setup and the unavailability of the experiment. We will present the models used for the oven's emission of atoms and the forces acting on the individual atoms. We will explore a few configurations corresponding to changing different elements of the transverse molasses setup: the oven, the laser diode, and the beam shape of the lasers.

2.2.1 Framework of the simulation

For these simulations, we decided to model the evolution of the atom transverse phase-space distribution along the propagation axis by solving the trajectory of individual atoms. We will first describe the general procedure that we use. An overview of the different steps and parameters is displayed in Figure 2.1, we will then detail each step in the following sections.

The first step is to model the initial distribution of velocities for the atoms at the oven's output. We sample the initial velocity from a probability distribution modeling the emission of atoms. Then, the atoms propagate ballistically (including gravity or not) until the atoms enter the transverse molasses beams[3]. The beams are modeled by

[3]We checked that the gaussian intensity profile of the real beams does not invalidate the results obtained with this simple model. Including the gaussian profile results in a relative reduction of the flux

a constant intensity profile over a disk or an ellipse. There, we solve the trajectory by numerical integration of Newton's second law. We extract the final positions and velocities to compute the ballistic propagation until the input of the Zeeman slower. The behavior inside the Zeeman slower is treated similarly to the transverse cooling. Finally, the atoms arrive in the MOT chamber.

Along the propagation axis, different "filters" are applied to the distribution of atoms. They are used to model atoms lost because they hit a vacuum chamber wall. In particular, the differential vacuum hole that is placed after the transverse cooling stage will stop a significant fraction of the atoms if the collimation is not efficient. A second filter is applied at the entrance of Zeeman slower. Another type of filter is the one used to count the number of atoms collected in the blue MOT. For this one, the filter removes the atoms that have velocities greater than the capture velocity of the blue MOT ($\sim 14\,\mathrm{m}\cdot\mathrm{s}^{-1}$); it also discards the atoms that are at a distance from the center greater than 6 mm, to account for the finite size of the MOT's laser beams.

This simulation does not include the diffusion in momentum space caused by the random direction of spontaneous emission. In particular, the divergence of the atomic beam at the output of the Zeeman slower might be significantly greater than the one we find here. We also neglected the fact that the $^1S_0 \leftrightarrow {}^1P_1$ transition is not perfectly closed. Some atoms will fall in the metastable $^3P_2$. Those atoms will not interact anymore with the laser beams at 461 nm and will not contribute to the atom number in the MOT. To give an order of magnitude of the losses due to that phenomenon, we compare the velocities of the atom which are efficiently cooled by the TM to the recoil velocity from one blue photon ($v_{\mathrm{rec}} = \hbar k_b/m = 10\,\mathrm{mm/s}$). In Figure 2.4, we see an impact of the TM for atoms with velocities below 40 m/s, this requires scattering of 4053 photons. Using a branching ratio to the loss of 1/50000 (neglecting returns to the ground state), we find a probability of 8% to be lost after 4053 scattering events. This effect should indeed be marginal.

2.2.2 Main studied configurations

The changes planned for the transverse collimation of the atomic beam concern three distinct parts of the setup, which we will compare in the following sections. We defined below the names that will be used to refer to those different configurations; the corresponding characteristics are summarized in Tables 2.1 and 2.2.

- As we have already mentioned in chapter 1, the oven has been changed already. We will thus compare the "old oven" to the "new oven" setups. The old oven was at a distance of 16 cm from the molasses, while the new oven is placed only 2 cm before the molasses (including 1 cm to exit the thermal shield). The distances here are to be understood as the distance from the oven to the edge of the view port, corresponding to the "edge" of the laser beam (see Figure 2.1).
- We also changed the laser diode producing the beams for the TM setup. The diode we used previously had a nominal power of 100 mW,[4] the new one now has an output power of 500 mW.[5] We considered that the beams for the "old TM" had a power of

on the order of a few percents, while significantly increasing the computation times.

[4] ref: NBD4216E from *Nichia*

[5] ref: NDB4916E from *Nichia*

12 mW, and the ones for the "new TM" have a power of 80 mW.[6]

- Finally, we also considered changing the beam profile of the molasses beams. The laser-beam profile for the old TM and the new TM is a symmetric gaussian with $1/e^2$ diameters of 10 mm. The "elliptic new TM" will refer to the situation where we have a power of 80 mW per axis with a beam profile elongated along the propagation axis of the atoms. The diameters in that configuration will be 10 mm and 30 mm.

For that study, we kept fixed the parameters of the Zeeman slower and the blue MOT, in order to restrict the number of available parameters.

	Distance from the molasses beam
Old oven	160 mm
New oven	18 mm

Table 2.1: Working distance for both ovens. This distance is taken between the output of the oven and the edge of the laser beam modeled by a constant intensity profile.

	Oven	Laser power per axis	Beam diameter transverse	longitudinal
Without TM	old/new	0 mW		
Old molasses	old/new	12 mW	10 mm	10 mm
New molasses	new	80 mW	10 mm	10 mm
Elliptical new molasses	new	80 mW	10 mm	30 mm

Table 2.2: Summary of the main configurations considered for the TM. The transverse direction is perpendicular to the axis of propagation of the atomic beam. The longitudinal direction is the direction of propagation of the atomic beam. "old/new" means that both oven were considered. Since the new oven was already mounted on the experiment we did not investigate the new molasses with the old oven.

2.2.3 Models for the emission by the oven

Since the angular distribution of emission of our oven was not known at the time when the simulations were run, we resorted to a model proposed in an article from Giordmaine and Wang [33]. This article presents a model for the emission of a reservoir through an aperture which is a long and narrow tube. This model was suggested to us by Etienne Maréchal from Laboratoire de Physique des Lasers. This article presents different regimes for the emission through the tube. We will focus on the regime for which the collisions between the atoms are negligible, which the authors call the "transparent source" regime.

[6] The power here is the power of a single beam in single pass. Neglecting the losses, the second beam (retroreflection of the first one) will double the power on the atoms.

2.2.3.1 Validity of the transparent source approximation

In order to be able to neglect the collisions inside the tube, we require that the mean free path[7] λ is much greater than the tube's length L (which is itself much greater than the radius of the tube $a \ll L$). The mean free path is given by: $\lambda = \left(\sqrt{2}\pi n\sigma^2\right)^{-1}$. Here, $\sigma \sim 4$Å is characteristic size of an atom. Here, we used the covalence diameter of a strontium atom as an order of magnitude [29]. n is the density of the vapor. Using the typical temperature that we have for our oven (500 °C), we find a mean free path of 3 cm, which is only marginally greater than the length of our micro-tubes ($L = 15.2$ mm). At lower temperatures, the approximation gets better. For instance, at $T = 450$ °C, the mean free path is increased to 15 cm. To compute the density as a function of temperature, we used the following relation from Schioppo *et al.* [29]:

$$\log_{10} P = 14.232 - \frac{8572}{T} - 1.1926 \log_{10} \tag{2.2}$$

with P the vapor pressure of strontium in pascal, and T the temperature of the oven in kelvin.

2.2.3.2 Expected angular distribution

In the transparent source regime, the normalized emission pattern,[8] as a function of the angle from the axis of the tube θ, $I(\theta)$[9] is given by:

$$I(\theta) = \begin{cases} \frac{2}{\pi}\cos\theta\left(\arccos y - y\sqrt{1-y^2} + \frac{2}{3}y(1-\sqrt{1-y^2})\right) & (0 \le \theta < \theta_0) \\ \frac{4\cos\theta}{3\pi y} & (\theta_0 \le \theta \le \pi/2) \end{cases}, \tag{2.3}$$

where we introduced $\theta_0 = \arctan 2a/L$ and $y = L\tan\theta/2a$. This function is peaked around the axis, as expected, but the signal from the tails of the distribution is far from negligible, as can be seen in Figure 2.2.

2.2.3.3 Transverse velocity distribution

To obtain the distribution of transverse velocities, we need to know the distribution of the norm of the atomic velocities v, in addition to the angular distribution. We assume that the atomic velocities at the output of the oven can be modeled by a Maxwell-Boltzmann distribution, for which the probability density function (PDF) p_{MB} is:

$$p_{\mathrm{MB}}(v) = \left(\frac{m}{2\pi k_B T}\right)^{\frac{3}{2}} 4\pi v^2 \exp\left(-\frac{v^2}{2mk_B T}\right) \tag{2.4}$$

[7] To be more precise, we should compare the mean free path averaged over the length of the tube since the density is not constant along the tube. We will see that the mean free path, even at the entrance of the tube (high-density side), is already longer than L.

[8] Here, "normalized" means that the function has been divided by its maximum value, obtained on the axis ($\theta = 0$)

[9] The axial symmetry around the axis of the tube implies that there is no dependence on the angular distribution on the spherical angle ϕ.

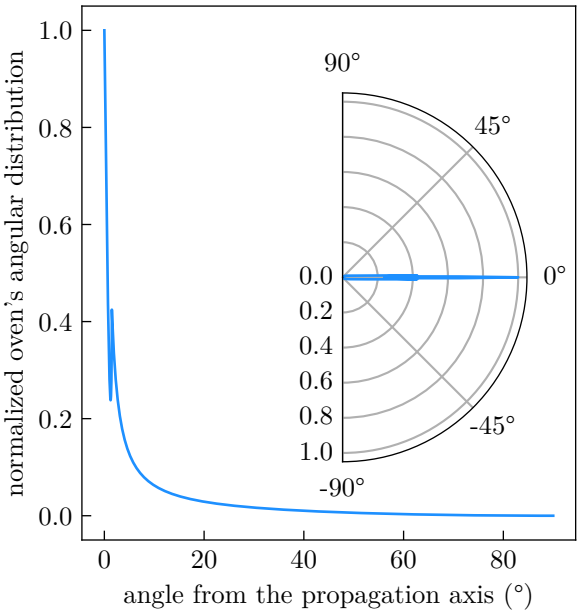

Figure 2.2: Probability density function for the angular distribution of atoms at the oven's output. In the main plot, we display only the PDF for the positive angles, the function being symmetric. We clearly see a discontinuity in the function at small angles, which is caused by the piece-wise definition of the function. The inset represent the same function (normalized by its maximum value) for angles in $[-90°; 90°]$ in polar coordiantes.

where T is the temperature of the oven, k_B the Boltzmann constant, and m is the mass of a strontium atom.

If we make the simplifying assumption that the norm of the velocity and its direction are independent random variables, we can draw an angle according to the PDF associated with $I(\theta)$ and the norm of the velocity according to p_{MB}. We extract from this the transverse velocity $v_\perp$ and the longitudinal velocity v_z by simple projections:

$$\begin{cases} v_\perp = v \sin\theta \\ v_z = v \cos\theta \end{cases}. \tag{2.5}$$

Figure 2.3 represents a histogram of the transverse velocities for an oven temperature $T = 500\,°\mathrm{C}$, a radius for the micro-tube $a = 200\,\mu\mathrm{m}$, a length of $L = 15.2\,\mathrm{mm}$. We recover the sharp maximum present on the graphs for the angular distribution in Figure 2.2.

2.2.4 Impact of the distance between the oven and the molasses

As discussed in section 2.1.2, we expect from simple geometric considerations that the flux should be increased simply by reducing the distance between the output of the oven and the beams of the transverse molasses, which we will call the *working distance*. To evaluate the impact of this parameter, we fix the configuration of the laser beams. We use the "old TM" configuration.

We plot the results of that study in Figure 2.5, where we plotted (left) the number of atoms passing through the differential vacuum hole placed after the molasses as a

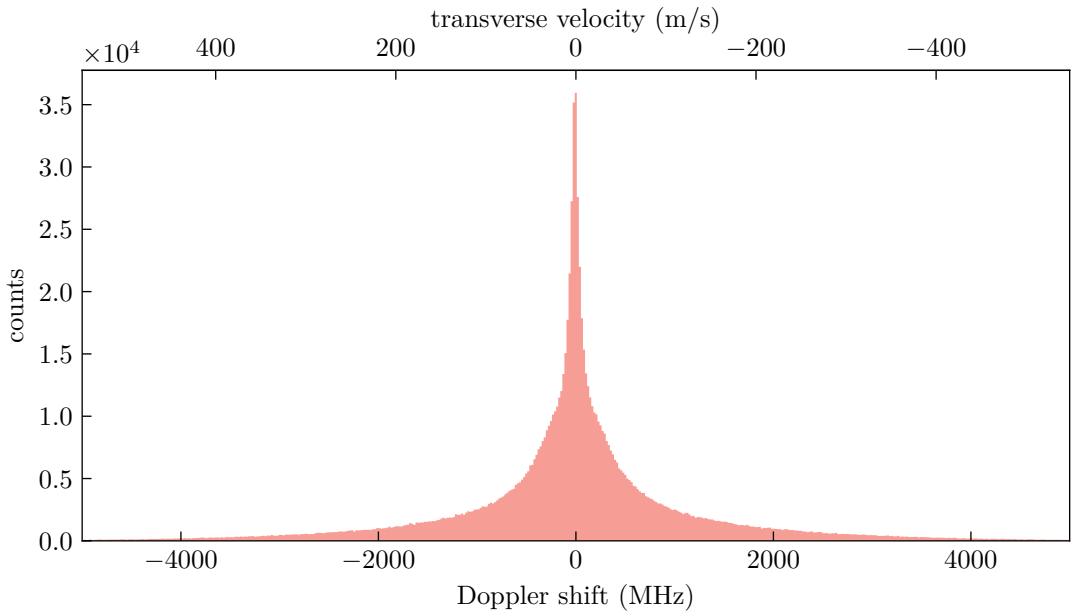

Figure 2.3: Histogram of the transverse velocities (Doppler shifts) at the oven's output. This distribution is obtained for a million atoms, at an oven temperature of 500 °C, with micro-tubes of radius 200 µm and length 15.2 mm. We obtain a full width at half maximum on the order of 100 MHz.

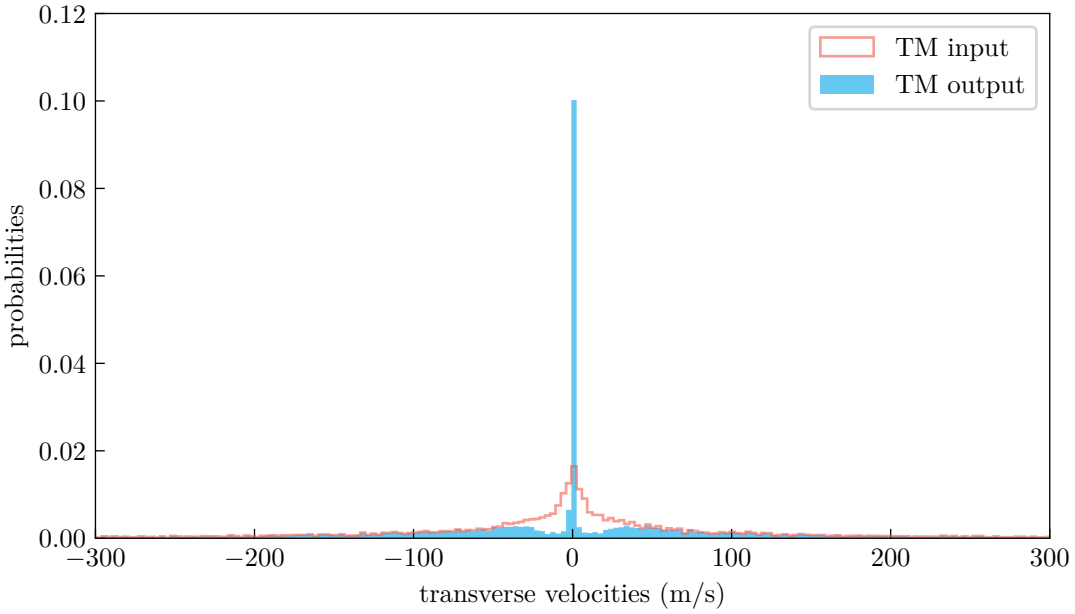

Figure 2.4: Histogram of the transverse velocities (Doppler shifts) at the transverse molasses output. This distribution is obtained for the configuration "elliptical new molasses". We clearly see dips in the wings of the distribution and an accumulation around $v = 0\,\mathrm{m}\cdot\mathrm{s}^{-1}$.

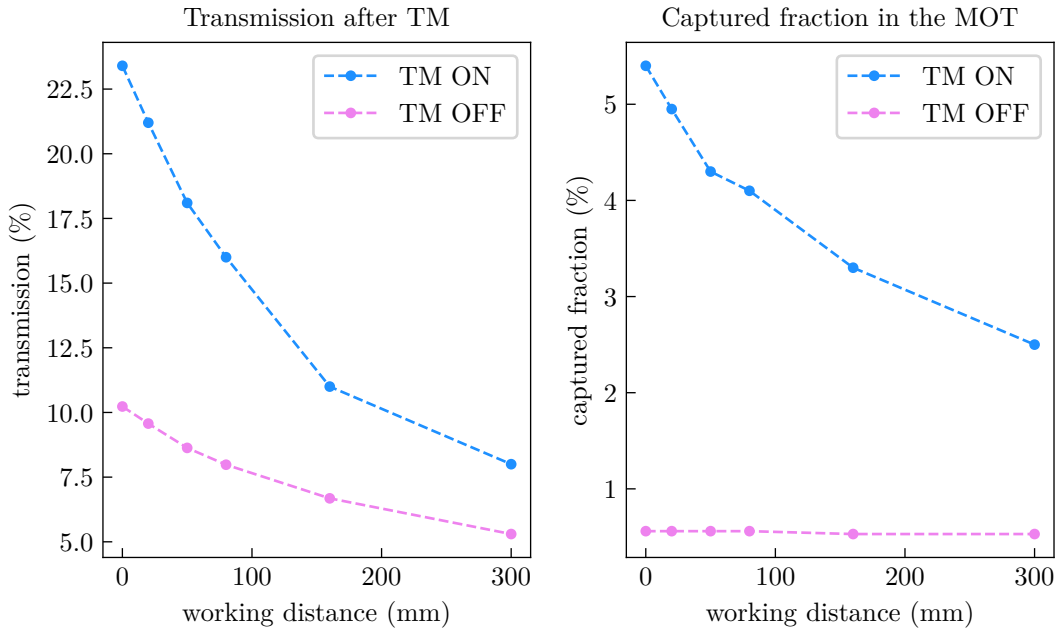

Figure 2.5: Fraction of atoms going through the differential vacuum hole after the TM beams (left) and the fraction of atoms that is capturable by the blue MOT (right). The fractions are obtained by dividing the number of atoms in the two situations by the initial number of atoms (10 000 at the oven's output). For reference, we also plotted the same quantities when the transverse molasses were turned off. The configuration used here is the "old TM".

function of the working distance of the oven. In the right panel, we plotted the fraction of capturable[10] atoms arriving at the MOT. For reference, we also plotted the same results when the molasse beams are turned off. We observe that the working distance has, as expected, an effect on the number of atoms going through the differential vacuum stage positioned after the TM. This effect is even increased when the TM are turned on. However, at the level of the MOT chamber, the effect of the TM is even more visible, with gains from 5 to 9. We interpret this effect as follows, at long distances, the differential vacuum stage filters many atoms that are not filtered with shorter working distances. Thus, at shorter working distances, the beam's divergence after the differential vacuum is greater, and more atoms will be lost at the entrance of the Zeeman slower tube (diameter of 5 mm). This explains that the gain from the TM is greater at short working distances.

2.2.5 Compromise between the beam shape and beam intensity

We expect that increasing the dimension of the laser beams along the direction of propagation of the atomic beam should improve the collimation of the atomic beam. However, increasing the area of the beam profile at constant power reduces the beam's intensity. Thus, it is not entirely evident at which point we should stop increasing the beam's longitudinal size l_z. Furthermore, the viewport we have in the experiment was a CF40 viewport

[10] That is, atoms with of velocity smaller than the capture velocity and a position within the MOT beams' diameters.

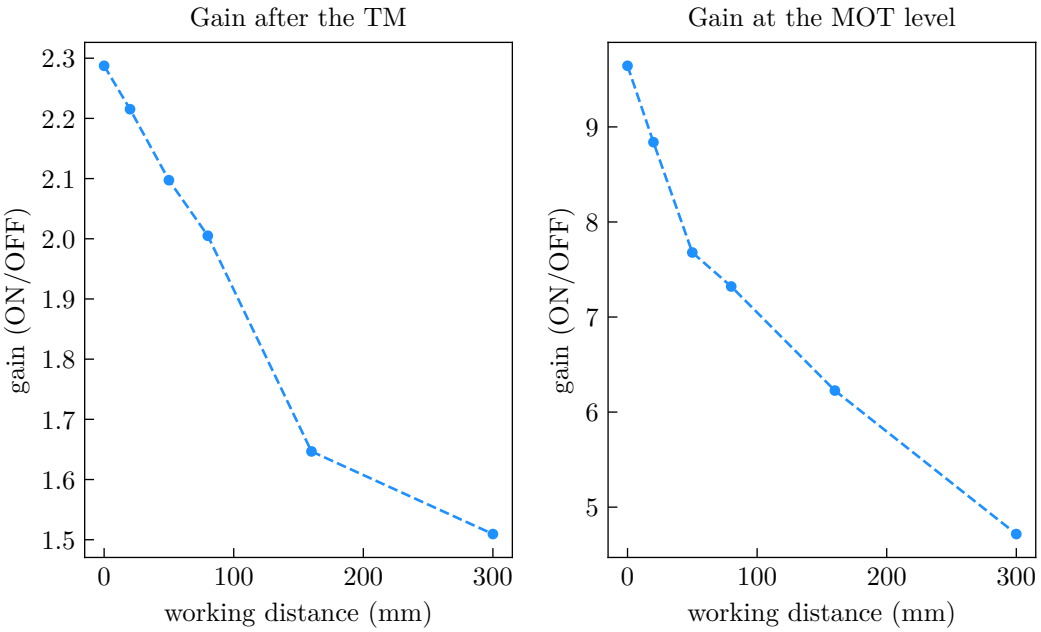

Figure 2.6: Gain introduced by the "old TM" for different working distance. The data is the ratio of the curves TM ON and TM OFF in Figure 2.5.

with a clear aperture of 32 mm. This means that the increase in l_z is limited if we do not change the vacuum system.

The results of that study are summarized in Figure 2.7. In particular, we note that, as expected, increasing the power without increasing the beam's size can be detrimental. We see in particular that with a power around 80 mW (70 mW is more typical on the actual setup), from a beam diameter of 30 mm the transmission reaches a plateau. We also see that not much gain was obtained by changing in the simulation the viewport to a CF63 with a clear aperture of about 60 mm.

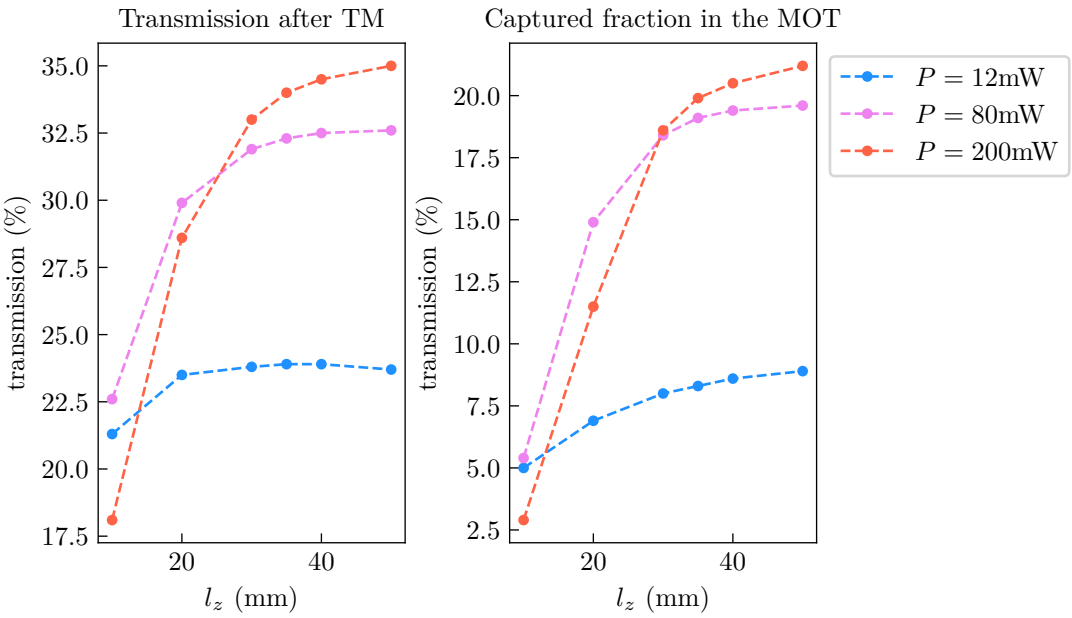

Figure 2.7: Fraction of atoms that are going through the differential vacuum hole after the TM beams (left) and the fraction of atoms capturable by the blue MOT for different powers. The fractions are obtained by dividing the number of atoms in the two situations by the initial number of atoms (10 000 at the oven's output). Increasing l_z (the beam diameter along the propagation axis) above the clear aperture (32 mm) presents only a marginal increase in the captured fraction, even at relatively high powers. Those graphs were obtained for a working distance of 18 mm and a detuning of $-\Gamma_b/2$.

2.3 Optical setup for the new TM

The simulations presented in the previous section 2.2, guided the development of a new setup for the transverse collimation. We discuss in this section the experimental results obtained after the modifications were made. The modifications are the following: the oven was changed to reduce the working distance, the laser diode has been changed to increase the available power, and the beams are now elongated along the propagation direction.

2.3.1 Measurement of the velocity distribution of the new oven

A measurement of the transverse velocity distribution at the output of the oven was performed to check that the model for the oven used in the simulations is qualitatively satisfying. This was done monitoring the absorption from the vertical axis of the TM. A schematic view illustrating the measurement is presented in Figure 2.8. We replaced the mirror for retroreflection with a convergent lens and a photodiode (PHD1). A second photodiode (PHD2), placed before the atoms, was used to monitor the laser's intensity sent to the atoms. PHD2 was used as a reference to cancel the intensity fluctuations. We then scanned the laser's frequency over 700 MHz around the resonance on the blue transition. This broad scan was performed using the piezo actuactor on the extended cavity mirror of the Toptica master laser.

The experimental signals are displayed in Figures 2.9a and 2.9b. On 2.9a, we observe a dip in the transmission we the laser crosses the atomic resonance. We also observe oscillations of the intensity during a sweep of the laser's frequency, this makes the use of a reference photodiode crucial to extract the absorption signal from the atoms.[11] On 2.9b, we observe an absorption curve that is reminiscent of the transverse-velocity distribution, but with a full width at half maximum of ~ 200 MHz instead of the expected ~ 100 MHz.

Two simple factors could explain this discrepancy. The first one is the presence of different isotopes in the atomic beam. In particular, the presence of ^{86}Sr introduce a secondary peak within the distribution, creating the slight bump on the left of the distribution. This second isotope at least explains the asymmetry in the experimental profile. A second cause of broadening can come from the collisions between the atoms that were neglected in our simple model.

2.3.2 New laser diode

As mentioned in the introduction of this chapter, the diode that was used previously for the TM has been replaced with a similar diode but with a power that is 5 times higher. We obtain a power available per axis of ~ 70 mW,[12] which is an increase by a factor of 5.8 compared to the previous setup (12 mW per axis).

2.3.3 Optics for the elongated beams

The elliptical beam profiles are produced from the initial circular beams (one per axis) of waist diameters 10 mm by introducing a beam expander for each axis of the transverse

[11] It is possible that those oscillations were caused by the scan of frequency.

[12] The simulations were performed at 80 mW but this is more typical in the experiment.

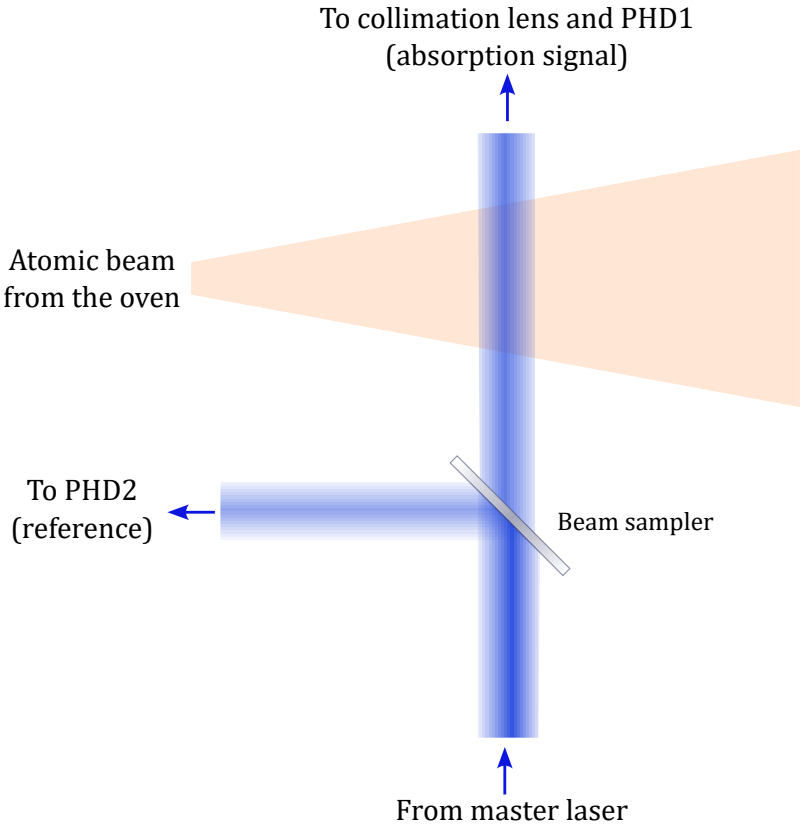

Figure 2.8: Schematic representation of the transverse velocity measurement at the output of the oven. Two photodiodes are used (PHD1 and 2), one for the reference of intensity at the input and one for the absorption signal.

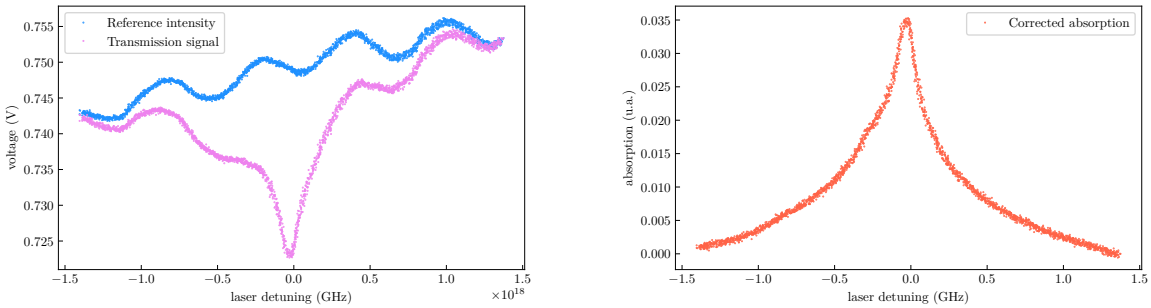

(a) Signals from PHD1 and PHD2

(b) Absorption curve

Figure 2.9: In 2.9a, we plot the voltages from the reference intensity (PHD2) in blue and the transmission signal (PHD1) in pink. We observe a dip in the transmission when the laser is close to resonance (detuning equal to 0). We compensated for the power imbalance between the photodiode by scaling the transmission signal to match the voltage of the reference at the endpoints of the scan. In 2.9b, we plot the absorption, that is, one minus the transmission, where the transmission is computed by taking the ratio of the transmission signal over the reference intensity. All signals have been averaged over 16 runs.

molasses right before the viewports. For those beam expanders, we used a pair of cylindrical lenses; one is a plano-concave lens[13] with a focal length of $-50\,\mathrm{mm}$, and the other

[13]ref: CKV050AR.14 from *Newport*

is a plano-convex lens[14] with a focal length of 150 mm. The resulting beams thus have a profile elongated along the propagation axis of the atoms.

2.4 Summary of the results for the transverse molasses

In this section, we summarize the expected gains introduced by the TM for the different configurations defined in tables 2.1 and 2.2. We then compare the theoretical results with the one obtained in the experiment by looking at the fluorescence of the magneto-optical trap. We will see that the change of oven grants only a limit gain and that increasing the laser power without expanding the beams does not improve the flux much either. We will see that the results of the simulations give a reasonable estimate of the gain for the atomic flux at the level of the MOT.

2.4.1 Expected gains at the MOT level

In Table 2.3, we summarize the results expected for the gains in terms of fluxes at the MOT level. The gain is defined here as the ratio between the number of atoms that are capturable by the blue MOT when the molasses are turned on, over that number when they are off. We can observe that the change of oven alone causes an increase on the order of 66% on the captured fractions with the TM. Furthermore, adding more power with a constant beam shape produces an increase of 80%. While the higher laser powers combined with the elongated beams result in fluxes 6 times higher than expected from the previous setup (old oven and molasses). In terms of gains, we see that using elongated beams (at 80 mW) makes a huge difference.

We must come back to the fact that the previous transverse molasses did not show any gain in the flux of atom, while we expect a gain of a factor 6 according to the simulation. This is probably due to an imperfect alignment of the beams, that proved sensitive on the new setup.

Oven	Configuration	Captured fraction		Gain
		TM off	TM on	
old	old molasses	0.5	3.0	6.0
new	old molasses	0.6	5.0	8.3
	new molasses	0.6	5.4	9.0
	elliptical new molasses	0.6	18	30

Table 2.3: Expected captured fraction for TM turn off or on, and gains for the different standard configurations. The gain is computed as the ratio of the fraction of atoms captured by the MOT when the TM are on or off for a given configuration.

[14]ref: CKX150AR.14 from *Newport*

2.4.1.1 Impact of the molasses in the experiment

After implementing the changes on the transverse collimation, we checked the gain obtained in the "elliptical new molasses" configuration (with the new oven). We found gains higher than expected by roughly a factor of 2. For a laser power of about 70 mW, we obtained gains on the order of 60 by looking at the fluorescence of the blue MOT.[15] Those measurements were performed with strontium 84, the isotope of interest for our experiment.

We attribute this discrepancy to the simplicity of our model. Firstly, the criteria we imposed on the "capturability" of the incoming atoms is motivated but somewhat arbitrary. Secondly, we have seen that our theoretical angular distribution of emission is two times narrower than the experimental one. This could explain why we get higher gains in the experiment, at least for the part of the broadening not coming from ^{86}Sr. Lastly, we have more degrees of freedom in the actual experiment, such as the imperfect colinearity of the laser beams, for instance. If, for instance, the axis of the oven is not precisely that of the Zeeman slower, we expect to gain some improvement by pushing the atomic beam in one direction, which is not accounted for in the model. This could lead to a reduction of the flux in the absence of the transverse molasses.

2.5 Summary

In this chapter, we have described how we redesigned the transverse collimation setup. We have identified three relevant and interdependent parameters, the distance between the oven's output and the transverse molasses beam, the available laser power, and the beam profile of the laser beams. We have demonstrated that we can increase the incoming flux of atoms at the level of the MOT chamber by a factor 60. This was performed by changing the oven to reduce its working distance, increasing the available power from 12 mW per axis to 70 mW, while also increasing the size of the laser beam along the propagation axis by a factor of 3. We saw that even if the model is only capturing the order of magnitude of the gain, the design of the new TM setup is still conclusive and leads to significant improvements. These improvements will allow us to obtain a sufficient number of atoms with loading times that will remain reasonable with respect to the rest of the experimental cycle, as will be seen in the next chapter.

[15] We checked on our experiment that the loading rate of the blue MOT is proportional to the fluorescence in steady-state from the MOT. Monitoring the fluorescence of the MOT is thus a time-efficient way to monitor increases in the flux entering the magneto-optical trap.

Chapter 3

Experimental advances: laser cooling to the microkelvin and transport to the microscope chamber

This chapter presents the advances and characterizations of the magneto-optical traps on the broad and narrow transitions of strontium. We also describe the advances in the transport of the atoms from the MOT chamber to the science chamber using the transport optical dipole trap.

We first present the measurement of atom numbers, loading times, and temperatures for the blue MOT. We characterize the magnetic trap in terms of the lifetime of the metastable atoms in the $^3P_2$ state. Then, we detail the performances of the laser cooling on the narrow transition (red MOT). Finally, we will report the first realization of the transport between our chambers.

3.1 Characterization of the blue MOT

In this section, we present the characterizations that were performed on the blue MOT, which is the first stage of laser cooling on the broad transition. We will present data for the two isotopes we have used so far, ^{88}Sr and ^{84}Sr. Until recently, our team only used the most abundant isotope of strontium (^{88}Sr) for the tests on the two MOTs. The first MOT on the less abundant isotope (^{84}Sr) was only performed after we changed the transverse molasses setup. The emphasis will be put on ^{84}Sr since it is the isotope of interest for our experiment.

3.1.1 Measure of the atom number

As we will see in this section, we calibrated the atom numbers in the MOT using fluorescence from the blue MOT. This method is not very precise but will mainly be used to compute rough estimates of the atom numbers or ratios of atom numbers to check if the transfer from one trap to the next is efficient.

Once we know how to estimate the number of atoms, we will apply the technique to measure the loading rate of the blue MOT and lifetime in the magnetic trap.

3.1.1.1 Principle of the measurement

To measure the atom number, we assume that all the atoms see approximately the same laser intensity (dilute regime). To enforce that condition for dense samples, we introduce a free expansion for some time before imaging the atoms. Then, the scattering rate γ_{sc} for one atom is given by:

$$\gamma_{\text{sc}} = \Gamma_b \Pi_e = \Gamma_b \frac{1}{2} \frac{s}{1+s} \, , \tag{3.1}$$

where we introduced Π_e the population in the excited state (^{1}P$_1$), and s the saturation parameter (on resonance), which is evaluated by summing all the intensities of the beams.[1] The flux scattered by the atomic sample is then N, the number of atoms times the scattering rate γ_{sc}:

$$F_{\text{sc}} = N \gamma_{\text{sc}} \tag{3.2}$$

A camera and its objective then collect the scattered photons. Under the assumptions of point-like source and isotropic emission,[2] the flux collected by the camera is given by:

$$F_{\text{camera}} = \eta \tau \frac{F_{\text{sc}}}{4\pi} \frac{\pi \phi_{\text{EP}}^2}{4d^2}, \tag{3.3}$$

where η is the quantum efficiency of the sensor at 461 nm, τ the transmission factor of the objective and viewport, ϕ_{EP} is the diameter of the entrance pupil of the camera objective,

[1] This is only approximate and neglects the spatial variations of the intensity and the Doppler shifts of the atoms.

[2] The isotropic approximation is motivated by the use of beams coming from all directions of space. The point source approximation is justified because we are considering objects with sizes small compared to the working distance of the camera's objective (17 cm).

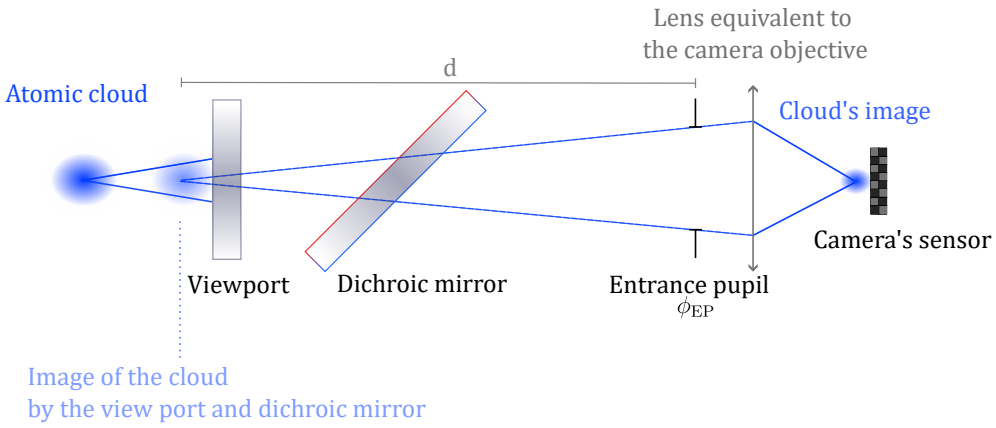

Figure 3.1: Simplified view of the collection of the light emitted by the atoms during fluorescence imaging. The atoms are inside the enclosure of the vacuum chamber (not represented), and the viewport makes the junction between vacuum and air. The dashed rays represent virtual rays coming from the image of the cloud by the viewport and the dichroic mirror. The camera's objective is represented by a single lens. The entrance pupil is the element that limits the aperture of the whole optical system; often, it will be the diaphragm inside the objective.

and d is the distance between the entrance pupil and the cloud of atoms (see Figure 3.1). During one exposure time t_{exp}, the number of photo-electrons is $N_{\text{el}} = F_{\text{camera}} t_{\text{exp}}$. Finally, using (3.1) to (3.3), we get the following relation for the atom number:

$$N = \frac{32}{\Gamma_b t_{\text{exp}} \tau \eta} \frac{d^2}{\phi_{\text{EP}}^2} \frac{(1+s)}{s} \tag{3.4}$$

This relation requires calibrations of several parameters that are not always easily accessible. In case where the aim of the measurement is not to specifically measure the absolute incoming flux of atoms it is advantageous to perform relative measurement directly using the intensity of the fluorescence. Indeed, relative measurements remove the uncertainties on the calibrations required to use (3.4). An example where only relative measurements are sufficient is the evaluation of the gain provided by the transverse collimation of the atomic beam, as we saw in section 2.4.1.1.

3.1.1.2 Comments on high-density effects

As we mentioned above, at high densities, the atomic medium will become opaque, and atoms at the center of the cloud might see less light due to absorption from the atoms in the outer parts of the cloud. Furthermore, there are 2-body losses at high densities in the presence of blue light; those arise from so-called light-assisted collisions (see, for instance, [34]). In the presence of light-induced losses, the atom number will not be constant over the imaging time. Thus, these losses introduce a dependence measured atom numbers on the cloud's initial density, the light's intensity, and the imaging duration. These effects are particularly visible if we shine blue light on the repumped cloud of atoms.

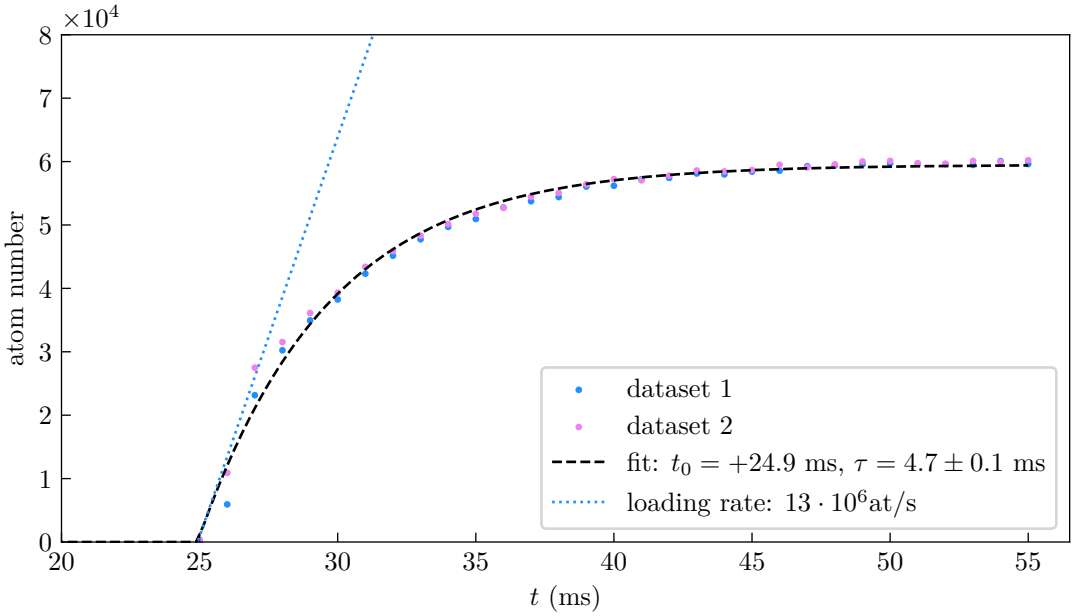

Figure 3.2: Atom number as a function of time for a blue MOT with a total power of 60.6 mW, corresponding to $s = 0.4 \times 2$ per beam where the factor 2 accounts for the retroreflexion, a magnetic gradient of $64\,\mathrm{G\cdot cm^{-1}}$ along the vertical (strong) direction, and detuning of $-\Gamma_b/2 = 15\,\mathrm{MHz}$ for ^{84}Sr. The black dashed line represents the exponential fit of the atom number. The blue dotted line represents the initial slope of the loading. The two datasets are two different runs with the same parameters. The delay t_0 corresponds to the time needed to open the atomic shutter after the oven.

3.1.2 Measure of the loading time and the loading rate

Once we know how to measure the number of atoms, we can apply this protocol to estimate the loading rate of the blue MOT. The protocol is the following: we turn on the blue MOT for a given time t, then measure the atom number, and finally, we fit the profile by exponential to extract the characteristic time of the loading of the MOT. In Figure 3.2, we plot the number of atoms as a function of time. We fit a loading time of 4.7 ms, and a loading rate of $13 \cdot 10^6$at/s. We observe saturation of the atom number in the blue MOT after a few tens of milliseconds. This saturation is caused by the leak of atoms from $^1\mathrm{P}_1$ to $^3\mathrm{P}_2$ which leads to losses from the blue MOT.

3.1.3 Temperature

We perform laser cooling on the broad $^1\mathrm{S}_0 \leftrightarrow {}^1\mathrm{P}_1$ transition in a magneto-optical trap. From Doppler theory [31], we expect a minimal temperature at the end of the cooling on the order of:

$$k_B T_{\mathrm{Doppler}} = \frac{\hbar\Gamma_b}{2} = 733\,\mu\mathrm{K}. \tag{3.5}$$

The measure of the temperature is performed using the time-of-flight method. The

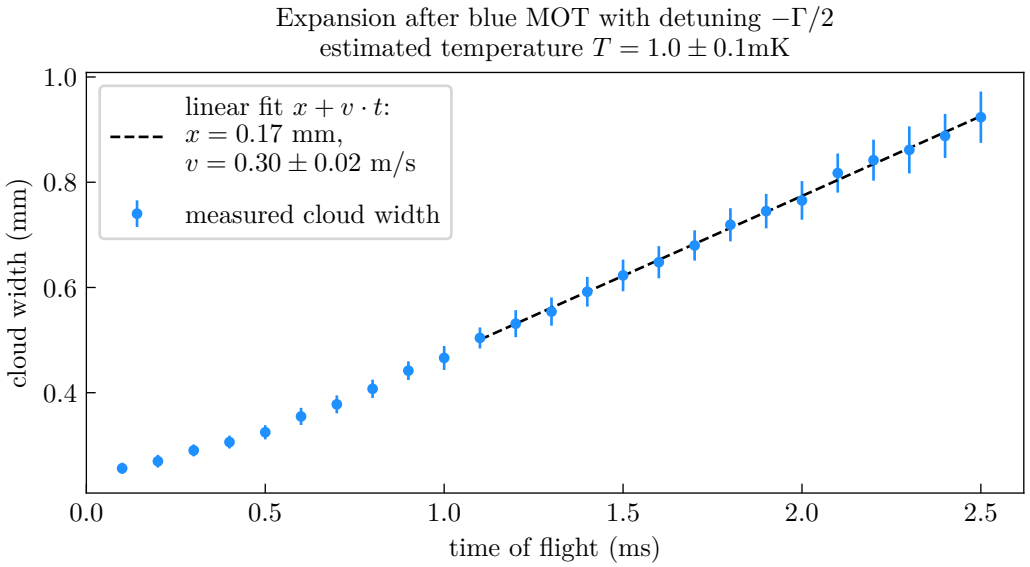

Figure 3.3: Time-of-flight expansion of a blue-MOT cloud of ^{84}Sr. The parameters for the MOT are $\Delta = -\Gamma/2$ and a laser power of 3 mW for the sum of the three axes (6 mW including the retro-reflection). The power is chosen so that the exposure time can be small compared to the expansion dynamics but sufficiently low so that view do not saturate the transition. The cloud width is the result of a Gaussian fit. The temperature we obtain is $T = 1$ mK. The error bars are extracted from the covariance matrix of the fit routine. The uncertainty given for the temperature takes into account only the fitting uncertainties for the cloud width. As such, the uncertainty on the temperature is likely to be optimistic.

profile of the cloud should be a Gaussian of standard deviation along one direction, say x:

$$\sigma_x(t) = \sqrt{\sigma_x(0) + \frac{k_B T}{m} t^2}\,, \tag{3.6}$$

In our case, "sufficiently long" would mean times so that $\sigma(t)$ gets much greater than the initial size of the cloud, $t > \sigma_x(0)/v_{\text{rms}}$. An example of such a measurement is displayed in Figure 3.3, where we see that after a few milliseconds, the RMS size seems to increase linearly. In principle, we would like to wait for even longer times, but the atoms would leave the zone where the laser beams are located. The linear fit of the last data points gives a temperature of 1.0 ± 0.1 mK.

3.2 Magnetic trap and repumping

As mentioned previously, the $^1S_0 \leftrightarrow {}^1P_1$ transition is not perfectly closed. It has a decay channel leading to the creation of population in the metastable $^3P_2$ state. The Zeeman sub-levels with $m_J = +1, +2$ are trapped in the quadrupole magnetic field of the blue MOT and accumulate. We use this process to accumulate atoms to reach a high atom number[3] at the beginning of the red MOT sequence (see [20, 35]). The number of

[3] In our case, we measured numbers from a million to hundreds of millions depending on the isotope and the loading time.

atoms available after repumping the reservoir is higher (for sufficient loading time and low enough losses) than that of a continuously repumped blue MOT, as it circumvent the two-body losses that appear at high densities in presence of blue light.

In this section, we describe the measurement of the lifetime of the metastable in the magnetic trap. We also the protocol we used to repump the atoms from the metastable state to the ground state. Finally, we estimate the transfer efficiency from the magnetic trap to the ground state after repumping.

3.2.1 Lifetime and atom number in the magnetic trap

3.2.1.1 Protocol

In order to measure the lifetime τ of the metastable atoms in the magnetic trap, we perform a measurement of the number of atoms in the trap as a function of time, according to the following protocol:

1. We load atoms in the magnetic trap by running a blue MOT continuously for some fixed duration.
2. We then turn off the laser beams for the MOT and wait for a variable time t_{hold}.
3. We then repump the trapped atoms using a pulse from the laser at 403 nm.
4. We take a fluorescence image of the repumped atoms to evaluate the atom number (see section 3.1.1.1). Measuring the number of atoms in the magnetic trap is, in fact, very challenging an is the object of next paragraph.

3.2.1.2 Measurement of the atom number in the magnetic trap

If we try to assess the number of trapped atoms, we are faced with a variety of problems:

- The cloud of trapped metastable atoms has a size (~ 10 mm) that is on the order of the laser-beam sizes available to repump the atoms. Since the initial size of the cloud of repumped atoms is already on the order of the imaging beams, the repumped atoms will be outside the illuminated area before being seen by the camera.
- We could do a blue MOT after repumping to prevent the fast escape of the atoms, and collect the fluorescence. However at high densities, fast losses appeared most likely due to light-assisted collisions [34].

So instead of actually measuring the number of atoms in the trap, we measure only a fraction of that number arising from the distribution of atoms with different velocities and positions. We then assume that the transferred fraction of atoms does not depend on the number of trapped atoms.

The lifetime of atoms in the magnetic trap is the characteristic time scale of the decay of the number of trapped atoms. At low enough densities, we expect that the losses from the trap are dominated by so-called 1-body losses. Those losses can arise from collisions with the background gas,[4] Majorana losses, or depumping of the atoms. The depumping can be done by the ambient blackbody radiation using the transitions from $^3\mathrm{P}_2$ to the $5s4d\,^3\mathrm{D}$ manifold at around 3 µm, for detail see Yasuda *et al.* [30]. Under the assumption that only 1-body losses contributes, the atom number in the magnetic trap is given by:

$$\dot{N} = -\frac{1}{\tau}N \tag{3.7}$$

[4]The pressure in the MOT chamber is typically of 5×10^{-11} mbar.

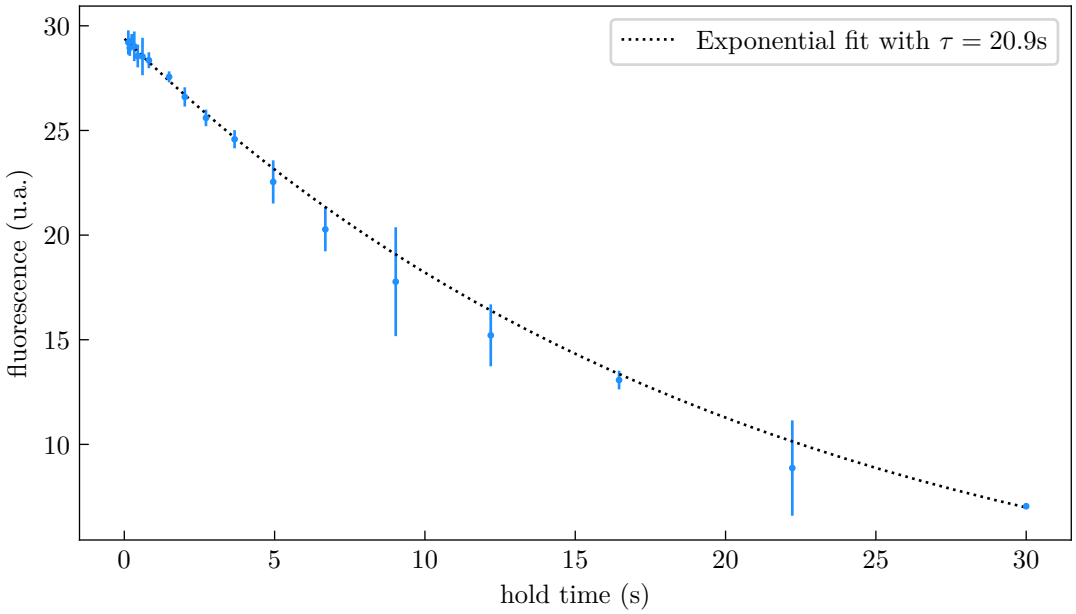

Figure 3.4: Lifetime measurement for the magnetic trap.

where τ is the lifetime of the trapped atoms. Such losses induce exponential decay of the atom number with characteristic time τ. Measuring the number of atoms in the trap as a function of time and fitting with an exponential decay, we extract a lifetime of 20.9 s from the data presented in Figure 3.4.

It is worth noting that the input of the fiber bringing the repumping light to the atoms is not protected by a shutter. It is thus possible that some 403 nm stray photons continuously depump the atoms during the hold time in the magnetic trap. This would reduce the lifetime, and could be easily circumvented if necessary.

3.2.2 Repumping protocol

To repump the atoms with the 403-nm laser, we illuminate the atoms with about 12 mW (sum of the 3 axes, without including the retroreflexions) on resonance, for around 50 ms. Simultaneously, we ramp down the magnetic-field gradient to go from 64 $\mathrm{G \cdot cm^{-1}}$ to about 1 $\mathrm{G \cdot cm^{-1}}$ in about 4 ms.[5] The atom number after that sequence is estimated at 3 million after a loading time of the magnetic trap of 1.5 s, for strontium 84.

3.3 Cooling on the narrow line

The first successful narrow-line MOTs of ^{88}Sr were obtained in April 2019. However, the study of that part of the experimental cycle was delayed until 2021. These delays came from works on stabilizing the first steps of the cycle, particularly improvements on the stability of the blue laser system. Then, we had to break the vacuum to add the science

[5]The lower value of the magnetic-field gradient still needs to be optimized, and the exact value of the magnetic-field gradient in the chamber is not known for now. This might be due to the magnetization of the chamber. We estimate this residual gradient to be on the order of 0.5 $\mathrm{G \cdot cm^{-1}}$.

chamber that was not initially present in the experiment. Finally, Covid-19 occurred, postponing the advances on the red MOT once more.

Nowadays, the cooling on the narrow transition can routinely be obtained for both strontium 84 and 88, with atom numbers on the order of a few millions (a few tens of millions for ^{88}Sr) and temperatures on the order of 1 µK.

As discussed in chapter 1, the cooling on the narrow transition of strontium is a multi-step process. This section describes the experimental sequence we use and compares it to other sequences or parameter ranges available in the literature. We conclude this section by presenting typical values obtained for the laser-cooled atoms at the end of the red MOT sequence.

3.3.1 Spectral broadening

We already mentioned in chapter 1 that the mismatch between the linewidths of the blue and red transitions made the capture of the atoms cooled on the blue transition by a "monochromatic" red MOT highly inefficient ($v_{\text{capt}}/v_{\text{th}} = 1/100 \propto \sqrt{\frac{\Gamma_r}{\Gamma_b}}$). The standard remedy to this issue is to broaden the spectrum of the red laser so that atoms from different velocity classes can still see the red laser on resonance (see, for instance, [20, 32, 36, 37]). This broadening is achieved by frequency modulation of the red laser using a double-pass AOM, generating a frequency comb, as can be seen in Figure 1.6.

3.3.1.1 Two alternate choices for the frequency modulation

We will start by comparing two different approaches to generate the broadened spectrum. The difference between the two approaches is the asymmetry of the waveform used for the frequency modulation. Interestingly, those ways of doing the modulation are described by distinct physical pictures when discussed in the literature [20, 32, 38–40]. Following Snigirev *et al.* [40], we can use the Landau-Zener probability for adiabatic passage p_{LZ} to estimate the "adiabaticity" of a modulation scheme:

$$p_{\text{LZ}} = 1 - \exp\left(-\frac{\pi}{2}\frac{\Omega^2 t_{\text{sweep}}}{\Delta_{\text{sweep}}}\right), \tag{3.8}$$

where Ω is the Rabi frequency, t_{sweep} is the period of the modulation, and Δ_{sweep} is the width of the modulated spectrum. The adiabaticity criterion is matched when $\Omega t_{\text{sweep}}/\Delta_{\text{sweep}} \gg 2/\pi$. Using the parameters described in the next section we find that we have rather $\Omega t_{\text{sweep}}/\Delta_{\text{sweep}} \gtrsim 2/\pi$, this marginal situation is also the one descibing the experiment discussed in [40]. Therefore in practice the modulation is neither fast nor slow, and both physical pictures are somewhat abusive.

The first case is the one we have been describing until now; we consider a frequency modulation with, typically, a sine wave [32] or a symmetric triangular wave [20]. The resulting spectrum is broadened by the modulation and has a comb-like structure. An atom at a given velocity and position is depicted as interacting with a single line in the comb, bringing it closer to the center of the trap and lower velocities, where the next line in the spectrum will take over. Repeating the process over and over, we obtain atoms with low velocities located near the center of the trap. In this representation of the interaction between the atom and the laser, we heavily rely on a frequency domain picture. The atom

is not sensitive to the instantaneous frequency of the laser field, but rather to a stationary spectrum, obtained from the integration of the signal on time scales long compared to the response time of the atoms.

The second approach goes by the name SWAP cooling (for sawtooth-wave-adiabatic-passage cooling) [38–41]. It uses ascending frequency ramps for the frequency modulation, that is, ascending sawtooth waveform, hence the method's name. The interpretation made by the authors is different from the previous one. They present the atom's interaction with the laser in a time-domain picture. More precisely, they consider that during one period of the sawtooth, that is, during one frequency ramp, the atom will be brought from the ground state to the excited state[6] by adiabatic passage [42]. Then, the ramp starts back at a low frequency, and the time needed to be on resonance again with the atom should be greater than the lifetime of the excited state. This assumption allows the atom to make one spontaneous emission per cycle. This picture relies on the fact that the change in the frequency is sufficiently slow so that the adiabatic passage is efficient. It also requires a period of the ramp at least on the order of $1/\Gamma_r$. However, it can not be too long if we want to keep the scattering rate high enough in order to keep an efficient cooling.

3.3.1.2 Capture efficiency

The capture efficiency is obtained by dividing the number of repumped atoms by the number of atoms trapped in the broadband red MOT. We obtained transfer efficiency on the order of 50% with ^{88}Sr. We did not perform that measurement with ^{84}Sr. This measurement thus only gives an estimate of the actual transfer efficiency for ^{84}Sr.

To characterize the symmetry of the ramp performing the frequency modulation, we introduce the parameter α. When $\alpha = 50\%$, we have a triangular waveform, while $\alpha = 100\%$ (resp. 0%) corresponds to the sawtooth with a positive (resp. negative) slope. The typical parameters used for the broadband cooling are listed below:

- the frequency-comb spacing is 50 kHz, and the detuning range spanned by the comb goes from -6 MHz to -200 kHz,
- the intensity per beam is $5\,\mathrm{mW/cm^2}$, corresponding to a saturation parameter per line in the spectrum of 14,
- the magnetic-field gradient is set to $1\,\mathrm{G\cdot cm^{-1}}$,
- $\alpha = 50\%$ or $\alpha = 100\%$.

This comparison showed that using the sawtooth waveform only gave marginal improvements in the atom number on the few percents level, for a relatively wide range of comb-spacings. This negative result is somewhat surprising but we did not investigate the reasons behind it.

3.3.2 From broadband to narrow-line MOT

To harness the full potential of the narrow transition, one typically wants to reduce the frequency comb of the broadband MOT to a single line. Indeed, this procedure leads to colder temperatures than the broadband MOT. Since there are various protocols to

[6] Here, since we have $\sigma_\pm$-polarizations like in a standard MOT, the excited state will be either: $\left|^3\mathrm{P}_1, m_J = +1\right\rangle$ or $\left|^3\mathrm{P}_1, m_J = -1\right\rangle$ depending on the initial direction of the velocity.

switch from broadband to narrow-line MOT, we will start by presenting the parameters that can be adjusted to switch between the two red MOTs. Having done that, we will present the protocol currently used in the experiment.

3.3.2.1 Overview of possible sequences

There is a variety of parameters that we need to change to switch from broadband to narrow-line MOT. Indeed, the starting point is a frequency comb with a given width and center of mass, with laser power spread out over many lines. In contrast, the final laser spectrum should be a single line with a reduced laser power (compared to the total power of the broad spectrum). Furthermore, we might also want to adjust the magnetic-field gradient while switching from one configuration to the next. Therefore, there are four parameters that we might want to change:

- the comb width,
- the center-of-mass of the laser spectrum,
- the laser power,
- and the magnetic-field gradient.

For each parameter, we also need to define a way to change it. Should the change be continuous or directly jump to the final value? Of course, we also need to define the timings to make all those changes. All of those possibilities have led different teams to use protocols with substantial differences.[7] For a review of different configurations used for the broadband and narrow-line red MOTs, we refer the reader to Tables 5.1 and 5.2 of D. Boddy's Ph.D. thesis [43].

3.3.2.2 Experimental sequence

We now present the experimental sequence that is used to go from broadband red MOT to narrow-line red MOT. This sequence is not fully optimized since we still have to decide was is best for loading the transport trap and transporting the atoms. Indeed, it remains unclear to this day if we will want to have a dense or dilute cloud, or if we want to favor temperature or atom number for instance.

We start from the broadband MOT described in section 3.3.1.2. It stays on for 100 ms. The sequence is done in 5 steps; all the changes of parameters are done linearly:

1. In 100 ms, we reduce the range of the comb from $[-6\,\mathrm{MHz}; -200\,\mathrm{kHz}]$ to $[-1.5\,\mathrm{MHz}; -200\,\mathrm{kHz}]$. Simultaneously, we ramp the magnetic-field gradient from $1\,\mathrm{G}\cdot\mathrm{cm}^{-1}$ to $0.6\,\mathrm{G}\cdot\mathrm{cm}^{-1}$ and the laser power from $5\,\mathrm{mW/cm^2}$ to $1\,\mathrm{mW/cm^2}$.
2. In 20 ms, we linearly close the comb to get a single-line spectrum at a detuning of $-200\,\mathrm{kHz}$. The intensity is further reduced to $0.5\,\mathrm{mW/cm^2}$.
3. In 50 ms, the laser frequency is taken from $-200\,\mathrm{kHz}$ to $-100\,\mathrm{kHz}$.
4. We then wait for at least 20 ms.

This sequence is meant to be merely an example; the number of steps and the slopes of the different changes can vary from one run to the other.

[7] It is worth noting that even the starting point has variability. Indeed, as described, for instance, by Loftus *et al.* [36], the broadband red MOT can be operated in three different regimes depending on the ordering of the laser's detuning, the power broadened linewidth and the recoil energy.

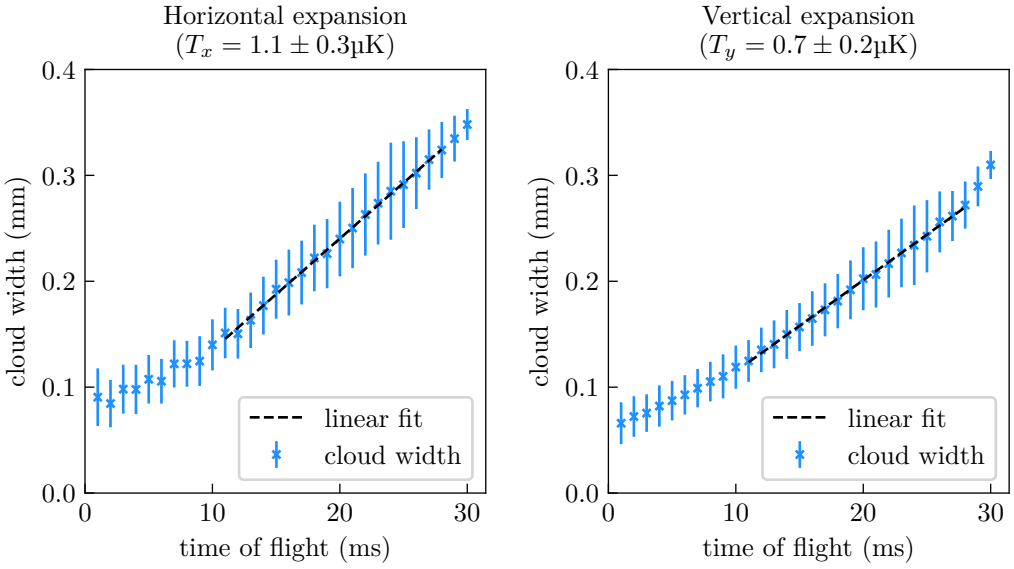

Figure 3.5: Time-of-flight measurements of the temperature in the horizontal and vertical directions. The last points are not used for the fit as the cloud gets outside of the field of view of the camera for those times, making the fit of the width unreliable. The width are obtained by a 2D Gaussian fit on the fluorescence images. The error bars correspond to one standard deviation computed from the diagonal element of the covariance matrix of the Gaussian fit. The temperatures in both directions are slightly different, $1.1 \pm 0.3\,\mu K$ in the horizontal direction and $0.7 \pm 0.2\,\mu K$ in the vertical one.

3.3.3 Characterization: atom number and temperature

In this section, we present the typical atom numbers and the temperatures obtained from the experimental sequence described above. The atom numbers are obtained after a time of flight of 20 ms, by fluorescence imaging on the blue transition as described in section 3.1.1.1 for the blue MOT. Time of flights were used to reduce the density of the cloud. We obtained atom numbers N_{at} of 1 to 4 million atoms for loading times of the magnetic trap between 0.5 to 1.5 s.

Once more, the temperature measurement is performed. The maximum expansion time we used was 30 ms. Like previously, achieving longer times is challenging due to the limited clear aperture of our viewports (CF16). In the case of the red MOT, we notice that the temperatures extracted from the expansion of the cloud are different in the vertical and horizontal directions as can be seen in Figure 3.5. We find a temperature in the vertical direction of $0.7 \pm 0.2\,\mu K$ and $1.1 \pm 0.3\,\mu K$ in the horizontal direction. Both those values are on the order of the typical temperature achieved in strontium experiments [20, 32, 36, 37].

These two measurements provide an estimate of the phase-space density $\mathcal{D}$ at the end of the red MOT. The phase-space density is defined as the product of the density n (usual density in real space) times the de Broglie thermal wavelength cubed λ_T^3 (see for instance [31]), where:

$$\lambda_T = \frac{h}{\sqrt{2\pi m k_B T}} \,. \tag{3.9}$$

At the end of the red MOT, the atoms are confined in a volume V on the order of $(100\,\mu\text{m})^3$. From those values, and assuming constant density, we get:

$$\mathcal{D} \approx \frac{N_{\text{at}}}{V}\lambda_T^3 \approx 0.01\ , \tag{3.10}$$

We see from this last result that at the end of the red MOT, we are quite close to Bose-Einstein condensation, which occurs when $\mathcal{D}$ reaches values on the order of unity.

The results presented here are typical for red MOTs of strontium [20,32] and are sanity checks, showing that the cooling is working as expected in our setup. Those characteristics are still to be optimized to obtain higher numbers of atoms or lower temperatures. However, we have seen experimentally that it might be challenging to reach higher phase-space density. When we load the magnetic trap for longer times to increase the number of atoms, the cloud's size, and temperature increase leading to approximately the same phase-space density. Additionally, when trying to increase the phase-space density in the red MOT, we face rapid losses of atoms.

3.4 Transport optical dipole trap

As we have mentioned in chapter 1, after cooling in the red MOT, we transfer the atoms into an optical dipole trap and transport the trapped cloud from the MOT chamber to the science chamber where the optical lattices and microscope are located.

We will now describe the advances made with the transport of the atoms from the MOT chamber to the science chamber. We will present the protocols explored until now to load the atoms from the MOT into the transport ODT. We also describe preliminary results obtained for the transfer efficiency, the lifetime in the ODT, and the fraction of atoms that survive the transport to the science chamber. Finally, we discuss the stability of the setup and, in particular, its sensitivity to perturbations from temperature fluctuations in the lab room.

3.4.1 Transfer from the narrow-line MOT

3.4.1.1 Protocol

The transfer from the red MOT to the transport ODT is done by overlapping the two traps carefully and letting the atoms migrate from the MOT to the ODT without changing the MOT parameters. The reasoning behind this protocol is that the lightshift induced by the ODT lasers at 1064 nm is smaller in the excited state than in the ground state.[8] Thus, the detuning will always be increased (in absolute value) by the trap's presence, as seen in Figure 3.6. Therefore, we do not expect heating from the presence of the MOT light, even without changing the detuning of the cooling laser.

Of course, this protocol is quite simplistic; it can and will, be optimized in the future since many questions remain open. One can wonder about how to turn on the transport trap. What are the optimal MOT parameters to transfer? Should we change the red laser frequency or power?

[8] This will be discussed at length in chapter 5.

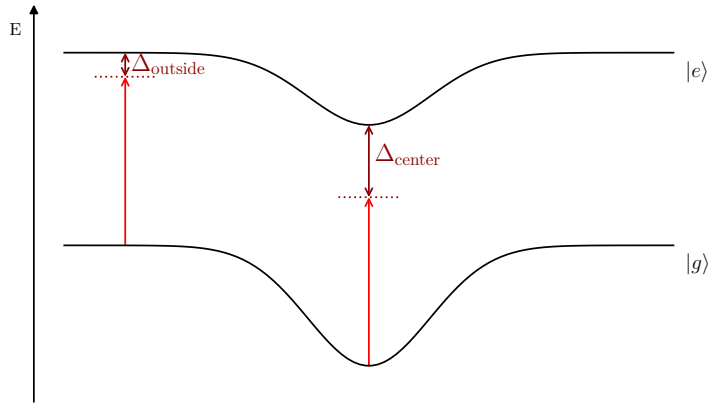

Figure 3.6: Energy curves for a two-level atom in an optical dipole trap with polarizability in the excited state $|e\rangle$ is lower than in the ground state $|g\rangle$. We see that the detuning is greater (more negative) inside the trap than outside the trap. Thus, the atoms both inside and outside the trap will interact with a red-detuned laser.

3.4.1.2 Transfer efficiency and heating

The preliminary results on the transfer from the red MOT to the transport ODT showed that we can transfert almost all the atoms, with resulting temperatures on the order of a 2 to 3 µK. We would also like to reduce the heating caused by the transfer, as it should mitigate the losses during transport. In particular, as mentioned above, we expect to be able to perform laser cooling in the ODT. This could also be used to cool the atoms after their transport to the science chamber. More details on laser cooling in an optical dipole trap will be presented in chapter 6. The size of the cloud along the transport's direction is increased dramatically compared to the one at the end of the narrow red MOT, going from about 100 µm to more than 10 mm.

Even though this step of the experimental sequence is still to be improved, we moved on to the next steps, which are the study of the transport trap and transporting the atoms to the science chamber.

3.4.2 Characterization of the ODT in a static configuration

We will start by describing the characteristics of the transport ODT in "static configuration", by this, we mean a configuration in which the transport trap is overlapped with the MOT, and no transport of the atomic cloud is performed.

3.4.2.1 Depth and trapping frequencies

In this section, we compare the expected characteristics of the transport trap from its design (see [23]), presented in chapter 1 with the ones we have in the experiment. For now, the measurements of the trap frequencies with the atoms were inconclusive. We will instead present expected characteristics from the measurements on the trap beams directly.

The waist radii for the transport beams at their focus were planned to be 50 µm in the vertical direction and 100 µm in the horizontal direction transverse to the transport's direction. The measures on the laser beams at their focus showed that this ideal situation was not realized in practice. From Figure 3.7, we can compare the ideal beam parameters to one of the best beam profile we have obtained in the experiment. From this picture, we can make two comments:

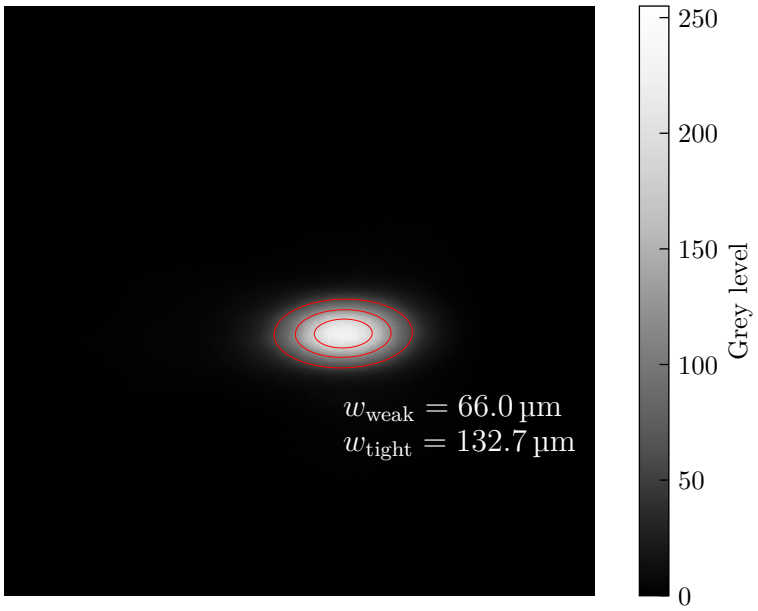

Figure 3.7: Grey-level picture of one of the transport beam at its waist. The red ellipses represent level lines of the Gaussian fit of the profile. The profile is tilted because of the orientation of the camera was not exactly matching that of the beam. $w_{\text{weak/tight}}$ are the beam's waist radii of the beam.

- The profiles in the experiment are wider than the ones expected from the Gaussian optics model used to design the apparatus.
- The aspect ratio of 1:2 is not exactly realized in the experiment but is 0.5-0.55 after optimization, which is quite satisfactory.

The degraded performances in terms of overall size at the focus are interpreted as arising from the high-power optical fiber[9] that we use to filter the output of the ODT laser spatially. The M^2 of the output beam for such a fiber is not estimated by the manufacturer. However, we can expect that it is far from ideal since the photonic-crystal core of the fiber has a hexagonal shape (see Appendix A). Concerning this last point, one explanation might have been astigmatism introduced by the cylindrical beam expander producing the 1:2-elliptical beam profile. In fact, we explain this defect by the diffraction on the aperture of the variable beam expander placed before the setup splitting the beam into two arms. Indeed, the output clear aperture of this component is 33 mm, which must be compared to the $1/e^2$-diameters of the beam at its output $\gamma \times (4.4\,\text{mm} \times 2.2\,\text{mm})$, where $\gamma \in [4; 8]$ is the magnification. This beam expander introduces clipping effects that are noticeable only in the vertical direction, producing the imperfect aspect ratio we observe. Those two observations mean that we can not compensate for the degraded performance due to the optical fiber by increasing γ because it leads to more clipping from the beam expander's aperture.

One more difference with the designed trap is the total power of at most 20W (instead of the planned 35W) at the entrance of the science chamber; given the beam profile that we measured, we can deduce the trapping frequencies of the ODT.[10] Those results are summarized in Table 3.1, we expected $3400 \times 750 \times 16$ Hz and should obtain $1200 \times 360 \times 5$ Hz, where the order of the axis is (vertical×transverse×longitudinal). We see that we have trap frequencies that should be 31 to 55% of the values expected from the design.

[9] ref: LMA-PM-15, from *NKT Photonics*

[10] Here, we assumed that the only effect of the deviation from the planned beam profile is a reduction of the intensity. In particular, there could be effect of the imperfect beam shape along the transport axis.

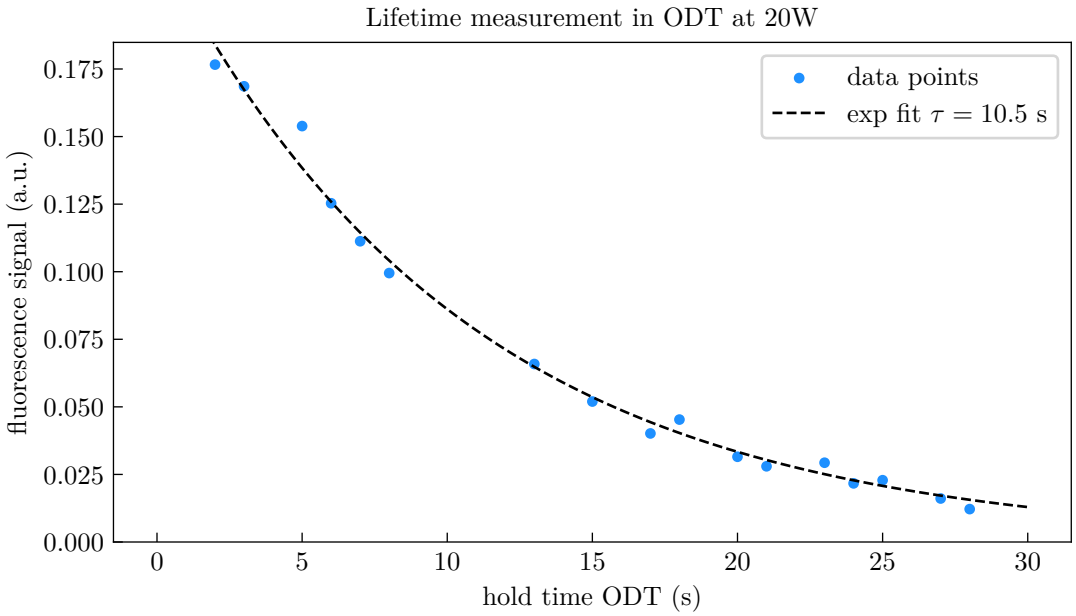

Figure 3.8: Lifetime measurement of the atoms in the transport optical dipole trap with the same protocol as for the magnetic trap. We find a lifetime of 15 s.

The expected impact of those reductions will make the transport harder but as we will see is not prohibiting.

	Design	Experimental
Total laser power	35 W	20 W
Vertical radius	50 µm	70 µm
Horizontal radius	100 µm	130 µm
Peak intensity	$8.9 \times 10^5\,\mathrm{W \cdot cm^{-2}}$	$2.8 \times 10^5\,\mathrm{W \cdot cm^{-2}}$
Trapping frequencies (vertical×transverse×longitudinal)	$3400 \times 750 \times 16$ Hz	$1200 \times 360 \times 5$ Hz

Table 3.1: Comparison of the expected and experimental transport ODT characteristics. These values are obtained assuming that the dominant effect of the imperfect beams was to dilute the available laser intensity. In particular, the beams are still modeled as perfect TEM_{00} Gaussian beams. The radii are given at $1/e^2$. By "Total laser power", we mean the sum of the power of the two beams, which produce the trap.

3.4.2.2 Lifetime in the ODT

We perform lifetime measurements on the atoms in the transport trap to check that the alignment of the transport is correct at the level of the MOT chamber. The protocol is the same as the one described in section 3.2.1 for the magnetic trap. The results are plotted in Figure 3.8. We obtain a lifetime of 15 s. This should not cause significant losses during the transport between the chambers since this should last between 1 and 2 seconds.

3.4.3 Travel to the microscope chamber

We will describe in this section the preliminary tests on the transport of the atomic cloud from the center of the MOT chamber to the science chamber. We will check that the transport can be achieved within times on the order of one to a few seconds, depending on how many atoms we accept to lose. For now, the survival probabilities are about 50% for transport in about 6 s.

3.4.3.1 Sequence

As mentioned in chapter 1, the transport of the trap is done by moving a lens with a translation stage. The default profiles is an "s-gamma profile", for the translation are represented in Figure 3.9. The translation stage goes from the starting point to the endpoint in the minimal time given the following constraints:

1. Keep the velocity below a specified value, $v_{\max}$,
2. Keep the acceleration below a specified value, $a_{\max}$,
3. Change the value of the acceleration in a time comprised between two bounds called the minimum and maximum "jerk time" t_{jerk},[11]
4. If possible, the translation stage tries to reach the maximum velocity and the maximum acceleration, prioritizing the acceleration.

These default constraints are the ones that were used to test the transport of the atoms. In Figure 3.9, we plotted the experimental profiles of position, velocity, and acceleration for typical values of the parameters mentioned above. These profiles are recorded directly by the translation stage. We observe that the acceleration profile is noisy; this means that some tuning of the PID controlling the movement should be performed.

In order to estimate the losses during the transport, we measured the number of atoms in the MOT chamber after transporting them to the science chamber and back to the MOT chamber. The parameters of the transport are the same for the forward and backward travels; thus, we estimate that the losses of atoms are roughly double compared to transport to the science chamber only.

3.4.3.2 Characteristics of the transported cloud

With the protocol described above, we obtain 50% of losses during a round-trip transport, from the MOT chamber to the science chamber and then back to MOT chamber, in 2×2.5 s. This should lead to losses of around 70% for a transport done in 2.5 s. The temperature after the transport was measured in the science chamber, we found $T \sim 4\,\mu$K. This heating might be mitigated in the future either by optimization of the transport protocol, by performing some laser cooling on the narrow transition, or while transferring the atoms from the transport trap to the vertical lattice trap.

[11] As a reminder, the jerk is the third time derivative of the position, *i.e.*, the time derivative of the acceleration. To simplify the situation, we impose equal minimum and maximum values.

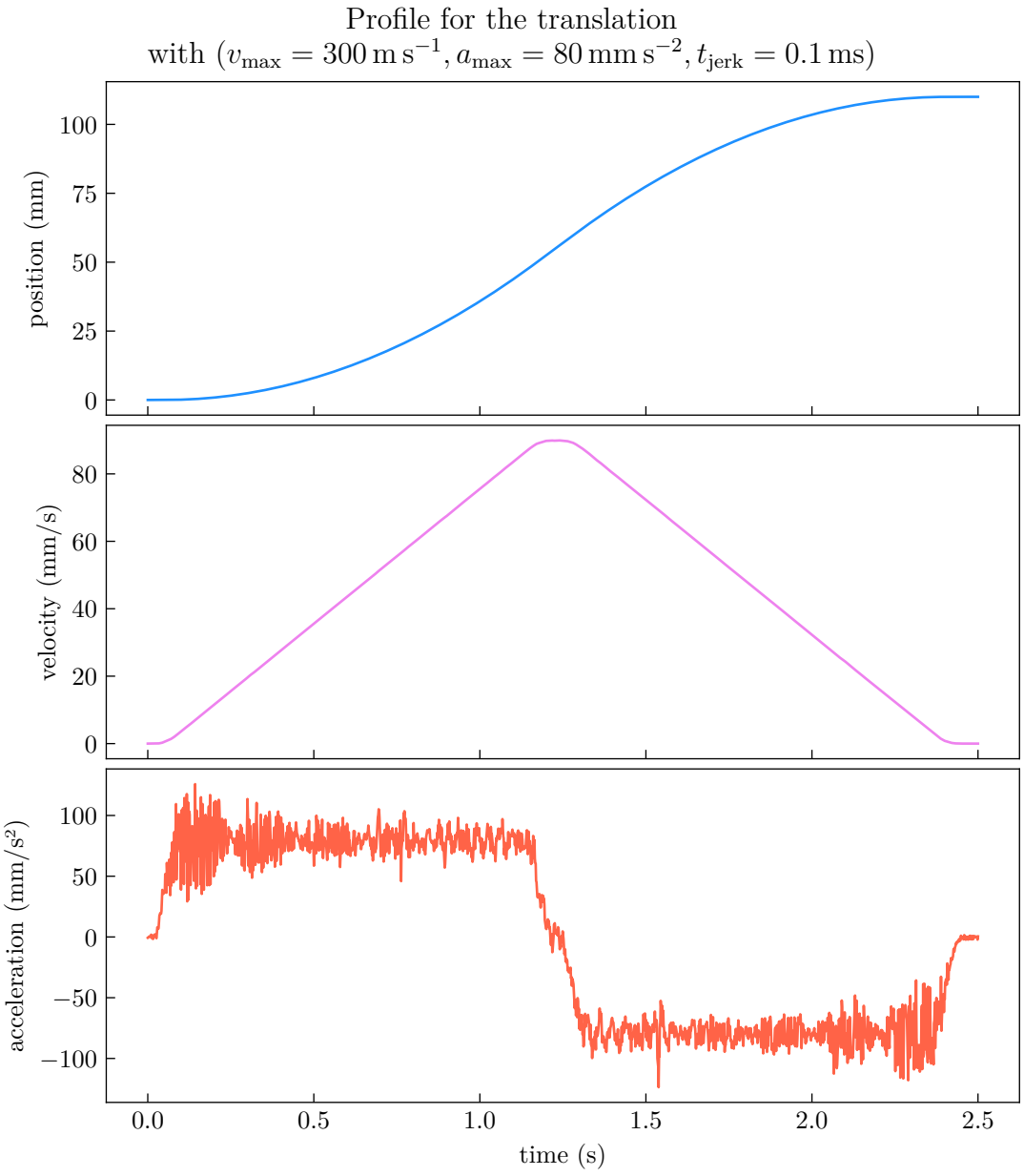

Figure 3.9: Experimental profiles for the translation of the translation stage. The parameters ($v_{max} = 300\,m \cdot s^{-1}$, $a_{max} = 80\,mm \cdot s^{-2}$, $t_{jerk} = 0.1\,ms$) are set to typical values that we use in the experiment. The total time for the transport is 2.5 s. That acceleration profile shows noise which we hope to mitigate in the future by improving the settings of the PID controller of the translation stage. This noise is also present in static mode and is probably partially caused by the ambient vibrations. Note that the value of t_{jerk} is the one used for the first tests as it is the default value for that parameter. We recently realized that $t_{jerk} = 100\,ms$ was a more reasonable value in practice.

3.5 Perspectives: Building of the optical lattices

After the atoms arrive in the science chamber, they must be transferred to the optical lattice. The building of the optical setups for the lattice traps is almost finished, and testing should start in the coming weeks. Once this is done, the first images with the microscope should be within our reach.

There are three independent optical dipole traps for the optical lattice (see chapter 1). A pair of crossed beams provides the confinement in a planar (2D) configuration. We call that trap the "vertical lattice"; it is similar to the transport trap in its principle and implementation. It will be overlapped with the transport trap to transfer the atoms in it. This setup has already been implemented, and preliminary tests have started. The other two traps are the "horizontal lattice" standing waves, which are used to superimpose a periodic modulation on top of the 2D trapping. Those setups are partially implemented and will be tested once a satisfactory transfer from the transport trap to the vertical lattice has been obtained.

Now that we have presented the current status of the experiment, we will start thinking ahead of time and discuss in the three following chapters the imaging of the atoms loaded in the optical lattice. We will imagine that an experiment has been performed and that we now want to image the atoms trapped in a square lattice in a single plane. Chapter 4 will be dedicated to presenting the imaging system and the reconstruction algorithms that were developed to analyze future images. In chapter 5, we present the computations of the dynamic polarizabilities for strontium, at 1064 nm, for both the $5s^2\ {}^1\mathrm{S}_0$ ground state and for the excited state $5s5p\ {}^3\mathrm{P}_1$. Finally, in chapter 6, we will investigate a model describing the fluorescence of a trapped strontium atom in a shallow trap.

Chapter 4

Reconstruction of microscope images

This chapter presents the algorithms developed to extract physical information from future microscope images. We first give an overview of the experimental context and emphasize the information we want to extract from the images. Then, we expose how simulated images were obtained since the experiment has yet to produce microscope images. Then, we will expose the three approaches developed to deconvolve the microscope images: an iterative fitting procedure, an algorithm using the Wiener filter, and a neural network. We then move on to the thresholding problem, that is, the attribution of labels ("empty" or "occupied") to each site from the deconvolved image. Finally, we conclude by presenting a comparison of the performance of these three approaches.

The work presented in this chapter is a long-standing project in the team. The iterative fit approach was started already by Marc Cheneau and Anaïs Molineri during her Ph.D. (see the fifth chapter of her thesis [22]) in collaboration with Matthieu Boffety and Caroline Kulcsár from the Imaging and Information group in Laboratoire Charles Fabry. This

algorithm was partly developed after I arrived in the team, mainly by Marc. My role was mostly suggesting tests to check the reliability of the algorithms, detecting bugs and biases of the method, and then using it to explore the constraints the image processing is imposing on the photon fluxes from the atoms. The Wiener filter approach was developed as a baseline to compare to the other algorithm. The neural network was developed and trained by Pauline Trouvé from the department "*Traitement de l'Information et Système*" at ONERA.[1] The details of the methodology and implementation of the neural network will be presented in an article comparing the different methods presented in this chapter and their performance. This chapter is a compilation and synthesis of different approaches explored throughout the years. The aim is to reference approaches that might be useful for the quantum gas microscope community, especially in cases where the optical resolution is insufficient to separate the neighboring atoms easily.

Our study was not restricted to only modeling our experimental situation, we rather tried to explore the limitations of our processing methods. The aim of this exploration was to simulate situation more demanding than ours, for instance, with lower optical resolutions, or lower photon fluxes, and determine to what extent signal processing can compensate for the corresponding degradation of the microscope images. We also explored the impact of imperfections in the model of the lattice grid or on PSF size. In particular, we will show that our experimental apparatus should enable error rates below 1% for around 200 photo-electrons per atom with a numerical aperture of 0.53, and that this result is robust to experimental errors on the model of the imaging system. These results pave the way for the conception of quantum gas microscopy with simpler and cheaper optical setup, smaller lattice periods, or lower photon numbers.

4.1 Context: Observables of interests

In our system, we will start with a Mott insulator with one atom per site at the center of the field of view of the imaging system. A "quantum quench",[2] creates excitations in the system, and dynamics starts. After some evolution time, we freeze the evolution by abruptly increasing the optical lattice's depth to its maximum, effectively suppressing the tunneling between the lattice sites. Once the dynamics have stopped, we image the atomic cloud by collecting photons scattered by the atoms.

Naively we expect the signal from a site to be proportional to the number of atoms on that site, and we expect to measure the atom number on each site. In this kind of system, however, light-assisted collisions expel atoms by pairs [44, 45] when the imaging light is turned on, on a time scale that is typically small compared to the imaging time. Thus, during the imaging phase, we can only have empty or singly occupied sites, meaning that we do not measure the atom number but its parity.

4.2 Simulation of the images

In order to test our algorithms on images with known occupancies, and because authentic images are not available yet, an algorithm producing simulated images was developed by

[1] ONERA: Office national d'études et de recherches aérospatiales.

[2] An abrupt reduction of the lattice depth, for instance.

the team. We first randomly draw a distribution of atoms. Then, we simulate the image obtained from the optical system using a model for the objective's point spread function (PSF), assuming that the atoms are all independent of their neighbors. At that stage, we also include photonic shot noise for each atom. Finally, we digitize the image using our sensor's matrix of pixels, and add the read noise from the camera.

4.2.1 Atom distribution generation

4.2.1.1 Simple model for the distribution of atoms

We start by generating a random atom distribution in the lattice. The distribution of atoms is represented by a matrix (n_{ij}) of size $N \times N$, where the matrix's entry (i, j) corresponds to the site (i, j). We then fix a disc of a given radius r_{disc} at the center of the image, where we will put atoms. Outside of the disc, there are no atoms. Within this disc, the occupancies are modeled by independent Bernoulli variables of parameter p; there is one atom on a site with probability p and zero with probability $1 - p$. p represents the average density in the disc. The simplicity of this model is interesting for investigating the reconstruction performance without focusing on too many physical parameters.

4.2.1.2 Physics-based model for the distribution

Previously [22], another model was used to emulate microscope images with a more realistic model of the physics of the atoms in the lattice. This model accounted for the residual harmonic trapping in the lattice, the chemical potential, and the temperature, in the so-called atomic-limit of the Hubbard model. However, the cloud's shape and the average density depend on multiple parameters, which is inconvenient for systematic exploration. Furthermore, our image processing procedure should be independent of the physical details of the behavior of atoms in a lattice. For those reasons, we do not use this physical model to investigate the performance of the image processing algorithms.

4.2.1.3 Comments on the relevance of the disc

Since we argued that we wanted to keep the model simple, one might wonder why we have introduced a disc limiting the extent of the "atomic cloud" instead of simply having a uniform distribution of atoms with density p. However, an empty zone surrounding the cloud benefits all the methods we have explored. For the iterative least-square method, starting the algorithm in a region with no atoms is helpful as we will see later. For the Wiener deconvolution, this empty area is equivalent to a window applied to the uniform image. The windowing prevents the "ringing" phenomenon that would appear at the edges of the reconstructed image. For the neural network method, it is essential that the network has "seen" edges during its training; otherwise, the reconstruction will not work for a realistic cloud with edges.

4.2.2 Generation of the simulated image

In the experiment, the atoms will be pinned down by a 2D optical lattice, as described in chapters 1 and 5. The position that the atoms can occupy will thus be a square grid, with a lattice spacing given by half the wavelength of the trapping laser $a = \lambda/2 = 532\,\text{nm}$.

To simplify the discussion, we will treat the case of a single atom on a single site (i, j). The image for a more complex distribution of atoms can be obtained by summing the contribution of the individual emitters.

The pair of indices (i, j) correspond to coordinates in the object plane $(x = ia,\, y = ja)$.[3] The optical system maps it to its geometrical image:

$$(x,\, y) \to (x' = \gamma x,\, y' = \gamma y) \tag{4.1}$$

with $\gamma \sim 40$, the magnification of the system. The prime notation will indicate quantities in the image plane.

The sensor represented is a matrix of size $N' \times N'$ with:[4]

$$N' = \lceil \gamma N \rceil \tag{4.2}$$

where $\lceil \cdot \rceil$ denotes the ceiling function. We now need to fill the pixels with photons from our atom, knowing that its geometric image is at $(x',\, y')$. The number of photons emitted by the atom is supposed to have a fixed value of N_{ph},[5] and we must distribute them into the different pixels around $(x',\, y')$. We use the PSF as a probability density function (PDF). The probability for a given pixel $(k,\, l)$ to receive a photon, denoted p_{kl}, is given by the integral of the PSF on the pixel:

$$p_{kl} = \int_{\text{pixel } (k,l)} \text{PSF}(u' - x',\, v' - y')\mathrm{d}u'\mathrm{d}v'. \tag{4.3}$$

We draw the pixels on which each photon will fall using the probabilities $\{p_{kl}\}$. The fact that, for a given configuration, the number of photons incident on a pixel is random means that we will have photonic shot noise even with a fixed value for the number of photons emitted by the atom. The number of incident photons on the pixel (k, l), n_{kl} is thus a sum of independent Bernoulli variables with a probability of success of p_{kl}.[6] Thus, n_{kl} follows a binomial law of parameters $(n = N_{\text{ph}},\, p = p_{kl},\, q = 1 - p)$, instead of a Poisson law $\mathcal{P}(N_{\text{ph}})$. This results in a reduction of the variance of n_{kl} by a factor $(1 - p_{kl})$. This represents a small correction as p_{kl} is typically small, which means the simplification of fixing the number of photons per atom should not change the photonic shot noise on the sensor by much.

We now need to convert the photons received by each pixel (n_{ph}) into a photo-electron number (n_{el}). This conversion will have the following form:

$$n_{\text{el}} = \eta\, n_{\text{ph}} + n_{\text{read}}, \tag{4.4}$$

where $\eta \sim 70\%$ is the quantum efficiency of our camera at 689 nm, and n_{read} is the read noise of the considered pixel. In (4.4), we assume that the only noise source is the read noise. In particular, the dark noise is expected to be negligible for sCMOS

[3] A more rigorous notation would be $(x_i,\, y_j)$. It would, however, be redundant as long as we consider a single atom.

[4] In fact, the situation is slightly more complicated if we introduce an angle between the axes of the lattice and those of the camera, but for simplicity, we will not discuss that case.

[5] To be precise, this is the number of photons collected and transmitted to the camera. We can also use a random number of photons for each atom, using a Poissonian random variable of average N_{ph}.

[6] In the case were there are multiple occupied sites, p_{kl} depends on i and j and we have to sum over these additional indices. The result is thus a sum of binomial random variables.

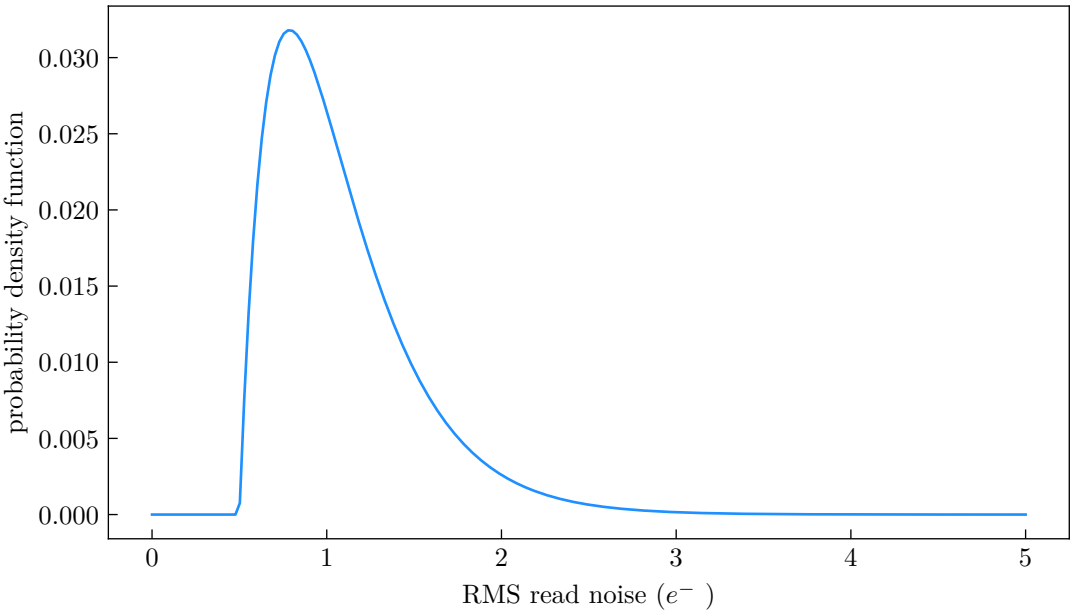

Figure 4.1: Approximation of the read noise distribution over the matrix of pixels, from the data provided by the manufacturer.

cameras (see Andor's website https://andor.oxinst.com). For our camera, we expect a dark noise on the order of $0.019e^-$/pixel/s (water-cooled sensor) compared to the typical $0.9e^-$ (median value in "slow read mode") read noise; this value includes the readout noise and analog-to-digital conversion noise [46]. Note that we refer to photo-electrons and not to analog-to-digital units (ADU) in this discussion. This means we back-propagated the noise in ADU from the analog-to-digital conversion, using the conversion gain.

The read noise is specific to each pixel and is assumed to be Gaussian with zero average. The constructor of the camera provides a histogram of the variances of the read noises over the whole matrix of pixels (see Figure 4.1). The simulation of the read noise is done as follows:

1. For each pixel, we draw a variance using the histogram from the constructor as a PDF.
2. We then draw a random number of photo-electrons using a Gaussian distribution with zero average and the variance obtained in the previous step.

In principle, it would be possible to calibrate the variance of the read noise for each pixel of our camera; this refinement has yet to be implemented.

4.2.3 Length scales of the problem

Our imaging problem has three length scales: the lattice spacing $\lambda/2$, the pixel size r_{px}, and the PSF size r_{PSF}. In the following, we will model the PSF by an Airy disc, and r_{PSF} will be the Abbe radius:

$$r_{\text{PSF}} = \frac{\lambda_r}{2\text{NA}},$$

where we noted $\lambda_r = 689\,\text{nm}$, the wavelength of the imaging. The Abbe radius corresponds to the inverse of the inverse of the maximal spatial frequency that an imaging system can

transmit for given wavelength and numerical aperture. It is 1.22 times smaller than the radius of the first dark ring of the Airy disc. From those, we can construct new dimensionless quantities to parametrize our problem:

1. the *magnification* that is the ratio of the lattice spacing in the image plane to the pixel size given by $\gamma' = (\gamma\lambda/2)/r_{\text{px}}$ in pixels per lattice spacing,
2. the *pixelation* of the PSF, that is, the PSF size in the image plane divided by the pixel size $\gamma r_{\text{PSF}}/r_{\text{px}}$
3. the *size of the PSF* in lattice sites can be obtained from the previous two using:

$$\frac{r_{\text{PSF}}}{\lambda/2} = \frac{\lambda_r/\lambda}{\text{NA}}.$$

We can choose two independent parameters to explore the parameter ranges of the imaging system. We will use the pixelation and the PSF size in section 4.5 when we evaluate the performance of the different algorithms. The values of parameters that correspond to our system are $\gamma' = 3.55$ pixels per lattice spacing, and a pixelation of 3.3, where we used: $\lambda = 1064\,\text{nm}$, $\gamma = 40$. It was observed on a test bench (see [23] that the PSF of our system has degraded performance compared to the expected numerical aperture of 0.64. To model the PSF with degraded performance, we will suppose the PSF is an Airy disc of size 1.2 (lattice sites) corresponding to a numerical aperture of 0.53.

4.2.3.1 Standard resolution criteria

The value obtained of 1.2 lattice period for the Abbe radius places our system below the standard resolution limits in optical microscopy. A few resolution criteria are summarized in Table 4.1, where we included the Rayleigh, Abbe, and Sparrow criteria. The Rayleigh criterion correspond to having the atoms spaced by at least the radius of the first dark ring of the Airy disc. The Abbe criterion asks that the distance is at least that Abbe radius. Finally, the Sparrow criterion requires that there is a local minimum of intensity between the peaks corresponding to the image of the two atoms. We are indeed working below the resolution limit imposed by all three criteria. Furthermore, we will see that we can obtain good performances for resolutions even poorer than 1.2 lattice period.

Criterion	Minimal distance	Maximum r_{Abbe}
Rayleigh	$1.22 r_{\text{Abbe}}$	0.82 $\lambda/2$
Abbe	r_{Abbe}	$\lambda/2$
Sparrow	0.94 r_{Abbe}	1.06 $\lambda/2$

Table 4.1: Resolution criteria for a two point objects and a diffraction limited imaging system in term of minimal separation and maximum Abbe radius assuming a distance of a lattice period $\lambda/2$.

4.3 Calibration of the lattice grid and of the PSF

To image the cloud of atoms trapped in our optical lattices and extract the occupation of each lattice site, we will first need to determine the position of the lattice grid relative

to the camera's matrix of pixels. In practice, this could be obtained by imaging a "hot" thermal gas and making sure that the atom number is low enough. This can be achieved by using image with dilute clouds in which there are isolated atoms. We will not develop the details of the methods used here, but simply define the parameters that we measure with these calibration images.

Using such images one can calibrate the lattice period in the image plane, which is equivalent to measuring the magnification γ'. We also extract the relative orientation of the lattice grid with respect to the pixel grid of the sensor. These two parameters are not expected to fluctuate a lot in time as they only depend on the alignements of the optical elements in the system.

One additional parameter that we estimate is the "offset" of the lattice grid with respect to the pixel grid. The offset of the grid is defined as the distance in lattice period, from the center of the $(0, 0)$-pixel. This last parameter will depend on the relative phases of the different pairs of beams producing the optical lattice, and might therefore fluctuate on faster time scales. It might require doing a calibration image every few experimental cycle to measure its drift in time and correct it (numerically).

Finally, the sparse samples can also be used to obtain images of individual atoms giving access to the PSF of the system. Such measurement can even be local to include spatial variation of the PSF in the field of view.

4.4 Deconvolution algorithms

For our model, we will consider as an input the vector X which is a "flattened"[7] version of the matrix of occupancies of the lattice sites, restricted to some region of interest (ROI). For readability, we will note in this part $X_{i,j}$ the occupancy of site (i, j) instead of n_{ij}. The output Y of the model will be a vector composed of the photo-electron numbers on each pixel of the camera. The *deconvolution* procedure aims at reconstructing the data X from the observations Y. It can be achieved using different approaches, as shown in the following.

We consider that each atom is an independent point source, therefore, our model for the imaging is linear in X; thus, *if there were no noise*, we could write:

$$Y = AX, \tag{4.5}$$

where A is called the design matrix of the system, and models the effect of the objective and the matrix of pixels.

The design matrix can be computed as follows: we first compute the intensity in the image plane, then we pixelize it to model the sensor's action. The intensity in the image plane $\mathcal{I}(x', y')$ is given by:

$$\mathcal{I}(x', y') = \mathcal{I}_0 \sum_{i,j} X_{i,j} \mathrm{PSF}(x' - ia, y' - ja)\,, \tag{4.6}$$

where x' and y' are the coordinates in the image plane, and $\mathcal{I}_0$ represents the intensity from each atom and was taken to be the same for all the atoms for simplicity. Note

[7] Flattened here means that we take the columns of the matrix and concatenate them to obtain a column vector.

that we could include spatial variation of the PSF inside the field of view by replacing $\mathrm{PSF}(x' - ia, y' - ja)$ by $\mathrm{PSF}(x', y', x' - ia, y' - ja)$. Using (4.6), we can pixelize it to obtain the (average) number of photons incident on the (k, l) pixel $N_{\mathrm{ph}\,k,l}$:

$$N_{\mathrm{ph}\,k,l} = \iint \mathrm{d}x'\,\mathrm{d}y'\,\mathbf{1}_{k,l}\mathcal{I}(x', y') \tag{4.7}$$

$$= \mathcal{I}_0 \sum_{i,j} X_{i,j} \iint \mathrm{d}x'\,\mathrm{d}y'\,\mathbf{1}_{k,l}\mathrm{PSF}(x' - ia, y' - ja) \tag{4.8}$$

$$= \sum_{i,j} \alpha_{k,l,i,j} X_{i,j} \tag{4.9}$$

where we introduced the notation:

$$\alpha_{k,l,i,j} = \mathcal{I}_0 \iint \mathrm{d}x'\,\mathrm{d}y'\,\mathbf{1}_{k,l}\mathrm{PSF}(x' - ia, y' - ja) \tag{4.10}$$

and $\mathbf{1}_{k,l}$ is one inside the (k, l) pixel and zero outside. Now relabelling the sites and pixels by replacing $(i, j) \to I$ and $(k, l) \to K$ gives:

$$N_{\mathrm{ph},\,K} = \sum_I \alpha_{K,I} X_I = AX, \tag{4.11}$$

with $A = (\alpha_{K,I})_{K,I}$. Taking into account the quantum efficiency η and adding the read noise, we finally obtain the photo-electron number as:

$$Y = n_{\mathrm{el}} = \eta N_{\mathrm{ph}} + n_{\mathrm{read}} \tag{4.12}$$

$$= \eta AX + n_{\mathrm{read}}. \tag{4.13}$$

From here on, we will redefine A such that it includes the quantum efficiency η ($\eta A \to A$). Note that we fixed a constant value for the intensity associated to each site $\mathcal{I}_0$. In practice, one might have to account for homogeneities in the trapping potentials leading to different scattering rates. Furthermore, due to losses of atoms, the intensity for each site could be modeled by a random variable, representing the loss of the atom at a random time. In equation (4.13), we neglected the shot noise, a more realistic model would be to replace the vector of photon numbers N_{ph} by a vector of Poisson variables $\mathcal{P}(N_{\mathrm{ph}})$.[8] This was not included in the model as neither Wiener filter nor the linear least-squares are designed to treat Poisson noise. Instead, these two methods are optimal (in the mean squared error sense) when the data includes an additive Gaussian noise N uncorrelated with the data with 0 mean, giving rise to the following relation:

$$Y = AX + N. \tag{4.14}$$

If we further assume the system is shift invariant, we can rewrite the previous equation in the form of a convolution:

$$Y = K * X + N. \tag{4.15}$$

The shift-invariance hypothesis boils down to assuming that the PSF of the optical system is the same in all the field of view. This assumption can be quite demanding for the optical system or quite restrictive for the size of the samples we can observe.

[8] A more refined procedure, including Poisson noise arising from the shot noise, is treated in [47].

4.4.0.1 Comment on the absence of background noise

In principle, we could have introduced a term representing the background noise. This term occurs to be the main nuisance to the imaging performance in some microscope experiments (see, for instance, [48]). We will briefly discuss the impact of the background in the last section of this chapter. We decided to neglect it for most of our study as we expect to be able to filter the background in our experiment. Indeed, unlike typical quantum gas microscope experiments using high-NA microscope objectives, our setup will present an intermediate image plane in which we will do filtering with a pin hole.

4.4.1 Iterative linear least-square (ILS) method

4.4.1.1 Principle of the method

The least-square problem is the following, given the output vector (measurements) Y and the design matrix A, we want to find the input vector $\hat{X}$ minimizing the squared error:

$$\hat{X} = \arg\min_X \|Y - AX\|^2. \tag{4.16}$$

where $\|\cdot\|$ is the euclidean norm. $\hat{X}$ is used to estimate the "real" input X that generated $Y = AX + N$ in the presence of additive noise N. In our case, A represents the effect of the microscope (magnification and PSF) and digitization by the camera. We can see that this model does not rely on the shift-invariance hypothesis, the ILS method can therefore account for local variations of the PSF, arising for instance from field aberrations. In that sense, the iterative least-square method is more flexible and adaptable than the Wiener filter which rely on the shift-invariance assumption.

In this approach, we use our knowledge of the PSF and the grid of the lattice sites' positions, to implement a "fit procedure" where the fit parameters are the occupancies n_{ij}. In practice, for a relatively large sample size, say 100×100 sites, processing the whole image at once is very demanding in terms of computation time. One way to obtain faster processing of the images is to split the image into blocks and apply the fit to each of them. However, independently fitting the sub-pictures leads to errors on the frontiers of the blocks. These errors are caused by the occupied sites at the edge of one block contributing to the signal in the neighboring block (see Figure 4.2).

To reduce the errors introduced by the subdivision in blocks, we fit the blocks sequentially. We fit a first block and move on to the next, but instead of applying the fit routine directly on the image of the second block, we remove the signal coming from the *fitted* sites of the neighboring blocks that have already been updated. We follow that protocol for all the blocks of the image, and then iterate by going back to the first block and restarting the protocol. The procedure is iterated over the blocks until convergence has been reached. If a block and its neighboring sites did not change in the previous iteration, it is not fitted at the next iteration.

4.4.1.2 Reduction of the problem to a non-negative linear least-square problem

A first observation is that the model's parameters, the occupancies of the site n_{ij}, are positive numbers. We can implement these constraints in the linear least-square problem

using so-called Non-Negative Least Square algorithms (see, for instance, `optimize.nnls` from the `scipy` python library [49]). The constraint of positivity is crucial in our case since it drastically reduces the computation times compared to non-constrained linear least-square solvers (at least by a factor 10).

4.4.1.3 Implementation of the ILS method

Choice of the solver

To implement the fit procedure, we use the `ElasticNet` solver from the `scikit-learn` python library [50]. It solves the linear minimization problem, including the positivity constraint. It also provides two regularizations, which use the l_1- and l_2-norms of the X vector. The minimization problem is thus slightly different than the one presented in (4.16). It reads:

$$\hat{X} = \arg\min_X \left[\frac{1}{2N} \|Y - AX\|^2 + \alpha\rho \|X\|_1 + \alpha \frac{(1-\rho)}{2} \|X\|_2^2 \right]. \tag{4.17}$$

where N is the dimension of X, α is the "strength" of the regularization, and ρ is the relative weight of the two regularizations. Typically, we use $\alpha = 0.01$ and $\rho = 0.5$, these parameters, however, do not seem to require fine-tuning.

The need for regularization comes from the fact that in general the least-square problem is ill-posed or ill-conditioned, that is, it is very sensitive to the noise.[9] The introduction of a regularizing term can solve the ill-posedness of the problem at the expense of having an approximate solution to the least-square problem. A trade-off must be found by tuning the α parameter: if it is too small the solution $\hat{X}$ will be too sensitive to the noise; if the regularization is too strong, the solution will not reproduce faithfully the data Y.

Block structure for the iterations

The images that we treat typically have 128×128 sites. They are split into blocks of 50×50 pixels.[10] The first block to be fitted is the one at the top left corner, which is most likely empty and also has empty neighboring blocks. Starting in an "easy" part of the image helps the convergence. Then, we move on to the next block on the right. We subtract the signal from the neighboring sites outside of a block when they are at a distance smaller than twice the radius of the first dark ring of the PSF; this defines a shell around each block in which there can be cross-talk with its neighbors.

To be more precise, the image is split into a set of blocks label by the index b. The fitted occupancies at iteration n in block b are written $X_b^{(n)}$ and the image in block b is Y_b. To compute $X_b^{(n+1)}$, we apply the least-square procedure to Y_b from which we first remove the signal arising from $X_{b'}^{(n+1)}$ if $b' < b$ and $X_{b'}^{(n)}$ if $b' > b$. Therefore, we always use the most recent information about each block to perform the updates.

A schematic view of the situation is drawn in Figure 4.2. There the PSFs are represented by Gaussian-like red spots. The situation is simplified since the pixel and site grids are commensurate. For readability, the blocks are 9×9 pixels instead of 50×50. The shaded blue area represents the cross-talk shell around the central block.

[9] For a rigorous definitions the interested reader can consult [51].

[10] The pixels that do not fit into 50×50 blocks are grouped into smaller blocks.

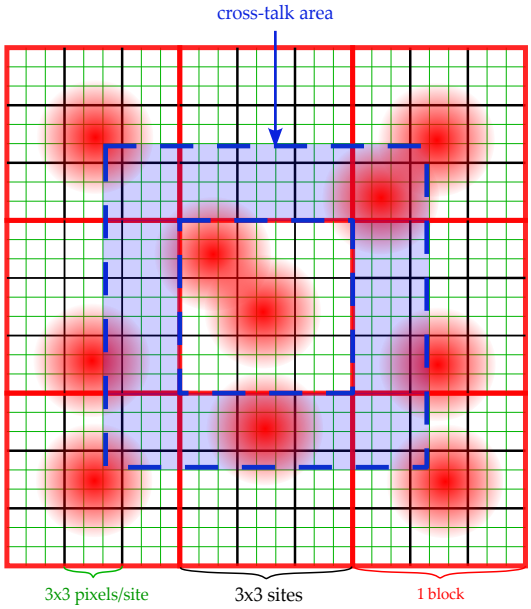

Figure 4.2: Simplified block structure for the iterative least-square method. The green grid represents the pixels in the image space, the black square are centered on the lattice sites whose sides have a length equal to the lattice period, and the red grid represents the blocks for the fit. The shaded blue area represents the region in which atoms can influence the signal of neighboring blocks. This region is displayed only for the central block. *Adapted from A. Molineri's thesis [22].*

Computational performance

For our experiment, we would like to monitor the results of the reconstruction algorithm in real-time. This imposes that we analyze an image in a time shorter than the experimental cycle, which will have a duration of a few seconds, most likely on the order of 5 s. This already guided us towards splitting the image into blocks over which we iterate the fit procedure.

Another critical point for the efficiency is the choice of the solver. There are a variety of available python solvers for linear least-square problems. A few of them were investigated during this study. We found that a crucial feature was the ability to implement the non-negativity constraint. Indeed, we improved a factor of 10 in the computation times by enabling the non-negativity constraint. This, in turn, is used to reduce the number of blocks, hence reducing the side effects at the edges of the blocks, while maintaining reasonable computation times on the order of the second. We also found that using the `ElasticNet` function from `scikit-learn` was beneficial in terms of computation times, for instance, compared to the `Ridge` function also from `scikit-learn` (which only include the l_2 regularization). This probably arises from the different algorithms used to minimize the criterion in (4.17). The `elastic net` solver of `scikit-learn` implements the coordinates descent method [52], while the `ridge` function uses the L-BFGS algorithm (Limited-memory Broyden–Fletcher–Goldfarb–Shanno algorithm) [53] when the non-negative constraint is included.

Fitted amplitudes from ILS method

In Figure 4.3, we plot the histogram of the amplitudes after a simulated image was processed using the ILS method. The parameters for the generated image are the follow-

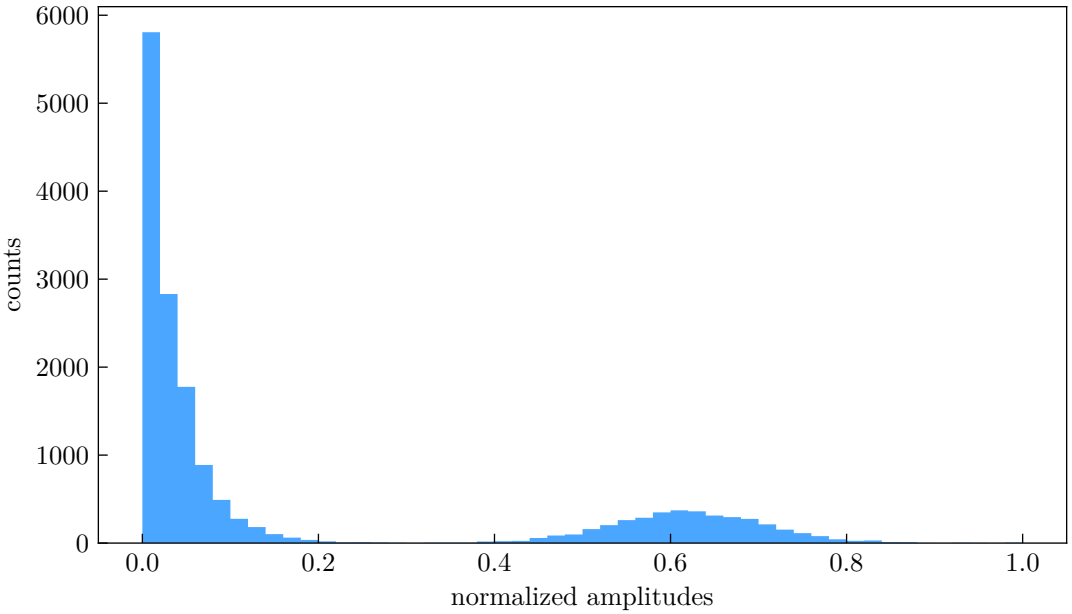

Figure 4.3: Histogram of the amplitudes obtained with the ILS method for the following parameters: 20×20 blocks, $\alpha = 0.01$, $\rho = 0.5$, an Abbe radius of 1.2 lattice period, a pixelation of 3.3, and 200 photo-electrons per atom.

ing: an Abbe radius of 1.2 lattice period, a pixelation of 3.3, and 200 photo-electrons per atom. We used 20×20 blocks, $\alpha = 0.01$, and $\rho = 0.5$. We observe that the histogram is composed of two lobes corresponding to the empty and occupied lattice sites. There is an accumulation in zero as the empty regions outside the disc of atoms are easier to deconvolve. Furthermore, the positivity constraint prevents negative amplitudes from appearing in contrast to what we will obtain for the Wiener deconvolution (see Figure 4.6).

4.4.1.4 Impact of the block size for the ILS

The block size is a crucial parameter for the iterative least-square method. Anticipating on the discussions on the computation of the deconvolution methods' performance, we present here a graph showing the "performance" of the ILS method as a function of the block size.[11]

In Figure 4.4, we plot the precision and recall for 120 photo-electrons per atom and Abbe radii of 1.2 and 1.5. We observe that the performance converges for block sizes above 20 and 40 respectively. The convergence is slower when the size of the PSF is increased. This can be interpreted as follows: when the PSF gets wider, the "couplings" between the blocks are increased; thus, we wish to mitigate the increased cross-talk between the blocks by reducing the number of blocks. Unsurprisingly, the results are better with a smaller PSF at fixed SNR. In what follows, we will use a block size of 50 pixels to ensure that we reach the plateau without increasing to much the computation times.

[11]The precision and recall will be defined in section 4.5.1. They are scores sensitive to the false positive and false negative, respectively.

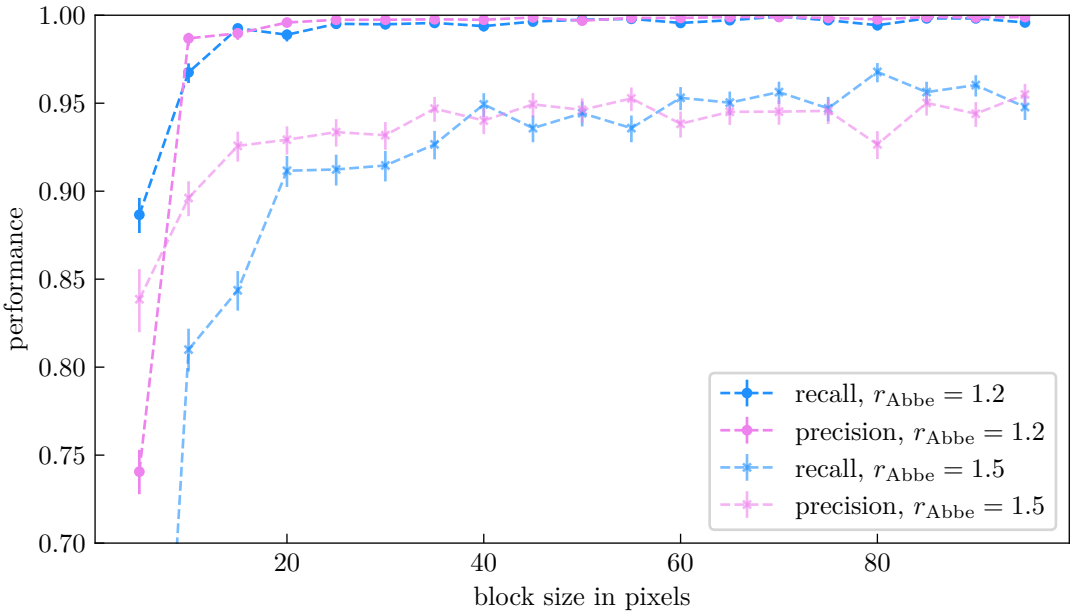

Figure 4.4: Performance of the ILS for increasing block sizes for an SNR of 3, a pixelation of 3.3, and Abbe radii of 1.2 and 1.5. The performance saturates in both cases after a block size above 20 and 40 roughly.

4.4.2 Wiener filter

In order to compare our algorithm to a standard deconvolution method, we used the Wiener filter routine from the python library `scikit-image` [54]. Let us first describe the spirit of the Wiener filter deconvolution before describing the implementation in more detail. The derivations of the formulas and the hypotheses were not all mentioned as this section is merely a qualitative introduction to the Wiener filter. For more details on the Wiener filter, we refer the reader to [55, 56]

4.4.2.1 Wiener filter: overview of the method

The Wiener filter method operates in the Fourier domain, taking the Fourier transform of equation (4.15), we get:

$$\tilde{Y}(f) = \tilde{K}(f)\tilde{X}(f) + \tilde{N}(f)\,, \tag{4.18}$$

where the "$\sim$" is a shorthand notation for the (discrete) Fourier transform, and f represents the spatial frequencies of the 2D picture we are studying. The spirit of the Wiener filter is to find W such that:

$$(W * Y)(n) = \hat{X}(n) \approx X(n)\,, \tag{4.19}$$

with n denoting the spatial variables, and $\hat{X}(n)$ the estimator of $X(n)$. Since it depends on the realization of the noise $\hat{X}$ is itself a random variable. We impose that the mean-squared error is minimized by W, *i.e.*:

$$\forall n, \quad \frac{\partial}{\partial W}\mathbb{E}\left[(X(n) - \hat{X}(n))^2\right] = 0\,. \tag{4.20}$$

In the absence of noise, we can simply choose:

$$W(n) = \mathcal{F}\left[1/\tilde{K}(f)\right](n)\,, \tag{4.21}$$

with $\mathcal{F}$ the Fourier transform. This choice is called the *inverse filter*, it gets catastrophically bad as soon as the signal-to-noise ratio (SNR) is not extremely high; therefore, we can not resort to it with real-world noisy data.

The Wiener filter is the solution to (4.19) and (4.20). In the case where the noise and the signal are decorrelated, and the noise has zero average, we get the following expression for the Fourier transform of the Wiener filter:[12]

$$\tilde{W}(f) = \frac{1}{\tilde{K}(f)}\frac{1}{1+1/\mathrm{SNR}(f)}\,, \tag{4.22}$$

where $\mathrm{SNR}(f)$ represents the "signal-to-noise ratio" in the frequency domain, and is given by:

$$\mathrm{SNR}(f) = \frac{|\tilde{K}(f)|^2\tilde{\Gamma}_{XX}(f)}{\tilde{\Gamma}_{NN}(f)}\,, \tag{4.23}$$

with Γ the covariance matrices of X or N, whose Fourier transforms are the associated power spectral densities. From (4.22), we can interpret the action of the Wiener filter depending on the value of the SNR. If the SNR is much greater than one, we see that the Wiener filter is close to the inverse filter. On the contrary, if the SNR is low, the Wiener filter will filter out the corresponding frequency component at which the noise is dominant in the image's spectrum ($\tilde{W}(f) \approx \tilde{K}^*(f)\tilde{\Gamma}_{XX}(f)/\tilde{\Gamma}_{NN}(f)$ is small).

For the details of the algorithm used by the implementation of the Wiener filter from `scikit-image`, the reader can consult the documentation of `scikit-limage` here or in [54],[13] or the references [57, 58].

4.4.2.2 Implementation

We implement the Wiener deconvolution using the following protocol inspired from La Rooij *et al.* [48]:

1. First, we apply a windowing step to remove some background noise in regions with no atoms. It also enforces periodic boundary conditions that are required by the Wiener filter. If there where discontinuities at the edges, the Wiener filter would introduce high frequencies oscillations called "ringing". In practice, the window function is a disc of radius 1.2 times larger than the radius of the cloud, and a Gaussian filter (convolution by a gaussian kernel) is applied outside this region of interest.

2. The image is then up-sampled to reduce the impact of pixelization on the PSF. Indeed, the Wiener filter assumes that the PSF is the same throughout the image.

[12] This hypothesis is reasonable for the read-noise contribution. The shot noise, however, is notoriously not independent of the signal. An alternative could be to use the Richardson-Lucy deconvolution that is designed to be optimal in the presence of shot noise, but does not include the read noise that dominates in the absence of emitters.

[13] https://scikit-image.org/docs/stable/api/skimage.restoration.html#skimage.restoration.wiener

However, if the pixel size is not small compared to the PSF and the lattice period in the image plane is not commensurate with the pixel size, two distinct sites will have different digitized PSF. The up-sampling is performed using zero padding on the discrete Fourier transform of the image and then performing the inverse Fourier transform. We found that the zero padding approach provided slightly better results than the up-sampling without interpolation used in [48]. We typically use an up-sampling factor of 4.

3. We then apply the Wiener filter from `scikit-learn`. Using the PSF and the default Laplacian kernel for regularization. This Laplacian kernel is used to replace the unknown ratio of power spectral densities $\tilde{\Gamma}_{NN}/\tilde{\Gamma}_{XX}$. It penalizes the high frequencies since its spectrum goes as f^2. This choice amounts to assuming that we the signal's spectrum decays as $1/f^2$ at high frequencies, while the noise is white, thus with constant power spectral density. The choice of the exponent 2 is standard but we could in principle use an arbitrary exponent α and look for the best performance for different f^α-regularization.[14] The strength of the noise K is the only adjustable parameter of the Wiener deconvolution (once the noise model has been chosen). This corresponds to `balance` parameter of the `scikit` implementation of the Wiener filter.

An example of the procedure is displayed in Figure 4.5.

4.4.2.3 On-site amplitudes from the Wiener filter output

To extract the amplitude of the signal at each lattice site from the image filtered using the Wiener deconvolution, we compute the sum of the pixel's value inside a disc of half a lattice period (following the methodology from [48]). We obtain the same structure for the output of Wiener filtering and ILS method. We will now discuss how to determine if a site is occupied or empty from the amplitudes on each site.

Using a noise strength $K = 8$ and an up-sampling factor of 4, we obtain the histogram in Figure 4.6, with a pixelation of 3.3, an Abbe radius of 1.2 lattice period, and 200 photo-electron per atom. We obtain an histogram composed of two lobes resonably well separated. The narrow peak at zero corresponds to the empty sites outside of the disc of atoms, for which the deconvolution is much easier and produces lower dispersion of the amplitudes. We will discuss in details the performance of the deconvolution in section 4.4.3.

[14] This choice differs from the one used in [48], where the authors used a regularization independent of f corresponding to having a white signal in addition to a white noise.

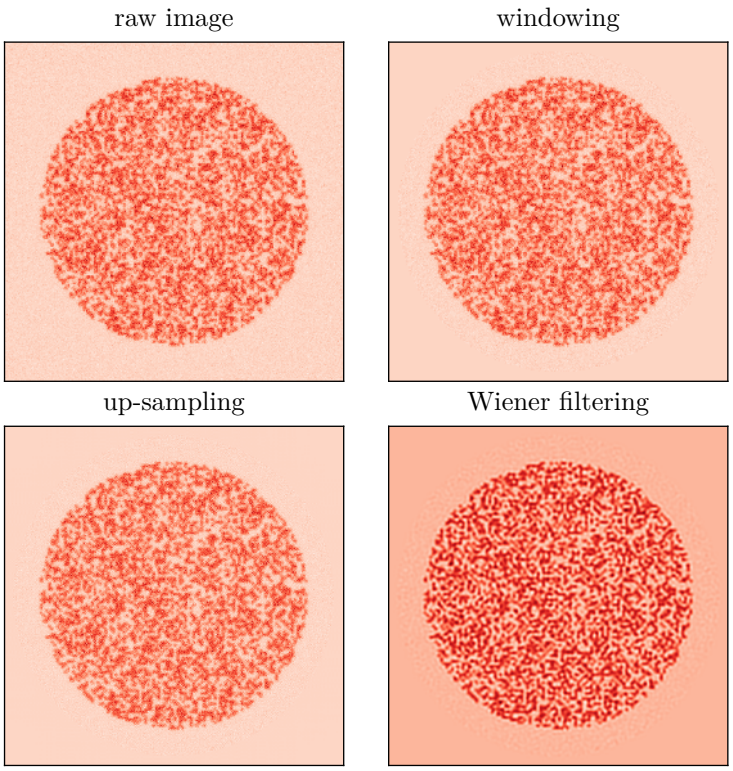

Figure 4.5: Images representing an instance of the different steps of the procedure used for the Wiener filtering of the microscope images, as described in item 3. The up-sampling factor is set to 4 in that example and the noise strength is set to 8. An histogram of the amplitude corresponding to this situation is displayed in Figure 4.6.

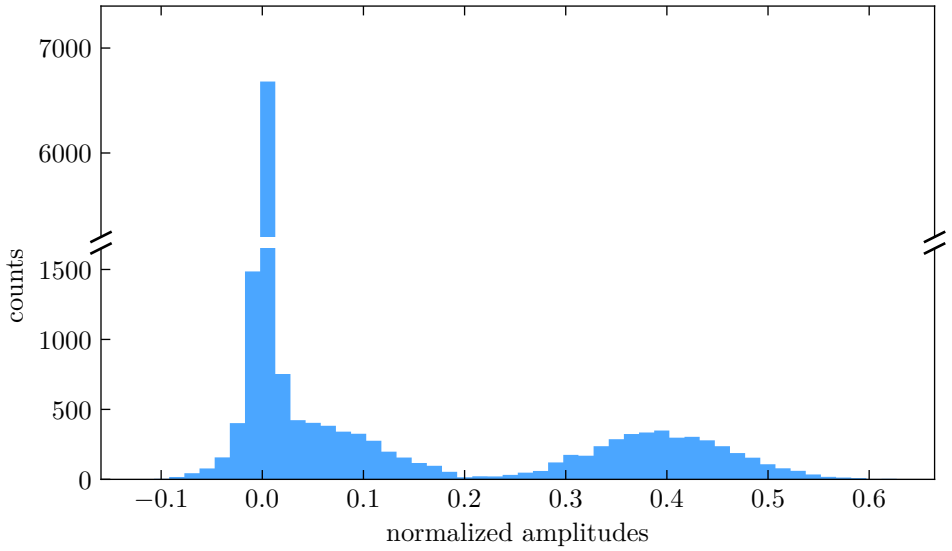

Figure 4.6: Histograms of the amplitudes obtained by Wiener deconvolution for $\lambda = 8$ and an up-sampling factor of 4. The parameters for the image generation and deconvolution are: a pixelation of 3.3, an Abbe radius of 1.2 lattice period, and 200 photo-electron per atom. The histogram obtained presents two lobes with an accumulation around zero due to the empty area outside the disc of atoms.

4.4.2.4 Impact of the K parameter and of the up-sampling factor for the Wiener deconvolution

As for the block size discussion for the ILS, we anticipate here on the discussion of the scores to show the impact of the parameters of Wiener methods.

The parameter K modeling the noise strength in the Wiener filter. It should be chosen appropriately, in order to avoid the introduction of artifacts such as correlations between the neighboring sites (see Figures 4.11 and 4.14). In Figure 4.7, we present the precision and recall for different value of K in the case were we have about 120 photo-electrons per atom, a pixelation of 3.3, and an Abbe radius of 1.2 lattice period. We observe a plateau of performance between $K = 0.1$ and 10, with a maximum around 1. In what follows, we will keep K constant and equal to 1 in the remainder of the chapter.

The second parameter to be tuned in the Wiener approach is the up-sampling factor. In Figure 4.8, we scan the up-sampling factor for the same configuration as in previous section. The optimal up-sampling factor is equal to 4 for this configuration and will be set at this value for the remainder of this chapter.

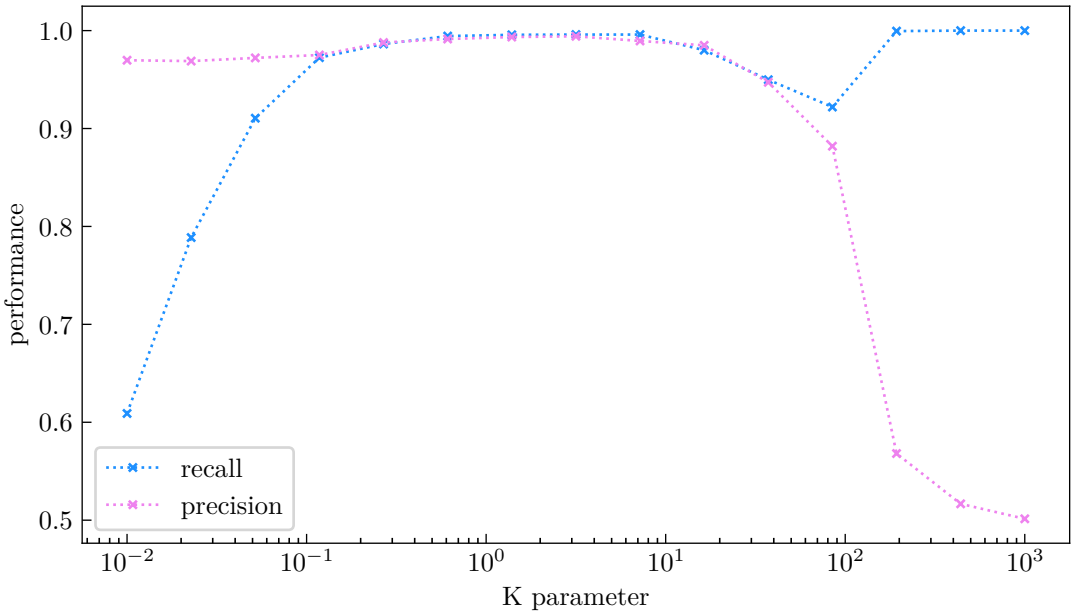

Figure 4.7: Precision and recall for different value of K in the case were we used an SNR of 3, a pixelation of 3.3, and an Abbe radius of 1.2. A soft optimum is obtained around $K = 1$. The performance does not depend too much on K, when K is in the range $[0.1; 10]$.

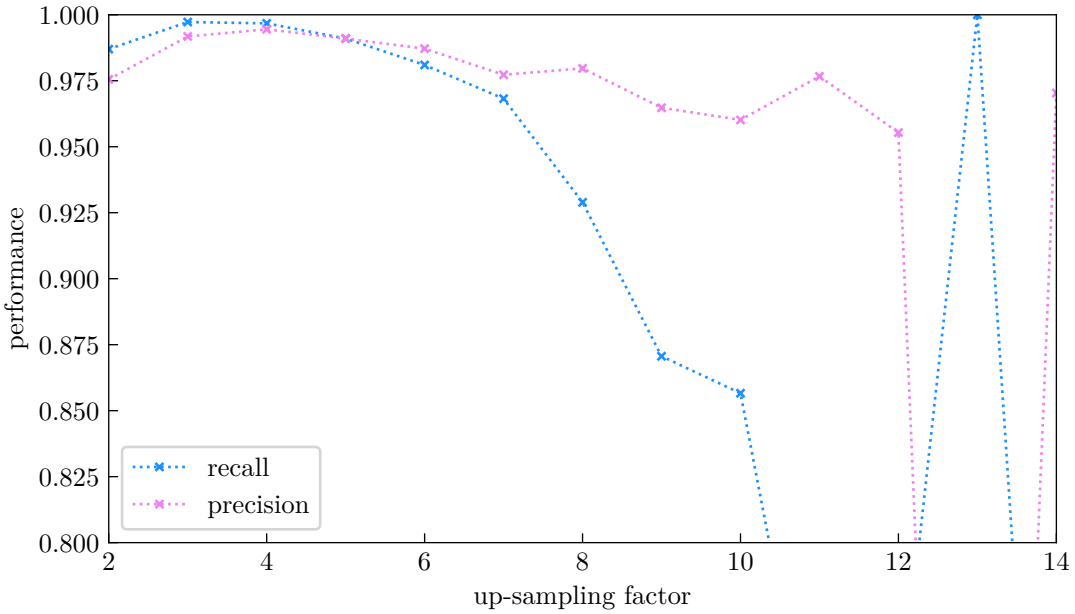

Figure 4.8: Precision and recall for different value of K in the case were we used an SNR of 3, a pixelation of 3.3, and an Abbe radius of 1.2. The maximum of performance is reached for an up-sampling of 4.

4.4.3 Clustering and thresholding of the deconvolved images

In the case of the ILS method and Wiener filter, we have to add one more step after the deconvolution. Indeed, those results of the procedures are not the occupancies of the sites, but instead, they are the signal's amplitudes on each site. We still have to decide if the sites are empty or occupied depending on the amplitude level.

4.4.3.1 Thresholding on the amplitudes

A standard approach in the field of quantum gas microscopes [45, 59] is to determine the occupation of a lattice site by comparing its amplitude with a threshold. This threshold is typically fixed by looking at the histogram of the amplitudes. It is bimodal, as can be seen in Figure 4.9, and in the case where the optical resolution and number of photons are sufficiently high, the two modes in the histogram are reasonably well separated. Three examples of histograms for the literature [45, 60, 61] obtained after the processing of the images are depicted in Figure 4.9. These histograms are quite similar to the one we presented in Figures 4.3 and 4.6, apart from the truncation of negative value in the ILS's histogram and the presence of a peak at zero corresponding the outside of the disc of atoms.

$$P(\text{empty})P_{\text{f.a.}}(\mu) = P(\text{occupied})P_{\text{n.d.}}(\mu)\,, \tag{4.24}$$

where $P_{\text{f.a.}}$ is the false alarm probability, corresponding to having an empty site whose amplitude is above the threshold μ, and $P_{\text{n.d.}}$ is the probability of non detection, corresponding to an occupiedd site with an amplitude below μ. Looking at Figure 4.10, we see that modeling the low amplitude lobe by a Gaussian does not seem so reasonable, due to the very intense peak around 0. One can use various procedures to automatically find a threshold from a bimodal distribution (see, for instance, the thresholding section of `scikit-image` [54]).

The method we use for setting the threshold in the histograms is the `threshold-minimum` method from `scikit-image`. It iteratively smoothen the histogram until there are only to maxima, the threshold is set to the position of the minimum between these two maxima.

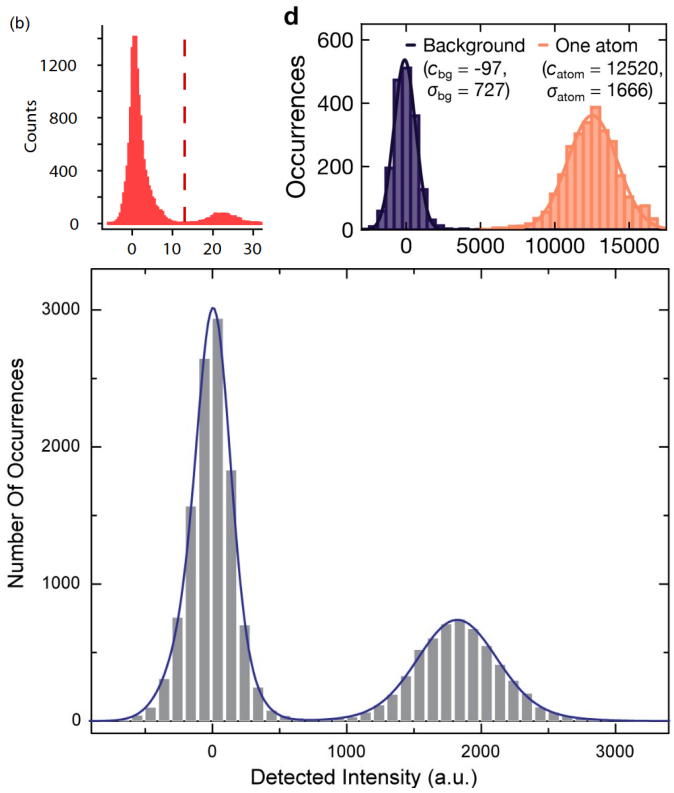

Figure 4.9: Examples of experimental photo-electron histograms after deconvolutions taken from different quantum gas microscope experiments. *The histograms are extracted from* [45, 60, 61].

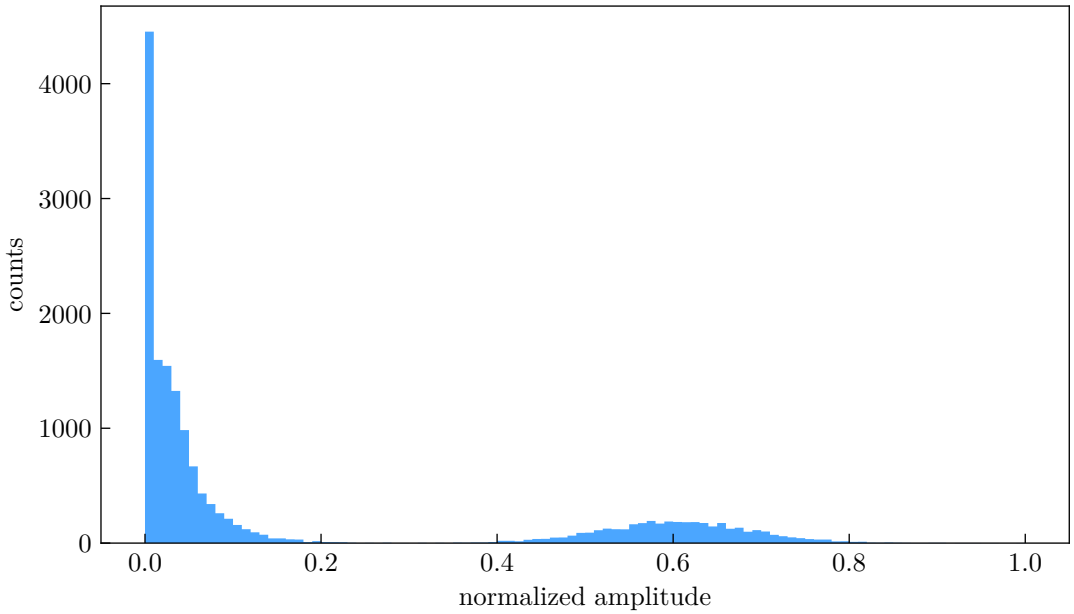

Figure 4.10: Histogram of the fitted amplitude for PSF with Abbe radius of 1.2 lattice spacing, a pixelation of 3.3, and a photo-electron number of 200 per atom. The two lobes are well separated. However, the overlap is non zero an some errors will be made even in this seemingly favorable situation; this parameter set allows obtaining error rates below 1%.

4.4.3.2 2D presentation and clustering methods

We noticed that the low-amplitude peak's width depends on the filling fraction; this happens in cases that are more marginal than ours, or when the deconvolution is poorly tuned, or when the PSF used for the deconvolution is not identical to the one used to generate the data. In Figure 4.11, we overlap the histograms for the case of half-filling and for an empty image. This effect arise from the correlations between the sites introduced by the deconvolution procedure. This means that an empty site with occupied neighbors might get a higher fitted amplitude than an empty site with no neighbors. This means that in the presence of correlations, the overlap between the two lobes of the histogram is increased, leading to degraded performance. This remark suggests that some information can be extracted from those correlations, as we will see in what follows.

2D scatter plots

Instead of plotting the fitted amplitudes as a 1D histogram, we can use a scatter plot in a 2D space where the axes are the amplitude on the site of interest and the averaged amplitude on the nearest neighbors. The situation depicted in Figure 4.11 is plotted in 2D in Figure 4.12, where the *ground truth* labels means that the colors correspond to the "true" occupancies used to generate the image. There, we see that there are indeed correlations between the sites and their nearest neighbors (n.n.).

From the example plotted in Figure 4.12, we see that the data points seem to be organized in (at least) two groups (red and blue). If there were no correlations between the sites and their neighbors, the eigenaxes of those groups would be along the vertical and

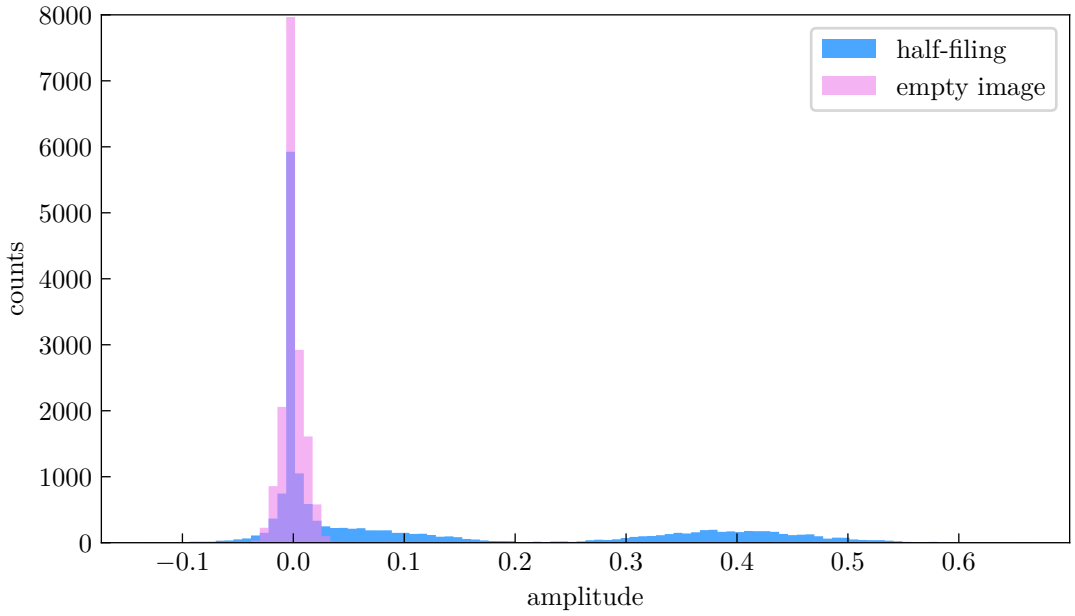

Figure 4.11: Histogram of the amplitude from Wiener deconvolution ($K = 8$ and an up-sampling of 4) for PSF with Abbe radius of 1.2 lattice spacing, a pixelation of 3.3, and a photo-electron number of 200 per atom. The blue distribution is obtained for a sample with half-filling inside the disc and the pink one without atoms in the image. We see clearly that the low amplitude is broadened in the presence of atoms.

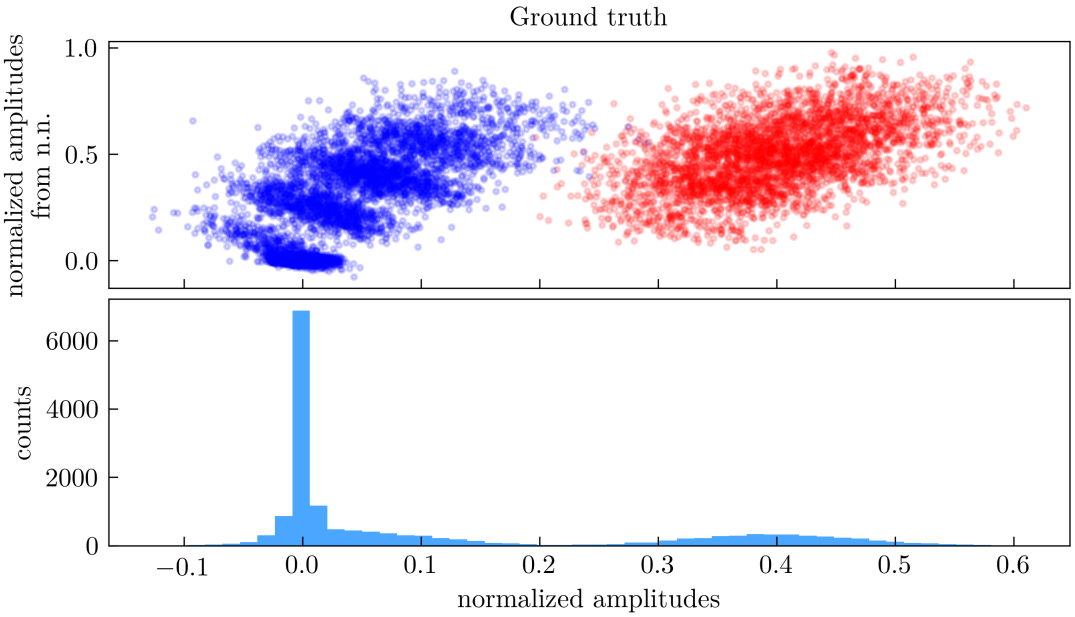

Figure 4.12: Scatter plot of the amplitudes obtained from Wiener deconvolution as a function of the averaged amplitudes on the nearest-neighbor sites. The parameters are the same as in Figure 4.11 in the case at half-filling. The colors label the "true" occupancy of each site, blue for empty and red for occupied. The bottom plot is a histogram obtained using only the amplitude information.

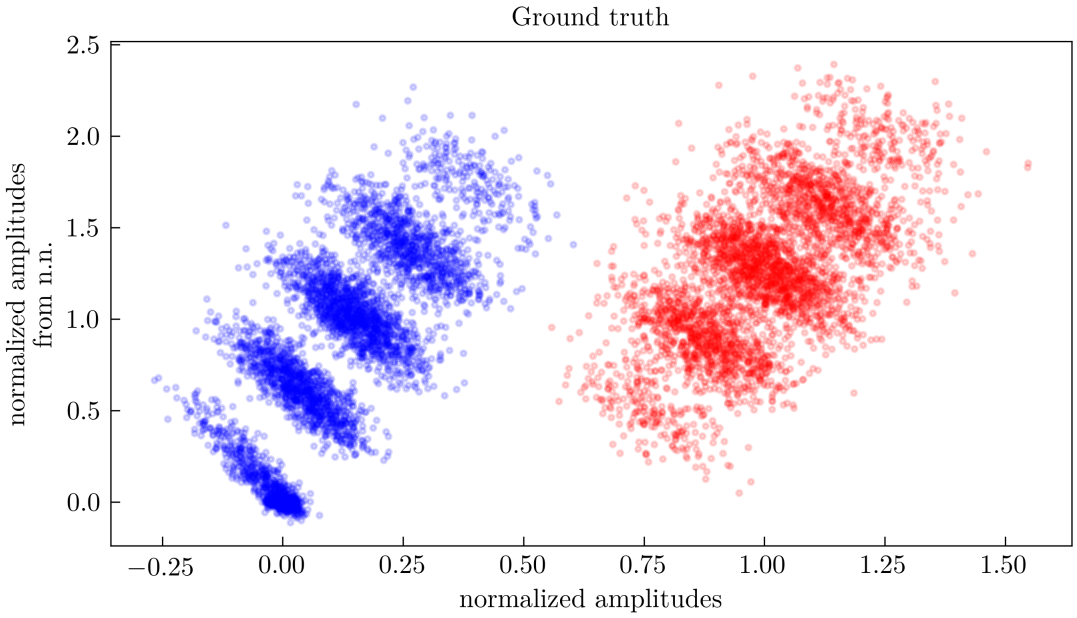

Figure 4.13: Scatter plot of the amplitudes obtained with the Wiener deconvolution ($K = 8$, up-sampling of 4) as a function of the averaged amplitudes on the nearest neighbors. The colors label the "true" occupancy of each site, blue for empty and red for occupied. The parameters used are the following: an Abbe radius is of 1.2 lattice site, a pixelation of 3.3, and a photo-electron number of 500 per atom.

horizontal axes of the plot. Here, however, we notice that the lobes are tilted, indicating correlations between the on-site amplitude and the amplitudes of the nearest neighbors. At high resolutions/signals, for instance in Figure 4.13, we see that the two clouds of points split into 5 clusters of points. We interpret those clusters as arising from the possible numbers of neighbors a site can have (from 0 to 4).

Clustering vs. thresholding

From the 2D plot in Figure 4.12, we are tempted to use these plots to group the data points instead of simply using the histogram corresponding to the projection on the horizontal axis. This problem belongs to the family of clustering problems. We tried different methods from the `scikit-image` python library [54] but the performance were not significantly better in cases where the parameters of the deconvolution method were properly tuned. These methods however proved typically less robust than the one consisting in simply applying a threshold on the histograms.

Assessment of the quality of the deconvolution using the 2D plots

As we have already mentioned the apparition of correlations is symptomatic of a poorly tuned deconvolution. It is mostly there for the Wiener approach, especially if the K parameter of the filter is not tuned correctly or if the PSF is not well calibrated for both the ILS and Wiener filter. An example of autocorrelation curves for a poorly tuned and a reasonably well-tuned deconvolution is presented in Figure 4.14; from these curves we

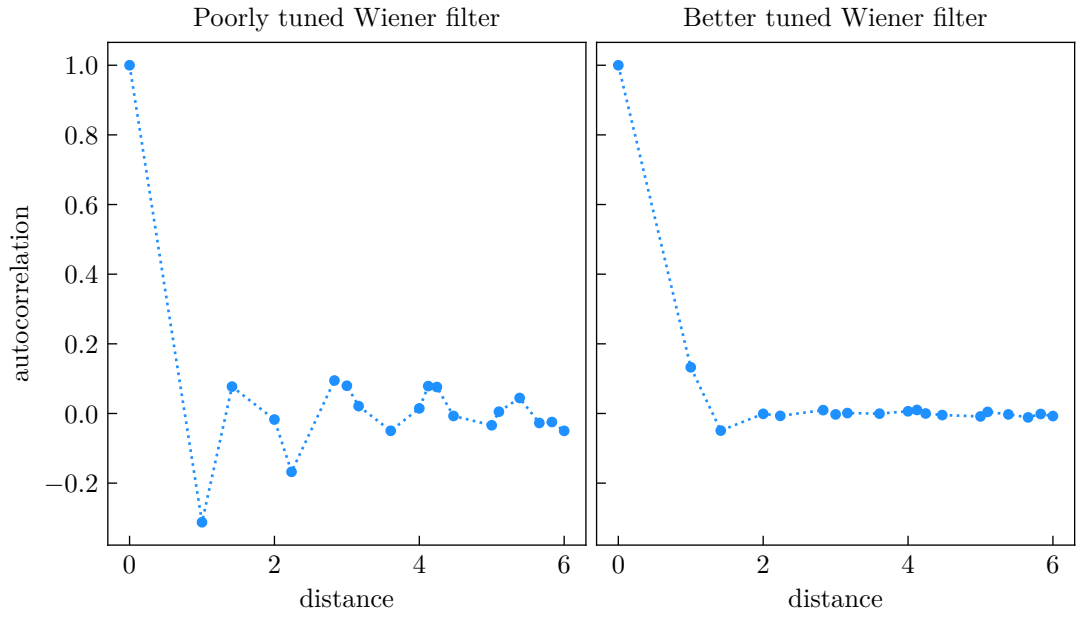

Figure 4.14: Autocorreletion of deconvolved images as a function of distance for a parameter K that is too high (left) and for a reasonable value of K. We see that when K is not properly tuned the deconvolution introduces correlations and anti-correlations between the sites.

can qualitatively check if the filter's parameters are reasonable. A way to tune the K parameter of the Wiener filter is proposed by La Rooij *et al.* [48]. They maximize the contrast of the peaks appearing at the spatial frequencies corresponding with the lattice period in the Fourier transform of the deconvolved image.

From the above discussion, we expect to be able to remove the correlations introduced by the image processing by tuning it properly. Therefore, we do not expect that the 2D representation will increase much the performance of a well-tuned deconvolution. However, this representation is a convenient way to display the data points and check that the model is tuned.

4.4.4 Neural network

This section introduces the concepts of neural networks (NN) for non-specialists (including ourselves in this group). We will present the spirit of the neural network that Pauline Trouvé developed, without digging too much into the technical details.

4.4.4.1 Crash course in neural networks

We will first introduce the concepts of neurons, neural networks (NN), and convolutional neural networks. The resources used to write this section are the MOOC "Deep learning with Tensorflow" from IBM, and the lectures on the YouTube channel MachineLearnia (in French).

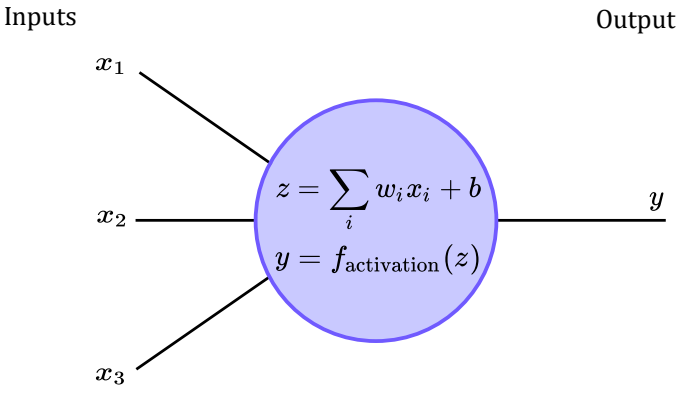

Figure 4.15: Graphical representation of a single neuron for three inputs $\{x_1, x_2, x_3\}$. $f_{\text{activation}}$ represents the activation function of the neuron.

Anatomy of an artificial neuron

A neuron in the field of machine learning takes a vector of inputs $\{x_1, x_2, \ldots, x_n\}$ and maps it to a number. The map has two parts:

1. First, the input is transformed using a vector of *weights* w and a *bias* b to obtain $z = w^{\mathrm{T}}x + b$.

2. Then, z is passed through a non-linear function called the *activation function* to provide an output y. The activation function can be, for instance, a sigmoid, softplus, or ReLu functions. The nonlinearity is what differentiates a neuron from a simple linear regression.

In Figure 4.15, we display the graphical representation of a single neuron, with three inputs.

Training of a model

For generality, we will call our single-neuron the "model". We present here the different steps used to train the model. The training of a model is essentially the protocol by which we tune the parameters of the model (w and b) so that it faithfully represents the data. This is very similar to using experimental measurements and fitting them by adjusting the parameters of a model to minimize a cost function; see, for instance, the right handsides of (4.16) and (4.17). The aim of the cost function is to quantify the prediction error, *i.e.*, the difference between the outputs y and the "true value" or *ground truth* y_{true}, which will be known for the training of the neuron.

To train the model, we use a dataset composed of pairs of inputs $x = \{x_1, ..., x_n\}$ and the corresponding known outputs $\{y_{\text{true}}\}$. This ensemble is called the *training set*. The training is done according to the following step:

1. *Forward propagation*: a set of input vectors $\{x\}$ are passed to the neuron and outputs $\{y\}$ are obtained.
2. The prediction error is computed by giving the known values $\{y_{\text{true}}\}$ and comparing it with the computed values $\{y\}$, using a *cost function* and the current values of w and b.
3. We then apply the *backward propagation* to compute the gradient of the cost function. The derivatives are taken with respect to the weights and bias.
4. We update the values of the weights w and the bias b to perform a step in the gradient descent procedure.

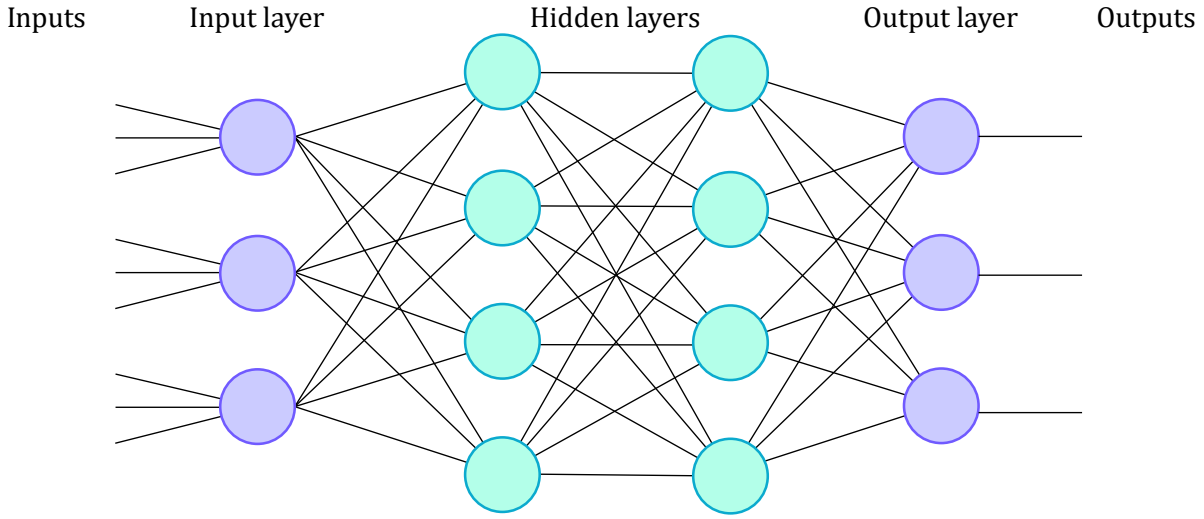

Figure 4.16: Dense neural network with four layers of neurons. All the outputs from a neuron are equal. The hidden layers are simply the inner layers for which we do not monitor the inputs or outputs.

5. We iterate the procedure from step 1 to step 4 until the model "has converged". Each iteration is called an *epoch*.

Testing of the model
After we have trained the model, we need to check its reliability. One straightforward check is to compute the error after the training on the training set. The model was trained to reproduce the outputs of that dataset; it is only fair to expect that it reproduces those data well. A second, even more crucial check is to test the model with a new dataset, called the *test set*, for which we also know both the input variables and the the ground truth, but that the model has never seen during the training. This is used to check the *generalization* performance of the model. This step ensures that the neural network did not simply "memorize" the training dataset.

4.4.4.2 Neural networks and convolutional neural networks

The term "neural network" often designates the case where we use multiple layers so that the outputs of the neuron from the first layer are fed as inputs to the second layer, and so on and so forth. In Figure 4.16, we displayed a case of dense layers where all the neurons within a layer are connected to the following layer.

However, for image processing, a different type of network has been developed, the so-called "convolutional neural networks" (CNN). Instead of using fully connected layers, the notion of locality in the image is retained by using convolution kernels (filters). The equivalent of the weights for the neurons are here the coefficients of the matrix representing the set of kernels.

To clarify the situation, let us imagine a 128×128 image representing the input and a set of 32 kernels represented each by a 3×3 matrix. The output will be a set of 32 images resulting from the convolution of the input image by each kernel. This set of images is represented by a "cube of data", with dimensions $128 \times 128 \times 32$. This output is then

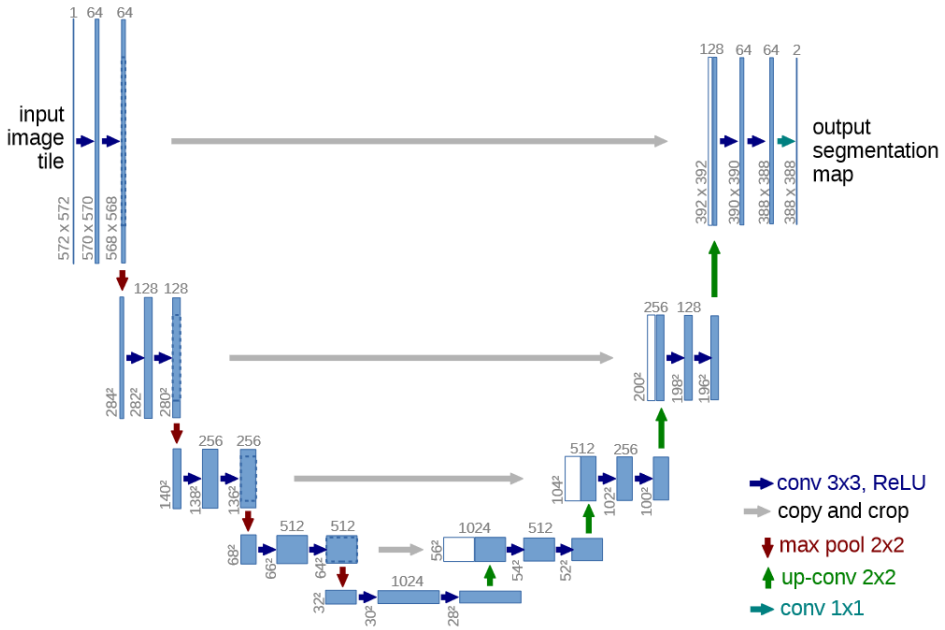

Figure 4.17: Example of a U-net architecture from Ronneberger *et al.* [62]. The grey numbers represent the dimensions of the data, the numbers at the bottom left are product of the dimensions of the images, and the number at the top of each rectangle represent the number of images.

passed through an activation function (applied on each entry of the cube of data). This represent the effect of one convolutional layer in the network, corresponding to one blue arrow in Figure 4.17. The bloc of data that we obtained by this procedure can then be fed to another convolutional layer, or we can perform other kind of operations, such as dimensionality reduction/augmentation (red/green arrows in Figure 4.17). Each kernel in the convolutional layers will be trained to detect some specific feature, say a vertical line or a spot of bright pixels.

Combining several convolutional layers, the model can learn to detect more and more complex features, say an eye, an array of windows on a building or single atoms on a microscope picture.

4.4.4.3 U-net architecture

The architecture implemented for our problem by Pauline Trouvé is called U-net. A schematical representation of the U-net structure is depicted in Figure 4.17; this picture is extracted from Ronneberger *et al.* [62], who first introduced this architecture. The input, in our case, is the raw image from the microscope (or the simulation of it) and an image of the lattice grid (see Figure 4.19), and the output of the network is designed to be an image of the same size with all pixel to zero except where an atom has been detected. This is, in essence, very different from the other two approaches, where the amount of signal emitted from each site was evaluated in the lattice space, not in the image directly.

There are two distinct stages in this type of architecture. First, on the descending direction in Figure 4.17, we have the "contracting path", known as the *encoder path*. The

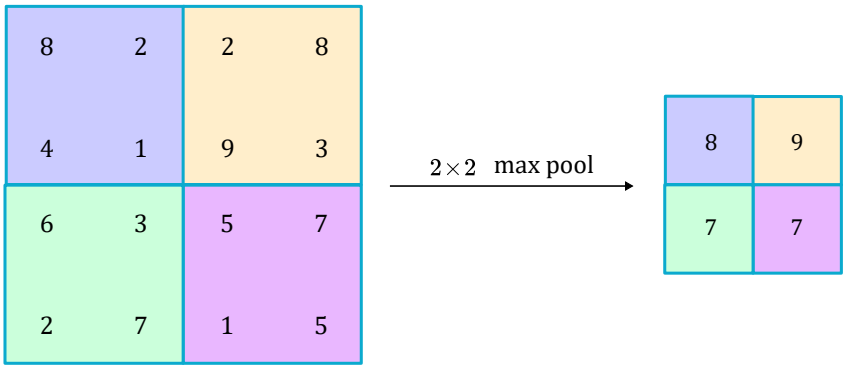

Figure 4.18: Example of the action of a 2×2 max pooling on a 4×4 matrix. In each block of color the max pool function selects the highest entry and discard the others.

original image undergoes features extraction composed of a succession of convolutional layers, and dimensionality reduction designated by the `maxpool` arrows. Here, the 2×2-max-pooling operations produce an $n \times n$ matrix out of a $2n \times 2n$ matrix by keeping only the maximum entry in each 2×2 block, as depicted in Figure 4.18:

The second phase of the processing is a succession of up-sampling operations, the "expanding path", known as the *decoder path*; this increases the resolution of the localization of the feature extracted during the contracting phase. To help recover the localization information during decoding stage, we provided to the layer in that path with images[15] that were not (totally) contracted by the encoder. This provides some "context" containing the spatial information that we want to recover. This is represented by the gray arrows labeled "copy and crop". The images must be cropped so that the copied images (white) are of the same size as the processed images (blue).

Training and testing of the U-net

The inputs of the network is a patch of 160×160 pixels taken at random in a database of 800 images with the associated known lattice grids. A zoom of an image of lattice grid is presented in Figure 4.19a, it is constructed by taking the coordinates of the sites in image space and turning on the pixel whose center is closer to each sites' coordinates. The training is done over 150 *epochs*, which means that the network sees the whole training set 150 times. The test set is composed of 200 images and their grids, as the ones displayed in Figure 4.19.[16]

The training stage of the neural network is critical. Since many parameters can vary it is essential to identify the relevant parameters to avoid generating a database with millions of images, including all kinds of variations. The identification of the relevant parameters is still an ongoing process. However, we have already acquired some knowledge on that part.

For instance, we saw that it is mandatory to train the NN with clouds of finite and varying size, and not on simply uniform images. The exact size of the cloud is, however, not crucial, so we do not need to include all the possible sizes the NN could encounter in

[15]The adapted term here would be "feature channels" instead of images.

[16]The picture of the atomic cloud presents more isolated atoms on the edges than on the pictures in Figure 4.5. The explanation is that the this image was generated with the physical model for the atomic distribution (see section 4.2.2)

practice. Even though, introducing some variations of the cloud's size in the training set improves the results.

We also saw that minor errors in the offset of the grid of sites only degrade the performance marginally, even if the training was performed with perfect knowledge of the offset. Note that we tried to train the NN without giving the grid as an input of the NN. This task was difficult for the neural network. It was a somewhat unfair comparison, since the lattice grid is needed for the ILS and Wiener deconvolution methods.

Finally, for a NN trained with a given size of PSF, we checked that small changes in the PSF's radius did not prevent the NN from working. The performance is degraded if the PSF is expanded and is similar if the PSF size is reduced.

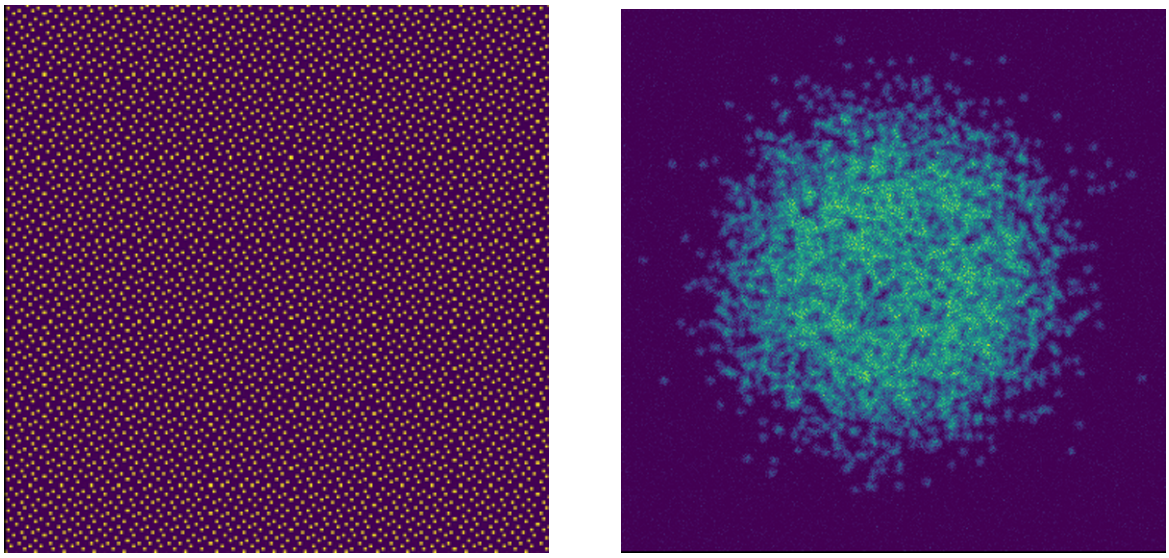

(a) Input grid (b) Input image

Figure 4.19: One instance of input for the neural network. The shape of the cloud differs from the ones presented previously. This is because this picture was generated from the physical model described in section 4.2.2. The parameters used to generate the atomic sample are the following: a temperature of $0.27U$, a chemical potential of $0.7U$, where U is the on site interaction energy in the Bose-Hubbard model. The optical system parameters are: an Abbe radius of 1.6 lattice period, a magnification$\gamma' = 3$, and 300 photo-electrons per atom. The axes of the lattice are rotated by an angle of 34° with respect to the axes of the matrix of pixels.

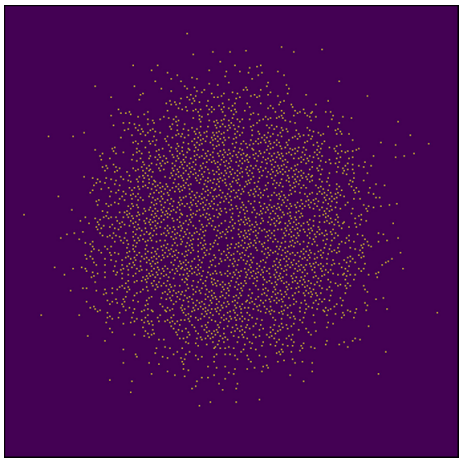

Figure 4.20: Output of the neural network (after training) for the example of input displayed in Figure 4.19. The output takes the form a the matrix with the shape of the sensor's matrix of pixels, where the occupied sites are displayed as bright pixels (yellow) as in the input grid.

Output of the network
The outputs of the neural network have the size of an image similar to Figure 4.19a. The bright pixels in Figure 4.20 indicate occupied sites of the optical lattice. Checking the presence of a bright pixel in the neighborhood of each site allows reconstructing an occupancy matrix.

4.5 Simulated performance

In order to compare the results provided by the different algorithms that were developed, we need a way to compare the performance fairly. Even the concept of performance needs to be clarified, as different metrics could be used to quantify the number of errors.

In this section, we will first expose how the scores of the different algorithms are computed. Then, we give the results from the Wiener filtering and the iterative least-square method as a function of the relevant parameters, such as the Abbe radius, the signal-to-noise ratio, or the pixelation of the PSF. We will first focus on variations of performance around the parameters that we expect to have in the experiment; that is, a pixelation of 3.3, and an Abbe radius of around 1.2 lattice period. Then, to explore in more depth the performance of our methods, we will use more challenging sets of parameters for the images, such as lower signal level or bigger PSF. The final results for the scans of the neural network are not yet available for the final configurations, and will not be discussed here. Overall, the three methods tend to give similar results in the configurations that we tested. Finally, we check the robustness to errors in the lattice grid's phase and in the size of the PSF.

4.5.1 Scoring

For our experiment, we want to detect occupied and empty sites with similar accuracy, since both the presence or absence of atoms contains information relevant to the measurements of density-density correlators. Instead of simply counting the number of errors, we compute the *precision* and *recall*.

The precision is a measure of how accurate the algorithm is when it labels a site as "occupied". It is defined as the number of true positives divided by the number of sites that were labeled as occupied, that is, the true positives and the false positives. The precision in the ideal case should be one and penalizes the attribution of the occupied label to empty sites.

The recall measures the number of occupied sites that were "forgotten" by the algorithm. It is defined as the number of true positives divided by the actual number of occupied sites, the true positive and the false negatives. The recall should also be one and decreases when an atom goes undetected.

Using those two metrics instead of simply the error rate is interesting, especially in cases where there is an imbalance between the empty and occupied classes. For instance, if the sample we consider is a small cloud of atoms surrounded by empty sites, predicting that all the sites are empty might lead to low error rates, while the recall would detect that this is not a good guess. It also allows us to check that there will be no drastic biases from the reconstruction algorithm that would favor empty or occupied sites.

4.5.2 Signal-to-noise ratio in our system

To have a general approach to the problem, we want to introduce a notion of signal-to-noise ratio (SNR). We define the signal S as the number of photo-electrons obtained by integrating the PSF over a pixel centered on its maximum. The motivation behind this definition is that the signal should increase with the photon number and should decrease if those photons are spread over many pixels; that is, when the pixels get smaller or the PSF bigger. The noise will have three contributions in what follows: the shot noise, the read noise, and the background noise.[17] By default the background noise will be neglected except when stated otherwise. We obtain:

$$\mathrm{SNR} = \frac{S}{\sqrt{S + \sigma_{\mathrm{read}}^2 + \sigma_{\mathrm{bg}}^2}} \tag{4.25}$$

with σ_{read}^2 and σ_{bg}^2 the variances of the read noise and background noise respectively.

In order to check the relevance of this definition, we draw randomly pairs of photon number per atom and background-noise standard deviations with uniform law, and plot the performance as a function of the SNR. The random data point are presented in Figure 4.21, the photo-electron numbers are ranging from 100 and 5000, while the background standard deviations are ranging from 0 to 100.

The scatter plots in Figure 4.22 display the precision and recall for the deconvolution using these random samples. We observe that for each quantity the data points collapse on a curve. This validate our definition of the SNR, as we see it is a relevant parameter to vary and that we do not need to explore the space of parameters by varying independently the photo-electron number and the background noise. We removed from the performance plots the data points for which the precision and recall were different (in absolute value) by more than 0.2. These data points correspond to too low SNRs for which the deconvolution methods typically over estimate the number of occupied or empty sites leading to high precision and low recall or the reverse. In the following we will keep using this filtering of the data points as we are not interested in the results of the deconvolution if there is a bias towards either the occupied or empty sites.

Minimum SNR in our configuration

As a bonus, the graphs in Figure 4.22 give us a minimum SNR to have on our experiment to reach 99% of recall and precision with an Abbe radius of 1.2 and a pixelation of 3.3. These are the parameter that we expect to have in our setup. The minimum SNR is at around 4 corresponding to 200 photo-electrons per atom in the absence of a background. This result will fixed our aim when we simulate the fluorescence of a trapped atom in chapter 6.

[17] The background noise will be modeled by a Gaussian random variable, with a non-zero mean. The value of the background are truncated so that it only takes positive values.

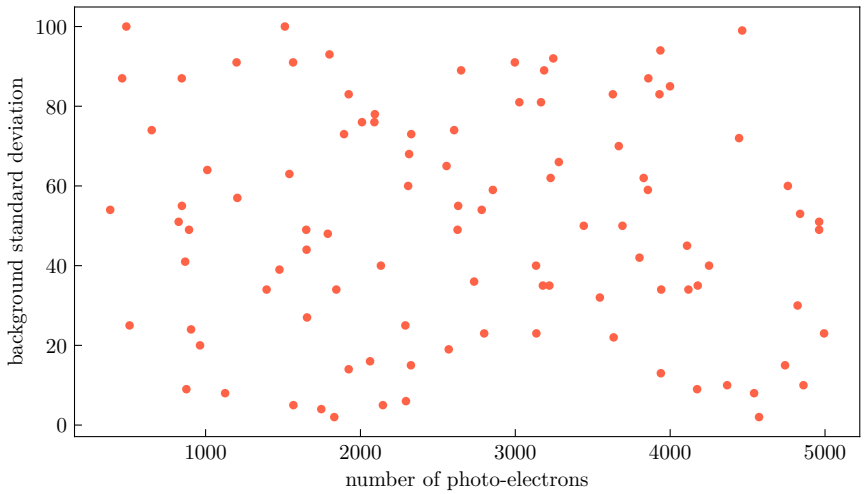

Figure 4.21: Random samples for the photo-electron number per atom and the standard deviation of the background noise. They are distributed uniformly between 100 and 5000 for the photo-electron number, and between 0 and 100 for the background noise.

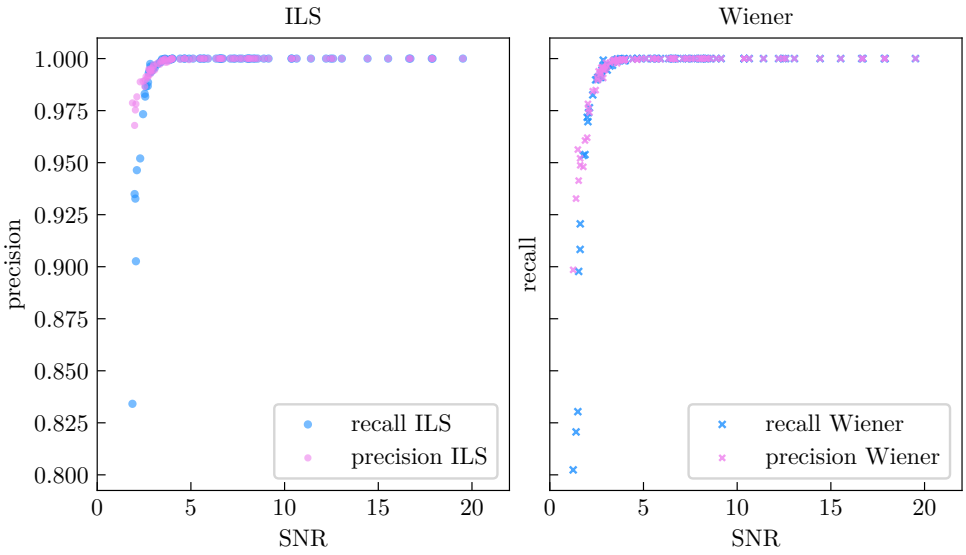

Figure 4.22: Performance as a function of the SNR obtained for the random samples displayed in Figure 4.21, the Abbe radius is 1.2, and the pixelation 3.3. We observe that the data points collapse on curves, validating the relevance of our definition of the SNR. The precision and recall presents a plateau at SNRs higher than 4 and decays rapidly below 4. The samples corresponding to a difference between the precision and the recall larger than 0.2 in absolute value were removed. Similar results are obtained for other PSF sizes.

4.5.3 Influence of the Abbe radius and pixelation at high SNR

In this section, we give results for the Wiener and ILS method, in terms of precision and recall as a function of pixelation, and PSF size. This study will be conducted at a high SNR of 10, that is far in the plateau of Figure 4.22, in order to see only the impact of the parameter that is varied.

At the time we are writing this manuscript, the systematic scans for the neural network were not available. However, the comparisons in various configurations showed that the results with the neural network are typically similar to the other methods, with sometimes a slight advantage at low signals or resolutions.

As a reminder, the typical parameters that we will use are: a PSF size of 1.2 lattice sites, a pixelation of 3.3, corresponding to a magnification of 3.55 pixels per lattice site. We characterize the performance of the Wiener filter and ILS method by varying one parameter while keeping the others at the reference value for our system. Also note that the parameters of the deconvolution algorithms are kept constant in this study. The block size for the ILS is kept at 50 pixels. For the Wiener filter the up-sampling factor is set to 4 and the K parameter is kept at 1.

4.5.3.1 Scan of the pixelation at high SNR

We start by scanning the value of the pixelation at a fixed signal-to-noise ratio of 10 and with an Abbe radius of 1.2 lattice period. Changing the value of the pixelation at fixed PSF size and SNR has the effect of decreasing the number of pixels per lattice period while reducing the number of photo-electron needed to reach the fixed SNR; it also increasing the pixelization of the PSF.

In Figure 4.23, we plot the performance as a function of the pixelation. We see that for the ILS the performance is stays above 99% even down to one pixel per lattice period,[18] and it saturates for pixelations above ~ 1.5. Wiener deconvolution is less robust and requires at least a pixelation of 2 to be above 99%. The data points for which the precision and recall have a difference higher than 0.2 were filtered out. In particular, this happens when the pixelation is such that there is less than one pixel per period.

We observed the same kind of behavior for lower SNR or higher PSF size, albeit with a plateau reached at higher pixelation with lower performance. Since the number of photons need to reach a fixed SNR increases with the pixelation, it is not necessary to have many pixels per PSF. The pixelation of 3.3 that we plan on using in our experiment seems acceptably far in the plateau especially since we will probably not be able to work at an SNR of 10.

4.5.3.2 Scan of the PSF size at high SNR

We now explore the impact of the PSF size on the deconvolution performance still with an SNR of 10. In Figure 4.24, we plot the performance for the ILS and Wiener deconvolutions, as a function of the Abbe radius. We also indicated the corresponding numerical aperture at 689 nm. We see that the performance of the ILS are better than that of the Wiener filter. In particular, the performance of the ILS remains above 99% until the Abbe radius

[18] In particular, we can work below the Nyquist-Shannon sampling criterion.

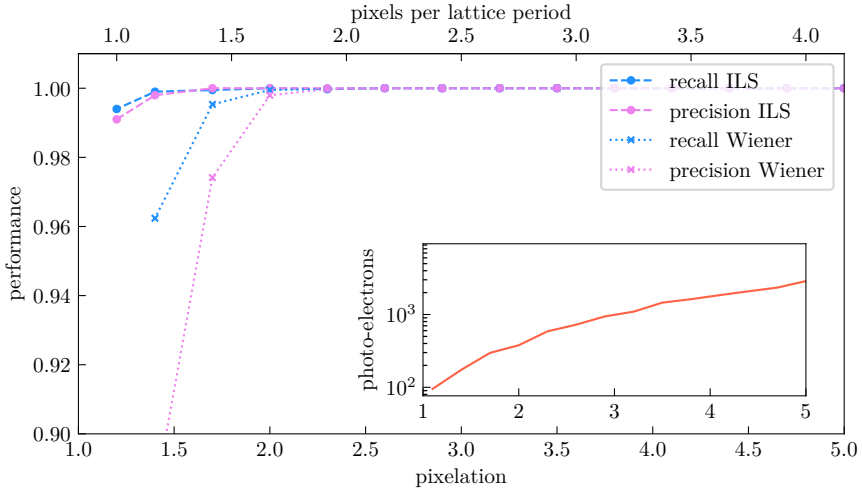

Figure 4.23: Precision and recall for the ILS method and Wiener filter as a function of the pixelation. The Abbe radius is 1.2 lattice sites and the SNR is of 10. The inset represent the number of photo-electrons as a function of the pixelation for an SNR of 10. The pixelation has no impact on the performance as long as it is above 1.5 for the ILS, while Wiener deconvolution requires higher pixelation for the same performance.

reaches 1.5 lattice period, while the Wiener filter is limited to 1.4 period. We observe that both method perform well even far below the resolution limits defined in table 4.1.

4.5.4 Deconvolution in more challenging regimes

We will now try to push our deconvolution methods to their limit by considering the case of a large PSF and of the low signals. The case of the large PSF is interesting for building experiment with simpler optical system for the imaging or in cases where the lattice period is small. The case of low signal can be interesting either if there are losses of atoms during imaging or to reduce the exposure time needed to make a microscope picture.

4.5.4.1 Performance for a large PSF

In this section, we fix the Abbe radius at 1.8, we study the impact of the SNR at a pixelation of 5 pixel per Abbe radius and the impact pixelation at an SNR of 30.

In Figure 4.25, we plotted the performance for the ILS method in that configuration. We see that attaining the aim of 99% requires going to SNRs above 13. Therefore, the ILS can accomodate this degradation of the PSF if we are able to increase the SNR. The Wiener deconvolution does not reach this performance at least for the SNR that we have explored.

In Figure 4.26 , we observe that the ILS method is able to compensate the degradation of the optical response by going to pixelation above ∼5-6. Wiener deconvolution does not perform as well and needs higher pixelations.

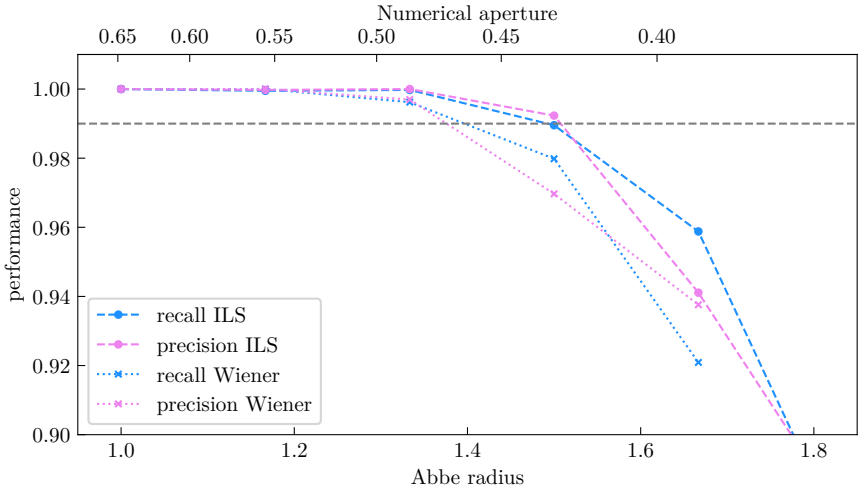

Figure 4.24: Recall and precision for ILS method and Wiener filter for an SNR of 10, and a pixelation of 3.3. The grey dashed line indicates the 99% that is our aim. The ILS method match this criterion for Abbe radii as high as 1.5 lattice period, corresponding to numerical apertures of 0.43 while Wiener deconvolution only performs well for Abbe radii below 1.4.

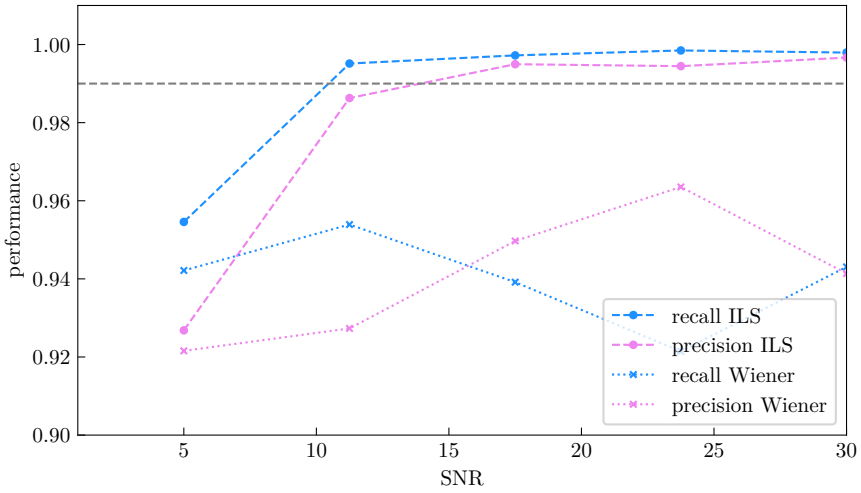

Figure 4.25: Precision and recall for the ILS method as a function of the SNR. The Abbe radius is 1.8 lattice sites, the pixelation is 5 pixels per Abbe radius, and an SNR of 10. The ILS obtain satisfying results for SNRs above 13. The data points corresponding to a difference between the precision and the recall larger than 0.2 in absolute value were removed.

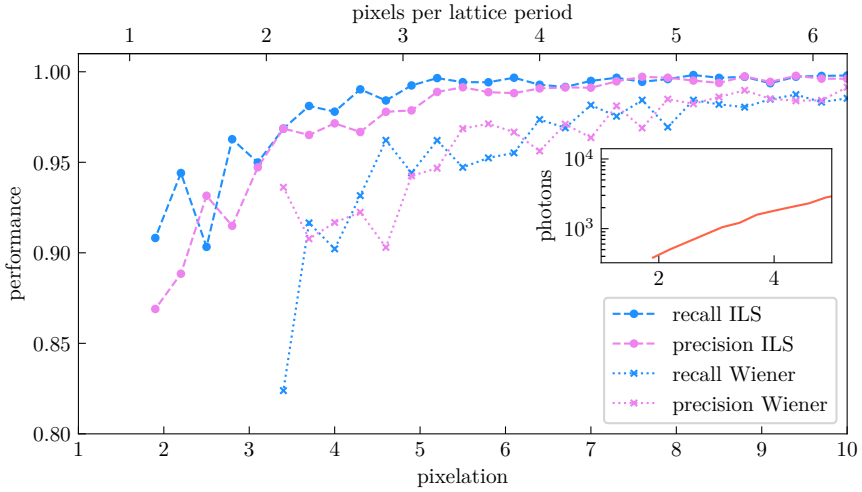

Figure 4.26: Precision and recall for the ILS method and Wiener filter as a function of the pixelation. The Abbe radius is 1.8 lattice sites, colorredthe pixelation is 3.3 pixels per Abbe radius, and an SNR of 10. The inset represent the number of photo-electrons as a function of the pixelation for an SNR of 10. The performance increases with the pixelation in this more challenging case. The performance saturates at lower pixelation and is higher for the ILS. The data points corresponding to a difference between the precision and the recall larger than 0.2 in absolute value were removed.

4.5.4.2 Performance for a small SNR

To study the limit of small signals, we set the SNR to 2 and perform scans around the configuration with a pixelation of 5 and an Abbe radius of 1.2 lattice period. We also consider two situations: the case with no background noise, and the case with a background noise that has a standard deviation of 50 photo-electrons.

In Figure 4.27, we plot the precision and recall for the ILS and Wiener methods for both cases as a function of the Abbe radius. Both methods can work in the regime of low SNR although they require better resolutions than what we saw previously. The ILS achieves to get a performance above 99% for Abbe radii smaller than 1.2, with and without a background.

Figure 4.28 represents the performance with and without a background for both deconvolution methods. We see that with an SNR of 2 and a PSF of 1.2 lattice period, the pixelation should be chosen above 5, in presence of a background, and 4 without a background. The ILS method gives better results in both cases except at low pixelations, where the performance is low for both algorithms.

Interestingly, we see in these graphs that at low SNR the nature of the noise *does* matter. We interpret this phenomenon as an effect of the statistics of the noises. Without a background, the dominant noise is the Poissonian and depend on the signal. In the presence of a background with a standard deviation of 50 photo-electrons, the dominant noise becomes a Gaussian one and is additive and independent of the signal. As we have already explained at the beginning of this chapter, neither the ILS nor the Wiener filter are designed to be used with Poissonian noise. It might be that the change of the noise's nature is responsible for the loss of performance in the presence of a background. It could

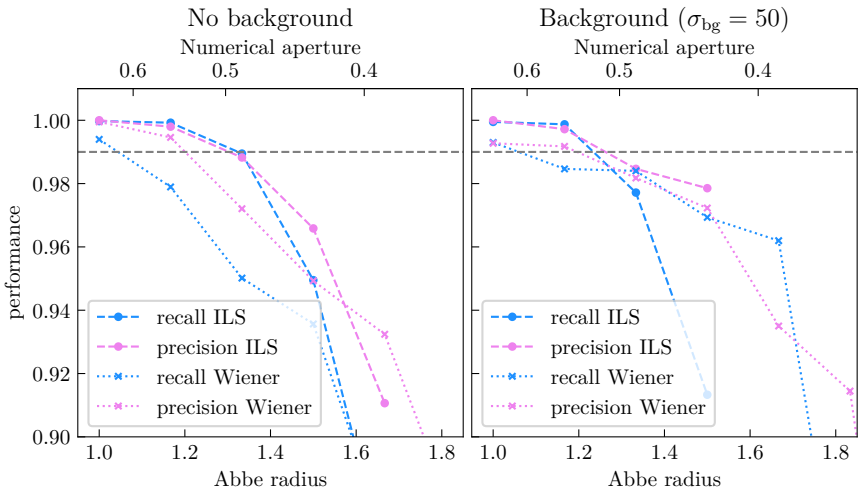

Figure 4.27: Precision and recall for the ILS and Wiener methods, without a background (left) and with a Gaussian background with a standard deviation of 50 photo-electrons (right) as a function of the Abbe radius. The SNR is set to 2 and the pixelation to 5. A safe value for the Abbe radius seems to be 1.2 lattice period for the ILS and 1 for the Wiener filter. Wiener deconvolution is more robust than the ILS at the highest values of the Abbe radius in presence of a background. The data points corresponding to a difference between the precision and the recall larger than 0.2 in absolute value were removed.

be beneficial to explore procedures of deconvolution using mixed Poisson-Gaussian-noise models, such as the one from [47] to check if some gain can be obtained with a more faithful model for the noise.

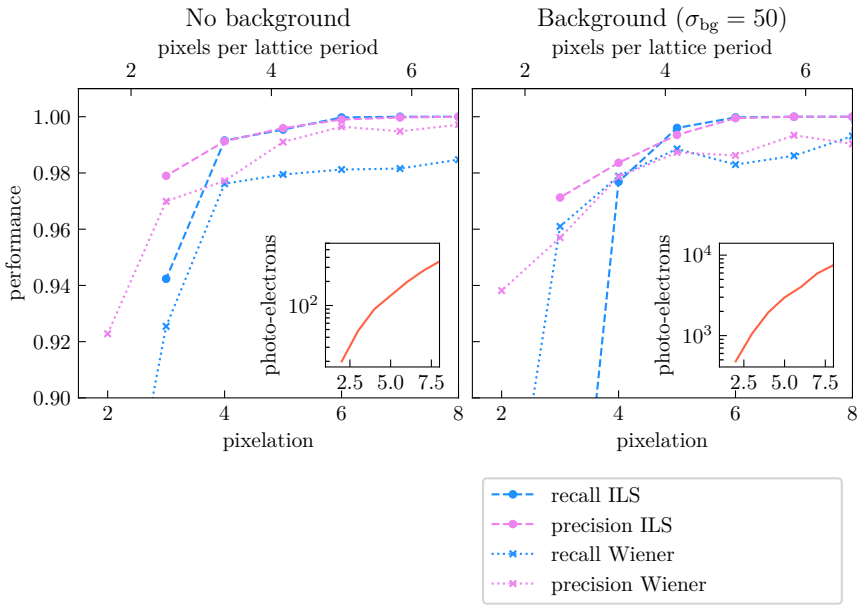

Figure 4.28: Precision and recall for the ILS and Wiener methods, without a background (left) and with a Gaussian background with a standard deviation of 50 photo-electrons (right) as a function of the pixelation. The data points corresponding to a difference between the precision and the recall larger than 0.2 in absolute value were removed.

4.5.5 Robustness to modeling errors

The methods we presented depend on the knowledge of the grid of sites in the image plane as well as of the PSF. To check that our predictions are robust with respect to errors in either one of these parameters, we introduce errors in the model and check the performance. First, we introduce a shift in the grid for the reconstruction, that is we process the images with an offset of the grid that present an error. Then, we process the images with a PSF that has a size differing from the one used to generate the data.

4.5.5.1 Error on the offset of the grid

By definition, the offset error can be of at most half a lattice period in each direction. Since we did not expose the details of the grid estimation we will not go into the details here. We checked that the performance is maintained for errors below 10% of a lattice period on the offset; that is, when the error is at most of $\varepsilon = (0.1, 0.1)\,\lambda/2$. This puts a constraint on the detection of the grid that is compatible with tests that were performed with the grid estimation procedure. This precision is attainable with our method.

4.5.5.2 Error on the PSF size

We model the error in the estimation of the PSF by a scaling factor on the size of the PSF used to *process* the images. We check the robustness for the PSF size parameter by varying it between -10% to $+50\%$ from the reference point of 1.2 used to generate the images. This corresponds to varying the Abbe radius between 1.08 and 1.8 lattice spacings. The results are plotted in Figure 4.29, we observe that the performance of the Wiener

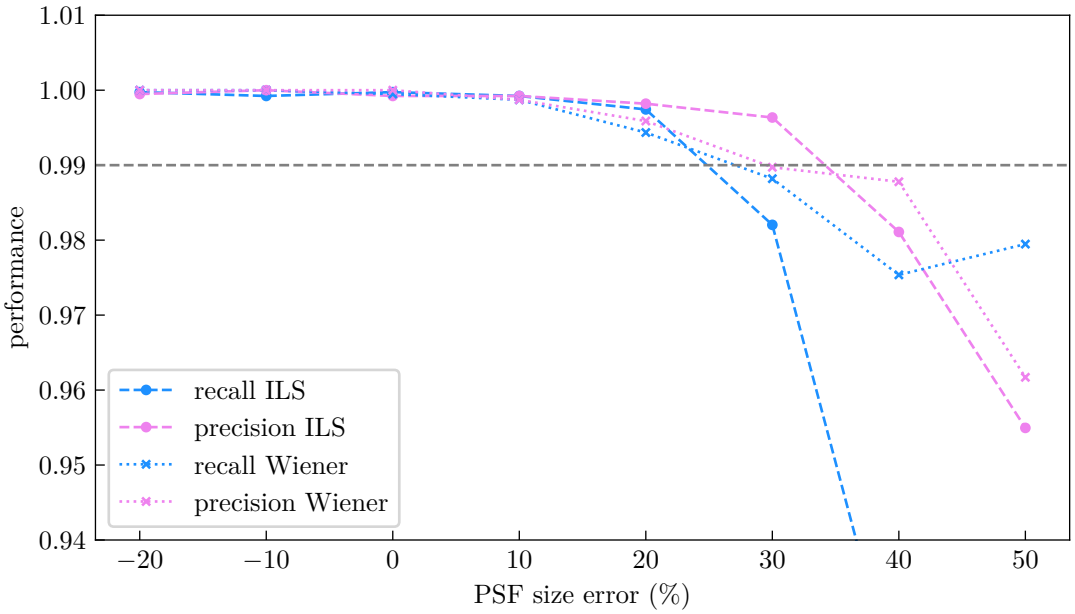

Figure 4.29: Precision and recall for the iterative least-squares and Wiener filter as a function of the relative error in the PSF radius. The radius used to generate the images is varied from −20% to +50% around 1.2 lattice period which is the value used to reconstruct the images. The pixelation is 3.3, and the SNR is set to 4. The deconvolution works well for errors up to +10%, that is, for PSF used to generate the images at most 10% bigger than the one used to deconvolve.

deconvolution degrade gradually as the relative error is increased. The underestimation of the PSF radius has almost no effects for both methods. For the ILS method however, the performance drop dramatically when the error is increased above 20%.

These results show that the deconvolution methods are resilient to errors in the estimation of the PSF. In particular, if the PSF is not homogeneous over all of the field of view, it might still offer good performance. However, as we have already mentioned, the ILS method does not need to have a unique PSF over the whole field of view. A refinement of the method could be to adapt the PSF used for reconstruction to the position in the image. Also notice that not all

Variations of the PSF in the image are yet to be tested in the simulation but could be an interesting perspective to this work since it would relax the constraint of having a near-diffraction-limited microscope objective over all of the region of interest. This would in turn give access to the study of bigger systems with simpler optical setups.

4.5.6 Summary: Constraints on the imaging process

From the results of the previous section, we can identify the requirements for the operation of our microscope with recall and precision above 99%. We need an SNR of 4, corresponding to a photo-electron number of about 200 per atom in the absence of a background. The lower bound on the photo-electron number gives a constraint on the minimum number of photons emitted by each atom during the imaging phase. If we correct those 200 photo-electrons by the quantum efficiency of our camera at 689 nm (74%),

the collection efficiency (14%) and the transmission of the optical system ($\sim 90\%$),[19] we get an emitted photon number of 2100 per atom.

We also saw that we can obtain performance above 99% with Abbe radii as high as 1.5 lattice period in the case of high signal (SNR = 10) and up to 1.4 for an SNR of 2 in the absence of a background.

Finally, we showed that at low signals the pixelation should be increased to recover good performance. At high signals the pixelation has no real impact as long as we have more than one pixel per atom.

4.6 Conclusion and perspectives

In this chapter, we presented three approaches allowing us to measure the occupancies in a 2D lattice, with single-site resolution and single-atom sensitivity. In particular, we saw that having an optical resolution better than the lattice period, in the sense of standard optical microscopy criteria, is not mandatory, even in the case where the SNR is as small as 2. These results show that the requirements on signal levels and optical resolution can be deduced from the data processing methods. Therefore, knowing the performance and limitations of the deconvolution methods could enable the conception of quantum gas microscopes with simpler and cheaper optical setups, smaller lattice periods, or lower photon numbers.

As we already discussed, the underlying model for the noise for the Wiener filter and ILS is that of an additive noise uncorrelated with the signal. This assumption seems very crude, since it is obviously violated by the photonic shot noise. In spite of this, we obtained results that are quite satisfactory. Nevertheless, we would like to investigate in the future two other approaches. The first one is the Richardson-Lucy deconvolution method [63], which is designed to treat Poissonian noise. This would amount to neglecting the read noise but account for the shot noise (which is a bad assumption on the edges of the images). This method can readily be implemented using `scikit-image.restoration`. The second method is based on a maximum-likelihood approach, via the optimization of a loss function constructed from an approximation of mixed Poisson-Gaussian model for the noise, as described in Ikoma *et al.* [47]. It accounts for shot noise and read noise, albeit in an approximate way for the read noise.

Another test that remains to be done is to introduce fluctuations of the number of photons emitted by different atoms. Indeed, in practice the number of emitted photons will be a random variable as the atom can be lost during the imaging procedure. In typical situations, this would be due to a collision with the background gas. In our scheme, as we will see in chapter 6, the imaging procedure itself will induce losses. Including this effect into the simulation will improve the estimation of the real performance of our treatment. Furthermore, it will enable optimization of the imaging process (for instance the detuning of the laser and its intensity) with respect to the deconvolution performance.

[19] This was not measured on the experiment but corresponds to a rough estimate given that the aspheric lens is uncoated and that there are a few AR-coated elements outside of the vacuum chamber.

Chapter 5

Optical lattice for strontium atoms

This chapter describes the computation of the AC-Stark shift (or lightshift) for strontium at 1064 nm. The calculations of the AC-Stark shift are necessary to predict the characteristics of the optical lattice trap, and of the optical dipole trap for the transport. We will compute the polarizabilities of the atoms in the electronic ground state ($^1S_0$) and in the excited state of the narrow transition ($^3P_1$). The polarizability in the ground state is required to compute the lightshift for the transport trap and the optical lattices for all the stages (loading, dynamics, imaging). The polarizability for the excited state is necessary to predict the behavior of the atoms for the imaging in the optical lattice. It might also be useful in case we want to do laser cooling in one of the traps at some intermediate stage.

Update the trap parameters that were computed by Clémence Briosne-Fréjaville in her thesis, with the new values of polarizabilities and using powers closer to the experimental values that we obtained. The polarizability of the excited state needs to be known with precision as its value will determine three distinct regimes for the laser cooling in the an optical dipole trap, depending on the relative magnitudes of the ground and excited polarizabilities [18].[1] In addition of requiring a more sophisticated formalism, the computation of the excited state polarizability required bibliographic work to compile spectroscopic data. We will see that, contrary to the ground state case, the polarizability of the excited state has significant contribution from multiple states. Some of those states are absent from some sources, we thus had compare different sources [18, 64–66] to make sure we included as many contributing transitions as possible.

We first present the formalism used to compute the polarizabilites of the two states of interest. We discuss the impact of the different irreducible components of the polarizability tensor and, in particular, the interplay between the choices of polarization of the trapping beams and the bias magnetic field. We finally specialize this formalism to the case of our optical lattice in the imaging configuration, and present the choice of quantization axis, internal state, and of polarizations for the beams.

5.1 Dynamic polarizability tensor

5.1.1 Second-order perturbation theory for an atom in a far detuned laser field

The coupling between an atom and an incident monochromatic laser field can be described by the perturbation $V^E = -\vec{d}\cdot\vec{E}$, where $\vec{d}$ is the electric dipole operator and $\vec{E} = \mathrm{Re}\left(\mathcal{E}e^{-i\omega t}\vec{u}\right)$ represents in our case the far-detuned laser field, with angular frequency ω, complex amplitude $\mathcal{E}$, and complexe polarization $\vec{u}$.[2] There are no contributions to the energy shifts at first order in V^E, since the diagonal matrix elements of $\vec{d}$ are zero. The leading order contribution will come from second-order time-dependent perturbation theory. This part will only summarize the key formulas in that framework; the derivations of those results are done in Appendix B, following the article of Le Kien *et al.* [67] closely but adapted to the case of bosonic strontium. The energy shift induced by the laser field on a level $|a\rangle$ is given by the sum-over-state formula:

[1] We will indifferently refer to all the traps generated by AC-Stark shift as optical dipole trap (ODT), even when the trap has an optical lattice structure.

[2] The polarization vector is a complexe vector with unit norm $\vec{u}^*\cdot\vec{u} = 1$.

$$\delta E_a = -\frac{|\mathcal{E}|^2}{4\hbar}\sum_b \mathrm{Re}\left(\frac{|\langle b|\,\vec{u}\cdot\vec{d}\,|a\rangle|^2}{\omega_b-\omega_a-\omega-i\Gamma_{ba}/2}+\frac{|\langle a|\,\vec{u}\cdot\vec{d}\,|b\rangle|^2}{\omega_b-\omega_a+\omega+i\Gamma_{ba}/2}\right)\,, \tag{5.1}$$

where the index b stands for all the energy eigenstates other than $|a\rangle$, ω_s is the energy associated to state $|s\rangle$, $\Gamma_{ba}=\Gamma_b+\Gamma_a$ is the sum of the decay rates from each state.

Following [67], we define an AC-Stark shift operator V^{EE} whose diagonal matrix elements are given by $\delta E_a = \langle a|\,V^{EE}\,|a\rangle$, while the off-diagonal elements represent the couplings between states introduced by the AC-Stark shift. Thus, using this operator as the perturbation and going to first order is equivalent to using V^E at second order, if we define V^{EE} as

$$V^{EE} = \frac{|\mathcal{E}|^2}{4}\left[\left(\vec{u^*}\cdot\vec{d}\right)\mathcal{R}_+\left(\vec{u}\cdot\vec{d}\right)+\left(\vec{u}\cdot\vec{d}\right)\mathcal{R}_-\left(\vec{u^*}\cdot\vec{d}\right)\right]\,, \tag{5.2}$$

with

$$\mathcal{R}_\pm = -\frac{1}{\hbar}\sum_b \mathrm{Re}\left(\frac{1}{\omega_b-\omega_a\pm\omega\pm i\Gamma_{ba}/2}\right)|b\rangle\langle b|\,. \tag{5.3}$$

5.1.2 Polarizabily tensor

The expression for V^{EE} from 5.2 can be rewritten as the dot product[3] between two tensors, one depending only on the polarization of the trapping beam and the other containing the operators acting on the internal degrees of freedom of the atom (see Appendix B):

$$V^{EE} = \frac{|\mathcal{E}|^2}{4}\sum_{K=0,1,2}(-1)^K\left\{\vec{u}^*\otimes\vec{u}\right\}_K\cdot\left[\left\{\vec{d}\otimes\mathcal{R}_+\vec{d}\right\}_K+(-1)^K\left\{\vec{d}\otimes\mathcal{R}_-\vec{d}\right\}_K\right]\,, \tag{5.4}$$

where K is the rank of the tensor. Here, it runs from 0 to 2 since this tensor results from the coupling of 2 vector operators.[4] Indeed vector operators are spherical tensors of rank 1 and thus obey the same coupling rules as angular momenta, the coupling of two spin-1 states resulting in states of spin 0, 1, and 2. (5.4) can be rewritten introducing the irreducible parts of the polarizability tensor of rank K, $\alpha^{(K)}$:

$$V^{EE} = \frac{|\mathcal{E}|^2}{4}\sum_{K=0,1,2}(-1)^K\left\{\vec{u}^*\otimes\vec{u}\right\}_K\cdot\alpha^{(K)}\,, \tag{5.5}$$

with the irreducible components of the polarizability tensor:

$$\alpha^{(K)} = \{\vec{d}\otimes\mathcal{R}_+\vec{d}\}_K+\{(-1)^K\vec{d}\otimes\mathcal{R}_-\vec{d}\}_K\,. \tag{5.6}$$

[3]The dot product between two tensors U and V of (the same) rank K is given by

$$(U_K\cdot V_K)=\sum_{-K\leqslant q\leqslant K}(-1)^q U_{Kq}V_{K-q}\,,$$

where the index q is used to label the components in the spherical basis of U_K and V_K.

[4]The notation $\left\{\vec{A}\otimes\vec{B}\right\}_K$ denotes the tensor of rank $K=0,1,2$ obtained by coupling the vector operators $\vec{A}$ and $\vec{B}$. The component of such a tensor will be denoted by $\left\{\vec{A}\otimes\vec{B}\right\}_{Kq}$, where $q=-K,\ldots,K-1,K$. Those components can be calculated using (B.28) from Appendix B

The parenthesis in the superscript are there to signal that K is not an exponent in that case. Although equations (5.4) and (5.6) are fine for calculations, they are not easily interpretable. If we restrict the state space to a single fine-structure multiplet $|\gamma J\rangle$,[5] the polarizability tensor can be expressed in terms of the total angular momentum operator $\vec{J}$ [67,68], giving rise to an AC-Stark shift operator:

$$V_J^{EE} = -\frac{1}{4}|\mathcal{E}|^2\left[\alpha_J^s - i\alpha_J^v\frac{\left[\vec{u^*}\times\vec{u}\right]\cdot\vec{J}}{2J} + \alpha_J^t\frac{3\left[\left(\vec{u^*}\cdot\vec{J}\right)\left(\vec{u}\cdot\vec{J}\right)+\left(\vec{u}\cdot\vec{J}\right)\left(\vec{u^*}\cdot\vec{J}\right)\right]-2\vec{J}^2}{2J(2J-1)}\right], \tag{5.7}$$

where α_J^s, α_J^v, and α_J^t are respectively the scalar, vectorial, and tensorial polarizabilities given by:

$$\alpha_J^s = \frac{1}{\sqrt{3(2J+1)}}\alpha_J^{(0)}\,, \tag{5.8a}$$

$$\alpha_J^v = -\sqrt{\frac{2J}{(J+1)(2J+1)}}\alpha_J^{(1)}\,, \tag{5.8b}$$

$$\alpha_J^t = \sqrt{\frac{2J(2J-1)}{3J(J+1)(2J+1)(2J+3)}}\alpha_J^{(2)}\,. \tag{5.8c}$$

where

$$\alpha_J^{(K)} = (-1)^{K+J+1}\sqrt{2K+1}\sum_{J'}(-1)^{J'}\begin{Bmatrix}1 & K & 1\\ J & J' & J\end{Bmatrix}|\langle J'\|\vec{d}\|J\rangle|^2 \times\frac{1}{\hbar}\,\mathrm{Re}\left(\frac{1}{\omega_{J'J}-\omega-i\Gamma_{J'J}/2}+\frac{(-1)^K}{\omega_{J'J}+\omega+i\Gamma_{J'J}/2}\right)\,, \tag{5.9}$$

Each term of (5.7) can be interpreted as an operator acting in the γJ-manifold.

- The scalar part produces a shift in energy on the manifold's center of mass.
- The vector part gives rise to a splitting of the Zeeman sublevels, similar to what happens when an atom is subjected to a magnetic field. For that reason it is convenient to think of that term as an effective magnetic field which couples to the total angular momentum of the atom, with:

$$\vec{B}_{\text{eff}} = \frac{\alpha_J^v}{8\mu_B g_J J}i\left[\vec{\mathcal{E}}^*\times\vec{\mathcal{E}}\right]\,, \tag{5.10}$$

$$V_J^{EE\,v} = \mu_B g_J\vec{J}\cdot\vec{B}_{\text{eff}}\,. \tag{5.11}$$

[5] Here, γ represent the list of all the quantum numbers required to specify unambiguously the fine-structure multiplet. To improve the readability of the subsequent formulas, we will not include the γ index to the different α coefficients, or to the restriction of V^{EE} to the $|\gamma J\rangle$ manifold. This simplification of notation means that whenever J is the label for a state or an index of summation, one should remember to replace it by γJ.

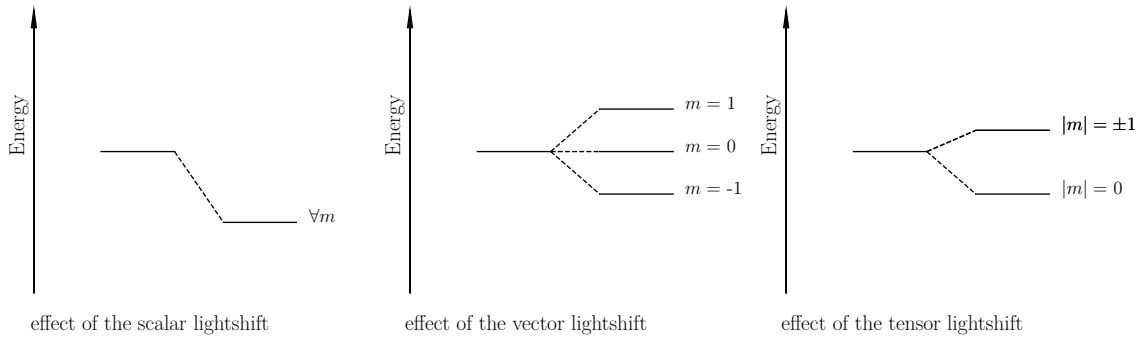

Figure 5.1: Each subplot represent the energy-level diagram for a $J = 1$ state submitted to the different term in (5.9). We have from left to right the effect of scalar, vector and tensor part of V_{nJ}^{EE} for arbitrary coefficients. The line on the left represents the unperturbed degenerate $|Jm_J\rangle$ states and on the right the corresponding displaced levels after the perturbation was added.

We can note that since this term is proportional to $[\vec{u}^* \times \vec{u}]$, the vector part of the AC-Stark shift is vanishing for linear polarization. It is oriented along the axis of propagation for elliptically polarized beams.

- Finally, the tensor part shifts the Zeeman sublevels in a way that depends only on the magnitude of m_J independently of its sign. This term can be interpreted as arising from an effective electric field gradient coupling to the electric quadrupole moment of the atom (details can be found in [68, 69]).The behavior of the different terms in (5.7) is summarized in Figure 5.1.[6]

5.1.3 Strong magnetic field limit

From the above discussion we can guess that the choice of the so-called "quantization axis" might be a thorny issue. There is indeed a conflict between the ambiant bias field $\vec{B}_{\text{bias}}$, the effective magnetic field $\vec{B}_{\text{eff}}$, and the orientation of the effective electric field gradient. The quantization axis could also be that of the polarization of the trapping beam, for instance in the case of atoms trapped in single-beam optical tweezers [18]. Moreover, in the case of optical lattices, there are multiple non-colinear beams for the trapping which complexify the situation even further . These tensions between the different "good bases" in the general case lead to non-trivial coupling between the different Zeeman sublevels (with respect to a specific choice of axis). There will be mixing of states and that the coupling matrix must be diagonalized to obtain the new eigenstates in that context.

One way to circumvent this issue is to impose a "strong"[7] bias magnetic field so that the state mixing from the other couplings can be neglected. In this part, we assume that a strong bias magnetic field is present and that we can neglect all the couplings between Zeeman sublevels. We introduce a cartesian basis $(\vec{e}_x, \vec{e}_y, \vec{e}_z)$, with $\vec{e}_z$ along the bias

[6] It is worth noting that α_J^v is non-zero only if $J \geq 1/2$, and α_J^t is automatically zero for $J \leq \frac{1}{2}$ states.
[7] In a sense that will be discussed in section 5.1.3.

magnetic field. We will also use a spherical basis ($\vec{e}_{-1}$, $\vec{e}_{+1}$, $\vec{e}_0$) defined by:

$$\begin{cases} \vec{e}_{\pm 1} = \mp\dfrac{1}{\sqrt{2}}(\vec{e}_x \pm i\vec{e}_y), \\ \vec{e}_0 = \vec{e}_z. \end{cases} \tag{5.12}$$

We perform this approximation because in practice, we want to split the Zeeman sublevels to reduce our trapped atom to a two-level system, to simplify the study of the dynamics. This approximation amounts to neglecting the off-diagonal elements in V_J^{EE}. The unperturbed Zeeman sublevels are shifted in energy, but are not mixed by V^{EE}; they still form a "good basis" for the system. We are then left with its diagonal elements labelled by m_J:

$$\langle Jm_J|\, V_J^{EE}\, |Jm_J\rangle = V_{Jm_J}^{EE} = -\frac{1}{4}|\mathcal{E}|^2 \left[\alpha_J^s + C\alpha_J^v \frac{m_J}{2J} - D\alpha_J^t \frac{3m_J^2 - J(J+1)}{2J(2J-1)}\right], \tag{5.13}$$

where

$$C = |u_{-1}|^2 - |u_1|^2 = 2\,\mathrm{Im}(u_x^* u_y), \tag{5.14}$$
$$D = 1 - 3|u_0|^2 = 1 - 3|u_z|^2. \tag{5.15}$$

Note that the definition of the basis for the components of $\vec{u}$ is relative to the direction of the bias magnetic field, and might not coincide with the axes of the optical lattice.

5.1.4 Validity of the derivation

To derive the expression above for the lightshift operator, we used (see Appendix B) the following assumptions:

1. The mixing of states induced by V^{EE} should be negligible so that we can keep the Zeeman substates as the eigenbasis for our problem. We thus want Zeeman splittings to be large compared to the off-diagonal matrix elements of V^{EE}, namely:

$$\frac{\langle Jm_J|\, V_J^{EE}\, |Jm'_J\rangle}{\Delta E_{m_J m'_J}} \ll 1 \tag{5.16}$$

   where $\Delta E_{m_J m'_J}$ is the energy difference between the Zeeman sublevels labelled by m_J and m'_J.

2. To neglect the imaginary part of V^{EE}, that is related to absorption, and thus obtain a conservative trap, we need to be far from resonance for all intermediate states $|J'm'_J\rangle$:

$$\frac{\Gamma_{J'J}/2}{(\omega_{J'} - \omega_J \pm \omega)^2 + \Gamma_{J'J}^2/4} \ll 1 \tag{5.17}$$

.

3. (For convenience) The Zeeman shifts within the fine-structure manifolds were neglected in the denominators of $\mathcal{R}_\pm$, that is (also neglecting the $i\Gamma$ term):

$$\frac{1}{\omega_{J'm'_J} - \omega_{Jm_J} \pm \omega} \approx \frac{1}{\omega_{J'} - \omega_J \pm \omega} \tag{5.18}$$

$\hbar\omega_{Jm_J}$ is the energy of $|Jm_J\rangle$ including the Zeeman shift, while $\hbar\omega_J$ is the energy of the same state at zero magnetic field. This approximation was made to simplify the numeric implementation and for the convenience of not having an extra free parameter in the problem, namely the amplitude of the magnetic field. In practice those shifts are small compared to the detunings unless the laser is close to resonance, which we specifically avoid here.

5.1.5 Calculations from available spectroscopic data

In this section, we describe the calculation of the polarizabilities from the available spectroscopic data in the literature [18,64–66] and the formalism described previously. We will compute those values for our ODT at 1064 nm and benchmark the method by comparing the results with available data at 515.2 nm and 1064 nm.

5.1.5.1 Dynamic polarizabilities of strontium at 1064nm

While working on the computation of the polarizabilities for strontium at 1064 nm, we realized that some relevant transitions were absent in the NIST database [64], which we used exclusively before this work. This required bibliography work to compile spectroscopic data from different sources. The contributions of the different transitions are summarized in Tables 5.4 and 5.5. From these calculations, we get the value of the polarizabilities for our two levels of interest, $g := 5s^2\ {}^1\mathrm{S}_0$ and $e := 5s5p\ {}^3\mathrm{P}_1$, summarized in Table 5.1 in atomic units.[8] Since the ground state of strontium has $J = 0$, it has only a scalar polarizability. We used atomic units to express our results, the relevant atomic units in that context are the atomic unit of electric dipole moment, 1 a.u. $= 8.4783536255(13) \times 10^{-30}\mathrm{C}\cdot\mathrm{m}$; and the atomic unit of polarizability, 1 a.u. $= 1.64877727436(50) \times 10^{-41}\mathrm{C}^2 \cdot \mathrm{m}^2 \cdot \mathrm{J}^{-1}$

Table 5.1: Polarizabilities at 1064 nm for the states ${}^1\mathrm{S}_0$ and ${}^3\mathrm{P}_1$ in atomic units calculated from (5.8a) to (5.8c) and (5.9), Tables 5.4 and 5.5.

State	α^s	α^v	α^t
${}^1\mathrm{S}_0$	247		
${}^3\mathrm{P}_1$	132	−172	19

First of all, we can see immediately that the scalar polarizabilities for the two levels are distinct. This will prove important when we try to apply laser cooling in the optical lattice

[8] The relevant atomic units for the computation of this chapter are:
- the atomic unit for electric dipole moment $ea_0 = 8.4783536255(13) \times 10^{-30}\mathrm{C}\cdot\mathrm{m}$, where e the electron charge, and a_0 is the Bohr radius,
- the atomic unit of polarizability $e^2a_0^2/\alpha m_e c^2 = 1.64877727436(50) \times 10^{-41}\mathrm{C}^2\cdot\mathrm{m}^2\cdot\mathrm{J}^{-1}$, where α is the the fine strucutre constante, m_e is the electron mass, and c is the speed of light in vacuum.

(see Chapter 6); the difference in polarizability produces new cooling/heating mechanisms that are absent in the so-called "magic-wavelength trap".[9] We see from (5.13), we see that by choosing $m_J \neq 0$ and tuning the ellipticity of the trapping beam, we can tune the AC-Stark shift on $\left|{}^3\mathrm{P}_1, |m_J| = 1\right\rangle$, by tuning the ellipticity one can recover the equality of the polarizabilities for the two states [18]. However, the tuning range is not sufficient at 1064 nm, in which case one has, for every choice of polarization, a greater polarizability in the ground state.

5.1.5.2 Comments on the spectroscopic data

As stated previously, we used four different sources [18, 64–66]. Most of the transitions we used before this study were from [64]. We replaced existing transitions in the NIST database by data from [18] whenever the uncertainties were smaller. We also added transitions taken from [18, 65, 66], when they were missing. One important instance of missing transition was the $5s5p\ {}^3\mathrm{P}_1 \rightarrow 5p^2\ {}^3\mathrm{P}_{0,1,2}$, which gives rise to a relative error of $\frac{\Delta\alpha^s}{\alpha^s} = 40\%$ on the scalar polarizability when omitted.[10]

For the ground state polarizability, the transition to $5s5p\ {}^1\mathrm{P}_1$ is dominant, with more than 97% of the contribution.

5.1.5.3 Benchmarking of the calculation

In order to estimate the reliability of our calculations, we chose to compare them with results from another group.We compare our results with the values from Cooper, *et al.* [18], where they provide tables containing the polarizabilities for strontium at 515.2 nm.[11] Recently, results became available at 1064 nm for the ${}^1\mathrm{S}_0$ state (and also ${}^3\mathrm{P}_2$) in Trautmann *et al.* [21].

In Table 5.2, we compare the results from their calculations and ours. We can see that we reproduce their results reasonably well, within a margin of 5%. This was not granted in principle because their model includes effects beyond the sum-over-state formula, such as the polarizability of the ionic core.

Trautmann *et al.* obtained a polarizability of 240.49 a.u. for the ground state. Their value, however, includes the contribution from the core polarizablity, evaluated at 5.3 a.u.[12] Substracting this contribution that is not included in our approach we get a relative error of 5%. In both cases, our results are close from the values available in the litterature.

[9] Here, *magic* means that the polarizabilites are equal. Such configurations are used, for instance, in optical clocks [70] or tweezer experiments [71]

[10] The fact that these $P \rightarrow P$ transitions have a strong impact might be surprising because it might look as if we were doing a transition without changing the parity, which is forbidden for electric-dipole (E1) transitions. In fact, these transitions are perfectly allowed if we remember that the parity of a term is not given by $(-1)^L$ but rather by $(-1)^{l_1+l_2}$ (in the case of a two-electron atom), where l_1, l_2 are the orbital quantum number of each valence electron and L is the total angular momentum quantum number. A more rigorous spectroscopic notation would be to include the term's parity. For instance, in the NIST database, the odd terms are signaled by an "o" superscript so that we can distinguish $(5s5p)\ {}^3\mathrm{P}_1{}^o$ from $(5p^2)\ {}^3\mathrm{P}_1$

[11] In fact, those are the results that brought to our attention the role of some transitions that were missing from our spectroscopic database , namely the tranisitions to $5p^2\ {}^3\mathrm{P}_\mathrm{J}$ states.

[12] Since this value was published very recently, it is not including in our calculations of the lightshifts for the ODTs.

Source	$\alpha(^1S_0)$	$\alpha^s(^3P_1)$	$\alpha^t(^3P_1)$	$\frac{\Delta\alpha}{\alpha}$
Cooper [18]	942	769	−111	
This work	989	727	−116	5%

Table 5.2: Comparison between the tabulated values from [18] and our results in atomic units at 515.2 nm. The relative errors for the different terms are all equal so we specified only one value in the last column $\frac{\Delta\alpha}{\alpha}$.

5.2 2D lattice setup

In this section, we expose the details of the configuration that was chosen to produce the 2D optical lattices[13] for our experiment. We discuss the role of the bias magnetic field $\vec{B}_{\text{bias}}$, the polarization of the beams on the trapping parameters, and the emission diagram for the atom, which in turn will have an impact on the collection of the emitted photons by the microscope.

5.2.1 Lattice potential

To produce a 2D optical lattice, as exposed in chapter 1 section 1.4.3, we use one pair of beams crossing at an angle of 12° (see Figure 5.2), providing the vertical confinement in a single plane of the resulting interference pattern. This trap confines the atoms in a planar (2D) configuration inside the XY plane, by introducing a trapping potential[14] along the Z direction. We will refer to this pair of beams as the "vertical trap" or the "vertical latttice".

Additionally, we have two pairs of retroreflected beams crossing at an angle of 90°, producing a square lattice pattern, formed by the superposition of two standing waves along X and Y, forming the "horizontal lattice".

The beam's geometric configuration is summarized in Figure 1.11. X, Y and Z will designate the lattice axes to avoid confusion with the basis relative to $\vec{B}_{\text{bias}}$. The details of the parameters of the different beams are presented in Chapter 1. To avoid interferences between the beams producing the confinements along the different axes, the beams along X, Y and the vertical-trap beams have been shifted in frequency using acousto-optic modulators by a few MHz (see Table 1.1). Assuming that the beams of axis i have the same polarization $\vec{u}^{(i)}$. Note that the superscript is written in parenthesis to avoid confusion between the label corresponding to each laser beam and exponentiation with a power i. The resulting potential is obtained by summing the contributions of the different traps:

[13] As a reminder from chapter 1, we mean by 2D optical lattice a trap used to form a single plane on top of which we add periodic modulation forming a square lattice.

[14] If we neglect the Gaussian envelops and the zone in which the beam are crossing.

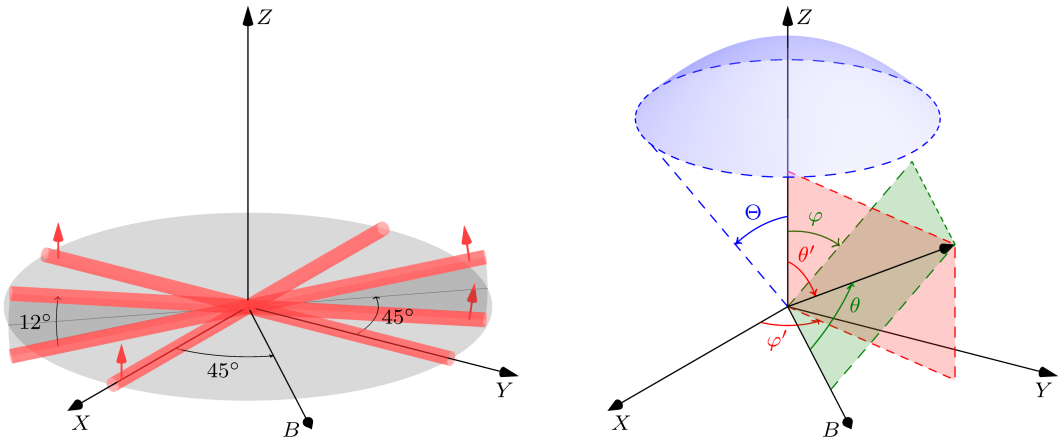

Figure 5.2: The left picture shows the lattice geometry, the lattice beams' polarizations, and the orientation of the magnetic field. The right picture illustrates the two spherical coordinates systems used to parameterize the radiation patterns in figure 5.3: with the zenith on the quantization axis (green), and on the imaging axis (red). The solid angle viewed by the lens (drawn here with NA = 0.6) is also represented in blue.

$$
\begin{aligned}
H_{\text{latt}}(\vec{r}) &= \langle g| \overbrace{V_g^{E_X E_X} + V_g^{E_Y E_Y}}^{\text{Horizontal lattices}} + \overbrace{V_g^{E_Z E_Z}}^{\text{Vertical lattice}} |g\rangle\, |g\rangle\langle g| \\
&+ \sum_{m_J, m'_J = 0, \pm 1} \langle e, m_J| \overbrace{V_e^{E_X E_X} + V_e^{E_Y E_Y}}^{\text{Horizontal lattices}} + \overbrace{V_e^{E_Z E_Z}}^{\text{Vertical lattice}} |e, m'_J\rangle\, |e, m_J\rangle\langle e, m'_J| \qquad (5.19) \\
&= -\frac{1}{2\varepsilon_0 c} \sum_{i=X,Y,Z} \mathcal{I}_i(\vec{r}) \left[\alpha_g^{(i)} |g\rangle\langle g| + \sum_{m_J, m'_J = 0, \pm 1} \alpha_{e, m_J, m'_J}^{(i)} |e, m_J\rangle\langle e, m'_J| \right] ,
\end{aligned}
$$

where the intensities of the interference patterns for each axis is given as a function of its peak intensity $\mathcal{I}_i$, the waists of the Gaussian envelope w_j, and the period of the fringes a_i by:

$$
\mathcal{I}_i(\vec{r}) = \frac{\varepsilon c}{2} |\mathcal{E}_i(\vec{r})|^2 = \mathcal{I}_i \sin^2(\pi r_i / a_i)\, e^{-\sum_{j \neq i} 2 r_i^2 / w_j^2} \quad (i, j = X, Y, Z) , \qquad (5.20)
$$

r_i are the are the cartesian coordinates along X, Y, and Z. The α coefficients are given by the matrix elements of the kind $\langle e, m_J| V_e^{E_i E_i} |e, m'_J\rangle$ from (5.7).

We can see from (5.19) that H_{latt} will *a priori* induce a coupling between the motion of the atom and the spin degree of freedom of the excited state.

This is caused by the non-separability of position and internal state in the Hamiltonian H_{latt}. Indeed, H_{latt} is formed by the sum (over the axes) of three operators wheighted by the local intensities. Thus, changing the position of the atom induces a change in the action on the internal state, in particular there are variations on the couplings between the Zeeman substates of the excited state. There are two simple ways to prevent this effect from happening. We can make sure that the α coefficients are independent of the axes index i; this is achievable by setting the polarizations of all beams equal (orange

path in Figure 5.4), given the geometry of our beams the only possibility is to have all the beams polarized vertically. The other work-around is to decouple the Zeeman substates by imposing a strong bias magnetic field (blue path in Figure 5.4).

Although these couplings might be of interest to engineer spin-orbit systems, it is, for now, a complexification of the system that we will try to avoid. We will suppose that we have a bias magnetic field strong enough that the mixing of Zeeman sublevels induced by the ODT can be neglected.[15] In that case, the AC-Stark shift will be a perturbation of the Hamiltonian, including the free atom and the Zeeman coupling to the bias field. We obtain a diagonal Hamiltonian for the lattice:

$$H_{\text{latt}}(\vec{r}) = -\frac{1}{2\varepsilon_0 c}\sum_{i=X,Y,Z}\mathcal{I}_i(\vec{r})\left[\alpha_g^{(i)}\,|g\rangle\langle g| + \sum_{m_J=0,\pm1}\alpha_{e,m_J}^{(i)}\,|e,m_J\rangle\langle e,m_J|\right], \tag{5.21}$$

where the $\alpha_{e,m_J}^{(i)}$ are given by (5.23), C and D represent the effect of the i^{th} beam's polarization, replacing the J index by g or e:

$$\alpha_g^{(i)} = \alpha_g^s, \tag{5.22}$$

$$\alpha_{e,m_J}^{(i)} = \alpha_e^s + C\left[\vec{u}^{(i)}\right]\alpha_e^v\,\frac{m_J}{2J} - D\left[\vec{u}^{(i)}\right]\alpha_e^t\,\frac{3m_J^2 - J(J+1)}{2J(2J-1)}. \tag{5.23}$$

Here, we introduced the convenient but somewhat abusive notation $\alpha_{e,m_J}^{(i)}$. Indeed, strictly speaking the polarizability should not depend on the polarization $\vec{u}^{(i)}$. However, for the case where we neglect the off-diagonal elements of the lightshift operator, this notation allows us to write a "polarizability" for each Zeeman substate. In fact, $\alpha_{e,m_J}^{(i)}$ is the lightshift obtained for an intensity of $1\,\text{W}\cdot\text{m}^{-2}$.

We now have reduced our problem to a configuration in which each atomic state will feel its own potential, this choice thus performs a decoupling of the internal and external degrees of freedom:

$$H_{\text{latt}}(\vec{r}) = V_g(\vec{r})\,|g\rangle\langle g| + \sum_{m_J=0,\pm1}V_{e,m_J}(\vec{r})\,|e,m_J\rangle\langle e,m_J| \tag{5.24}$$

with $V_k(\vec{r}) = -\frac{1}{2\varepsilon_0 c}\sum_{i=X,Y,Z}\mathcal{I}_i(\vec{r})\alpha_k^{(i)}$ where k is a label for the internal state of the atom. From (5.24), the system can be reduced to a two-level atom by making sure the Zeeman splitting between the states $|e,m_J\rangle$ is significantly larger than the trap depth for each internal state,[16] which is on the order of the sum of the trap depth $\sim 2.5\,\text{MHz}$. This corresponds to magnetic field of at least a few gauss, *e.g.* 2.1 MHz corresponds to 1 G (see (5.32)).

[15] Given the value summarized in Table 5.1 and equation (5.7), the matrix elements of the vector lightshift will, at most, be on the order of half those of the scalar part and those of the vector part will be an order of magnitude less. Since for our trap the lightshifts will be on the order of 1 MHz at peak intensity, we would need a bias magnetic field on the order of a few gauss to obtain Zeeman shifts on the order of a few MHz. That condition has to be fullfilled to make the two-level approximation since the width of the vibrational manifolds of a trapped atom will be on the order of the trap depth (1 MHz).

[16] In a quantized description of the motion of the atom, the condition would require that the vibrational manifold of each internal state are well separated.

5.2.2 Orientation of the quantization axis

As previously discussed, we want to impose a preferential direction in our problem in the form of a bias magnetic field, $\vec{B}_{\text{bias}}$. We already imposed a constraint on the norm of this field, but none on its direction yet.

The impact of the direction of $\vec{B}_{\text{bias}}$ will be two-fold. First, it will determine the preferential directions of emission for the dipole transition, depending on wether a circular or linear dipole is excited, allowing us to optimize the flux of photons sent to the microscope. Second, by picking up a cartesian basis $\{\vec{e}_x, \vec{e}_y, \vec{e}_z\}$ (or a spherical one $\{\vec{e}_0, \vec{e}_{-1}, \vec{e}_{+1}\}$), it will change the value of the polarizabilities *via* the $C\left[\vec{u}^{(i)}\right]$ and $D\left[\vec{u}^{(i)}\right]$ coefficients in (5.23). This gives, in principle, some freedom to try to optimize the trap depths.

5.2.2.1 Maximization of the photon flux to the imaging system

We know from classical electrodynamics (or quantum mechanics) [72, 73] that an oscillating linear dipole does not radiate along its axis. Thus, for the $m_e = 0 \to m_g = 0$ (π-transition), the quantization axis should not be directed along the imaging axis (Z-axis) but rather in the XY-plane in which the emission diagram is maximal. Conversely, if we drive one of the $m_e = 0 \to m_g = \pm 1$ ($\sigma_\pm$-transitions), then spontaneous emission will be more intense in the direction of $\vec{B}_{\text{bias}}$, in which case we should choose $\vec{B}_{\text{bias}}$ parallel to $\vec{e}_Z$. Those two choices are summarized in Figure 5.3, where the radiation patterns are displayed for the choice of magnetic field maximizing the flux towards the optical system (Z-axis).

We will now compute the collection efficiency in the two configurations that we just described. We will find that the two situations are in fact equivalent in terms of photon collection. For that we will compute the integral over the emission pattern.[17] More precisely the radiation pattern f_0 for a linear dipole along $\vec{z}$ is given, in spherical coordinates relative to the quantization axis (see Figure 5.3), by:

$$f_0(\theta, \phi) = \frac{3}{8\pi}(1 - \cos^2\theta) \,, \tag{5.25}$$

and, for circular dipoles we have:

$$f_{\pm 1}(\theta, \phi) = \frac{3}{16\pi}(1 + \cos^2\theta) \,, \tag{5.26}$$

with the normalization $\int \mathrm{d}\theta \, \mathrm{d}\phi \sin\theta f_q(\theta, \phi) = 1$ for $q = 0, \pm 1$. Choosing the orientation of the magnetic field as in Figure 5.3, and assuming that the atom is on the optical axis of the imaging system, we can compute the collection efficiency for the linear and circular dipoles as a function of the acceptance angle α ($\text{NA} = \sin\alpha$ of the imaging system). For $q = 0, \pm 1$:

$$\eta_q(\alpha) = \int_0^{2\pi} \mathrm{d}\phi' \int_0^{\alpha} \mathrm{d}\theta' \sin\theta' f_q(\theta, \phi) \tag{5.27}$$

[17] The emission pattern $f(\theta, \phi)$ of a light source is defined as the normalized photonic flux per solid angle in the direction given by (θ, ϕ). It can be seen as the probability density function for the emission of a photon in the direction (θ, ϕ).

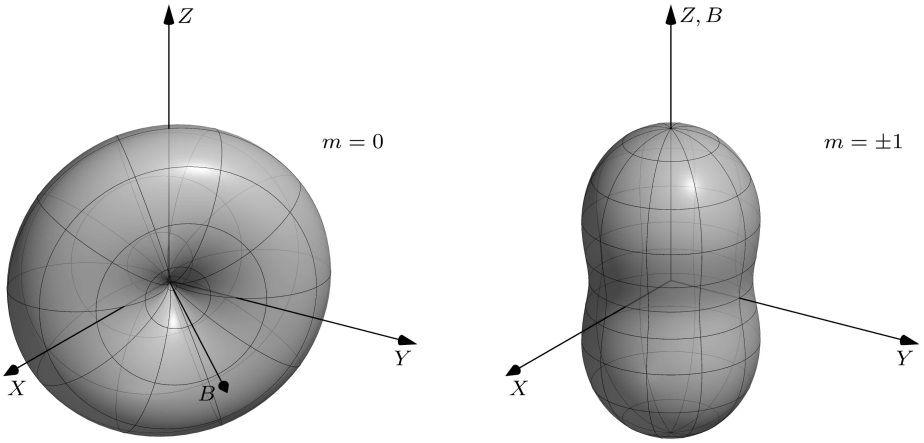

Figure 5.3: The left picture shows the emission diagram for the π-transition with a magnetic field contained in the XY-plane. The right picture shows the emission diagram for the $\sigma_\pm$-transitions with a magnetic field along Z.

where we used (θ', ϕ') the spherical angles relative to the optical axis of the system, introduced in Figure 5.3. We can then make the following replacements in f_q:

$$\begin{cases} \cos\theta \to \cos\theta' & (q = \pm 1)\ , \\ \cos\theta \to \frac{1}{\sqrt{2}}(\cos\phi' + \sin\phi')\sin\theta' = \cos\Big(\phi' - \frac{\pi}{4}\Big)\sin\theta' & (q = 0)\ , \end{cases} \tag{5.28}$$

whence:

$$\eta_q(\alpha) = \begin{cases} \frac{3}{16\pi}\int_0^{2\pi} \mathrm{d}\phi' \int_0^{\alpha} \mathrm{d}\theta' \sin\theta'(1 + \cos^2\theta') & (q = \pm 1)\ , \\ \frac{3}{8\pi}\int_0^{2\pi} \mathrm{d}\phi' \int_0^{\alpha} \mathrm{d}\theta' \sin\theta'(1 - \sin^2\theta' \cos^2(\phi' - \frac{\pi}{4})) & (q = 0)\ . \end{cases} \tag{5.29}$$

Finally integration of the above expressions give a result that is indepenent of q:

$$\eta_q(\alpha) = \frac{1}{8}(4 - 3\cos\alpha - \cos^3\alpha) \qquad (q = 0, \pm 1)\ . \tag{5.30}$$

(5.30) shows that the freedom on the choice in m does not grant access to higher fluxes of photons in the imaging system, as long as we choose the direction of the quantization axis appropriately, that is like in Figure 5.3.

5.2.3 Maximization of the trap depths

As mentioned in Section 5.2.1, we will split the Zeeman sublevels sufficiently that each is selectively addressable by a laser. In this configuration, we can assume that the atom will only emit on a given transition $\sigma_\pm, \pi$.

We thus have to choose between the two configurations from last section, either we take $m_J = 0$ with a horizontal magnetic field, or $m_J = \pm 1$ with a vertical magnetic field. The states associated to those configurations have different interesting features:

- $m = \pm 1$ can benefit from the tunability in the polarizability granted by the vector part of the polarizability tensor (in case we decide to relax the constraint of having linearly polarized trapping beams). As we can see in Table 5.1, the value of the α_e^v

is on the same order as the value of its scalar counterpart, thus providing a broad range of tunability. The downside of using those states is that they are sensitive to magnetic field fluctuations. If we wanted stability on the order of $\Gamma_r = 2\pi \cdot 7.4\,\mathrm{kHz}$, we would need to reduce magnetic field fluctuations down to the milligauss range.[18] However, we will see in the next chapter that the detuning need not be controlled with that level of precision, but more likely on the order of 15-20 mG roughly.

- $m = 0$ on the other side grants insensitivity to the external magnetic field fluctuations, but the accordability by polarization is small since α_e^t is 7 times smaller than α_e^s.

To simplify our setup, we decided to use (at least for now) the $m = 0$ state. This is compatible with the simpler choice of linear polarizations for the trapping beams. We discuss the possibility of using the states $m_J = \pm 1$ in Appendix C, where we conclude that the polarizations of the beams should be all linear and vertical.

The maximum trap depth is obtained for $m_J = 0$ when the choice of polarization maximizes:

$$\alpha_{e,0}^{(i)} = \alpha_e^s - (1 - 3|u_z|^2)\alpha_e^t \frac{-J(J+1)}{2J(2J-1)}. \tag{5.33}$$

Since α_e^t is positive, this is maximized for $u_z = 0$, that is a polarization orthogonal to the magnetic field. Given the geometry of our optical lattice, and the fact that the magnetic field lies in the horizontal plane, the only option is to orient all the polarizations in along the vertical direction.

5.2.4 Expected trap for the $m_J = 0$ with horizontal magnetic field and vertical polarizations

Table 5.3 presents a summary of the properties of the optical lattice for the laser configuration described in chapters 1 and 3. The lattice depth refers to the difference in potential energy at the peak intensity $\mathcal{I}_i$ and at zero intensity. The trap frequencies refer to the frequencies of the 3D harmonic potential used to approximate the potential well on a lattice site. In our case, we have two degenerate directions ($\Omega_X = \Omega_Y$) and one direction in which the trap is much shallower ($5\Omega_Z \approx \Omega_X = \Omega_Y$). Note that those values are given in imaging configuration were the lasers intensities are at there maximum values.

[18] Using the formula for the linear Zeeman energy shift on $\left|{}^3\mathrm{P}_1, m_J = 1\right\rangle$:

$$\Delta E_{Zeeman} = \mu_B g_J B m_J \,, \tag{5.31}$$

where $\mu_B = 9.273\,\mathrm{J}\cdot\mathrm{T}^{-1}$ is the Bohr magneton, $g_J = \frac{3}{2}$ is the Landé g-factor and, B the amplitude of the magnetic field. Thus imposing a limit on energy flucutuations of $\hbar\Gamma_r$ amounts to imposing:

$$\Delta B \leq \frac{\hbar\Gamma_r}{\mu_B g_J} = 3.5\,\mathrm{mG} \leftrightarrow 7.4\,\mathrm{kHz}. \tag{5.32}$$

Table 5.3: Lattice beam properties and resulting lightshifts in the imaging configuration. The beam power corresponds to the power in each of the two beams forming a given lattice axis. Here we display the maximum available intensities since we are studying the imaging configuration of the microscope. The lattice depth is the lightshift calculated for the maximum light intensity using the polarizabilities table 5.1. The excited state is $\left|{}^3\mathrm{P}_1, m_J = 0\right\rangle$, abbreviated e.

axis	wavelength [nm]	waist w [µm]		power P [W]	intensity $\mathcal{I}_i$ [kW/cm^2]	lattice depth ΔV [kHz]		trap frequency Ω_i [kHz]	
		horiz.	vert.			g	e	g	e
X, Y	1064	275	275	15	50.5	585	356	67	55
Z	1064	500	60	15	127	1480	899	12	9

5.3 Conclusion

In this chapter, we developed the formalism required to compute accurately the AC-Stark shift for strontium at 1064 nm for the ${}^1\mathrm{S}_0$ ground state and ${}^3\mathrm{P}_1$ excited states. That is required for the trapping of the atoms in all the optical dipole traps. In particular, the polarizability of the excited state is crucial for the imaging stage of the atoms in the lattice.

This study showed that the use of a strong bias magnetic field can be beneficial to simplify the action of the lightshift operator. It allowed us to choose the direction of that field in order to maximize the flux to the microscope. Finally, we saw that some gain in the polarizabilities can be obtained by choosing vertical polarizations for the trap's beams. If no bias field is used, we can still simplify the lightshift operator by choosing equal polarizations for all the laser beams of the optical lattice setup. In our geometry this amounts to having vertically polarized beams. The reasoning between the different choices that were discussed in this chapter is summarized in Figure 5.4.

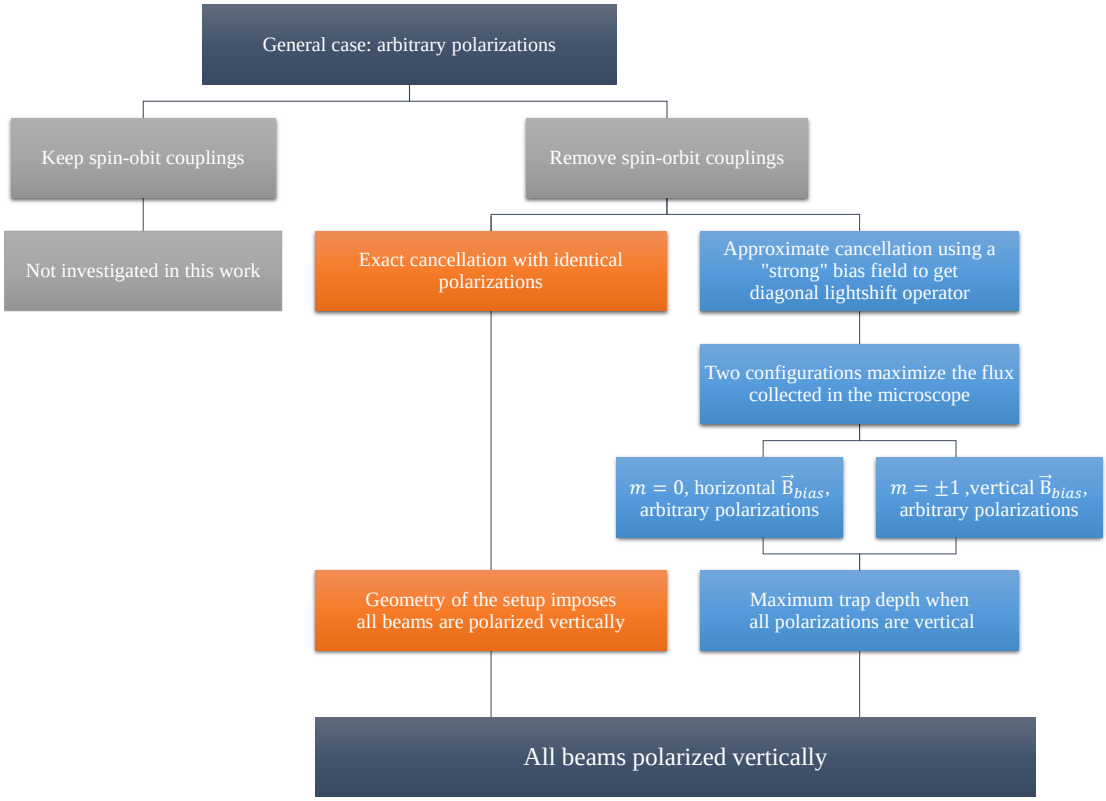

Figure 5.4: Workflow of the reasoning underlying the different choices that were made in this chapter.

Final state	λ (nm)	D (a.u.)	α^s (a.u.)	weight (%)	source
5s5p $^1P_1$	460.87	5.4e+0	2.4e+2	97.65	[64]
4d5p $^1P_1$	242.88	6.0e-1	1.3e+0	0.55	[64]
5s8p $^1P_1$	235.5	5.9e-1	1.3e+0	0.51	[64]
5s9p $^1P_1$	230.8	4.6e-1	7.4e-1	0.30	[64]
5s7p $^1P_1$	257.02	3.6e-1	5.2e-1	0.21	[64]
5s10p $^1P_1$	227.59	3.5e-1	4.2e-1	0.17	[64]
5s5p $^3P_1$	689.46	1.5e-1	4.0e-1	0.16	[64]
5s6p $^1P_1$	293.27	2.7e-1	3.3e-1	0.13	[64]
5s11p $^1P_1$	225.4	2.5e-1	2.2e-1	0.09	[64]
5s12p $^1P_1$	223.83	2.0e-1	1.4e-1	0.06	[64]
5s13p $^1P_1$	222.7	1.6e-1	8.8e-2	0.04	[64]
5s14p $^1P_1$	221.85	1.4e-1	6.4e-2	0.03	[64]
5s6p $^3P_1$	295.26	1.1e-1	5.5e-2	0.02	[65]
5s15p $^1P_1$	221.2	1.2e-1	4.7e-2	0.02	[64]
4d5p $^3D_1$	275.76	9.2e-2	3.7e-2	0.01	[65]
5s16p $^1P_1$	220.69	1.0e-1	3.4e-2	0.01	[64]
5s17p $^1P_1$	220.29	8.9e-2	2.7e-2	0.01	[64]
5s18p $^1P_1$	219.96	8.1e-2	2.2e-2	0.01	[64]
5s19p $^1P_1$	219.69	7.1e-2	1.7e-2	0.01	[64]
5s20p $^1P_1$	219.47	6.3e-2	1.3e-2	0.01	[64]
5s7p $^3P_1$	253.64	5.3e-2	1.1e-2	0.00	[65]
4d5p $^3P_1$	268.08	4.3e-2	7.7e-3	0.00	[65]
5s8p $^3P_1$	239.69	3.3e-2	4.0e-3	0.00	[65]
5s9p $^3P_1$	232.61	1.7e-2	1.0e-3	0.00	[65]
5s10p $^3P_1$	228.51	1.2e-2	5.0e-4	0.00	[65]
5s11p $^3P_1$	225.91	9.0e-3	2.8e-4	0.00	[65]

Table 5.4: Contributions to the scalar polarizability of the ground state ($^1S_0$), for the different transitions taken from [64, 65], in descending order. We remark that the two-level approximation, including only the $5s^2\,{}^1S_0 \leftrightarrow 5s5p\,{}^1P_1$ transition, gives the right value for the polarizability of the ground state with an error on the order of 3%.
The atomic unit of electric dipole moment is 1 a.u. $= 8.4783536255(13) \times 10^{-30} C \cdot m$.
The atomic unit of polarizability is 1 a.u. $= 1.64877727436(50) \times 10^{-41} C^2 \cdot m^2 \cdot J^{-1}$.

Final state	λ (nm)	D (a.u.)	α^s (a.u.)	α^v (a.u.)	α^t (a.u.)	source
5s6s $^3S_1$	688.04	3.4e+0	6.8e+1	-6.6e+1	3.6e+0	[18]
5s5d $^3D_2$	487.38	3.7e+0	4.1e+1	2.8e+1	-4.3e-1	[18]
5s4d $^3D_2$	2692.51	4.0e+0	-3.9e+1	-1.5e+2	4.1e-1	[18]
$5p^2$ $^3P_2$	472.37	2.9e+0	2.4e+1	1.6e+1	-2.5e-1	[18]
$5p^2$ $^3P_0$	483.35	2.7e+0	2.1e+1	-2.9e+1	-2.2e+0	[18]
$5p^2$ $^3P_1$	478.56	2.4e+0	1.6e+1	-1.1e+1	8.6e-1	[18]
5s4d $^3D_1$	2735.98	2.3e+0	-1.3e+1	4.9e+1	-6.8e-1	[18]
5s5d $^3D_1$	487.73	2.0e+0	1.2e+1	-8.4e+0	6.4e-1	[18]
$4d^2$ $^3P_2$	330.84	2.2e+0	8.7e+0	4.1e+0	-9.2e-2	[65]
$4d^2$ $^3P_1$	332.31	1.7e+0	5.3e+0	-2.5e+0	2.8e-1	[65]
$4d^2$ $^3P_0$	333.09	1.7e+0	5.1e+0	-4.8e+0	-5.4e-1	[65]
5s7s $^3S_1$	436.3	9.2e-1	2.2e+0	-1.3e+0	1.1e-1	[18]
$5p^2$ $^1S_0$	441.38	2.9e-1	2.2e-1	-2.7e-1	-2.3e-2	[18]
5s4d $^1D_2$	1771.48	1.9e-1	-1.8e-1	-4.4e-1	1.9e-3	[18]
5s7s $^1S_0$	417.71	2.5e-1	1.5e-1	-1.8e-1	-1.6e-2	[65]
$5p^2$ $^1D_2$	445.3	2.3e-1	1.4e-1	8.6e-2	-1.4e-3	[18]
$5s2$ $^1S_0$	689.46	1.5e-1	-1.3e-1	-2.6e-1	1.4e-2	[64]
5s5d $^1D_2$	494.49	6.1e-2	1.1e-2	8.0e-3	-1.2e-4	[18]
5s6s $^1S_0$	621.62	4.5e-2	9.3e-3	-1.6e-2	-9.8e-4	[18]
5s6d $^3D_2$	936.11	6.2e-3	7.8e-4	1.0e-3	-8.2e-6	[66]
5s6d $^3D_1$	936.54	3.6e-3	2.6e-4	-3.5e-4	1.4e-5	[66]
5s7d $^3D_2$	777.55	3.6e-3	1.1e-4	1.2e-4	-1.1e-6	[66]
5s8d $^3D_2$	711.14	2.4e-3	3.6e-5	3.6e-5	-3.8e-7	[66]
5s7d $^3D_1$	777.84	2.1e-3	3.6e-5	-3.9e-5	1.9e-6	[66]
5s8s $^3S_1$	850.84	1.6e-3	2.9e-5	-3.5e-5	1.6e-6	[66]
5s8d $^3D_1$	711.32	1.8e-3	2.0e-5	-2.0e-5	1.1e-6	[66]
5s9s $^3S_1$	743.89	9.7e-4	6.7e-6	-7.0e-6	3.5e-7	[66]
5s10s $^3S_1$	693.52	6.8e-4	2.7e-6	-2.7e-6	1.4e-7	[66]

Table 5.5: Contributions to the polarizabilities (scalar, vector, and tensor) of the excited state ($5s5p\,^3P_1$) in descending order of $|\alpha^s|$, for the different available transitions from [18, 64–66].
The atomic unit of electric dipole moment is 1 a.u. $= 8.4783536255(13) \times 10^{-30}\mathrm{C}\cdot\mathrm{m}$.
The atomic unit of polarizability is 1 a.u. $= 1.64877727436(50) \times 10^{-41}\mathrm{C}^2\cdot\mathrm{m}^2\cdot\mathrm{J}^{-1}$.

Chapter 6

Fluorescence of strontium atoms in a shallow lattice

6.1 Review on laser cooling of a trapped atom

We start this chapter concerning the fluorescence imaging and laser cooling of strontium atoms in an optical lattice by presenting a review of the development of laser cooling of single trapped particles and the imaging of atomic samples with single-atom resolution. This review will not be exhaustive but is instead a way to introduce the different concepts

relevant to our study and highlights the similarities with known techniques. We will also expose the peculiarities of our approach. After this review, we present the model used to describe the interaction of a trapped atom with a classical laser field. We then compare two distinct approaches used to solve the system's dynamics and, in particular, determine the number of scattered photons during the imaging sequence.

The two approaches that we use are a Monte Carlo wavefunction simulation and a rate-equation model. The rate equations are efficient in terms of computation times and are used to explore systematically the parameter space. It is also used to model the losses of atoms from the trap, this is with the photon number the second crucial parameter for the image processing, as losses of atoms during the imaging time will result in fluctuation of the number of photons per atom. The role of the Monte Carlo simulations is to validate the rate-equation appraoch which assumes that the coherences are in steady-state and are following adiabatically the populations.

The reasons to cool atoms in micro-traps mainly fall into two categories:

- We want to image those atoms *in situ*, that is, while they are still trapped. This means we want to induce light scattering, which will cause heating. This heating might lead to the atom escaping the trap and being lost or transferred to another neighboring trap.
- Some applications benefit from reducing the temperature in order to get more localized atoms; for instance, reducing the fluctuations on the inter-atomic distances in Rydberg atoms with tweezers arrays leads to better coherence times favorable for quantum computing protocols [74].

We should emphasize that cooling is not always required. For instance, if the traps are well resolved optically, only a few photons are required to detect an atom [75]. Another instance is when the traps are sufficiently deep to accommodate many recoils, for example, in [76, 77] with ytterbium and erbium quantum gas microscopes. Additionally, in some cases, molasses beams were already available in the region of the trapped atom(s) [78]; thus, using the available beams was an economical approach, more than an absolute necessity.

We will see that the imaging in our system will prove challenging since the imaging process can expel the atom very fast from the trap before it has had time to scatter enough photons. Those losses are induced by the differential polarizability between the ground and excited ($^3P_1$) state. We will see that the monochromatic single-beam scheme that we study in this chapter leads to marginal results compared to the expectation of the imaging system described in chapter 4. In the perspectives of this chapter, we give schemes that should enable us to overcome the limits of our method.

6.1.1 Review of laser cooling in microtraps

Nowadays, laser cooling of single particles has been applied to a variety of systems, including trapped ions [79], single trapped atoms [80], or nano-particles [81]. We will mainly restrict the scope of this discussion to the case of neutral atoms in micrometer-size traps. This includes atoms in optical tweezers and optical lattices.

6.1.1.1 Different regimes for laser cooling of trapped atoms

We start by describing the different relevant energy scales in the problem of single trapped atoms. Since we will discuss photon fluorescence and laser cooling, we must consider the natural linewidth of the transition Γ and the recoil energy from an absorption/emission event. The recoil energy is given by $E_{\text{rec}} = \hbar^2 k^2/2m$, where k is the wavevector of the absorbed/emitted photon, and m is the mass of the particle.[1] Additionally, the potential introduces trapping frequencies (from the harmonic approximation near its minimum) Ω_i, where i is the index running over the different principal axes of the trap.

From these parameters, we can construct three dimensionless parameters, $\xi = \hbar\Gamma/E_{\text{rec}}$, $\rho = \Omega/\Gamma$, and the Lamb-Dicke parameter η defined by:

$$\eta = \sqrt{\frac{E_{\text{rec}}}{\hbar\Omega}} = \frac{\pi a_0}{\lambda} \,, \tag{6.1}$$

where we omitted the i index, introduced $\lambda = 2\pi/k$ and $a_0 = \sqrt{2\hbar/m\Omega}$ the characteristic size of the harmonic oscillator wavefunction in the ground state. Note that if the atom is not in the motional ground state (6.1) should be corrected by a factor $\sqrt{2n+1}$ for a Fock state $|n\rangle$ representing a vibrational level of the trap, and $\sqrt{k_B T/\hbar\Omega}$ for a thermal state [82].

Each of these parameters has simple physical interpretations:

- The parameter $\xi = \hbar\Gamma/E_{\text{rec}}$ tells us if the recoil from one photon induces a Doppler shift that is sizeable compared to the linewidth of the transition. ξ is used to discriminate between narrow ($\xi \ll 1$) and broad ($\xi \gg 1$) transitions. The Brownian motion or the Fokker-Planck approaches to laser cooling are valid in the broad-transition limit. In contrast, in the narrow-transition limit, these break down, and the shift from a single scattering event must be considered [31].

- The ratio $\rho = \Gamma/\Omega$ will be big if the motion of the particle is slow compared to the radiative lifetime of the atom; that is, the atom will emit a photon on time scales for which no change in its velocity and position has time to occur. This situation is called by S. Stenholm [83] the "heavy-particle limit" for a particle with higher mass has reduced Ω. If, on the contrary, we have $\Gamma \leq \Omega$, the emission spectrum of the atom is modulated at frequency Ω and acquires sidebands. If $\Gamma \ll \Omega$, we enter the "resolved-sideband regime", where the spacing between adjacent sidebands is much greater than the linewidth of the resonance.

- The Lamb-Dicke parameter characterizes if the atom is well localized within a wavelength of the laser field ($\eta \ll 1$), which is called the Lamb-Dicke limit (LDL). The Lamb-Dicke parameter governs the number of sidebands contributing to the spectrum of the bound atom. More precisely, the number of sidebands will behave as $\mathcal{O}(\eta^2)$ [84]. This can be interpreted as follows, the bound atoms oscillate in the trap, it therefore has an oscillating velocity corresponding to an oscillating Doppler shift or in the rest frame of the atom a modulated laser spectrum. The typical velocities

[1] In all the discussion, the energy of the photon $\hbar\omega$ will be much greater than any other energy scale and will thus be irrelevant when comparing the different regimes.

Table 6.1: Limiting cases for a trapped atom interacting with a laser field.

	$\ll 1$	$\gg 1$
ρ	heavy-particle limit	resolved sidebands
η	Lamb-Dicke limit (LDL)	non-LDL

are on the order of $a_0\Omega$, the modulation of the Doppler shift is $ka_0\Omega\cos\Omega t$ giving rise to a modulation index on the order of the Lamb-Dicke parameter.

Since $\xi = \rho/\eta^2$, we will discuss the different regimes in terms of the resolved character of the sidebands (ρ) and the width of the modulated spectrum governed by η^2.The limiting cases are summarized in Table 6.1.

In the case where the trapping potentials for the two internal levels are different, there is an additional parameter to consider:

$$\alpha = \frac{\Omega_e}{\Omega_g} , \tag{6.2}$$

where the label g, e refers to the two internal states of the atom. The discussion of the effect of α will be treated as the last example of cooling processes. Until then, we will assume that $\Omega_g = \Omega_e$.

6.1.1.2 Categories of laser cooling for trapped atoms

Optical molasses

A first approach to laser cooling in optical microtraps is to use optical molasses. Historically, laser-cooled atoms were alkaline species; those molasses could thus resort to Doppler and sub-Doppler cooling mechanisms. This was the case for the first experiments on single trapped atoms in the team of P. Grangier [44, 78]. This technique was also used in 3D lattices [85], in quantum gas microscopes with bosonic species [45, 86], or for arrays of optical tweezers [87].

We will not describe here the sub-Doppler mechanisms since they are absent in bosonic strontium. For the case of Doppler cooling in a trap, the qualitative picture is essentially the same as in free space. For a red-detuned laser beam, the atom will preferentially absorb photons when its velocity is anti-aligned with the wavevector of the laser (for details on the semi-classical and quantum treatment, see [88]). Since the atom oscillates in the trap, its velocity will periodically change sign, so only one beam is required, as long as it has a non-zero projection on all the principal axes of the trap [89].[2]

This method has typically been used for broad transitions of alkaline atoms with a natural linewidth on the order of 1 MHz to 10 MHz. The resolved sideband limit is difficult to obtain with optical dipole traps (requiring MW/cm^2 of laser intensity [90]). Thus this method with a broad transition places those experiments on the heavy-particle-limit. The Lamb-Dick limit is more easily reached than the resolved sideband limit since the recoil

[2]This imposes that the trap *must not* be isotropic so that those axes are well-defined. In an isotropic trap, there will be heating in the plane orthogonal to the wavevector of the cooling laser.

energies are typically in the few kHz to tens of kHz range (for instance, see Table. II.1. of [31]). In the case where a narrow transition is available, Doppler cooling has been performed outside the heavy-particle limit, as in [91] with ytterbium in "shallow optical tweezers".

Sideband cooling

Another common approach is to use sideband cooling techniques. In alkaline atoms, this is implemented via a two-photon process linking two ground states by a Raman transition with narrow effective width. This can be implemented directly with the beams creating the ODT like in [19] or with additional beams which is more common (see the other references of this part). In the case of alkaline-earth-like atoms, this method can directly be implemented on the intercombination line as shown by [18, 59, 92] and is often called "single-photon sideband cooling".[3]

The sideband-cooling method requires that the experiment is performed in the resolved-sideband regime ($\Omega \gg \Gamma$) and is often applied in the Lamb-Dicke limit, although this second assumption is not mandatory as described in [93]. In the case of one ground state and one excited state labeled $|g, n\rangle, |e, n'\rangle$, where n and n' are the vibrational quantum numbers, the process is done in two steps:

1. The atom is resonantly excited from $|g, n\rangle \to |e, n-1\rangle$.[4]

2. When a spontaneous emission occurs, the matrix element for the transition is proportional to:
$$\langle n'| e^{ik_x x} |n\rangle \ , \tag{6.3}$$
where k_x is the wavevector of the emitted photon, and x is the position operator acting on the motional part of the state. Here, we restrict the discussion to the case of a 1D system with vibration along the x direction. In the Lamb-Dicke limit, the operator $e^{ik_x x}$ can be expanded in powers of $k_x a_0/2 = \eta$, and at first order, we are left with:
$$\langle n'| e^{ik_x x} |n\rangle = \langle n'|n\rangle + ik_x \langle n'| x |n\rangle + \mathcal{O}(\eta^2) \tag{6.4}$$
$$= \delta_{n',n} + i\eta \langle n'|a + a^\dagger|n\rangle + \mathcal{O}(\eta^2), \tag{6.5}$$
where we used the ladder operators to express the position operator. From (6.4), the spectrum of emission will consist of a strong line at the "carrier frequency" ($|g, n\rangle \leftrightarrow |e, n\rangle$) and two sidebands with lower intensities (by a factor $\sim \eta^2$) corresponding to the first Stokes (or red sideband) and anti-Stokes (blue sideband) lines of the system.

Such a cycle removes one quantum of vibration and is used as the cooling mechanism. Spontaneous emission transferring from n to n' with $n > n'$ leads to cooling, while the opposite situation with $n \leq n'$ causes heating. The cooling is thus a competition between

[3] This denomination might seem redundant since it is essentially the same as the sideband cooling for trapped ions. When discussing sideband cooling for strontium, we will not specify that it is "single-photon".

[4] Outside the LDL, one should replace $n-1$ by $n-m$ with $m = \mathcal{O}(\eta^2)$ [84], so that the spontaneous emission is mostly occurring towards states $|g, n'\rangle$ with $n' < n$.

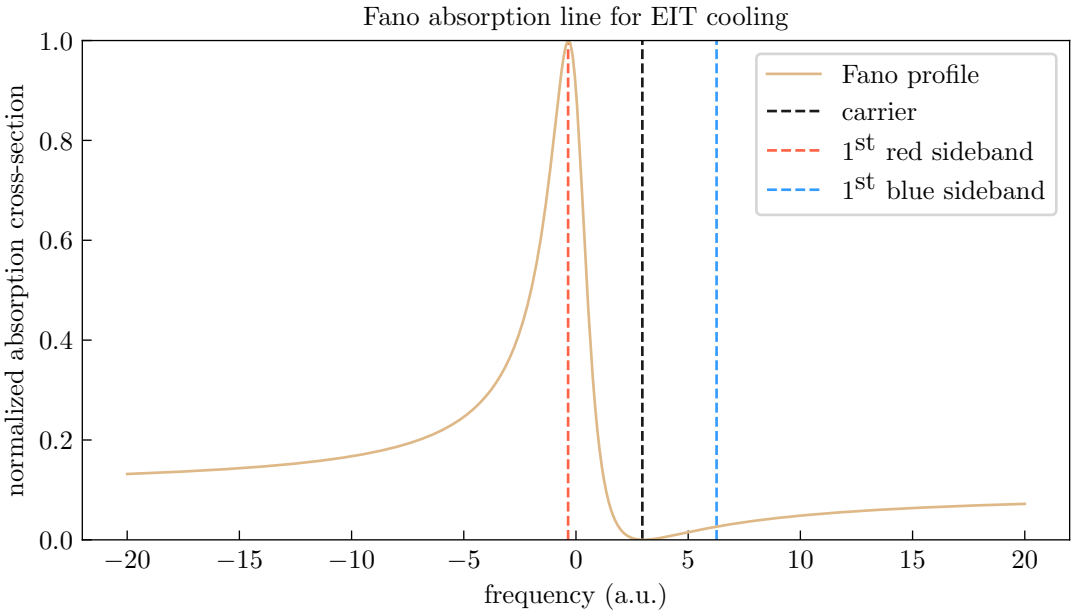

Figure 6.1: Fano profile normalized by its maximum, with Fano parameter $q = -3$ [103]. For EIT cooling, the resonance shape is chosen so that the first red sidebands coincide with the maximum of absorption, while the carrier is on the zero of the absorption and blue sidebands have smaller absorptions than their red counterparts.

the processes involving the red sidebands and processes involving the carrier or the blue sidebands.[5]

Sideband cooling has been used to cool atoms near the motional ground state in optical tweezers[6] [80, 94–96]. It is also used in lattice gases and microscope experiments to image the sample in several teams, including [59, 60, 76, 97, 98].

EIT cooling

EIT cooling (electromagnetically-induced transparency) can be seen as a refinement of the Raman sideband cooling. In this scheme, two lasers connect the two ground states of the atom to an excited state (Λ-configuration) resulting in quantum interference between the two paths to the excited state. In this situation, the absorption spectrum assumes a Fano-like profile which can be tailored to have a sharp maximum of absorption at the first red sideband frequency, while the carrier is on the zero of the Fano profile, and the blue sidebands have negligible absorption, as depicted in Figure 6.1. This scheme is described in [99, 100] and was implemented in the case of quantum gas microscopes with fermionic potassium ^{40}K [101, 102].

Differential polarizability and Sisyphus cooling

We now discuss what happens when the constraint $\Omega_g = \Omega_e$ is lifted. That is, in fact, the generic case; only for so-called "magic-wavelength traps" does this condition hold. When

[5] The spontaneous emission with $n = n'$ does not pump energy into the system along the x-axis but can still provide heating in the other directions of motion.

[6] At least along the axial directions where the trap is tighter.

$\Omega_g \neq \Omega_e$, the trapping potential becomes state-dependent, and a new cooling/heating mechanism manifests that falls into Sisyphus cooling category [18, 104–106].

Using a semi-classical picture, the atom oscillates in the trap for the ground state $U_g(x)$; when it is excited its potential energy will change by $\Delta E_p^{(abs)}(x) = U_e(x) - U_g(x)$ and when an emission happens, we similarly have $\Delta E_p^{(em)}(x') = U_g(x') - U_e(x')$. Neglecting for now the influence of the Doppler shift and recoil, we see that if we can favor absorption occurring at position x such that $\Delta E_p^{(abs)} + \Delta E_p^{(em)} < 0$, we would extract energy from the system over one cycle.[7] This selectivity can be achieved in the regime where $\Gamma \ll \Omega_{g,e}$, where we can tune the laser on resonance in a narrow (position) range. For instance, when $\Omega_e > \Omega_g$ we can tune the laser on resonance at $x = 0$; this leads to $\Delta E_p^{(abs)}(0) = 0$ and $\Delta E_p^{(em)}(x') \leq 0$ for all x'. This situation is referred to as "attractive Sisyphus cooling". In this situation, the atom will climb higher hills on its way up than on its way down.

The opposite case, $\Omega_g > \Omega_e$, turns out to be more challenging. It was claimed that this situation would not be amenable to efficient laser cooling [90]. However, it was later used in [18, 105, 106] even if the cooling of the atom near its motional ground state required a time-dependent detuning for the cooling laser. The semi-classical idea is similar to the attractive case, but instead of exciting near the trap's center, we need to excite at the edges of the trap. A detailed discussion of the semi-classical picture is included in Appendix D. As we will see in 6.3.4, a "vibrational resonance" increases the heating for the atoms with excited motional states.

6.2 Qualitative behavior in our configuration

6.2.1 Regime of parameters for our experiment

Now that we have described the panorama of common schemes used to laser-cool atoms in a optical microtrap, we summarize what regime of parameters we are going to work with. Let us summarize the energy scales for strontium when using the narrow transition at 689 nm:

- The natural linewidth of the transition $\Gamma_r = 2\pi \cdot 7.4\,\mathrm{kHz}$.
- The recoil energy is $E_{\mathrm{rec}} = 0.67\Gamma_r$, giving a contribution of $E_{\mathrm{rec}}/3 = 0.22\Gamma_r$ per axis assuming isotropic spontaneous emission. For non-isotropic emission, one should use the radiation patterns from (5.25) and (5.26).
- The trap frequencies are $\Omega_g^{(Z)} = 1.6\Gamma_r$, $\Omega_e^{(Z)} = 1.2\Gamma_r$ in the vertical direction, and $\Omega_g^{(X,Y)} = 9.1\Gamma_r$, $\Omega_e^{(X,Y)} = 7.4\Gamma_r$ in the horizontal directions. We used the axes defined in Figure 1.11.

Recasting these in terms of the dimensionless parameters from section 6.1.1.1, we obtain:

- $\Omega_e/\Omega_g = 0.8$
- $\eta_{g/e}^{(Z)} = 0.4/0.46$ and $\eta_{g/e}^{(X,Y)} = 0.15/0.17$ for the motional ground state. If we anticipate the results of the simulation (see Figure D.3), the typical effective temperatures

[7] Note that we do not have control on the position x' at which the spontaneous emission occurs.

that we obtain after one second are $k_B T_{eq} \sim 20\hbar\Gamma_r$, imposing a correction factor of $\sqrt{k_B T/\hbar\Omega} \sim \sqrt{10}$. The system will have Lamb-Dicke parameters ranging from about 0.5 to 1.4. Thus, the system is operated in the regime $\eta \sim 1$, even though the horizontal axes start near the LDL.

- $\rho_{g/e}^{(Z)} = 0.63/0.83$ and $\rho_{g/e}^{(X,Y)} = 0.11/0.14$. The horizontal axes are reasonably well in the resolved sideband regime, while the vertical axis is neither in the resolved-sideband limit nor in the heavy-particle limit.

6.2.2 Competing cooling mechanisms

We see that we will work outside the LDL and will not be in the resolved-sideband regime for the vertical axis (Z). The horizontal axes (X, Y) will be reasonably close to the resolved-sideband limit. We are thus considering an atypical case compared to the review of the previous sections. Note that the horizontal axes could be treated using the sideband cooling outside LDL proposed in [84].

For the vertical axis, we expect to have either Doppler or repulsive Sisyphus cooling (see the previous section). In fact, both mechanisms are relevant to our configuration. A discussion on the nature of the cooling mechanisms in the trap is presented in Appendix D.

As we will see in the simulations, those processes are insufficient to keep the atom trapped at the bottom of its potential well. Over time, the atom will slowly heat until it reaches the region where the vibrational resonance appears. Once the resonance has been crossed, the heating will get stronger, and the atom will eventually be lost. In the remainder of this chapter, we will try to find a range of parameters for which the atom scatters enough photons before being expelled from the trap.

6.2.3 Impact of the temperature on the imaging performances

The impact of the heating of the atom during the imaging time is twofold. First, the losses imply a maximum exposure time for the pictures, limiting the amount of fluorescence collected on the camera. Another issue is that as temperature increases, the spatial distribution of the atom spreads. Since we work with a high numerical aperture, a spread of the source in the direction of the optical axis will introduce blur in the image due to defocus. Assuming a temperature of $20\hbar\Gamma_r/k_B$, the extension along the optical axis will be of 0.4 µm. The depth of focus DOF of the microscope determined by the numerical aperture (NA = 0.6) is:

$$\mathrm{DOF} \approx \frac{c}{\mathrm{NA}} \approx 0.9\,\mu\mathrm{m} \tag{6.6}$$

where c characterizes the geometrical size of the blur tolerated for our system. We set $c = 532$ nm so that the spot caused by the defocus has a size at most on the order of the lattice spacing. We see that depending on the temperatures in the system, the limiting factor for the optical resolution of our microscope might be the delocalization of the atoms due to their temperature. In particular, increasing the numerical aperture of our system, without first taking care of the temperature of the atoms in the lattice, would not lead to significant improvements of the resolution.

6.3 Light-matter interaction for an atom in a state-dependent trap

In this section, we present the formalism that will be used to describe the interaction of a single trapped atom with the laser field during imaging. We will summarize the approximations performed to describe the internal and external state of the atom and discuss how we model the coupling between the light and the atom.

6.3.1 State basis

6.3.1.1 Internal state of the atom

As discussed in Chapters 4 and 5, we will use the $^1\mathrm{S}_0 \leftrightarrow {}^3\mathrm{P}_1$ transition to image the atoms. We can isolate the $m = 0$ state of $^3\mathrm{P}_1$ by introducing a bias magnetic field to lift the degeneracy between the Zeeman sublevels. The atom's internal state will thus be described by two levels $\{\left|5\,\mathrm{s}^2\ {}^1\mathrm{S}_0, \mathrm{m}{=}0\right\rangle, \left|5s5p\ {}^3\mathrm{P}_1, \mathrm{m}{=}0\right\rangle\}$ that will be referred to as $\{|g\rangle, |e\rangle\}$ in what follows. Approximating our atom by a two-level system will be a consistent description as long as the Zeeman splitting is much greater than the width of the vibrational manifolds ($\sim 1\,\mathrm{MHz}$) for each value of m (see Figure 6.14); so that we can have a near-resonant coupling to a manifold of given m without coupling to the other.

6.3.1.2 Motional state of the atom

We approximate the potential corresponding to one lattice site by a 3D harmonic potential (*cf.* 5.2.4). The motional state of the atom will be written in the Fock basis of that harmonic trap. Since the polarizabilities for the two internal states are different, so are the potentials. This implies that for a given set of vibrational quantum numbers (n_x, n_y, n_z), the associated wavefunction still depends on the internal state. The state bases for the motional degrees of freedom will then be:[8]

$$\{|n_x, n_y, n_z\rangle_s \,|s = g, e; (n_x, n_y, n_z) \in \mathbb{N}^3\}\,, \tag{6.7}$$

where the subscript is there to remind us whether we are using the representation in the basis linked to the ground or excited state. The unitary transformation mapping one basis onto the other can be expressed using a squeezing operator [90]:

$$S^{(i)}(r^{(i)}) = \exp\left(\frac{r^{(i)}}{2}(a_g^{(i)2} - a_g^{(i)\dagger 2})\right) \qquad (i = x, y, z), \tag{6.8}$$

$$S = S^{(x)} \otimes S^{(y)} \otimes S^{(z)}, \tag{6.9}$$

where $a_g^{(i)}$, $a_g^{(i)\dagger}$ are the annihilation and creation operators acting on the subspace i and:

$$r^{(i)} = \mathrm{sign}(\Omega_e^{(i)} - \Omega_g^{(i)})\,\mathrm{arccosh}\left(\frac{1}{2}\frac{\Omega_g^{(i)} + \Omega_e^{(i)}}{\sqrt{\Omega_g^{(i)}\Omega_e^{(i)}}}\right), \tag{6.10}$$

[8] This infinite basis will require the introduction of a cut-off to capture some physical features or for numerical implementation. We will restrict the number of excitations each direction can support by removing the harmonic levels above the trap's depth in the corresponding direction.

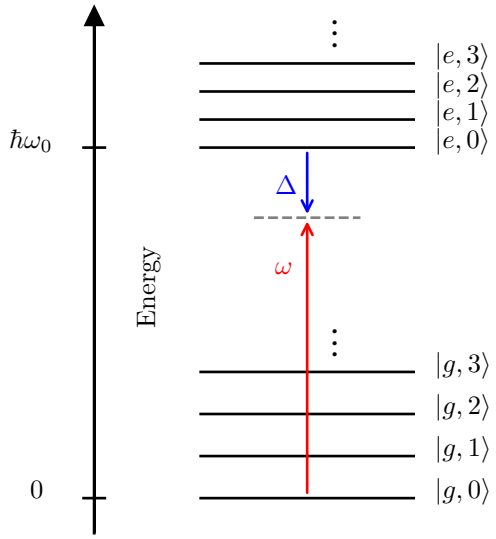

Figure 6.2: Level diagram of the two-level system coupled to a laser field of angular frequency ω and detuning δ from the $|g,0\rangle \leftrightarrow |e,0\rangle$ transition. To simplify the picture only one vibration number is displayed, and the zero-point energies were removed. Note that ω_0 is not the resonace of the free atom, it includes the Zeeman shift (if any) and the lightshift at the center of the trap.

where we have added the sign function so that the r's are positive when $\Omega_e > \Omega_g$, that is, when we want to squeeze the position representation of the wavefunctions. Conversely, when $\Omega_e < \Omega_g$, r is negative, giving rise to anti-squeezing.[9] The link between the bases is thus given by:

$$|\vec{n}\rangle_e = S\,|\vec{n}\rangle_g\,, \tag{6.11}$$

with the short-hand notation $|\vec{n}\rangle_s = |n_x, n_y, n_z\rangle_s$.

6.3.1.3 Total state

The state of the atom will be represented by the tensor product of the internal and external basis, namely, our Hilbert space will be:

$$\mathcal{H} = \text{span}\{|s, n_x, n_y, n_z\rangle\,|s = g, e; (n_x, n_y, n_z) \in \mathbb{N}^3\}\,, \tag{6.12}$$

where we dropped the i subscript from (6.7), as the internal state is already specified by the $|i\rangle$ part of the state. In the following, we will write this index only when we decompose the state corresponding to an excited atom in the basis of the ground-state wavefunctions.

6.3.2 Hamiltonian in the RWA

In this part, we describe the coherent coupling of the atom to an incident laser field. The Hamiltonian for the bound atom in the absence of the laser field is:

[9] We could also have kept the definition of r from [90] without the sign, but we would have needed to replace S with $S^\dagger$ when $\Omega_e < \Omega_g$. Those two choices are equivalent to the definition (6.8): $S(r)^\dagger = S(-r)$.

$$\mathcal{H}_{\text{at}} = \sum_{\substack{\vec{n}=(n_x,n_y,n_z)\\ i=x,y,z}} \hbar\Omega_i^{(g)}\left(n_i+1/2\right)|g,\vec{n}\rangle\langle g,\vec{n}| + \left[\hbar\Omega_i^{(e)}\left(n_i+1/2\right)+\hbar\omega_0\right]|e,\vec{n}\rangle\langle e,\vec{n}|\,, \quad (6.13)$$

where $\left(\Omega_x^{(g,e)},\Omega_y^{(g,e)},\Omega_z^{(g,e)}\right)$ are the trap frequencies for the internal states g and e, and $\hbar\omega_0$ is the energy of the atom at the center of the trap (including the Zeeman shift when $m \neq 0$ and the lightshift). The level diagram of our configuration is summarized for the 1D case in Figure 6.2.

We will consider an electric field:

$$\vec{E} = \frac{\mathcal{E}_0}{2} e^{i\vec{k}\cdot\vec{r}-i\omega t}\vec{u} + \text{h.c.}, \quad (6.14)$$

with $\vec{u}$ the polarization vector.

The coupling of the atom to the field is given by:

$$\mathcal{H}_{\text{drive}} = -\vec{d}\cdot\vec{E} \quad (6.15)$$

$$\begin{aligned}\langle e,\vec{m}|\,\mathcal{H}_{\text{drive}}\,|g,\vec{n}\rangle &= -\frac{\mathcal{E}_0}{2}e^{-i\omega t}\,\langle e|\,\vec{d}\cdot\vec{u}\,|g\rangle\;{}_e\langle\vec{m}|\,e^{i\vec{k}\cdot\vec{r}}\,|\vec{n}\rangle_g \\ &\quad - \frac{\mathcal{E}_0^*}{2}e^{i\omega t}\,\langle e|\,\vec{d}\cdot\vec{u^*}\,|g\rangle\;{}_e\langle\vec{m}|\,e^{-i\vec{k}\cdot\vec{r}}\,|\vec{n}\rangle_g\end{aligned} \quad (6.16)$$

To obtain a time-independent Hamiltonian (and remove the zero-point energies), we perform the following unitary transform using:

$$R(t) \;=\; \sum_{\vec{n}}\left[\prod\exp\left(i\frac{\Omega_i^{(g)}}{2}t\right)\right]|g,\vec{n}\rangle\langle g,\vec{n}| \;+\; \left[\prod\exp\left(i\frac{\Omega_i^{(e)}}{2}t\right)\right]e^{i\omega t}\,|e,\vec{n}\rangle\langle e,\vec{n}| \quad (6.17)$$

Then performing the rotating-wave approximation [72], the time evolution of the system is governed by the new Hamiltonian $\tilde{\mathcal{H}}$:

$$\begin{aligned}\tilde{\mathcal{H}} &= R(t)\mathcal{H}R(t)^\dagger - i\hbar\partial_t R(t)^\dagger \\ &= \sum_{\vec{n},i}\hbar\Omega_i^{(g)}n_i\,|g,\vec{n}\rangle\langle g,\vec{n}| + \hbar\Omega_i^{(e)}n_i\,|e,\vec{n}\rangle\langle e,\vec{n}| \\ &\quad - \sum_{\vec{n}}\Delta\,|e,\vec{n}\rangle\langle e,\vec{n}| \\ &\quad - \sum_{\vec{n},\vec{m}}\frac{\mathcal{E}_0}{2}\,\langle e|\,\vec{d}\cdot\vec{u}\,|g\rangle\;{}_e\langle\vec{m}|\,e^{i\vec{k}\cdot\vec{r}}\,|\vec{n}\rangle_g\,|e,\vec{m}\rangle\langle g,\vec{n}| + \text{h.c.}\,,\end{aligned} \quad (6.18)$$

where $\mathcal{H} = \mathcal{H}_{\text{at}} + \mathcal{H}_{\text{drive}}$, and $\Delta = \omega - \omega_0$ is the detuning from atomic resonance. In the following, we will omit the tilde on $\mathcal{H}$ to keep the notation reasonably simple.

6.3.3 Spontaneous emission

In order to model the spontaneous emission, we introduce "collapse operators" that will model an event of spontaneous emission on the $|e,\vec{m}\rangle \rightarrow |g,\vec{n}\rangle$ transition. Since the

photon can be emitted in all directions of space, we could introduce, in principle, two operators per direction of emission (for the two polarization states associated to each direction). This is not practical for numerical implementation. It is also not necessary, we only want to extract photon fluxes since the emission pattern is fixed by the magnetic field and the choice of the transition (see chapter 5). Therefore, we will instead compute averaged operators, where the average will be taken on the orientations, weighted by the emission pattern (5.29). We introduce one operator per transition from $|e, \vec{m}\rangle$ to $|g, \vec{n}\rangle$:

$$C_{\vec{m}\to\vec{n}} = \sqrt{\gamma_{\vec{m}\to\vec{n}}}\,|g,\vec{n}\rangle\langle e,\vec{m}|\ , \tag{6.19}$$

$$\gamma_{\vec{m}\to\vec{n}} = \Gamma_r \iint \mathrm{d}^2\Omega\, f_q(\Omega)\,|{}_g\langle\vec{n}|\, e^{i\vec{k}(\Omega)\cdot\vec{r}}\,|\vec{m}\rangle_e\,|^2\ , \tag{6.20}$$

where $\mathrm{d}^2\Omega = \sin\theta\,\mathrm{d}\theta\,\mathrm{d}\phi$ denotes the solid angle element, and $\gamma_{\vec{m}\to\vec{n}}$ gives the rates of the associated collapse operators (see, for instance, [107]). Summing over $\vec{n}$, we recover the decay rate of the untrapped excited state Γ_r from the fact that the f_q's are normalized to 1 (see section 5.2.2.1). These operators will be added to the Hamiltonian as an imaginary part, introducing decay from $|e, \vec{m}\rangle \to |g, \vec{n}\rangle$ of the form:

$$-i\frac{\hbar\,\gamma_{\vec{m}\to\vec{n}}}{2}C^\dagger_{\vec{m}\to\vec{n}}C_{\vec{m}\to\vec{n}}. \tag{6.21}$$

6.3.4 Losses and "vibrational resonances"

The model we presented in this section relies on the harmonic approximation of the trap, with a truncation of the state basis introduced to model the finite depth of the trap. For those approximations to remain valid, the atoms should stay in reasonably low-lying states. Therefore, we must check that the results of our simulations do not violate this harmonic hypothesis. For the Monte Carlo simulations, we verified that the population in the highest 10 % vibrational levels stays below 10^{-3}. This criterion is arbitrary and is there as a warning. For the rate-equation model, we introduced a loss term for the highest levels of the trap. This loss term is an *ad hoc* model of the losses due to tunneling to the neighboring lattice sites or expulsion from the trap.

Intuitively, a good criterion to prevent losses is having a temperature smaller than the trap depth. However, due to the "vibrational resonances" we mentioned previously, an atom can, in some cases,[10] find a "shortcut" to the top of the trap and be lost even when the temperature is low. Those resonances arise because the spacing between the vibrational levels is smaller in the excited manifold than in the ground one ($\hbar\Omega_e < \hbar\Omega_g$). Therefore at a given detuning, there exists a vibration number n_{res} such that some $|g, n\rangle$'s with $n > n_{\mathrm{res}}$ are close to resonance with $|e, n'\rangle$ with $\Delta n = n' - n > 0$. This means the levels above $|g, n_{\mathrm{res}}\rangle$ will predominantly be transferred to excited states with more motional energy. This effect is depicted in Figure 6.3. Note that the effect escalates since Δn is an increasing function of n. This phenomenon implies that we must compare the temperature with the resonance's position or with the trap depth, depending on which one is smaller. Also, note that this resonance is an indicative threshold above which the situation gets dangerous for the atom; it is not an effect localized in some small region of the spectrum.

[10] More precisely, this happens when the n_{res} is smaller than the maximum number of levels in the trap.

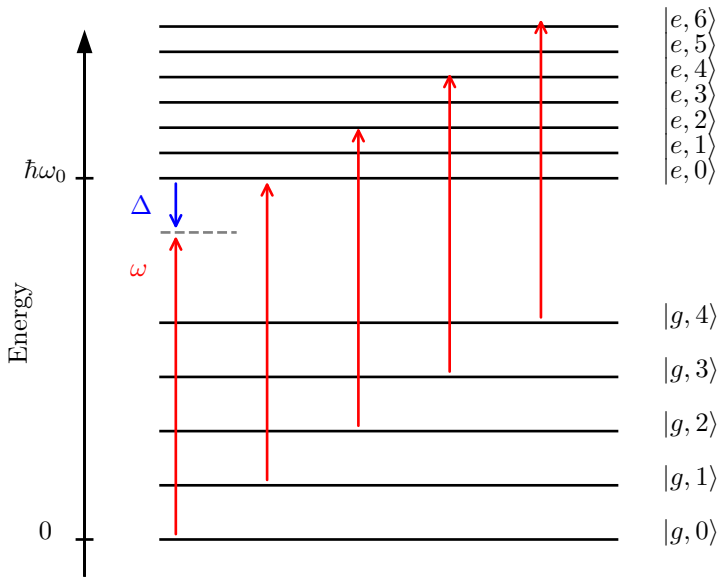

Figure 6.3: Schematic representation of the escalation of energy transfer due to $\Omega_e < \Omega_g$. The red arrows mark the laser coupling the electronic ground states level $|g,n\rangle$ to the excited electronic manifold levels $|e,m\rangle$. We see that as n is increased, the level $|g,n\rangle$ is coupled (quasi) reasonantly to levels with higher value of m. With a vibrational resonance occuring at $n = 2$ in this exaggerated situation.

6.4 Monte Carlo wavefunction simulations

In this section, we describe the implementation used to compute the dynamics of a trapped atom in the presence of a near-resonant laser field using the Monte Carlo wavefunction (MCWF) approach. This approach is described in detail in [107, 108]. Here, we describe the coupling to the environment with the formalism of collapse operators. The reason is that we used the QuTiP (Quantum Toolbox in Python) python library [109], where the solvers for time dynamics are written in a formalism resembling that of the Lindblad equation.

6.4.1 Principle of the method

The evolution of the system is represented by a Hermitian part of $\mathcal{H}$, responsible for the coherent evolution of the driven system, and an anti-Hermitian part expressed using collapse operators $C_{\vec{m}\to\vec{n}} = \sqrt{\gamma_{\vec{m}\to\vec{n}}}\,|g,\vec{n}\rangle\langle e,\vec{m}|$ to model spontaneous emission. The effective

Hamiltonian governing the evolution of the system coupled to the environment is thus:

$$\mathcal{H}_{\text{eff}} = \mathcal{H} - i\frac{\hbar}{2}\sum_{\vec{m},\vec{n}} \gamma_{\vec{m}\to\vec{n}} C^{\dagger}_{\vec{m}\to\vec{n}} C_{\vec{m}\to\vec{n}} \tag{6.22}$$

$$= \mathcal{H} - i\frac{\hbar}{2}\sum_{\vec{m}} |e,\vec{m}\rangle\langle e,\vec{m}| \sum_{\vec{n}} \gamma_{\vec{m}\to\vec{n}}$$

$$= \mathcal{H} - i\frac{\hbar\Gamma_r}{2}\sum_{\vec{m}} |e,\vec{m}\rangle\langle e,\vec{m}| \ . \tag{6.23}$$

We can see from (6.22) and (6.23) that introducing collapse operators is equivalent to giving an imaginary part to the energy of the excited states. Due to this imaginary part, the norm of the quantum state evolving under $\mathcal{H}_{\text{eff}}$ will decay in time. The decay rate is given by:

$$\langle\psi(t+\delta t)|\psi(t+\delta t)\rangle = \langle\psi(t)| e^{i\frac{\mathcal{H}^{\dagger}_{\text{eff}}}{\hbar}\delta t} e^{-i\frac{\mathcal{H}_{\text{eff}}}{\hbar}\delta t} |\psi(t)\rangle \tag{6.24}$$

$$= 1 - \delta t\,\Gamma_r \sum_{\vec{m}\to\vec{n}} \langle\psi(t)| C^{\dagger}_{\vec{m}\to\vec{n}} C_{\vec{m}\to\vec{n}} |\psi(t)\rangle + \mathcal{O}(\delta t^2) \tag{6.25}$$

$$= 1 - \sum_{\vec{m}\to\vec{n}} \delta p_{\vec{m}\to\vec{n}} + \mathcal{O}(\delta t^2) \tag{6.26}$$

$$= 1 - \delta p \ , \tag{6.27}$$

where i is a label representing all the $\vec{m}\to\vec{n}$ transitions. In our case, we have:

$$\delta p_{\vec{m}\to\vec{n}} = \gamma_{\vec{m}\to\vec{n}} \|\langle e,\vec{m}|\psi(t)\rangle\|^2 \delta t \ . \tag{6.28}$$

The probability of emitting a photon on the transition $\vec{m}\to\vec{n}$ is thus controlled by the rate $\gamma_{\vec{m}\to\vec{n}}$ that is the averaged matrix element in (6.20) and the population of the state from which the photon is emitted. This decay is used to select the random times at which the quantum jumps occur according to the following procedure:

1. Start from a *normalized* state $|\psi(t_i)\rangle$ and draw uniformly two random numbers $r_1, r_2 \hookrightarrow \mathcal{U}([0,1])$. r_1 will be used to determine the time at which the system undergoes a quantum jump, and r_2 will be used to determine which $\vec{m}\to\vec{n}$ transition caused the jump.

2. Evolve $|\psi(t_i)\rangle$ according to the Schrödinger equation with $\mathcal{H}_{\text{eff}}$ until t_{jump} such that $\langle\psi(t_{\text{jump}})|\psi(t_{\text{jump}})\rangle = r_1$. At $t = t_{\text{jump}}$, a quantum jump occurs.

3. Select the collapse process that caused the jump with the following rules:

   The n^{th} jump occurred if and only if n is the smallest integer verifying:

   $$\sum_{i=0}^{n} \mathbb{P}_i(t_{\text{jump}}) \geq r_2 \ , \tag{6.29}$$

   where we defined the probability of each jump $\mathbb{P}_i(t)$ as:

   $$\mathbb{P}_i(t) = \frac{\langle\psi(t)| C^{\dagger}_i C_i |\psi(t)\rangle}{\sum_k \langle\psi(t)| C^{\dagger}_k C_k |\psi(t)\rangle} = \frac{\delta p_i}{\delta p} \ . \tag{6.30}$$

4. Use the selected C_n to project the state to a new normalized state according to:

$$\left|\psi(t_{\text{jump}}^{+})\right\rangle = \frac{C_n \left|\psi(t_{\text{jump}}^{-})\right\rangle}{\left\|C_n \left|\psi(t_{\text{jump}}^{-})\right\rangle\right\|} , \tag{6.31}$$

where $\left|\psi(t_{\text{jump}}^{\pm})\right\rangle$ are the states just before $(-)$ or after $(+)$ the projection. We can then use this new state as a starting point and go back to step 1.

This protocol applied from t_i to t_f the final time gives a single "quantum trajectory". To obtain the "typical" behavior of the system, one must average the relevant observables over many trajectories.

6.4.2 Computation of the relevant operators

We will discuss the technicalities of the operator implementation using the QuTiP framework in this section. To keep the discussion simple, we will only describe the case of a two-level atom in a 1D harmonic potential, but the code can be operated with an arbitrary dimension.

6.4.2.1 Choice of units

For those simulations, we work in "natural units" for our system: we work with $\hbar \equiv 1$, and all energies (or equivalently angular frequencies) will be measured in units of $\Gamma_r = 2\pi \cdot 7.4\,\text{kHz}$, the unit of times will thus be $1/\Gamma_r$. The length unit is fixed by the norm of the wavevector of the laser beam $k = 2\pi/\lambda \equiv 1$.

6.4.2.2 Generation of the state basis

To generate states with QuTiP, we use the functions `basis` (or equivalently `fock`) and `tensor` to do the tensor products. To implement the spatial degree of freedom numerically, we need to introduce a cut-off in our basis, restricting the number of excitation n to values smaller than $n_{\text{max}}^{(g,e)} = \lceil \Delta E_{\text{depth}}/\hbar\Omega_{g,e} \rceil$. Since the polarizabilities in the ground and excited states are different, we might be tempted to introduce a different dimensions for the vibrational manifolds corresponding to each internal state. This would result in state vectors of different dimensions, which is not supported by the library. Instead, we will generate states with up to $n_{\text{max}} = \max_{g,e} n_{\text{max}}^{(g,e)}$ and conjugate all operators by the projector on the "physical basis":

$$P_{\text{phys}} = \sum_{n=0}^{n_{\text{max}}^{(g)}} |g,n\rangle\langle g,n| + \sum_{m=0}^{n_{\text{max}}^{(e)}} |e,m\rangle\langle e,m| , \tag{6.32}$$

$$\mathcal{O}_{\text{phys}} = P_{\text{phys}} \mathcal{O} P_{\text{phys}} , \tag{6.33}$$

where $\mathcal{O}$ is any operator defined "naively" on the space of dimension $n_{\text{max}} \times n_{\text{max}}$ and $\mathcal{O}_{\text{phys}}$ is the same operator but projected on the basis of interest of dimension $n_{\text{max}}^{(g)} \times n_{\text{max}}^{(e)}$. This also allows for artificially increasing the size of the state space so as to reduce the truncation errors in the computation of the matrix elements. In any case, we must be careful with the highest energy states since they might be out of the validity range for the

harmonic approximation. In those states, there might be anharmonic effects of the $\sin^2$ potential, risks of tunneling to other sites, or excitations into the continuum. All these effects are neglected in our model. We will therefore discard as "unphysical" any result with non-negligible populations in the high-lying energy states.

6.4.2.3 Hamiltonian

The diagonal part of the Hamiltonian is straightforward to implement. Indeed, QuTiP provides a number operator using `num`, identity with `qeye`, and projector on a state with `ket.proj()`. These allow for the implementation of the diagonal part of the Hamiltonian from (6.18).

The off-diagonal part of the Hamiltonian given in (6.18) requires the computation of matrix elements of $e^{i\vec{k}\cdot\vec{r}}$ between harmonic-oscillator eigenstates belonging to different bases, namely the factors ${}_e\langle\vec{m}|e^{i\vec{k}\cdot\vec{r}}|\vec{n}\rangle_g$. Different approaches are available to compute those matrix elements:

- Analytical formulas can be found in [110]. Implementing these formulas turned out to be quite inefficient in terms of computation times, so it was discarded.

- Since the wavefunctions ψ_n of the harmonic oscillator are known analytically, we can also evaluate numerically the integrals directly:

$$ {}_e\langle\vec{m}|e^{i\vec{k}\cdot\vec{r}}|\vec{n}\rangle_g = \prod_{i=X,Y,Z} \int \mathrm{d}x_i \, \psi_{m_i}^{(e)*}(x_i) e^{ik_i x_i} \psi_{n_i}^{(g)}(x_i) \, , \tag{6.34}$$

  where the product runs over the axes of the lattice, and x_i represent the coordinates along (X, Y, Z). The superscripts g, e is introduced to emphasize that the characteristic length of the two wavefunctions are different, that is, $a_0^{(g,e)} = \sqrt{\frac{\hbar}{m\Omega_{g,e}}}$ where m is the mass of the atom. This approach is satisfactory and not too time-consuming if implemented by considering the sampling and range of integration carefully, using the known form of the wavefunctions. [11]

- One approach would be to evaluate (6.34) in momentum space using the fact that $e^{ik_i x_i}$ is acting like a displacement operator along the momentum direction p_i. That is simply stating that the emission of a photon with wavevector $\vec{k}$ communicates a recoil of $-\hbar\vec{k}$ to the atom.

- Using the matrix forms of the operators, provided by QuTiP, we can directly evaluate those matrix elements by matrix multiplication. We can compute the product as $\bigotimes_i S^{(i)\dagger} e^{-ik_i x_i}$, using the operators `squeeze` and `pos` along with the matrix exponentiation `expm()`. An alternative would be to compute the product $\bigotimes_i S^{(i)\dagger} D(-ik_i/\sqrt{2})$ where $D(\alpha) = \exp\left(\alpha a^\dagger - \alpha^* a\right)$ [110] is the displacement operator implemented *via* `displacement`.

[11] $\psi_n^{(s)}$ has n nodes and a typical size of $a_0^{(s)}\sqrt{n+1}$

6.4.2.4 Collapse operators

The calculation of the collapse operators is similar to that of the off-diagonal part of the Hamiltonian, with the additional complexity that the wavevector for spontaneous emission is not fixed. The evaluation of the rate $\gamma_{\vec{n}\to\vec{m}}$ from (6.20) is done by numerical integration over the angular variables of the matrix elements of $\bigotimes_i S^{(i)\dagger} D(-ik_i/\sqrt{2})$ described in the previous section:

$$\gamma_{\vec{m}\to\vec{n}} = \Gamma_r \iint \mathrm{d}^2\Omega\, f_q(\Omega)\, |{}_g\langle\vec{m}|\bigotimes_i S^{(i)\dagger} D(-ik_i(\Omega)/\sqrt{2}) e^{i\vec{k}(\Omega)\cdot\vec{r}} |\vec{n}\rangle_g\,|^2 \tag{6.35}$$

Note that the choice of the emission pattern for the spontaneous emissions has an impact on the heating rates in the different axes of the lattice, as it can favor or suppress certain directions of emission.

The use of the MCWF algorithm has the advantage of providing information about spontaneous emission events. This grants access to the collapse operators responsible for the emission event in case we want to extract the emission spectrum. It also gives access to the number of scattered photons as a function of time since we can access the times of collapses for each simulated trajectory.

6.4.3 Results for the MCWF simulations

In this section, we present the results obtained with the Monte Carlo wavefunction approach. First, we compute the dynamics in 2D (one horizontal axis and the vertical one), with short evolution time, with a truncated basis.[12] We observe that the system acquires an effective temperature that is about the same for both axes. Then, we compute the dynamics at longer times in 1D (vertical axis), assuming that the temperatures along all the axes keep equilibrating with each other, allowing us to infer the state in the horizontal axes from that of the vertical axis. We check in section 6.5.3.2 the effective temperature in the vertical direction is not too high compared to the horizontal trap depth.

As a reminder, we aim at obtaining 2000 thousand photons ($\sim$ 200 photo-electrons) per atom in times on the order of 1 second, while maintaining the losses of atoms sufficiently low that we can neglect them. In particular, we want to have negligible population in the highest levels of the trap. Obtaining this photon number in 1 second corresponds to having a popualtion in the electronic excited state of around 5 %.

6.4.3.1 Results for short-time dynamics in 2D

In Figure 6.4, we present population histograms for the vibrational levels in the vertical and horizontal directions obtain from the Monte Carlo simulations in two dimensions (the vertical direction and one of the horizontal directions). The parameters used to obtain those results are the following:

- Hilbert-space dimension: $2 \times 60 \times 11$ (internal×vertical×horizontal),
- the system is initialized to the absolute ground state $|g, 0, 0\rangle$,

[12] The truncation allows obtaining reasonable computation times. As we will see, the effect of the losses is linked to the highest part of the trap, and only appears at long time scales. The truncation does not have too much impact here, as we focus on short time evolution.

- $\Omega_g^{(V,H)} = (1.6, 10.0)\Gamma_r$; $\Omega_e^{(V,H)} = (1.3, 7.8)\Gamma_r$ where we noted $V = Z$ and $H = X$ or Y,
- $I = 800 I_{\text{sat}}$, $\Delta = -45\Gamma_r$, corresponding to a saturation parameter:

$$s = \frac{I}{I_{\text{sat}}} \frac{1}{1 + 4\Delta^2/\Gamma_r} = 0.1\,. \tag{6.36}$$

  We use detunings that are quite high to have a vibrational resonance that corresponds to sufficiently high levels to avoid accumulation of populations in the highest levels of the trap. To compensate for this high detuning, have to use high intensities to obtain sufficiently high saturation parameters.
- $t \in [0, 7\,\text{ms}]$,
- excitation laser oriented along $\theta = 54°$ and $\phi = \pi/4$, where θ and ϕ are the spherical angles in the lattice basis (X, Y, Z)
- the emission was considered isotropic for simplicity,[13]
- the averages are taken over $n_{\text{traj}} = 500$ trajectories.
- the collapse operators with a rate inferior to $10^{-2}\Gamma_r$ have been neglected.
- the vibrational resonances in this configuration are located at $n = 15$ for the horizontal direction, which is above the trap depth (11 levels). In contrast, in the vertical direction, we have the resonance at $n = 127$. This means that we should not have problems from the horizontal direction, but we should be careful with the vertical axis.

The state space representing the vibrational motion in the vertical direction was truncated, using 60 levels instead of 150, to reduce computation time. After an evolution of 7 ms, the population in the excited state is 4.7 %, corresponding to 2200 photons (200 photoelctrons) per second. This value of the electronic excited state population is reach after a few Γ_r^{-1}, corresponding to a fast transient, then the dynamics slows down and we observe a slow increase of the vibrational energy. We assign an effective temperature to the system by fitting the decay of the populations in the vibrational levels as a function of energy. Examples of such fit are displayed in figure 6.7 for the case of the vertical direction. The temperatures along the two directions are similar. We observed that this is a generic behavior. Since the effective temperatures in the different axes will be on the same order, we can assess if a set of parameters will populate or not the highest vibrational states of the horizontal lattice by looking only at the dynamics in the vertical lattice.

6.4.3.2 Results of the long-time dynamics in 1D

The result presented in this section are obtained with the following parameters:

- Hilbert-space dimension: 2×150
- the system is initialized to the absolute ground state $|g, 0\rangle$,
- $I = 800 I_{\text{sat}}$, $\Delta = -45\Gamma_r$, corresonding to a saturation parameter of $s = 0.1$, $t \in [0, 270\,\text{ms}]$,
- excitation laser oriented along $\theta = 54°$, $\phi = \pi/4$,
- the emission was considered isotropic for simplicity

[13] This choice is made for the sake of simplicity. Changing this might lead to changes in the effective temperature in the different axes.

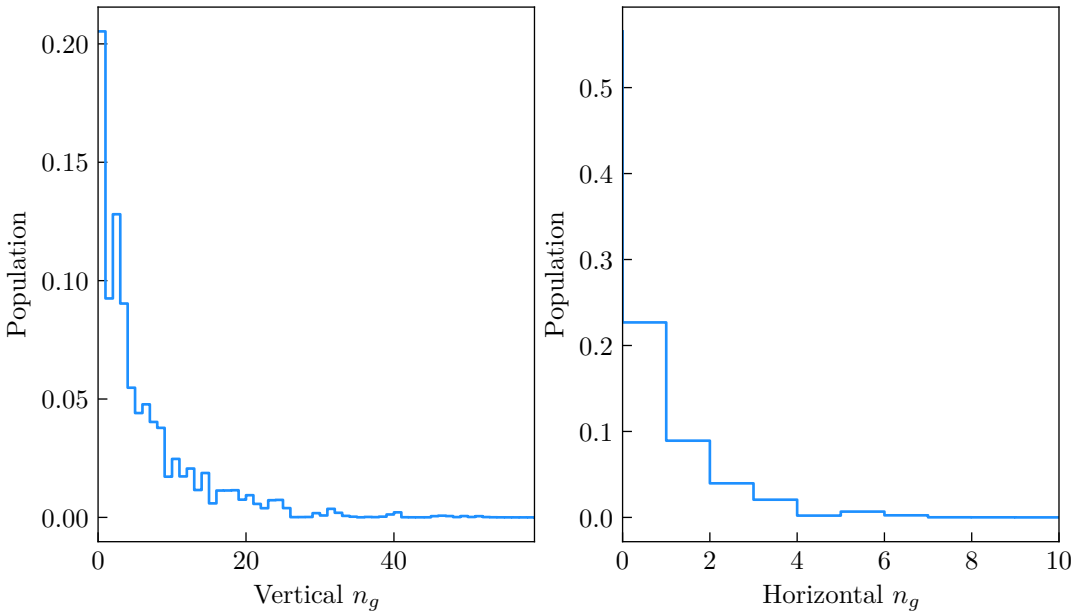

Figure 6.4: Populations in the vibrational states of the electronic ground state manifold in the vertical direction (left panel) and horizontal direction (right panel) obtained from the Monte Carlo simulation in 2D case. The populations are obtained by performing a partial trace on the density matrix of the final state ($t_f = 7\,\mathrm{ms}$) after projection on $|g\rangle$. These distributions correspond to an effective temperature of $7\Gamma_r$ in the vertical direction and $11\Gamma_r$ in the horizontal direction.

- the number of trajectories for the averaging was $n_{\text{traj}} = 500$.
- the jumps operators with a rate inferior to $10^{-2}\Gamma_r$ have been neglected.
- the vibrational resonance in this configuration is located at $n = 127$. This means that we should not have problems from the horizontal direction, but we should be careful with the vertical axis.

The histograms of populations in the vibrational levels in Figure 6.5 as a function of the number of vibration are similar to those in Figure 6.4 and will be compared to the results obtained by the rate-equation method in Figure 6.12. In Figure 6.6, we plot the number of scattered photons as a function of time; the linear fit is performed on the last percent of the data, to extract the scattering rate at long times. We find a scattering rate of 5 % of the decay rate of the excited state (Γ_r) consistent with the population in the excited state at long times (also $\sim 5\,\%$). We also see that the population in the excited state is similar to that obtained with the 2D computations at short times. Those results are encouraging since with about 5% of excited state population we can expect to obtain 2300 photons per second (210 photo-electrons per atom). However, we will see in the following that this favorable situation is linked to the absence of loss in the model.

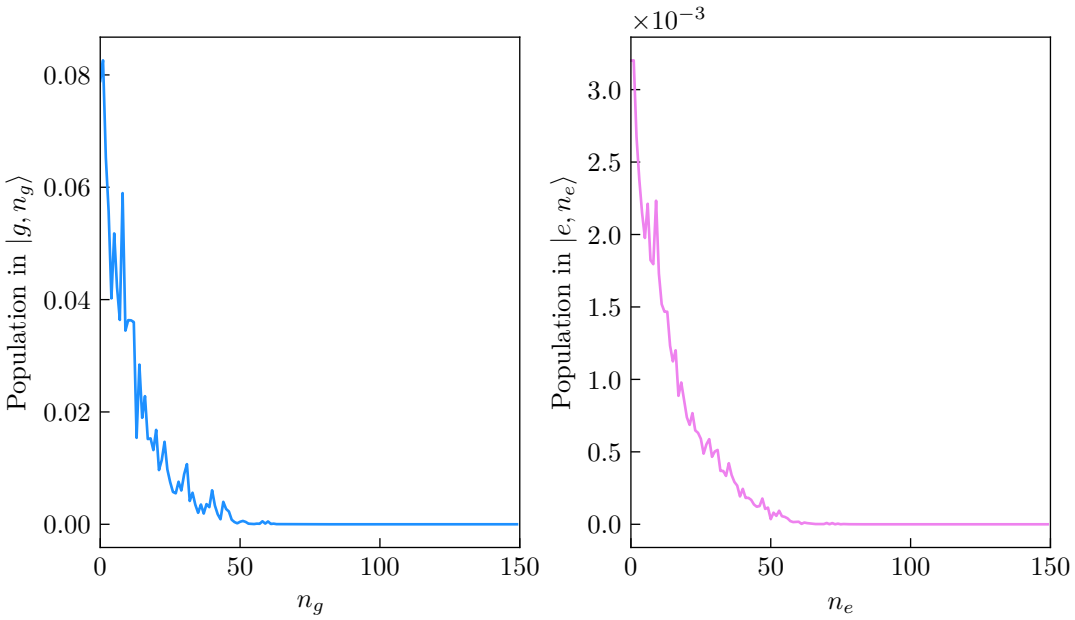

Figure 6.5: Population in the different vibrational states obtained by the Monte Carlo simulation in 1D for an evolution time of 270 ms, a detuning of $-45\Gamma_r$, and an intensity of $I = 800 I_{\text{sat}}$. The left (right) panel displays the populations of the vibrational levels in the ground (excited) state manifold.

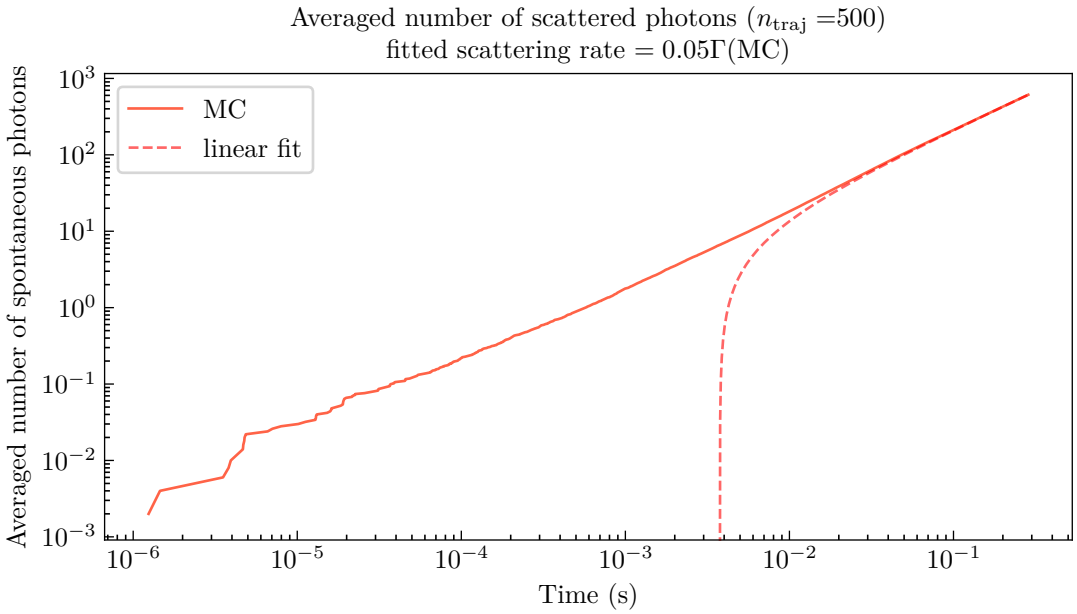

Figure 6.6: Plot of the number of scattered photons as a function of time. The dashed line is a linear fit performed on the last percent of the plain line data to extract a scattering rate at long times. This graph is obtain by the Monte Carlo wavefunction approach in 1D (vertical).

6.4.3.3 Unphysical states in the absence of losses

As we commented already, we expect that there will be losses if the atoms explore vibrational levels close to the top of the trap or close to the vibrational resonances. In Figure 6.7, we see that the exponential fit works fine for the lowest levels. After a long evolution (red curve), we get populations smaller than expected from a thermal distribution at intermediate vibrational numbers, and an excess at higher vibrational numbers. We interpret this as the effect of the resonance expelling the atoms to highly excited states.

This excess of populations in the highest levels shows that comparing the temperature to the trap depth will underestimate the losses. Furthermore, this accumulation of population creates an unphysical stationary state, as atoms at the top of the trap have to go back to lower levels (in our lossless description) instead of escaping the trap. For those reasons, we decided to introduce loss terms in our model. To simplify the implementation and get faster computations, we introduced the losses in the rate-equation model discussed in the next section.

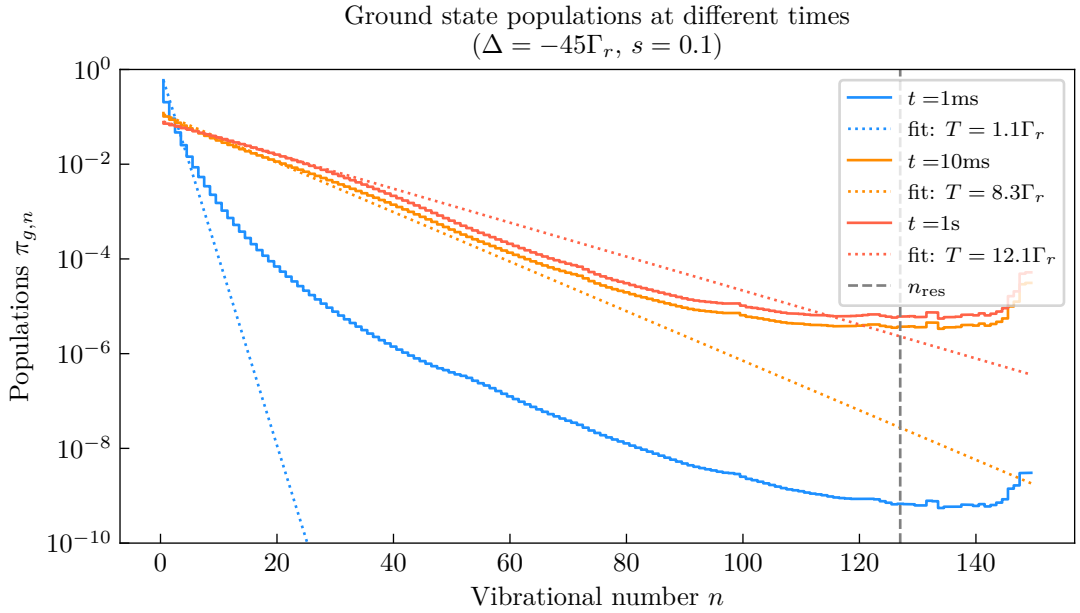

Figure 6.7: Populations of the $|g, n\rangle$ states at different evolution times for $\Delta = -40\Gamma_r$, and $s = 0.1$. The fits are obtained by adjusting a Boltzman distribution to the populations. The vibrational resonance is indicated by the grey dashed line. Those graphs were obtained from the rate-equation model (in the 1D vertical case) for convenience but display typical behaviors observed in the Monte Carlo simulations.

6.5 Rate equation model

In order to gain insight into the long-time limit of the dynamics (durations of about 1 s), we developed a complementary approach to the Monte Carlo simulation, as the cost in computation time for the MCWF approach becomes prohibitive for evolution times larger than a few tens of milliseconds.[14]

6.5.1 Principle of the methods

The critical assumption to derive rate equations is that the system's coherences are in steady state and are adiabatically following the populations. This should happen if the detuning is large compared to the damping rate (here Γ_r) [72] , which will be the case in our study since we use $\Delta \lesssim -30\Gamma_r$. We have learned in section 6.4.3.1 that when the dynamics start, the evolution of the populations happens on time scales on the order Γ_r^{-1} but then slows down significantly after just a few Γ_r^{-1}. Since the characteristic time of relaxation for the coherences is set by Γ_r; it seems reasonable to model the dynamics after this fast initial evolution using rate equations.

[14]It is prohibitive at least if we try to perform a systematic exploration of parameter space. The computation time was of 11 hours for the MCWF simulation of 270 ms with a Hilbert space of dimension 300 corresponding to the shallow trap (Z-axis) and for 200 trajectories.

6.5.1.1 Lossless rate-equation model

The rate equations are expressed in terms of the population of each state $\pi_{s,\vec{n}}$ where $s = g, e$. The couplings between the different levels are governed by the intensity of the laser I, the decay rates $\gamma_{m\to n}$, and the absorption cross-sections $\sigma_{m\to n}(\omega)$, where m, n are labels from the initial (excited) and final (ground) states (dropping the vector notations for now). The cross-sections are defined by [111] :

$$\sigma_{m\to n}(\omega) = \frac{\gamma_{m\to n}}{\Gamma_r}\frac{6\pi c^2}{\omega^2}\frac{\Gamma_r^2}{4\Delta_{mn}^2+\Gamma_r^2} = \sigma_0\frac{\Gamma_r^2}{4\Delta_{mn}^2+\Gamma_r^2} \tag{6.37}$$

where Δ_{mn} are the detunings of the laser at frequency ω with respect to the transition $|e,m\rangle \leftrightarrow |g,n\rangle$. We also introduced the notation σ_0 for the resonant absorption cross-section.

The generic form of the rate equations is:

$$\begin{cases} \dot{\pi}_{g,n} = \quad \sum_m(\beta_{m\to n}+\gamma_{m\to n})\pi_{e,m} - \left(\sum_m \beta_{n\to m}\right)\pi_{g,n} \\ \dot{\pi}_{e,m} = -\sum_n(\beta_{m\to n}+\gamma_{m\to n})\pi_{e,m} + \sum_n \beta_{n\to m}\pi_{g,n} \end{cases} \tag{6.38}$$

There are two types of terms in this system of equations:

- The terms containing a β coefficient represent absorption and stimulated emission, with the β coefficient defined by:

$$\beta_{m\to n} = \beta_{n\to m} = \frac{\sigma_{m\to n}}{\hbar\omega} I \ , \tag{6.39}$$

  where $\beta_{m\to n}$ corresponds to stimulated emission and $\beta_{n\to m}$ to absorption.
- The terms containing a γ coefficient represent the spontaneous emission.

The system of equations (6.38) is linear and can be cast in matrix form:

$$\dot{\vec{\pi}} = A\vec{\pi} \ . \tag{6.40}$$

6.5.1.2 *Ad hoc* loss model

In order to avoid unphysical states in the time evolution of the system, such as the accumulation of population in the highest vibrational states, we introduced an *ad hoc* model for the losses of atoms (see equation (6.41)). These losses account for different effects such as tunneling of the atom to a neighboring site or the escape of the trap.

The exact modeling of the losses would be difficult since it happens outside the harmonic approximation and can occur *via* different channels. We used the exponential *ansatz* parametrized by a characteristic decay "length" η, an amplitude L, and a cut-off indicating the lowest vibrational level for which we consider that the losses are non-zero.

This loss model is represented by a matrix $B_{\text{loss}}(\eta, L, n_{\text{cut-off}})$ which follows the equation:

$$B_{\text{loss}}(\eta, L, n_{\text{cut-off}})\vec{\pi} = \sum_{n=n_{\text{cut-off}}}^{n_{\max}} Le^{-\eta(n_{\max}-n)}(\pi_{e,n}+\pi_{g,n}) \tag{6.41}$$

The values we used in the simulations described in the subsequent sections are $L = \Gamma$, $\eta = 3$, $n_{\text{cut-off}} = 10$. For simplicity we chose to use identical value for both internal states.

Comments on the robustness of the model

We check that the results presented below are not drastically dependent on the details of the loss model. If the decay of the exponential η is too slow, then the loss term amounts to truncating the state basis and setting $n_{\max} \sim n_{\text{cut-off}}$. We will see that the losses become relevant at a point where the dynamics has slowed down, with typically variations on time scales of a few milliseconds.[15] Any loss term with an amplitude which is not small compared to that time scale have about the same contribution to the losses. For that reason, the cut-off parameter is mostly there to ensure that the loss matrix has a simple form.

6.5.1.3 Solving the dynamics

The system of equations that we need to solve is the following:

$$\dot{\vec{\pi}} = (A - B_{\text{loss}})\vec{\pi} \ . \tag{6.42}$$

where we included the rate matrix A from (6.40) and the loss matrix B_{loss} from (6.41). As for the Monte Carlo simulations, the initial state of the system is the absolute ground state $|g, 0\rangle$. This initial value problem can be solved by standard numerical integration using, for instance, `scipy.integrate.solve_ivp` from the python library `scipy` [49]. This gives access to the dynamics of the populations in times drastically shorter than with the MCWF simulations. Indeed, the rate-equation model can solve the 1D model's dynamics, with a state space of 2×150, in 3 minutes on a standard desktop computer with the default settings and less than 200 ms using the `BDF` solver.[16] The Monte Carlo solver needed 11 hours to solve the dynamics of the same system for about 270 ms (evolution time) and 200 trajectories.

The number of fluorescence photons is not directly included in the simulation. Still, it can be extracted from the populations in the excited states:

$$N_{\text{ph}}(t_i, t_f) = \int_{t_i}^{t_f} \mathrm{d}t \sum_{m,n} \gamma_{m\to n}\pi_{e,m}(t) = \Gamma_r \int_{t_i}^{t_f} \mathrm{d}t\, \pi_e(t) \tag{6.43}$$

where we introduced $\pi_e = \sum_m \pi_{e,m}$ the total population in the excited state.

6.5.2 Results for rate equations simulations

While we could have performed a full 3D simulation with this approach, the study with those simulations was done in 1D for two reasons. First, reducing dimensionality (of the state space) by a factor of $\sim 10 \times 10$ when going from the full 3D model to only a model for the vertical (shallow) direction is much less demanding in terms of computation times. Second, from the Monte Carlo simulations, it seemed that in typical situations (when the system did not accumulate populations in the highest levels of the trap), the atom acquires effective temperatures that are similar in all the directions of the trap. Thus,

[15] This can be obtained by looking at the eigenvalues of the rate matrix A.

[16] The advantage of this solver compared to the default Runge-Kutta method is that the Jacobian matrix of the system is passed to the solver as an argument instead of being evaluated at each time step. In our case, the Jacobian matrix is simply $A - B_{\text{loss}}$.

by estimating the effective temperature in the vertical direction, we can infer that in the horizontal directions and assess if the population in the high-lying vibrational states will be sufficiently small.

As we saw in the Monte Carlo simulations, most of the population dynamics happen during the first tens of μs. Then a slow drift occurs on time scales compatible with the slowest time constant extracted from the rate-equation model of a few milliseconds.

6.5.2.1 Exploration of the (s, Δ)-space

In this section, we explore the influence of the saturation parameter s, and the detuning Δ on the dynamics. In particular, we study the number of scattered photons and the losses since these two parameters are the most crucial for imaging.

Simulations of the dynamics

In order to have an estimate of the number of photon emitted before the atom leaves the trap, for our configuration of interest, we compute the system's dynamics starting from the initial state $|\psi(t=0)\rangle = |g, 0\rangle$, and let the system evolve for 10 s. In Figure 6.8, we plotted the time evolution of the population in the excited states, the energy in the $\{|g, n\rangle\}_n$ manifold, and the losses for different detunings and different saturation parameters s. First of all, we see that the dynamics can be separated into three distinct parts:

1. The dynamics is independent of the detuning during the first few hundred microseconds; the population in the electronic excited state builds up and saturates while the vibrational energy stays constant.

2. Then, from 1 ms to about 10 ms to 20 ms, the increase in vibrational energy starts to depend on the detuning. When the laser is closer to resonance, the vibrational energy saturates slightly faster and at lower values. The time scale for the saturation for the energy coincides with the apparition of the losses and an increase in the population in the electronic excited manifold. As the atom is heated up, it gets closer to the vibrational resonance, the laser is seen as less detuned therefore increasing the population in the excited state, while increasing the vibrational energy.

3. Finally, the last phase corresponds to a decay of the electronic excited state population to zero, the losses get accelerated, and the energy is stationary at a value that increases with the detuning. This decay comes from two factors, the losses as the atom escape the trap, and the fact that the highest levels of the trap are (blue) detuned with respect to all the $|e, m\rangle$ levels. We interpret the higher value of the plateau in energy when $|\Delta|$ is increased as an effect of the vibrational resonance occuring at higher n's for more negative detunings. Therefore, the trap can accomodate more vibrational energy before loosing atoms in those cases.

We see an optimal detuning to minimize the losses, around $-40\Gamma_r$. We interpret the apparition of this optimum as a compromise between the lower temperatures obtained at lower detunings (see Appendix D) and the resonance that occurs at smaller vibrational numbers when $|\Delta|$ is lowered.

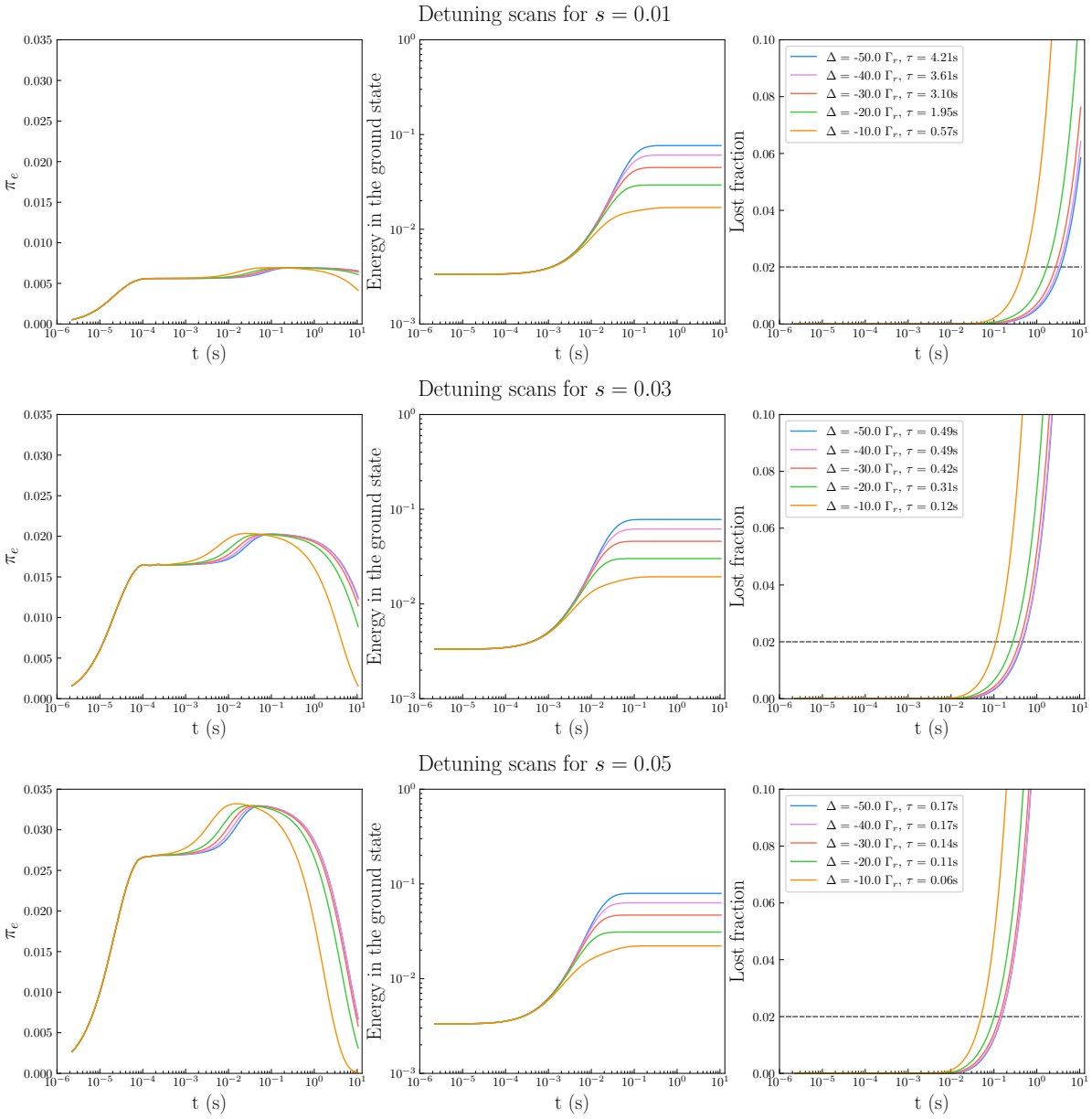

Figure 6.8: Population in the electronic excited manifold π_e, vibrational energy in the electronic ground state, and fraction of the atoms that are lost plotted as a function of time for different detunings and saturation parameters. The energy is normalized by the trap depth. τ is the lifetime of the trapped atom defined as the time when 2% is lost; this is delimited by the grey dashed line.

We remark that the population in the excited state does not depend drastically on the detuning but rather on the saturation parameter s, as in the case of an atom in free space. The impact of the detuning for π_e is mostly to accelerate the dynamics when the laser is brought closer to resonance.

Photon numbers

In practice not all the atoms will emit the same number of photons, depending on the time the atom actually spends in the trap, leading to a broadening of the "occupied" lobe in the histograms described in chapter 4. This situation would be challenging for the reconstruction algorithms. It is unclear what compromise between losses and photon fluxes would optimize the deconvolution of the images. This could be studied by varying the integration time and saturation parameter and looking at the histograms' width after deconvolution.

Thus, we are interested in situations where we image during a time over which the losses are small. To obtain this information, we define a lifetime for the atom in the trap $\tau(\Delta, s)$ from the loss curves as the time at which the losses reach 2%. We then compute the number of scattered photons during the lifetime using $\pi_e(t)$ and (6.43). We plot those results in Figure 6.9. The photon numbers above 1000 require going to integration times ranging from 1 s to 4 s, as can be seen in Figure 6.10

From these graphs, it seems that a working around $\Delta = -50\Gamma_r$ and $s = 0.01$ would give the best results in terms of number of scattered photons during the lifetime. However, this number is still insufficient compared to the signal levels required by the image processing algorithms, as we obtain on the order of a thousand photons while we wanted about 2000 to reach an SNR of 4.

Effects of the losses on the populations

In Figure 6.11, we display the populations of the vibrational levels of the electronic ground state manifold, obtained with the rate equations with losses, for a detuning of $-45\Gamma_r$ and a saturation parameter of 0.1. Contrary to the case dispalyed in Figure 6.7, there is no more an accumulation of populationat the top of the trap. Similar results are obtained for the lower saturation parameters that we identified as interesting in the last section. Therefore, the introduction of a loss term solved as expected the issue of the unphysical accumulation of population in the highest vibrational states.

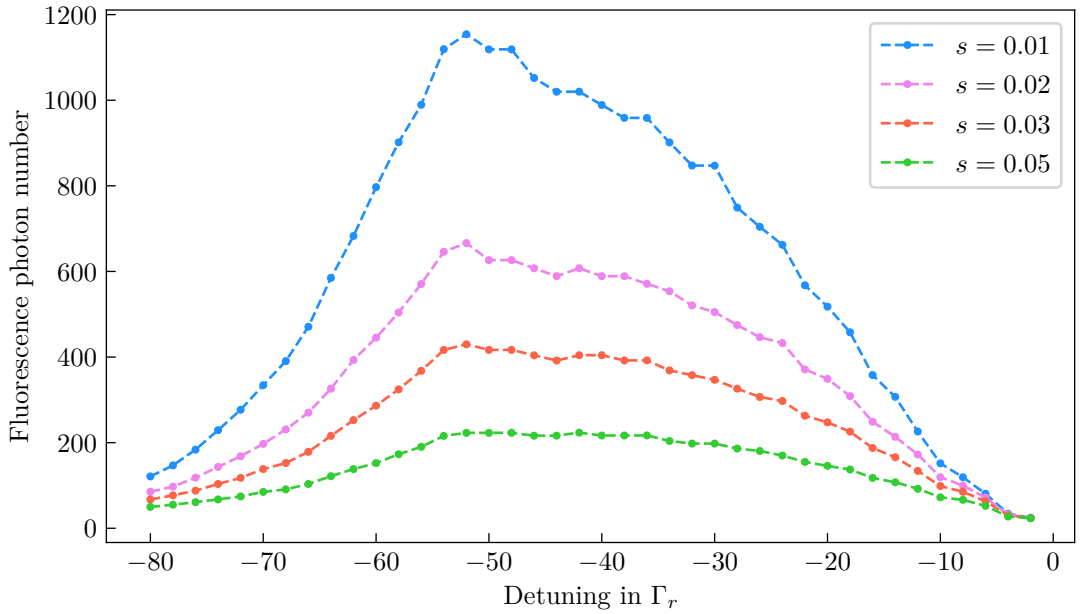

Figure 6.9: Number photons emitted by the atom during its lifetime. The lifetimes range from 60 ms to 4 s, and are plotted in Figure 6.10.

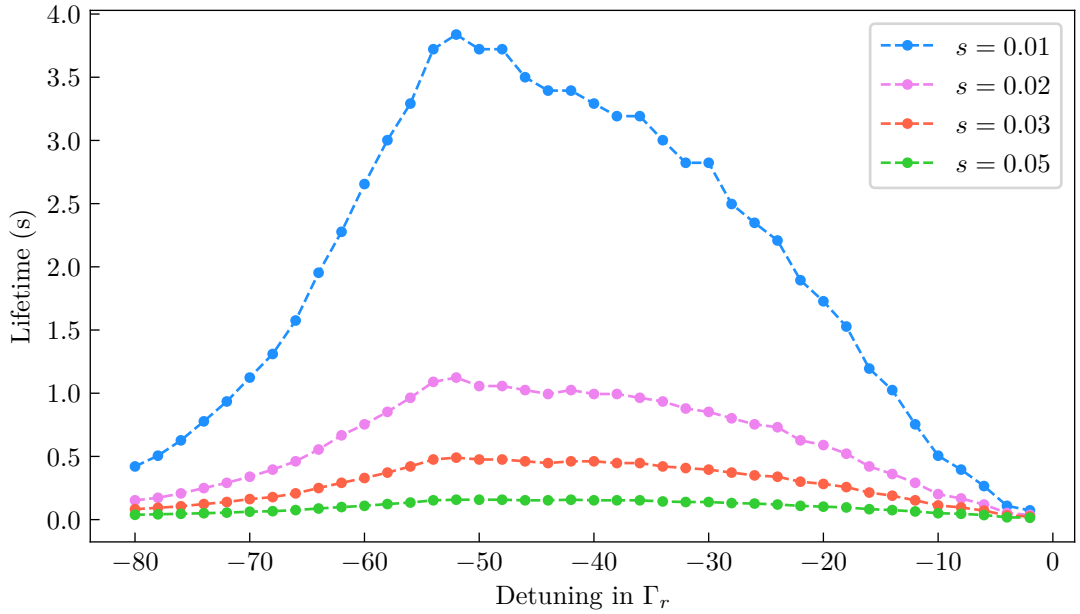

Figure 6.10: Lifetimes (98%) for the trapped atom corresponding to the data points plotted in Figure 6.9.

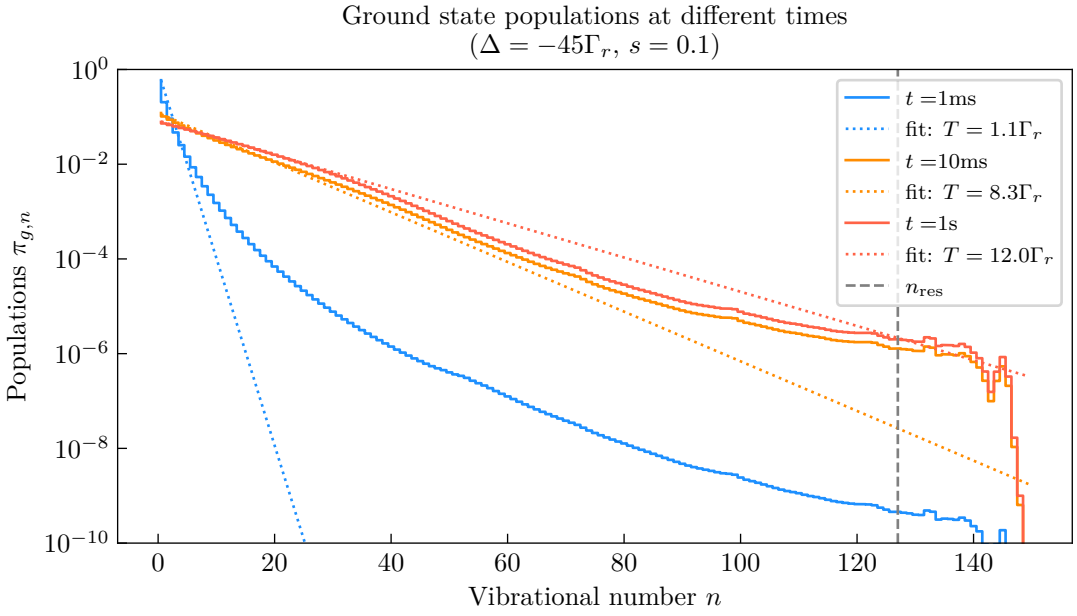

Figure 6.11: Populations of the $|g, n\rangle$ states at different times, like in figure 6.7, for a detuning $\Delta = -45\Gamma_r$ but with a saturation parameter $s = 0.1$ that is more adapted to our problem with the losses. The introduction of the loss removed the unphysical accumulation of atoms at the last levels of the trap that we saw in figure 6.7). The populations have been normalized so that $\sum_n \pi_{g,n} = 1$.

6.5.3 Validity of the approach

6.5.3.1 Comparison between the results from rate equations and MCWF

To validate the use of rate equations that was introduced in section 6.5, we compare in Figures 6.12 and 6.13 the results from the two methods in 1D. We chose to compare the populations in the different vibrational states (Figure 6.12) and the emission of photons (Figure 6.13).

In Figure 6.12, we observe that the population in the low vibrational number are similar using both method. For the higher vibrational numbers we interpret the differences as arising from the absence of losses in the Monte Carlo simulation, as the behavior is similar to the one observed in Figure 6.7. We can also notice a discrepancy for the excited state manifold at vibrational number above $n_e \sim 120$, this is due to the truncation of the basis that was applied on the Monte Carlo model but not for the rate equations. Adapting the loss model allows to truncate the basis above $n_e \sim 120$ without impacting too much the rest of the population distribution.

From the plot of the fluorescence photon numbers, we see that there is a good agreement between the methods, as soon as the evolution time is longer than a few $1/\Gamma_r = 21.5\,\mu\mathrm{s}$. This confirms that the rate-equation model faithfully reproduces the results of the Monte Carlo simulations, in terms of population distributions and photon scattering. We also can remark that the introduction of the losses in the rate equations does not yield much impact at least during the lifetime of the atom.

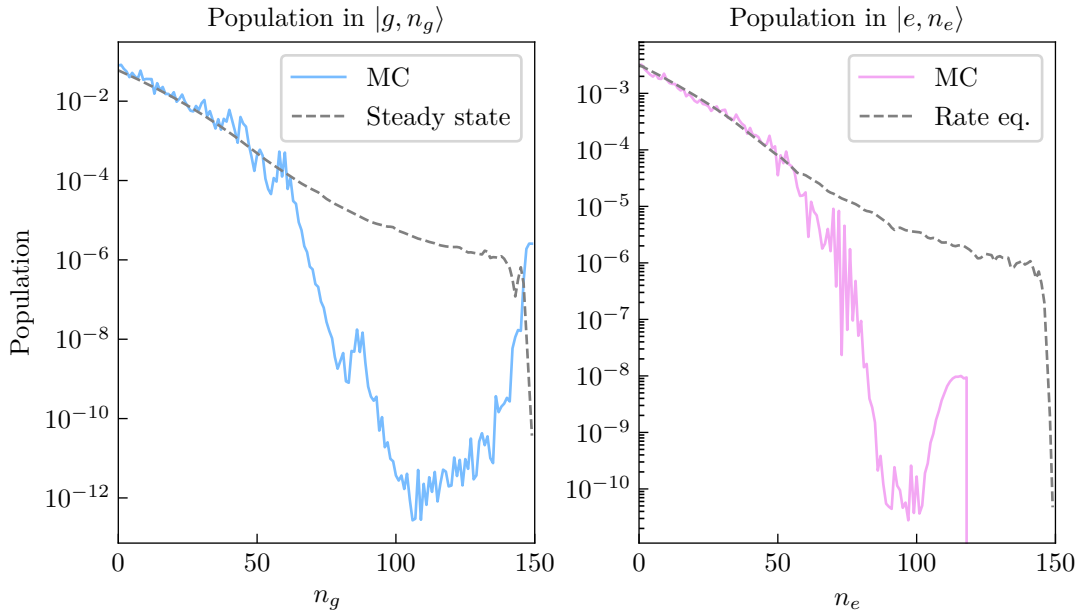

Figure 6.12: Comparison of the population in the different vibrational states obtained by the Monte Carlo simulation in 1D (solid curve) and the same data obtained from the rate-equation model (dashed curve) for an evolution time of one lifetime corresponding to 30 ms. The left (right) panel displays the populations in the ground state (excited state) manifold.

6.5.3.2 Validity of the 1D approximation

We still need to check that the atom's temperature is compatible with the trap depth in the horizontal axes. Indeed, it might be that the atom is lost from the top of the horizontal lattice well before it reaches the top of the trap in the vertical direction. We have identified that an interesting range of parameters to work with is around $s = 0.01$ and $\Delta = -40\Gamma_r$.

For that value of detuning, the vibrational resonance is higher than the last level in the trap. We then need to compare the temperature to the trap depth. In figure 6.11, we see that we reach a temperature of $10\Gamma_r$, which is reasonably small compared to the trap depth of $79\Gamma_r$. The fact that the thermal distribution is not much narrower than the horizontal trap depth means that there might also be losses from the horizontal directions; however, as long as the horizontal and vertical axes have similar temperature, we expect that reaching the top levels of the horizontal traps will correspond to also reaching the top levels of the vertical one. Therefore, up to a rescaling of the loss term, the 1D model should be able to account for those extra losses coming from the other axes. A follow-up to the study presented in this chapter could be to extend the rate-equation model to a 2D case to check that the distributions are thermal with similar temperatures.

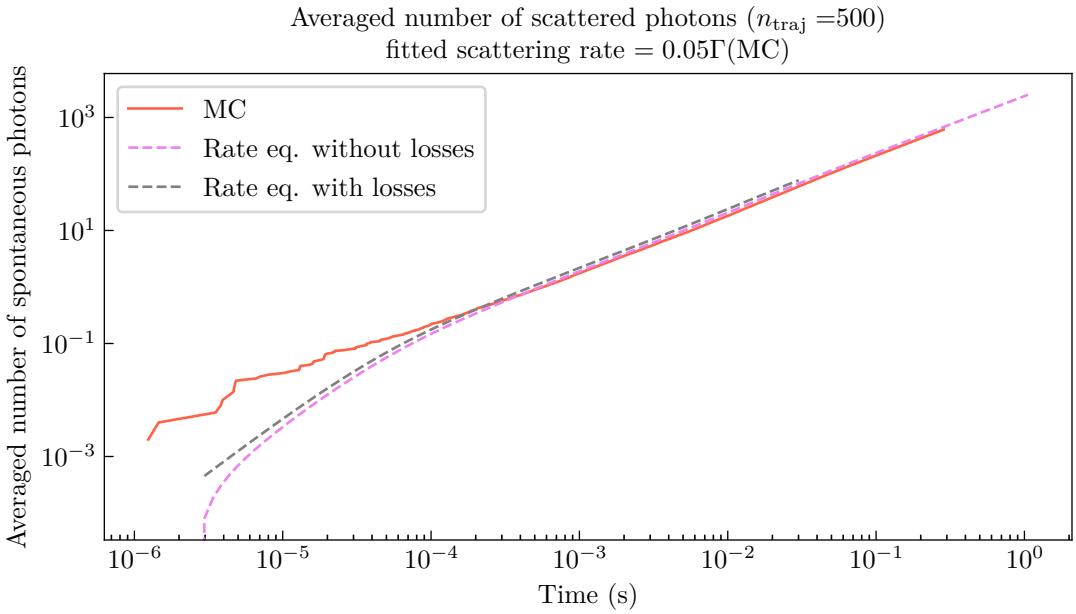

Figure 6.13: Number of photons scattered as a function of time. The solid line is obtained from the Monte Carlo simulation in 1D (section 6.4.3.2). The pink dashed line presents the result for the rate-equation model without losses, while the gray dashed line represents the number of scattered photons for the rate-equation with losses. Note the the evolution of the model with loss has been stopped after a lifetime (30 ms).

6.6 Conclusion

We have seen in this chapter that the imaging process for our trapped atoms can be modeled by a rate-equation model, at least for evolution times longer than $\sim 100\,\mu$s. At shorter times, the Monte Carlo wavefunction simulations can be used. The 2D Monte Carlo simulations show that the atom acquires effective temperatures that are similar in the horizontal (tight) and vertical (shallow) directions. Therefore, we concluded that the study of the system's dynamics can be reduced to the shallow vertical direction only.

Heating during imaging is accelerated by the presence of a vibrational resonance, leading the atom up to the last levels of the trap. This demanded that we introduce a loss mechanism in our rate-equation model to account for the possibility for the atom to escape. Due to the presence of those losses, the atom will scatter photons during a time that is finite and random, leading to fluctuations in the number of photons emitted per atom. Such fluctuations could impair the performance of the image processing and therefore require that we stop the imaging before the probabilty of losing the atom gets to high. We fixed the criterion of 2% of loss, leading to about a thousand scattered photons (~ 100 photo-electrons) for an imaging time of 3 s at $s = 0.01$, $\Delta = -40\Gamma_r$.

Those results are insufficient to use the image processing algorithms with good performance. A factor of 2, however, would bring us inside the targeted regime of 200 photo-electrons per atom. In the last section of this chapter, we present ideas that could allow us to overcome the limitations of the current setup. I did not have time to implement those alternative schemes in our simulations before writing this chapter, but I will start to work on them once this manuscript is finished.

6.7 Perspectives

The scheme that we studied until now was in fact very simple with a single beam and a single frequency. We expect to be able to reduce the loss channel in our model by using a bichromatic laser beam or by scanning its frequency. This reduction of the losses would allow us to work at higher saturation with greater scattering rates. We present here three different alternative schemes.

6.7.1 Frequency scan of the laser

In Berto *et al.* [105], the authors present a way to simulate the cooling of atoms in the case $\Omega_g > \Omega_e$ using a scan of the laser frequency. Their study is performed in the Lamb-Dicke limit ($\eta_g = 0.2$) and outside the resolved sideband regime, however the formalism used is very similar to the one developed (independently) in this chapter.

Their idea is to start from a detuning corresponding to the resonance between $|g, n_{\max}\rangle$ and $|e, 0\rangle$ and linearly ramping up the frequency to sweep over the $|g, n\rangle \leftrightarrow |e, 0\rangle$ resonances with decreasing n down to some $n_{\min}$. The values of $n_{\min}$ and $n_{\max}$ need to be optimized as well as the sweep time. In one example, they present the case of an ytterbium atom in an optical tweezer and show that this cooling can be performed in about 100 ms.

We could implement this scheme as a cooling stage, alternating our single frequency scheme with a sweep of cooling every so often to bring back the atoms to the bottom of the trap. This scheme could be implemented using the AOMs controlling the red laser's frequency.

6.7.2 Bichromatic scheme

We could also use two frequencies in our laser beam, as depicted in Figure 6.14. One beam is as before (ω_1) and an additional "cooling beam" (ω_2) that would connect $|g, n\rangle$ to $|e, m_J = -1, 0\rangle$, where n would be on the order of n_{res} or lower.

The process is as follows: the atoms heat up under the action of the imaging laser (ω_1). Then the motionally excited atoms are sent to $|e, m_J = -1, n \approx 0\rangle$. They can then decay back to $|g, n \approx 0\rangle$ by spontaneous emission. For that scheme, we expect that moderate intensities for the cooling beam (ω_2) should work since we need not be fast compared to the lifetime of the excited state. Note that in order to avoid the influence of the cooling beam on the $|g\rangle \leftrightarrow |e, 0\rangle$ transition, the Zeeman splitting should be larger than the sum of trap depth depth and the detuning of the imaging laser (ω_1), that is at least 1.3 MHz. Like for the frequency scan this scheme is straightforwardly implemented using an AOM.[17]

[17] After the sending of the initial version of this manuscript to the referees, we implemented and tested this bichromatic scheme with the rate equation model. We identified an interesting set of parameters: $\Delta_1 = -25\Gamma, \Delta_2 = -70\Gamma, s_1 = 0.01, s_2 = 0.01$ where the labels 1 and 2 are the same as in Figure 6.14, leading to a lifetime of 3.6 s and 2200 photons. Therefore this scheme would allow to gain about a factor of 2 on the photon number with similar lifetimes.

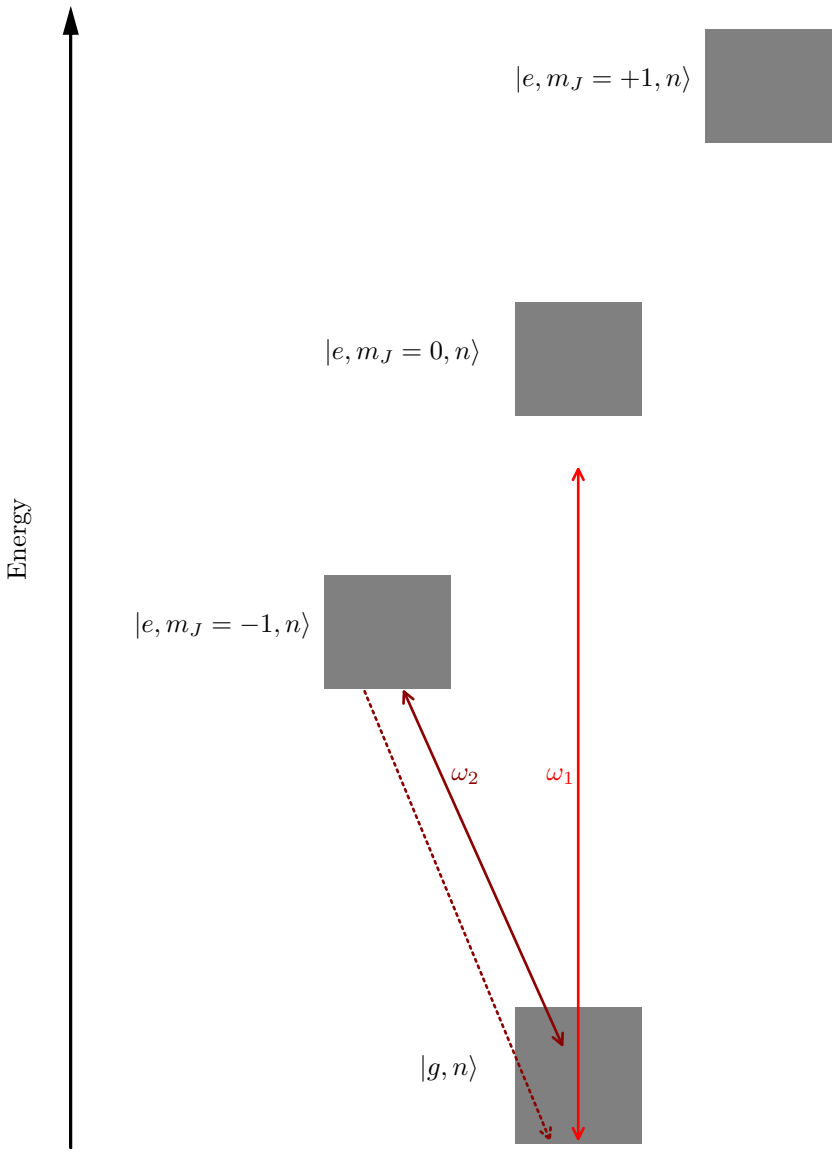

Figure 6.14: Level diagrams for the bichromatic cooling scheme and the RF coupling scheme. The main laser that was described in this chapter is the one denoted ω_1. The vibrational manifolds are represented by a continuum (gray rectangle) to emphasize that the trap frequencies are on the order of the natural linewidth. We introduce a second laser (ω_2) in order to redirect atoms that were heated up towards the absolute ground state $|g, 0\rangle$.

Conclusion and perspectives

In this manuscript, I presented the main results that where obtained by our team during my time as a Ph.D. student. The nature of these results were of two different types. The first part of the manuscript described experimental developments and advances toward the realization of a quantum gas microscope with strontium atoms. While the second part was focused on prospective theoretical work to plan and design the imaging system as a whole, including the illumination of the cloud, the trap configuration for the optical lattice, and the algorithms to process the images.

Here, we will first summarize the main results of this manuscrpit; then, we will highlight the main milestones that remain to be reached by the team.

I Synthesis of the results

I.1 Experimental results

When I arrived in the team in 2019, the blue MOT with ^{88}Sr was obtained on a daily basis and the team was working on obtaining the first red MOT. The first red MOT was obtained soon after my arrival but after its first apparition it remained elusive for a long time due to instability of the laser system and to the addition of the science chamber to the existing vacuum system.

Nowadays, red MOTs at 1 µK and a few million atoms are produced routinely with ^{84}Sr, the isotope of interest for our experiment. This was enabled among other things by the increase of the efficiency of the transverse collimation by a factor of 60 compared to the previous setup. The change of setup was motivated by the availability of new laser diodes with power five times higher than the one we used previously. This allow us to work with elongated beams to increase the interaction time of the atoms with the transverse molasses beams while keeping reasonably high intensities, and thus, radiation pressures.

The transport system was also built and tested, and first results were obtained. The transport can be done in 2.5 s with a survival on the order of 70% and a temperature at the arrival in the science chamber on the order of a few microkelvins. The first test on the vertical lattice system are currently being performed.

I.2 Theoretical results

The theoretical developments that were performed during my Ph.D were mostly focused on the imaging of the atoms inside the optical lattice. They were organized into three distinct parts: the performances of the image processing of simulated images, the computations of the properties of the optical lattice potential both in the ground state ($^1S_0$) and excited state ($^3P_1$), finally, we simulated the dynamics of a trapped atom during the imaging phase.

We presented in chapter 4 three approaches to reconstruct the occupancies of the lattice sites from the microscope images: an iterative linear least-square method, a Wiener deconvolution, and a neural network. Given our optical system, we used those simulations to fixe a lower bound of 2100 photons on the number of photons that we want to harvest for each atom. We also used these methods to study the performances of our methods for generic experimental configuration. In particular, we found that the distribution of atom can be reconstructed from image with resolutions well below the usual resolution criteria.

In chapter 5, we exposed the calculations of the dynamic polarizabilities for strontium at 1064 nm for the ground ($^1S_0$) and excited ($^3P_1$) states. We used those calculation to fixe the polarizations of the trapping laser beams, the orientation of the bias magnetic field, and the Zeeman sub-level of the excited state that we will address with the excitation laser. We found the polarizability in the ground state is higher than in the exicted state, for every choice of polarizations of the beams and orientation of the magnetic field.

The fact that the excited state is less polarizable than the ground state is the cause of the difficulty of the imaging strontium atoms, as we have seen in chapter 6. Indeed, this introduces vibrational resonances that tend to expel the atom from the trap. This phenomenon leads to lifetime in the trap that are incompatible with the imaging if the detuning of the excitation laser is not kept at around -50 to -40Γ_r. In order to maintain populations on the order of a few percents in the excited electronic state and therefore reasonable scattering rates, we had to use intensities on the order of a thousand I_{sat} to compensate the high detunings. We saw that with the scheme we proposed using only a single beam at a fixed frequency, we achieved to emit on the order of a thousand photons, in times on the order of a few seconds.

II Perspectives

II.1 Building of the experimental appartus

The main steps that remain to be performed are the following:

1. The transport protocol should be optimized and made more stable.
2. The testing on the vertical lattice setup is under investigation. Once we are able to load the transported atoms from the transport ODT into the vertical lattice trap, we will work on the Bose-Einstein condensation of our cloud.
3. The horizontal lattice system is already designed and purchased and will be implemented in the coming months.
4. Once we have a condensate and the horizontal lattice, we work on obtaining the first microscope images.

II.2 Prospects for the imaging stage

As we have seen in chapter 6, the results for the number of photons we can collect are slightly disappointing, as we would like to obtain photon numbers on the order of 2000 per atom, while the simulated value is on the order of 1000. These results were obtained for a single laser beam at a fixed frequency on the intercombination transition. A bichromatic scheme as well as one with a frequency scan for the excitation laser might resolve this issue, and will be simulated in the weeks after the end of the writing of this manuscript.

Moreover, in chapter 6, we fixed the lifetime as the time at which the probability of losing the atom is higher than 2%. This requirement results from an arbitrary constraint that we imposed on the system. A more consistent approach would be to include the losses of atoms in the generation of the simulated images described in chapter 4 and determine what is the optimal way to define the lifetime of the atom. This method could even be used to choose the best set of parameter for the excitation laser, namely the detuning, the intensity and the exposure time.

Appendix A

LMA-PM-15 fiber datasheet

NKT Photonics
the power of light

Crystal Fibre • *aero*LASE • Koheras • SuperK

LMA-PM-15

Large Mode-area · Single Mode · Polarization Maintaining

Single mode 15 µm polarization-maintaining fiber

- Low loss fiber from 500 to 1700 nm
- Single mode at all wavelengths
- Polarization Maintaining
- Radiation hard pure silica fiber
- Wavelength independent MFD

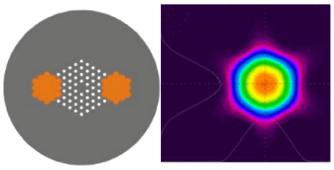

This polarization-maintaining single-mode fiber is optimized to exhibit low loss from 600 nm to 1700 nm while keeping an almost constant mode field diameter.

The fiber is endlessly single-mode (i.e. it has no higher order mode cut-off) and delivers excellent mode quality at all wavelengths.

This product is also available in a non polarization-maintaining version as the LMA-15

Optical properties	
Single mode cut-off wavelength*	None
Attenuation @ 1064 nm	‹ 10 dB/km
Mode field diameter @ 532 nm (1/e²)	12.2 ± 1.5 µm
Mode field diameter @ 1064 nm (1/e²)	12.6 ± 1.5 µm
NA @ 532 nm (5%)	0.04 ± 0.02
NA @ 1064 nm (5%)	0.07 ± 0.02
Birefringence Δn @ 1064 nm	≥ 1.3·10⁻⁴
Polarization Extinction Ratio**	≥ 18 dB
Physical properties	
Core diameter	14.8 ± 0.8 µm
Outer cladding diameter, OD	230 ± 5 µm
Coating diameter	350 ± 10 µm
Core and cladding material	Pure silica
Coating material, single layer	Acrylate
Coating-Cladding concent. error	‹ 10 µm
Proof test level	0.33 %
Standard interfacing options	
FC/PC PM connector	0.0 ± 0.5 deg angle
FC/APC PMconnector	8.0 ± 0.5 deg angle
SMA 905	0.0 or 5.0 ± 0.5 deg angle
Collapse and cleave	0.0 ± 0.5 deg angle

All interfaces are provided with a 150 ± 25 µm sealing length of the PCF structure. PM connectors are keyed to the slow axis. Please contact us for other custom interfacing options.

* TIA-455-80-C standard ** AKA PXtalk on a 2 m sample

Applications
- Single-mode PM short wavelength delivery
- Multi-wavelength transmission
- Mode filtering
- Single-mode PM pigtailing
- Short pulse delivery

Typical spectral attenuation and dispersion

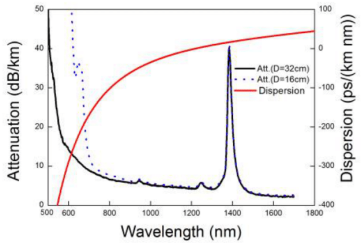

Typical spectral NA and MFD

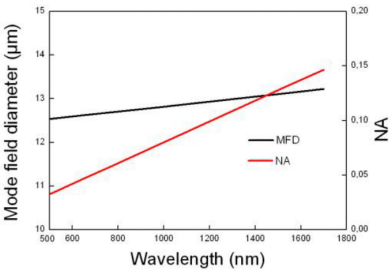

RoHS 2 2011/65/EU

LMA-PM-15-170222

NKT Photonics A/S (Headquarters)
Blokken 84 • 3460 Birkerød • Denmark
Phone: +45 4348 3900
Fax: +45 4348 3901
www.nktphotonics.com

NKT Photonics GmbH
Schanzenstrasse 39 • Bldg D9-D13
51063 Cologne • Germany
Phone: +49 221 99511-0
Fax: +49 221 99511-650

NKT Photonics Inc.
1400 Campus Drive West • Morganville
NJ 07751 • USA
Phone: +1 732 972 9937
Fax: +1 732 414 4094

Figure A.1: Source: *NKT Photonics*, available here.

Appendix B

Derivation of the dynamic polarizability tensor

In this appendix, we present the details of the calculation for the polarizability tensor described in Chapter 5. We follow closely the calculations done in appendix A of [67] but adapted to the case of an atom without nuclear spin, which is relevent for the bosonic isotopes of strontium and, in general, of alkaline-earth atoms. The last section II is a compilation of useful results on Wigner symbols and angular algebra.

I Derivation and reduction of the lightshift operator

The situation described here is that of an off-resonant monochromatic light field sent onto an atom without nuclear spin ($I = 0$). The (classical) electric field is $\vec{E} = \mathrm{Re}\,(\mathcal{E}e^{-i\omega t}\vec{u})$. This results in a perturbation, $V^E = -\vec{d}\cdot\vec{E}$ where $\vec{d}$ is the electric dipole operator, of the hamiltonian of the free atom in an external magnetic field $\vec{B}$: $H_0 = H_{at} + H_{Zeeman}(\vec{B})$.

I.1 The sum over state formula

From time-independent perturbation theory, we get that there is no shift at first order in V^E since the diagonal matrix elements of $\vec{d}$ are vanishing[1]. At second order, we get energy shifts on state $|a\rangle$:

$$\delta E_a = -\frac{|\mathcal{E}|^2}{4\hbar}\sum_b \mathrm{Re}\left(\frac{|\langle b|\,\vec{u}\cdot\vec{d}\,|a\rangle|^2}{\omega_b - \omega_a - \omega - i\gamma_{ba}/2} + \frac{|\langle a|\,\vec{u}\cdot\vec{d}\,|b\rangle|^2}{\omega_b - \omega_a + \omega + i\gamma_{ba}/2}\right)\,, \tag{B.1}$$

where the index b stands for all the energy eigenstates other than $|a\rangle$, ω_i is the energy associated to state $|i\rangle$, $\gamma_{ba} = \gamma_b + \gamma_a$ is the sum of the decay rates from each state. Those energy shifts can be seen as the diagonal matrix elements of an effective lightshift operator V^{EE} [68], and the off-diagonal matrix elements are the terms inducing state mixing. This operator is expressed as a sum over all states:

[1] Since $\vec{d}$ is odd and energy eigenstates of H_0 have a definite parity.

$$V^{EE} = \frac{|\mathcal{E}|^2}{4}\left[\left(\vec{u^*}\cdot\vec{d}\right)\mathcal{R}_+\left(\vec{u}\cdot\vec{d}\right) + \left(\vec{u}\cdot\vec{d}\right)\mathcal{R}_-\left(\vec{u^*}\cdot\vec{d}\right)\right] , \tag{B.2}$$

with

$$\mathcal{R}_\pm = -\frac{1}{\hbar}\sum_b \mathrm{Re}\left(\frac{1}{\omega_b - \omega_a \pm \omega \pm i\gamma_{ba}/2}\right)|b\rangle\langle b| \ . \tag{B.3}$$

This form is described by the authors of [67] as an educated guess, but they claim that it can be derived from Floquet formalism. The sum will be performed over the fine-structure states $|n_1 n_2 l_1 l_2 LSJm_J\rangle$, which for obvious reasons will be designated by much shorter notations such as $|\gamma Jm_J\rangle$ or even $|Jm\rangle$, since only the total angular momentum J and its projection on the quantization z-axis m_J. One notable simplification with respect to [67] is that since the nuclear spin $\vec{I}$ is zero, we get "for free"

$$\vec{F} = \vec{J} \tag{B.4}$$
$$I = 0 \tag{B.5}$$
$$J = F = F' \ , \tag{B.6}$$

where F and F' would be the different hyperfine levels of a given fine-structure term $\gamma^{2S+1}\mathrm{L_J}$. (B.6) will simplify a lot the angular algebra. Additionally, since we will be considering the case of bosons, the $(-1)^{2k}$ (for k any angular momentum quantum number) factors will always simplify to 1.

I.2 Refactoring of the dot products

Using (B.32), with the replacements $\vec{A} = \vec{u^*}, \vec{B} = \vec{d}, \vec{A}' = \vec{u}, \vec{B}' = \mathcal{R}_+\vec{d}$ and similarly for the second term in (B.2) containing the $\mathcal{R}_-$. We obtain

$$V^{EE} = \frac{|\mathcal{E}|^2}{4}\sum_{K=0,1,2}(-1)^K\left\{\vec{u^*}\otimes\vec{u}\right\}_K\cdot\left[\left\{\vec{d}\otimes\mathcal{R}_+\vec{d}\right\}_K + (-1)^K\left\{\vec{d}\otimes\mathcal{R}_-\vec{d}\right\}_K\right] \tag{B.7}$$

where the inner $(-1)^K$ comes from $\{\vec{u}\otimes\vec{u^*}\}_K = (-1)^K\{\vec{u^*}\otimes\vec{u}\}_K$. We see here that the operator V^{EE} is expressed as a sum of dot products between irreducible tensors, one arising from the electric field only and the other from the atomic dipole only. The components of $\{\vec{u^*}\otimes\vec{u}\}_K$ can be deduced from (B.28). We now want to compute the matrix elements of the lightshift operator within a fine-structure level. Expanding V^{EE} over the eigenbasis of H_0 and restricting the study to the acting in a subspace spanned by $\{|Jm\rangle\}_m$, we can write:

$$V^{EE} = \sum_{\gamma m,m'} V^{EE}_{mm'}|\gamma Jm\rangle\langle\gamma Jm'| \ . \tag{B.8}$$

Restricting the study to this subspace amounts to neglecting the mixing of states that belong to different spectroscopic terms or even to different electronic configurations. This approximation is motivated by the fact that the effect of the AC-Stark shift is, in practice, much smaller than the energy difference between levels belonging to distinct fine-structure manifolds.

From (B.7), we extract the matrix elements $V^{EE}_{mm'}$ after expanding the dot products using (B.29)

$$V^{EE}_{mm'} = \frac{1}{4}\sum_K (-1)^K \sum_q (-1)^q U_{Kq} \mathcal{O}^{Kq}_{mm'} \tag{B.9}$$

where we introduced the two notations:

$$U_{Kq} = \{\vec{u}^* \otimes \vec{u}\}_K \tag{B.10}$$

$$\mathcal{O}^{Kq}_{mm'} = \langle \gamma J m| \left[\left\{\vec{d} \otimes \mathcal{R}_+\vec{d}\right\}_K + (-1)^K \left\{\vec{d} \otimes \mathcal{R}_-\vec{d}\right\}_K\right] |\gamma J m'\rangle \tag{B.11}$$

Using (B.28) on the rank-1(vector) operators $\vec{d}$ and $\mathcal{R}_\pm\vec{d}$, and introducing a closure relation on the state $|\gamma'' J'' m''\rangle$, we get:

$$\begin{aligned}
\mathcal{O}^{Kq}_{mm'} &= \sum_{q_1 q_2} C^{K-q}_{1q_1 1q_2} \langle \gamma J m| d_{q_1}(\mathcal{R}_+ + (-1)^K \mathcal{R}_-) d_{q_2} |\gamma J m'\rangle \\
&= \sum_{q_1 q_2} C^{K-q}_{1q_1 1q_2} \sum_{\gamma'' J'' m''} \langle \gamma J m| d_{q_1} |\gamma'' J'' m''\rangle \langle \gamma'' J'' m''| d_{q_2} |\gamma J m'\rangle \\
&\qquad \times \langle \gamma'' J'' m''| (\mathcal{R}_+ + (-1)^K \mathcal{R}_-) |\gamma'' J'' m''\rangle \\
&:= \sum_{q_1 q_2} C^{K-q}_{1q_1 1q_2} \sum_{\gamma'' J'' m''} \langle \gamma J m| d_{q_1} |\gamma'' J'' m''\rangle \langle \gamma'' J'' m''| d_{q_2} |\gamma J m'\rangle \mathcal{R}^{(K)}_{\gamma'' J'' \gamma J}
\end{aligned} \tag{B.12}$$

Using Wigner-Eckart theorem (II.1) on both of the matrix elements of (B.12), we obtain:

$$\begin{aligned}
\mathcal{O}^{Kq}_{mm'} = \sum_{\substack{q_1 q_2 \\ \gamma'' J'' m''}} C^{K-q}_{1q_1 1q_2} \mathcal{R}^{(K)}_{\gamma'' J'' \gamma J} (-1)^{J-m} \begin{pmatrix} J & 1 & J'' \\ -m & q_1 & m'' \end{pmatrix} \langle \gamma J \| d \| \gamma'' J'' \rangle \\
\times (-1)^{J''-m''} \begin{pmatrix} J'' & 1 & J \\ -m'' & q_2 & m' \end{pmatrix} \langle \gamma'' J'' \| d \| \gamma J \rangle \ .
\end{aligned} \tag{B.13}$$

We replace the Clebsch-Gordan coefficient by a 3j-Wigner symbol using (B.20), and then use (B.30) to flip the order of the states in one of the reduced matrix elements to get:

$$\begin{aligned}
\mathcal{O}^{Kq}_{mm'} &= \sum_{\gamma'' J''} \langle \gamma J \| d \| \gamma'' J'' \rangle \langle \gamma'' J'' \| d \| \gamma J \rangle \mathcal{R}^{(K)}_{\gamma'' J'' \gamma J} \\
&\times \left[\sqrt{2K+1} \sum_{m'' q_1 q_2} (-1)^{J+J''-m-m''-q} \begin{pmatrix} 1 & 1 & K \\ q_1 & q_2 & q \end{pmatrix} \begin{pmatrix} J & 1 & J'' \\ -m & q_1 & m'' \end{pmatrix} \begin{pmatrix} J'' & 1 & J \\ -m'' & q_2 & m' \end{pmatrix}\right] \\
&= \sum_{\gamma'' J''} (-1)^{J''-J} |\langle \gamma J \| d \| \gamma'' J'' \rangle|^2 \mathcal{R}^{(K)}_{\gamma'' J'' \gamma J} \\
&\times \left[\sqrt{2K+1} \sum_{m'' q_1 q_2} (-1)^{J+J''-m-m''-q} \begin{pmatrix} 1 & 1 & K \\ q_1 & q_2 & q \end{pmatrix} \begin{pmatrix} J & 1 & J'' \\ -m & q_1 & m'' \end{pmatrix} \begin{pmatrix} J'' & 1 & J \\ -m'' & q_2 & m' \end{pmatrix}\right]
\end{aligned} \tag{B.14}$$

Using the sum formula for triple products of 3-j symbols (B.27), with the replacements (and a generous amount of equations (B.21) to (B.24)):

$$\begin{cases} (j_1, m_1) = (J, -m) & (j_2, m_2) = (J, m') & (j_3, m_3) = (K, -q) \\ (j_4, m_4) = (1, q_2) & (j_5, m_5) = (1, -q_1) & (j_6, m_6) = (J'', m'') \end{cases} \tag{B.15}$$

,
we can simplify the bracketed term in (B.14):

$$\sqrt{2K+1}(-1)^{J-m+2J+K}\begin{pmatrix} J & K & J \\ -m & -q & m' \end{pmatrix}\begin{Bmatrix} 1 & K & 1 \\ J & J'' & J \end{Bmatrix} = \left[\sqrt{2K+1}\sum_{m''q_1q_2}(-1)^{J+J''-m-m''-q}\begin{pmatrix} 1 & 1 & K \\ q_1 & q_2 & q \end{pmatrix}\begin{pmatrix} J & 1 & J'' \\ -m & q_1 & m'' \end{pmatrix}\begin{pmatrix} J'' & 1 & J \\ -m'' & q_2 & m' \end{pmatrix}\right] . \tag{B.16}$$

Inserting (B.16), into (B.14) and back into (B.9), and regrouping $(-1)^{J''-J}$ and $(-1)^{2J}$we obtain:

$$V^{EE}_{mm'} = \frac{|\mathcal{E}|^2}{4}\sum_K(-1)^K\sum_q(-1)^q U_{Kq}\sum_{\gamma''J''}(-1)^{J''+J}|\langle\gamma J\|d\|\gamma''J''\rangle|^2\mathcal{R}^{(K)}_{\gamma''J''\gamma J} \times\sqrt{2K+1}(-1)^{K+J-m}\begin{pmatrix} J & K & J \\ -m & -q & m' \end{pmatrix}\begin{Bmatrix} 1 & K & 1 \\ J & J'' & J \end{Bmatrix} .^2 \tag{B.17}$$

Finally, we introduce the polarizabilities $\alpha^{(K)}_{\gamma J}$:

$$\alpha^{(K)}_{\gamma J} = (-1)^{2J+K+1}\sqrt{2K+1}\sum_{\gamma''J''}(-1)^{J+J''}|\langle\gamma J\|d\|\gamma''J''\rangle|^2\begin{Bmatrix} 1 & K & 1 \\ J & J'' & J \end{Bmatrix} \frac{1}{\hbar}\,\mathrm{Re}\left(\frac{1}{\omega_{\gamma''J''}-\omega_{\gamma J}-\omega-i\gamma_{\gamma''J''\gamma J}/2}+\frac{(-1)^K}{\omega_{\gamma''J''}-\omega_{\gamma J}+\omega+i\gamma_{\gamma''J''\gamma J}/2}\right) , \tag{B.18}$$

whence

$$V^{EE}_{mm'} = \frac{|\mathcal{E}|^2}{4}(-1)^{J-m}\sum_K(-1)^K\alpha^{(K)}_{\gamma J}\sum_q(-1)^q\left\{\vec{u}^*\otimes\vec{u}\right\}_{Kq}\begin{pmatrix} J & K & J \\ -m & -q & m' \end{pmatrix} \tag{B.19}$$

I.3 Derivation of the J-form of V^{EE}

The formula (5.7) using the total angular momentum, instead of the $\{\vec{u}^*\otimes\vec{u}\}_K$ tensor. Is stated without proof in [67]. A proof of that formula is derived in [112] but in a slightly different formalism.

We do not include a derivation of the specific form here but the consistency of the two formulas was checked by computing the trap parameters either with (B.19) or with (5.7).

II Useful formulas

This section is a compilation of useful results for the derivations of this appendix.

II.1 Clebsch-Gordan coefficients and Wigner symbols

We follow the phase convention of [67] that is the Condon-Shortley convention [113]. The relation between the Clebsch-Gordan coefficients and Wigner 3-j symbols is

$$C^{jm}_{j_1m_1j_2m_2} = (-1)^{j_1-j_2+m}\sqrt{2j+1}\begin{pmatrix} j_1 & j_2 & j \\ m_1 & m_2 & -m \end{pmatrix} \tag{B.20}$$

II.1.1 Symmetry properties of the 3-j symbols

The 3-j symbols are highly symmetrical objects; they obey the following relations [114]:

- Invariance under even permutation of the columns

$$\begin{pmatrix} j_1 & j_2 & j_3 \\ m_1 & m_2 & m_3 \end{pmatrix} = \begin{pmatrix} j_3 & j_1 & j_2 \\ m_3 & m_1 & m_2 \end{pmatrix} = \begin{pmatrix} j_2 & j_3 & j_1 \\ m_2 & m_3 & m_1 \end{pmatrix} \tag{B.21}$$

- Phase factor for odd permutation of the columns

$$\begin{pmatrix} j_1 & j_2 & j_3 \\ m_1 & m_2 & m_3 \end{pmatrix} = (-1)^{j_1+j_2+j_3} \begin{pmatrix} j_1 & j_3 & j_2 \\ m_1 & m_3 & m_2 \end{pmatrix} \tag{B.22}$$

$$= (-1)^{j_1+j_2+j_3} \begin{pmatrix} j_3 & j_2 & j_1 \\ m_3 & m_2 & m_1 \end{pmatrix} \tag{B.23}$$

- Phase factor under time-reversal

$$\begin{pmatrix} j_1 & j_2 & j_3 \\ -m_1 & -m_2 & -m_3 \end{pmatrix} = (-1)^{j_1+j_2+j_3} \begin{pmatrix} j_1 & j_2 & j_3 \\ m_1 & m_2 & m_3 \end{pmatrix} \tag{B.24}$$

- Regge symmetry

$$\begin{pmatrix} j_1 & j_2 & j_3 \\ m_1 & m_2 & m_3 \end{pmatrix} = \begin{pmatrix} j_1 & \frac{j_2+j_3-m_1}{2} & \frac{j_2+j_3+m_1}{2} \\ j_3-j_2 & \frac{j_2-j_3-m_1}{2}-m_3 & \frac{j_2-j_3+m_1}{2}+m_3 \end{pmatrix} \tag{B.25}$$

$$\begin{pmatrix} j_1 & j_2 & j_3 \\ m_1 & m_2 & m_3 \end{pmatrix} = (-1)^{j_1+j_2+j_3} \begin{pmatrix} \frac{j_2+j_3+m_1}{2} & \frac{j_1+j_3+m_2}{2} & \frac{j_1+j_2+m_3}{2} \\ j_1-\frac{j_2+j_3-m_1}{2} & j_2-\frac{j_1+j_3-m_2}{2} & \frac{j_1+j_2-m_3}{2} \end{pmatrix} \tag{B.26}$$

II.1.2 The sum formula for triple products of 3-j symbols

From [114] we have the formula:

$$\sum_{m_4 m_5 m_6} (-1)^{j_4+j_5+j_6-m_4-m_5-m_6} \begin{pmatrix} j_5 & j_1 & j_6 \\ m_5 & -m_1 & -m_6 \end{pmatrix} \times \begin{pmatrix} j_6 & j_2 & j_4 \\ m_6 & -m_2 & -m_4 \end{pmatrix} \begin{pmatrix} j_4 & j_3 & j_5 \\ m_4 & -m_3 & -m_5 \end{pmatrix} = \begin{pmatrix} j_1 & j_2 & j_3 \\ m_1 & m_2 & m_3 \end{pmatrix} \begin{Bmatrix} j_1 & j_2 & j_3 \\ j_4 & j_5 & j_6 \end{Bmatrix} \tag{B.27}$$

II.2 Spherical basis formalism

II.2.1 Irreducible components of a product of spherical tensors

The irreducible components of the tensor resulting from the coupling of two tensors U and V of rank K_1 and K_2 respectively are

$$\{U_{K_1} \otimes V_{K_2}\}_{Kq} = \sum_{q_1,q_2} C^{Kq}_{K_1 q_1 K_2 q_2} U_{K_1 q_1} V_{K_2 q_2} \tag{B.28}$$

where $C^{Kq}_{K_1 q_1 K_2 q_2}$ are Clebsch-Gordan coefficients. The coupling of two spherical tensors thus follows the same rules as that of two angular momenta. K must follow the "triangle rule", $|K_1 - K_2| \leqslant K \leqslant K_1 + K_2$, and q obeys $-K \leqslant q \leqslant K$.

II.2.2 Dot product of spherical tensors

The dot product between two tensors U and V of (the same) rank K is given by:

$$(U_K \cdot V_K) = \sum_{-K \leqslant q \leqslant K} (-1)^q U_{Kq} V_{K-q} \,. \tag{B.29}$$

II.3 Wigner-Eckart theorem and reduced matrix elements

Theorem II.1 (Wigner-Eckart theorem)**.** *Let T_K be a spherical tensor of rank K, and two angular-momentum states $|jm\rangle$ and $|j'm'\rangle$, then there exists a constant $\langle j\|T_K\|j'\rangle$, called reduced matrix element*[3]

of T_K, such that for all m, m' and q:

$$\langle jm|\, T_{Kq}\, |j'm'\rangle = (-1)^{j-m} \begin{pmatrix} j & K & j' \\ -m & q & m' \end{pmatrix} \langle j\|T_K\|j'\rangle$$

with

$$\langle jm\|T_K\|j'm'\rangle = \sum_{m,m',q} (-1)^{J-m} \begin{pmatrix} j & K & j' \\ -m & q & m' \end{pmatrix} \langle jm|\, T_{Kq}\, |j'm'\rangle$$

An important corollary to this theorem is the *replacement formula* which we give here in a simplified version.

Corollary II.1.1. *Let $\vec{V}$ be any vector operator, its matrix elements in the angular momentum eigenbasis $\{|jm\rangle\}$ are proportional to those of the total angular momentum $\vec{J}$:*

$$\langle jm'|\, V_q\, |jm\rangle = \frac{\langle j\|V\|j\rangle}{\langle j\|J\|j\rangle} \langle jm'|\, J_q\, |jm\rangle \;, \tag{B.31}$$

This result remains true if we replace $\vec{V}$ and $\vec{J}$ by any two spherical tensors $T^{(k)}$ and $S^{(k)}$ of same rank k.

II.4 Product of dot-products refactoring

For the product of to dot products we can use the following identity: [67]

$$\left(\vec{A} \cdot \vec{B}\right)\left(\vec{A}' \cdot \vec{B}'\right) = \sum_{K=0,1,2} (-1)^K \left\{\vec{A} \otimes \vec{A}'\right\}_K \cdot \left\{\vec{B} \otimes \vec{B}'\right\}_K \tag{B.32}$$

where the $\left\{\vec{A} \otimes \vec{A}'\right\}_K$ are the irreducible components of rank K of the dyadic tensor[4] formed by the product of the vectors $\vec{A}$ and $\vec{A}'$, those components can be recovered from (B.28).

[3] The reduced matrix elements do not transform as simply as usual matrix elements when we exchange the "states" on the right and left. More precisely, one has

$$\langle j'\|T_K\|j\rangle^* = (-1)^{j-j'} \langle j\|T_K\|j'\rangle \,. \tag{B.30}$$

[4] The dyadic tensor resulting from the product of two vectors $\vec{a}$ and $\vec{b}$, can be represented, for instance, in cartesian coordinates by

$$\left(\vec{a}\,\vec{b}\right)_{ij} = a_i b_j \quad (i, j = x, y, z)$$

Appendix C

Proposal of a beam configuration for $m_J = \pm 1$ with vertical magnetic field

The configuration described in Chapter 5 presents the advantage of simplicity by using only linear and identical polarizations. Although this choice is convenient, one might want to relax some of the constraints we fixed previously, for instance, to maximize the polarizability in the excited state. We propose in this section a way to maximize the polarizability of the excited state by tuning the polarizations of the laser beams.

Given the predominance of the α_e^v compared to α_e^t, maximizing $\alpha_e^{(i)}$ from (5.23) will require that we use the vector part of the polarizability and $m \neq 0$. These last conditions impose using a bias magnetic field along the imaging axis (Z-axis) to maximize the flux of photons towards the imaging system.

I Optimization of the polarizations

We will first compute the optimal polarizations for the horizontal beams. Since this case is simplified by the fact that those beams are orthogonal to the quantization axis. The most general forms that the polarizations of the beams along X and Y are thus:

$$\vec{u}_X = \begin{pmatrix} 0 \\ \cos\phi \\ \sin\phi e^{i\chi} \end{pmatrix} \text{ and } \vec{u}_Y = \begin{pmatrix} \cos\phi \\ 0 \\ \sin\phi e^{i\chi} \end{pmatrix}. \tag{C.1}$$

We immediately see from (C.1) and (5.14) that for all values of χ and ϕ, the C-coefficient governing the vector term will be zero. We can only use the tensor part of the polarizability to optimize the total polarizability. Given that $\alpha_e^t > 0$ and $3m_J - J(J+1) > 0$ we want to have $D < 0$ and as large as possible in absolute value. Given (5.15), we want a linear polarization along Z. That was already the case for the configuration in the previous section for the case $m = 0$. On the contrary, if we wanted to minimize α_e from the X, Y-axes, we would use polarizations in the XY-plane, thus linear along $\vec{y}$ (resp. $\vec{x}$) for X-axis (resp. Y-axis).

Now, let us optimize the polarization of the vertical lattice beams. If we neglect the angle of $\pm 6°$ that the beams make with respect to the horizontal (XY-plane), we get laser

beams propagating along $\frac{\vec{X}-\vec{Y}}{\sqrt{2}}$, thus having a polarization with components along $\frac{\vec{X}+\vec{Y}}{\sqrt{2}}$ and $\vec{Z}$. We then get:

$$\vec{u}_Z = \begin{pmatrix} \cos\phi/\sqrt{2} \\ \cos\phi/\sqrt{2} \\ \sin\phi e^{i\chi} \end{pmatrix} . \tag{C.2}$$

The situation is similar to the one for the X, Y-beams, with the same conclusions: there is no vector shift, and the optimal is a polarization along $\vec{Z}$

Including the $\pm 6°$ angles, we get polarization vectors of the form:

$$\vec{u}_Z^{(\pm)} = \begin{pmatrix} \cos\phi/\sqrt{2} + \sin(\pm 6°)\sin\phi e^{i\chi} \\ \cos\phi/\sqrt{2} - \sin(\pm 6°)\sin\phi e^{i\chi} \\ \cos(6°)\sin\phi e^{i\chi} \end{pmatrix} , \tag{C.3}$$

where we have introduced the superscript $(\pm)$ to distinguish the orientation of the two beams composing the vertical trap. From (C.3), we can build four cross products of the form $\vec{u} \times \vec{u}^*$, but the C-coefficients from (5.14) will vanish unless we use twice the same polarization ($C^{+-} = C^{-+} = 0$) and:

$$C^{\pm\pm} = 2\,\mathrm{Im}(u_X^{\pm *} u_Y^{\pm}) = \pm\sqrt{2}\sin 6° \sin\phi\cos\phi\sin\chi , \tag{C.4}$$

since the C-coefficients are opposite in sign, the vector parts of the potential from the two beams will cancel out when summed together. This means that there will be no vector lightshift even if we do not neglect the angle between the beams.

To conclude this appendix, the choice of polarization is the same for both $m = 0$ and $m = \pm 1$, at least as long as we impose that the maximum of emission is along the optical axis of the system, that is as long as we use the quantization axes described in the previous parts.

Appendix D

Physical interpretations of the cooling mechanisms

In the introduction of chapter 6, we presented different mechanisms leading to cooling in a micro-trap. In this appendix, we discuss what are the mechanisms at play in our setup. This study was performed with the rate-equation model before the addition of loss terms and hence the losses might change the relative importance of the different effects leading to cooling. We will also use the steady-state solution of the rate-equation model, which is defined as the eigenvector corresponding to the eigenvalue 0 of the matrix A from equation (6.40).

We will see that two mechanisms are introducing dissipation. Both Doppler cooling and repulsive Sisyphus cooling have an impact of about the same order on the atom's temperature. Finally, note that we will discuss the laser cooling phenomena in the semi-classical picture,[1] even though the rate equations used to model the process rely on the quantized description described in chapter 6.

I Repulsive Sisyphus cooling? Doppler cooling?

We want to determine which mechanism provides the cooling in our system that balances the heating from photon diffusion by the atom. First, we present the semi-classical model we used for our setup. Then, to isolate the contributions of the different processes, we artificially tune the system's parameters to cancel the effect of one of the two mechanisms. Since the differential polarizability causes Sisyphus cooling, we can equalize the trap potentials to cancel this effect. We can cancel Doppler cooling by setting the wavevector of the cooling laser perpendicular to the axis of the movement.

I.1 Semi-classical model

In a semi-classical approach such as that of [104], we treat the motion of the atom classically. The atom is represented by its position and velocity. We can then define a position

[1] The internal degrees of freedom are treated quantum mechanically while the motion is treated classically.

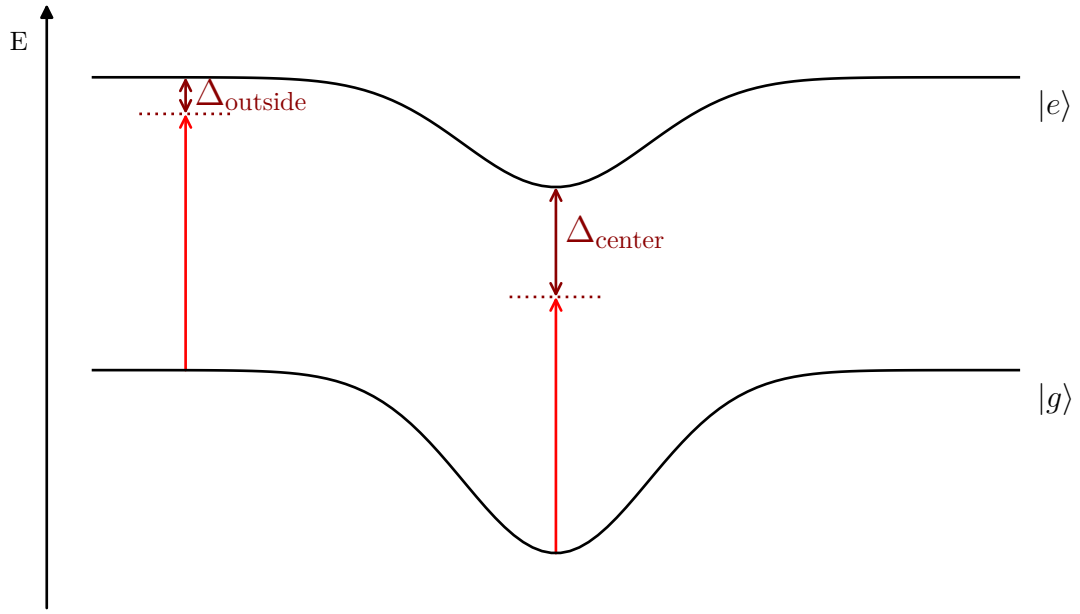

Figure D.1: Energies of the electronic ground and excited state as a function of the position z.

and velocity-dependent detuning:

$$\Delta(z, v) = \Delta - \delta(z) - k_z v \tag{D.1}$$

where Δ is the detuning from the bottom of the trap $\Delta = \omega - (\omega_{e,0} - \omega_{g,0})$ and $\delta(z) = 1/2(\Omega_g - \Omega_e)z^2$ is the change in detuning arising from the differential lightshift, and $-k_z v$ corresponds to the Doppler shift. The situation is schematically drawn in Figure D.1, where we see that the laseris more red-detuned in the center of the trap than on the edges.

In our case where $\Omega_g > \Omega_e$, we expect that there will be Sisyphus cooling if the atom absorbs preferentially on the sides of the trap (and thus at small velocities), where the potential energy reduction is the largest. On the other hand, the Doppler cooling is expected to work if the absorption occurs predominantly when the velocity is negative and large in absolute value, *i.e.*, at the bottom of the trap every period of oscillation (choosing a laser traveling along $+\vec{z}$). In Figure D.2, we plot the detuning $\Delta(z, v)$ seen by the semi-classical atom oscillating in the ground-state harmonic trap. It shows that at velocities corresponding to kinetic energies below the thermal energy, the detuning is almost uniform in space for $v < 0$ except near the edge of the trajectories, the so-called "turning points", which corresponds to the points where Sisyphus cooling occurs. As the energy is increased, the effect of the differential lightshift becomes gradually apparent. Indeed, an increased energy means larger values of z explored by the atom and therefore larger differential lightshifts. Still, this becomes clear only at energies above the thermal energy (fitted on the steady-state solution). This raises the question of the relevance of the Sisyphus picture in our case. More precisely, is our situation dominated by Doppler cooling leading to a temperature too low for Sisyphus mechanism to be relevant? In the next two sections, we will discuss the limiting cases where there is no Doppler cooling or Sisyphus cooling.

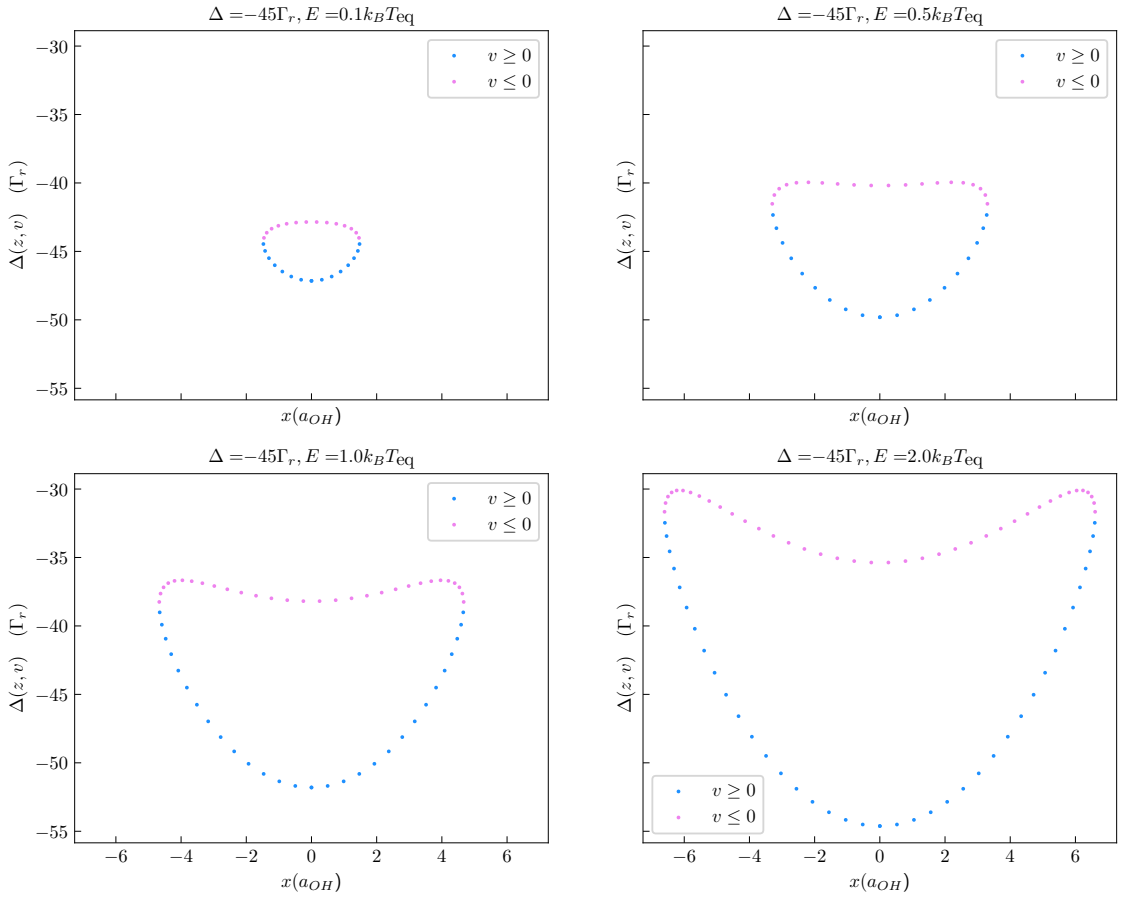

Figure D.2: These plots represent the detuning seen during one oscillation in the ground-state harmonic trap as a function of position for 4 different initial energies: $\{0.1, 0.5, 1.0, 2.0\} k_B T_{\text{eq}}$, where $k_B T_{\text{eq}} = -0.4\hbar\Delta + 2.9\hbar\Gamma$ from the empirical relation observed in Figure D.3. Since the detuning depends on the atom's velocity via the Doppler shift, we stressed the sign of the velocity by a change in color (violet for negative velocities and blue for positive ones). We see that below the thermal energy, the atom will see the laser closer to resonance when its velocity is negative; while as the energy is increased, the effect of the position gets more pronounced. Also, the detuning for $v < 0$ does not depend much on the position except near the turning points.

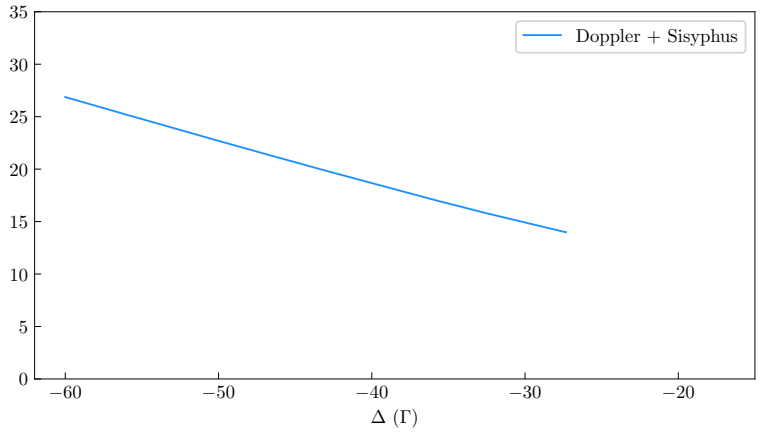

Figure D.3: Effective temperature as a function of laser detuning at a saturation parameter $I = 800 I_{\text{sat}}$. The temperature is obtained by fitting the exponential decay of the populations in the $\{g, n\}$ manifold. The curve stops at around $\Delta = -27\Gamma_r$, this corresponds to a breakdown of the model, *i.e.*, there was un physical accumulation of population in the highest vibrational levels.

I.2 Behavior of the complete system (Doppler + Sisyphus)

In Figure D.3, we plotted the temperature as a function of the laser detuning for the complete system, that is the one studied in Chapter 6, including (potentially) Doppler and Sisyphus cooling.

We observe that the temperature assumes a affine behavior as a function of the detuning for $I = 800 I_{\text{sat}}$. Furthermore, the temperature is not plotted for detunings above $\Delta = -27\Gamma_r$, as these situations corresponds to an accumulation of population in the 10% highest vibrational levels that was above 10^{-3} which we considered as unphysical.

I.3 Cancellation of Sisyphus cooling: $\Omega_e = \Omega_g$

To get the limit in which the Sisyphus cooling is canceled, we artificially impose in the simulation the magic-wavelength condition, that is, $\Omega_e = \Omega_g$. This condition means there can be no differential lightshift effects, neither cooling nor heating. We kept all the other parameters of the simulation constant.

The temperature also assumes a linear behavior as a function of the detuning. As we can see in Figure D.4 at least as long as we do not get to close to the resonance. Notice that in the absence of Sisyphus mechanism, there is no more an accumulation of population at the top of the trap, which is expected since there is no more a vibrational resonance as we set $\Omega_g = \Omega_e$.

This shows that even in the absence of Sisyphus cooling, the system still reaches an equilibrium temperature of the same order as the one for the complete system, albeit a higher one. This hints that Doppler cooling would suffice to maintain the atom trapped, but it also seems that Sisyphus cooling is helping to reach lower temperatures.

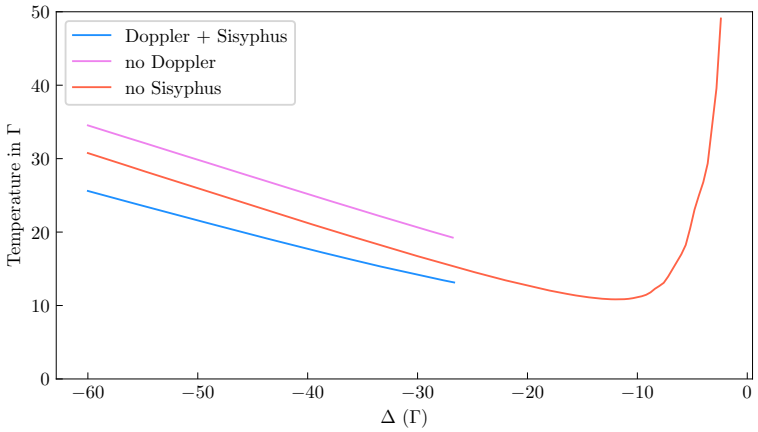

Figure D.4: The three curves represent the effective temperature as a function of laser detuning at a saturation parameter $I = 800 I_{\text{sat}}$. As a reminder the temperature is obtained by fitting the exponential decay of the populations in the $\{g, n\}$ manifold. The curve "Doppler + Sisyphus" is the generic case of our study. The "no Doppler" curve is the case where the Doppler effect has been canceled by setting $\vec{k} \perp \vec{v}$. The "no Sisyphus" curve is obtained by canceling Sisyphus effects by setting $\Omega_g = \Omega_e$. For the "Doppler + Sisyphus" curve, we observe a affine dependence of the temperature with the detuning given by $k_B T_{\text{eq}} = -0.4\hbar\Delta + 2.9\hbar\Gamma$. The blue and pink curves stop at around $\Delta = -27\Gamma_r$, this corresponds to a breakdown of the model, *i.e.*, there was un physical accumulation of population in the highest vibrational levels.

I.4 Cancellation of Doppler cooling: $\vec{k} \perp \vec{z}$

By setting $\vec{k} \perp \vec{z}$, we automatically cancel the Doppler term in equation (D.1), meaning that we cancel the cooling effect but *not* the heating from the random recoils. Once more the temperature is higher than in the complete case. This means that Doppler cooling is also contributing significantly to the behavior of our atom.

II Conclusion

From the different results exposed in this appendix, we can conclude that **both** Sisyphus and Doppler coolings are present and relevant in our model. As a sanity check, we verified that the system did not reach a steady state if both effects were canceled. This study was carried out without considering the losses due to the atom escaping the trap. There could be further developments including the losses but we do not expect drastic changes in the phenomenon at play for the cooling mechanisms.

Bibliography

[1] J. Dalibard, "Fluides quantiques de basse dimension et transition de kosterlitz-thouless," 2017.

[2] L. Villa, J. Despres, and L. Sanchez-Palencia, "Unraveling the excitation spectrum of many-body systems from quantum quenches," *Phys. Rev. A*, vol. 100, p. 063632, Dec 2019.

[3] J. Mossel and J.-S. Caux, "Exact time evolution of space- and time-dependent correlation functions after an interaction quench in the one-dimensional bose gas," vol. 14, p. 075006, Jul 2012. Publisher: IOP Publishing.

[4] E. H. Lieb and D. W. Robinson, "The finite group velocity of quantum spin systems," *Communications in Mathematical Physics*, vol. 28, pp. 251–257, Jan 1972. Publisher: Springer.

[5] S. Bravyi, M. B. Hastings, and F. Verstraete, "Lieb-robinson bounds and the generation of correlations and topological quantum order," *Physical Review Letters*, vol. 97, p. 050401, Jul 2006.

[6] B. Nachtergaele, Y. Ogata, and R. Sims, "Propagation of correlations in quantum lattice systems," *Journal of Statistical Physics*, vol. 124, pp. 1–13, Jul 2006.

[7] T. Fukuhara, S. Hild, J. Zeiher, P. Schauß, I. Bloch, M. Endres, and C. Gross, "Spatially resolved detection of a spin-entanglement wave in a bose-hubbard chain," *Phys. Rev. Lett.*, vol. 115, p. 035302, Jul 2015.

[8] P. Jurcevic, B. P. Lanyon, P. Hauke, C. Hempel, P. Zoller, R. Blatt, and C. F. Roos, "Quasiparticle engineering and entanglement propagation in a quantum many-body system," *Nature*, vol. 511, pp. 202–205, Jul 2014.

[9] P. Richerme, Z.-X. Gong, A. Lee, C. Senko, J. Smith, M. Foss-Feig, S. Michalakis, A. V. Gorshkov, and C. Monroe, "Non-local propagation of correlations in quantum systems with long-range interactions," *Nature*, vol. 511, pp. 198–201, Jul 2014.

[10] M. Cheneau, P. Barmettler, D. Poletti, M. Endres, P. Schauß, T. Fukuhara, C. Gross, I. Bloch, C. Kollath, and S. Kuhr, "Light-cone-like spreading of correlations in a quantum many-body system," *Nature*, vol. 481, pp. 484–487, Jan 2012.

[11] C. Gross and W. S. Bakr, "Quantum gas microscopy for single atom and spin detection," Oct 2020.

[12] M. Endres, M. Cheneau, T. Fukuhara, C. Weitenberg, P. Schauß, C. Gross, L. Mazza, M. C. Banuls, L. Pollet, I. Bloch, and S. Kuhr, "Single-site- and single-atom-resolved measurement of correlation functions," *Applied Physics B*, vol. 113, pp. 27–39, Oct 2013.

[13] W. Witczak-Krempa, E. S. Sørensen, and S. Sachdev, "The dynamics of quantum criticality revealed by quantum monte carlo and holography," *Nature Physics*, vol. 10, pp. 361–366, May 2014.

[14] J. T. Schneider, J. Despres, S. J. Thomson, L. Tagliacozzo, and L. Sanchez-Palencia, "Spreading of correlations and entanglement in the long-range transverse ising chain," *Physical Review Research*, vol. 3, p. L012022, Mar 2021.

[15] J. T. Wilson, S. Saskin, Y. Meng, S. Ma, R. Dilip, A. P. Burgers, and J. D. Thompson, "Trapping alkaline earth rydberg atoms optical tweezer arrays," *Phys. Rev. Lett.*, vol. 128, p. 033201, Jan 2022.

[16] K.-L. Pham, T. F. Gallagher, P. Pillet, S. Lepoutre, and P. Cheinet, "Coherent light shift on alkaline-earth rydberg atoms from isolated core excitation without autoionization," *PRX Quantum*, vol. 3, p. 020327, May 2022.

[17] C. L. Vaillant, M. P. A. Jones, and R. M. Potvliege, "Long-range rydberg–rydberg interactions in calcium, strontium and ytterbium," *Journal of Physics B: Atomic, Molecular and Optical Physics*, vol. 45, p. 135004, Jun 2012.

[18] A. Cooper, J. P. Covey, I. S. Madjarov, S. G. Porsev, M. S. Safronova, and M. Endres, "Alkaline-earth atoms in optical tweezers," *Phys. Rev. X*, vol. 8, p. 041055, Dec 2018.

[19] S. E. Hamann, D. L. Haycock, G. Klose, P. H. Pax, I. H. Deutsch, and P. S. Jessen, "Resolved-sideband raman cooling to the ground state of an optical lattice," *Phys. Rev. Lett.*, vol. 80, pp. 4149–4152, May 1998.

[20] S. Stellmer, *Degenerate quantum gases of strontium*. PhD thesis, 2014.

[21] J. Trautmann, D. Yankelev, V. Klüsener, A. Park, I. Bloch, and S. Blatt, "The $^1S_0$-$^3P_2$ magnetic quadrupole transition in neutral strontium," Nov 2022.

[22] A. Molineri, *Un nouveau dispositif pour étudier la relaxation d'un système quantique à N corps*. PhD thesis, 2019. Thèse de doctorat dirigée par Westbrook, Chris Physique Université Paris-Saclay (ComUE) 2019.

[23] C. Briosne Fréjaville, *Transport et confinement optique d'atomes de strontium pour une expérience de microscope à gaz quantique*. PhD thesis, 2020. Thèse de doctorat dirigée par Westbrook, Chris et Cheneau, Marc Physique université Paris-Saclay 2020.

[24] F. Sorrentino, G. Ferrari, N. Poli, R. Drullinger, and G. M. Tino, "Laser cooling and trapping of atomic strontium for ultracold atoms physics, high-precision spectroscopy and quantum sensors," *Modern Physics Letters B*, vol. 20, no. 21, pp. 1287–1320, 2006.

[25] J. H. Shirley, "Modulation transfer processes in optical heterodyne saturation spectroscopy," *Opt. Lett.*, vol. 7, pp. 537–539, Nov 1982.

[26] J. S. Lawrence and D. M. Kane, "Injection locking suppression of coherence collapse in a diode laser with optical feedback," *Optics Communications*, vol. 167, no. 1, pp. 273–282, 1999.

[27] E. Black, "Notes on the pound-drever-hall technique."

[28] I. Manai, A. Molineri, C. Fréjaville, C. Duval, P. Bataille, R. Journet, F. Wiotte, B. Laburthe-Tolra, E. Maréchal, M. Cheneau, and M. Robert-de Saint-Vincent, "Shelving spectroscopy of the strontium intercombination line," *Journal of physics. B, Atomic, molecular, and optical physics*, vol. 53, no. 8, p. 85005, 2020.

[29] M. Schioppo, N. Poli, M. Prevedelli, S. Falke, C. Lisdat, U. Sterr, and G. M. Tino, "A compact and efficient strontium oven for laser-cooling experiments," *Review of scientific instruments*, vol. 83, no. 10, pp. 103101–103101, 2012.

[30] M. Yasuda and H. Katori, "Lifetime measurement of the $^3P_2$ metastable state of strontium atoms.," *Physical review letters*, vol. 92 15, p. 153004, 2004.

[31] J. Dalibard, "Une brève histoire des atomes froids," *Cours du Collège de France*, vol. 143, 2015.

[32] H. Katori, T. Ido, Y. Isoya, and M. Kuwata-Gonokami, "Magneto-optical trapping and cooling of strontium atoms down to the photon recoil temperature," *Physical Review Letters*, vol. 82, no. 6, pp. 1116–1119, 1999.

[33] J. A. Giordmaine and T. C. Wang, "Molecular beam formation by long parallel tubes," *Journal of applied physics*, vol. 31, no. 3, pp. 463–471, 1960.

[34] A. R. L. Caires, G. D. Telles, M. W. Mancini, L. G. Marcassa, V. S. Bagnato, D. Wilkowski, and R. Kaiser, "Intensity dependence for trap loss rate in a magneto-optical trap of strontium," *Braz. J. Phys.*, vol. 34, no. 4, pp. 1504–1509, 2004.

[35] S. Stellmer and F. Schreck, "Reservoir spectroscopy of 5 s 5 p 3 p 2 – 5 s n d 3 d 1 , 2 , 3 transitions in strontium," *Physical Review A*, vol. 90, p. 022512, Aug 2014.

[36] T. H. Loftus, T. Ido, M. M. Boyd, A. D. Ludlow, and J. Ye, "Narrow line cooling and momentum-space crystals," *Phys. Rev. A*, vol. 70, no. 6, p. 063413, 2004.

[37] T. Chaneliere, L. X. He, R. Kaiser, and D. Wilkowski, "Three dimensional cooling and trapping with a narrow line," *The European Physical Journal D*, vol. 46, pp. 507–515, Mar 2008.

[38] J. A. Muniz, M. A. Norcia, J. R. K. Cline, and J. K. Thompson, "A robust narrow-line magneto-optical trap using adiabatic transfer," *arXiv:1806.00838 [physics, physics:quant-ph]*, Jun 2018.

[39] M. A. Norcia, J. R. K. Cline, J. P. Bartolotta, M. J. Holland, and J. K. Thompson, "Narrow-line laser cooling by adiabatic transfer," *New J. Phys.*, vol. 20, p. 023021, Feb 2018.

[40] S. Snigirev, A. J. Park, A. Heinz, I. Bloch, and S. Blatt, "Fast and dense magneto-optical traps for strontium," *Phys. Rev. A*, vol. 99, p. 063421, Jun 2019.

[41] J. P. Bartolotta, M. A. Norcia, J. R. K. Cline, J. K. Thompson, and M. J. Holland, "Laser cooling by sawtooth-wave adiabatic passage," *Physical Review A*, vol. 98, p. 023404, Aug 2018.

[42] A. Benseny and K. Mølmer, "Adiabatic theorem revisited: The unexpectedly good performance of adiabatic passage," *Physical review. A*, vol. 103, no. 6, 2021.

[43] D. Boddy, *First observations of Rydberg blockade in a frozen gas of divalent atoms.* PhD thesis, 2014.

[44] N. Schlosser, G. Reymond, and P. Grangier, "Collisional blockade in microscopic optical dipole traps," *Physical Review Letters*, vol. 89, p. 023005, Jun 2002.

[45] W. S. Bakr, J. I. Gillen, A. Peng, S. Fölling, and M. Greiner, "A quantum gas microscope for detecting single atoms in a hubbard-regime optical lattice," *Nature*, vol. 462, pp. 74–77, Nov 2009.

[46] Oxford Instruments - Andor, "Andor Zyla for physical sciences specifications."

[47] H. Ikoma, M. Broxton, T. Kudo, and G. Wetzstein, "A convex 3d deconvolution algorithm for low photon count fluorescence imaging," *Scientific Reports*, vol. 8, p. 11489, Jul 2018. Number: 1 Publisher: Nature Publishing Group.

[48] A. La Rooij, C. Ulm, E. Haller, and S. Kuhr, "A comparative study of deconvolution techniques for quantum-gas microscope images," 2022.

[49] P. Virtanen, R. Gommers, T. E. Oliphant, M. Haberland, T. Reddy, D. Cournapeau, E. Burovski, P. Peterson, W. Weckesser, J. Bright, S. J. van der Walt, M. Brett, J. Wilson, K. J. Millman, N. Mayorov, A. R. J. Nelson, E. Jones, R. Kern, E. Larson, C. J. Carey, İ. Polat, Y. Feng, E. W. Moore, J. VanderPlas, D. Laxalde, J. Perktold, R. Cimrman, I. Henriksen, E. A. Quintero, C. R. Harris, A. M. Archibald, A. H. Ribeiro, F. Pedregosa, P. van Mulbregt, and SciPy 1.0 Contributors, "SciPy 1.0: Fundamental Algorithms for Scientific Computing in Python," *Nature Methods*, vol. 17, pp. 261–272, 2020.

[50] F. Pedregosa, G. Varoquaux, A. Gramfort, V. Michel, B. Thirion, O. Grisel, M. Blondel, P. Prettenhofer, R. Weiss, V. Dubourg, J. Vanderplas, A. Passos, D. Cournapeau, M. Brucher, M. Perrot, and E. Duchesnay, "Scikit-learn: Machine learning in Python," *Journal of Machine Learning Research*, vol. 12, pp. 2825–2830, 2011.

[51] G. Dmoment and J. Idier, *Inverse Problems, Ill-posed Problems*, ch. 1, pp. 24–40. John Wiley & Sons, Ltd, 2008.

[52] S. J. Wright, "Coordinate descent algorithms," *Mathematical Programming*, vol. 151, pp. 3–34, Jun 2015.

[53] G. Andrew and J. Gao, "Scalable training of l1-regularized log-linear models," in *International Conference on Machine Learning*, January 2007.

[54] S. Van der Walt, J. L. Schönberger, J. Nunez-Iglesias, F. Boulogne, J. D. Warner, N. Yager, E. Gouillart, and T. Yu, "scikit-image: image processing in python," *PeerJ*, vol. 2, p. 453, 2014.

[55] F. Goudail, "Introduction au traitement du signal," 2021.

[56] G. Le Besnerais and J.-F. Giovannelli, *Inverse Filtering and Other Linear Methods*, ch. 4, pp. 80–116. John Wiley & Sons, Ltd, 2008.

[57] B. Hunt, "A matrix theory proof of the discrete convolution theorem," *IEEE Transactions on Audio and Electroacoustics*, vol. 19, no. 4, pp. 285–288, 1971.

[58] F. Orieux, J.-F. Giovannelli, and T. Rodet, "Bayesian estimation of regularization and PSF parameters for wiener-hunt deconvolution," *Journal of the Optical Society of America A*, vol. 27, p. 1593, Jul 2010.

[59] R. Yamamoto, J. Kobayashi, T. Kuno, K. Kato, and Y. Takahashi, "An ytterbium quantum gas microscope with narrow-line laser cooling," *New Journal of Physics*, vol. 18, p. 023016, Feb 2016.

[60] L. W. Cheuk, M. A. Nichols, M. Okan, T. Gersdorf, V. V. Ramasesh, W. S. Bakr, T. Lompe, and M. W. Zwierlein, "Quantum-gas microscope for fermionic atoms," *Physical Review Letters*, vol. 114, p. 193001, May 2015.

[61] A. Impertro, J. F. Wienand, S. Häfele, H. von Raven, S. Hubele, T. Klostermann, C. R. Cabrera, I. Bloch, and M. Aidelsburger, 2022.

[62] O. Ronneberger, P. Fischer, and T. Brox, "U-net: Convolutional networks for biomedical image segmentation."

[63] W. H. Richardson, "Bayesian-based iterative method of image restoration∗," *J. Opt. Soc. Am.*, vol. 62, pp. 55–59, Jan 1972.

[64] A. Kramida, Yu. Ralchenko, J. Reader, and NIST ASD Team. NIST Atomic Spectra Database (ver. 5.9), [Online]. Available: `https://physics.nist.gov/asd` [2022, July 25]. National Institute of Standards and Technology, Gaithersburg, MD., 2021.

[65] J. Ruczkowski, M. Elantkowska, and J. Dembczyński, "Semi-empirical analysis of the fine structure and oscillator strengths for atomic strontium," *Journal of Quantitative Spectroscopy and Radiative Transfer*, vol. 170, pp. 106–116, Feb 2016.

[66] X. Zhou, X. Xu, X. Chen, and J. Chen, "Magic wavelengths for terahertz clock transitions," *Phys. Rev. A*, vol. 81, p. 012115, Jan 2010.

[67] F. L. Kien, P. Schneeweiss, and A. Rauschenbeutel, "Dynamical polarizability of atoms in arbitrary light fields: general theory and application to cesium," *Eur. Phys. J. D*, vol. 67, p. 92, May 2013. arXiv: 1211.2673.

[68] W. Happer and B. S. Mathur, "Effective operator formalism in optical pumping," *Phys. Rev.*, vol. 163, pp. 12–25, Nov 1967.

[69] C. Cohen-Tannoudji and J. Dupont-Roc, "Experimental study of zeeman light shifts in weak magnetic fields," *Physical Review A*, vol. 5, pp. 968–984, 1972.

[70] B. J. Bloom, T. L. Nicholson, J. R. Williams, S. L. Campbell, M. Bishof, X. Zhang, W. Zhang, S. L. Bromley, and J. Ye, "An optical lattice clock with accuracy and stability at the 10-18 level," *Nature*, vol. 506, pp. 71–75, Feb 2014.

[71] J. P. Covey, I. S. Madjarov, A. Cooper, and M. Endres, "2000-times repeated imaging of strontium atoms in clock-magic tweezer arrays," *Physical Review Letters*, vol. 122, p. 173201, May 2019.

[72] D. A. Steck, "Quantum and atom optics."

[73] F. R. P. 1918-1988, *The Feynman lectures on physics*. San Francisco, Calif. Boston, Mass. New York [etc.: Pearson/Addison-Wesley, definitive edition. ed., 2006.

[74] D. Barredo, V. Lienhard, P. Scholl, S. de Léséleuc, T. Boulier, A. Browaeys, and T. Lahaye, "Three-dimensional trapping of individual rydberg atoms in ponderomotive bottle beam traps," *Physical Review Letters*, vol. 124, p. 023201, Jan 2020.

[75] K. D. Nelson, X. Li, and D. S. Weiss, "Imaging single atoms in a three-dimensional array," *Nature Physics*, vol. 3, pp. 556–560, Aug 2007.

[76] M. Miranda, R. Inoue, N. Tambo, and M. Kozuma, "Site-resolved imaging of a bosonic mott insulator using ytterbium atoms," *Phys. Rev. A*, vol. 96, p. 043626, Oct 2017.

[77] G. A. Phelps, *A dipolar quantum gas microscope*. PhD thesis, Harvard University, Graduate School of Arts & Sciences, 2019.

[78] N. Schlosser, G. Reymond, I. Protsenko, and P. Grangier, "Sub-poissonian loading of single atoms in a microscopic dipole trap," *Nature*, vol. 411, pp. 1024–1027, Jun 2001.

[79] F. Diedrich, J. C. Bergquist, W. M. Itano, and D. J. Wineland, "Laser cooling to the zero-point energy of motion," *Phys. Rev. Lett.*, vol. 62, pp. 403–406, Jan 1989.

[80] A. M. Kaufman, B. J. Lester, and C. A. Regal, "Cooling a single atom in an optical tweezer to its quantum ground state," *Phys. Rev. X*, vol. 2, p. 041014, Nov 2012.

[81] U. Delić, D. Grass, M. Reisenbauer, T. Damm, M. Weitz, N. Kiesel, and M. Aspelmeyer, "Levitated cavity optomechanics in high vacuum," *Quantum Science and Technology*, vol. 5, p. 025006, Mar 2020.

[82] C. Tuchendler, A. M. Lance, A. Browaeys, Y. R. P. Sortais, and P. Grangier, "Energy distribution and cooling of a single atom in an optical tweezer," *Phys. Rev. A*, vol. 78, p. 033425, Sep 2008.

[83] S. Stenholm, "The semiclassical theory of laser cooling," *Reviews of Modern Physics*, vol. 58, pp. 699–739, 1986.

[84] G. Morigi, M. Lewenstein, P. Zoller, and J. Cirac, "Ground state laser cooling beyond the lamb-dicke limit," *Europhys. Lett.*, vol. 23, no. quant-ph/9706017, pp. 1–5, 1993.

[85] M. T. DePue, C. McCormick, S. L. Winoto, S. Oliver, and D. S. Weiss, "Unity occupation of sites in a 3d optical lattice," *Phys. Rev. Lett.*, vol. 82, pp. 2262–2265, Mar 1999.

[86] J. F. Sherson, C. Weitenberg, M. Endres, M. Cheneau, I. Bloch, and S. Kuhr, "Single-atom-resolved fluorescence imaging of an atomic mott insulator," *Nature*, vol. 467, pp. 68–72, Sep 2010.

[87] K.-N. Schymik, S. Pancaldi, F. Nogrette, D. Barredo, J. Paris, A. Browaeys, and T. Lahaye, "Single atoms with 6000-second trapping lifetimes in optical-tweezer arrays at cryogenic temperatures," *Physical Review Applied*, vol. 16, p. 034013, Sep 2021.

[88] D. J. Wineland and W. M. Itano, "Laser cooling of atoms," *Phys. Rev. A*, vol. 20, pp. 1521–1540, Oct 1979.

[89] W. M. Itano and D. J. Wineland, "Laser cooling of ions stored in harmonic and penning traps," *Physical Review A*, vol. 25, pp. 35–54, 1982.

[90] R. Taïeb, R. Dum, J. I. Cirac, P. Marte, and P. Zoller, "Cooling and localization of atoms in laser-induced potential wells," *Phys. Rev. A*, vol. 49, pp. 4876–4887, Jun 1994.

[91] S. Saskin, J. Wilson, B. Grinkemeyer, and J. Thompson, "Narrow-line cooling and imaging of ytterbium atoms in an optical tweezer array," *Physical Review Letters*, vol. 122, p. 143002, Apr 2019.

[92] A. Jenkins, J. W. Lis, A. Senoo, W. F. McGrew, and A. M. Kaufman, "Ytterbium nuclear-spin qubits in an optical tweezer array," *Physical Review X*, vol. 12, p. 021027, May 2022.

[93] G. Morigi, J. I. Cirac, M. Lewenstein, and P. Zoller, "Ground-state laser cooling beyond the lamb-dicke limit," *Europhysics Letters (EPL)*, vol. 39, pp. 13–18, Jul 1997.

[94] J. D. Thompson, T. G. Tiecke, A. S. Zibrov, V. Vuletić, and M. D. Lukin, "Coherence and raman sideband cooling of a single atom in an optical tweezer," *Phys. Rev. Lett.*, vol. 110, p. 133001, Mar 2013.

[95] M. Norcia, A. Young, and A. Kaufman, "Microscopic control and detection of ultracold strontium in optical-tweezer arrays," *Physical Review X*, vol. 8, p. 041054, Dec 2018.

[96] N. Lorenz, L. Festa, L.-M. Steinert, and C. Gross, "Raman sideband cooling in optical tweezer arrays for rydberg dressing," *SciPost Physics*, vol. 10, p. 052, Mar 2021.

[97] Y. S. Patil, S. Chakram, L. M. Aycock, and M. Vengalattore, "Nondestructive imaging of an ultracold lattice gas," *Phys. Rev. A*, vol. 90, p. 033422, Sep 2014.

[98] J. Yang, L. Liu, J. Mongkolkiattichai, and P. Schauss, "Site-resolved imaging of ultracold fermions in a triangular-lattice quantum gas microscope," *PRX Quantum*, vol. 2, p. 020344, Jun 2021.

[99] G. Morigi, J. Eschner, and C. Keitel, "Ground state laser cooling using electromagnetically induced transparency," *Physical review letters*, vol. 85, no. 21, pp. 4458–4461, 2000.

[100] D. Leibfried, R. Blatt, C. Monroe, and D. Wineland, "Quantum dynamics of single trapped ions," *Rev. Mod. Phys.*, vol. 75, pp. 281–324, Mar 2003.

[101] G. J. A. Edge, R. Anderson, D. Jervis, D. C. McKay, R. Day, S. Trotzky, and J. H. Thywissen, "Imaging and addressing of individual fermionic atoms in an optical lattice," *Physical Review A*, vol. 92, p. 063406, Dec 2015.

[102] E. Haller, J. Hudson, A. Kelly, D. A. Cotta, B. Peaudecerf, G. D. Bruce, and S. Kuhr, "Single-atom imaging of fermions in a quantum-gas microscope," *Nature Physics*, vol. 11, pp. 738–742, Sep 2015.

[103] U. Fano, "Effects of configuration interaction on intensities and phase shifts," *Phys. Rev.*, vol. 124, pp. 1866–1878, Dec 1961.

[104] V. V. Ivanov and S. Gupta, "Laser-driven sisyphus cooling in an optical dipole trap," *Phys. Rev. A*, vol. 84, p. 063417, Dec 2011.

[105] F. Berto, E. Perego, L. Duca, and C. Sias, "Prospects for single-photon sideband cooling of optically trapped neutral atoms," *Phys. Rev. Research*, vol. 3, p. 043106, Nov 2021.

[106] A. Urech, I. H. A. Knottnerus, R. J. C. Spreeuw, and F. Schreck, "Narrow-line imaging of single strontium atoms in shallow optical tweezers," *Phys. Rev. Res.*, vol. 4, p. 023245, Jun 2022.

[107] K. Mølmer, Y. Castin, and J. Dalibard, "Monte carlo wave-function method in quantum optics," *Journal of the Optical Society of America. B, Optical physics*, vol. 10, no. 3, pp. 524–538, 1993.

[108] J. Dalibard, Y. Castin, and K. Mølmer, "Wave-function approach to dissipative processes in quantum optics," *Physical review letters*, vol. 68, no. 5, pp. 580–583, 1992.

[109] J. Johansson, P. Nation, and F. Nori, "QuTiP: An open-source python framework for the dynamics of open quantum systems," *Computer Physics Communications*, vol. 183, pp. 1760–1772, Aug 2012.

[110] M. M. Nieto, "Displaced and squeezed number states," *Physics Letters A*, vol. 229, no. 3, pp. 135–143, 1997.

[111] F. Hu, I. Nosske, L. Couturier, C. Tan, C. Qiao, P. Chen, Y. H. Jiang, B. Zhu, and M. Weidemüller, "Analyzing a single-laser repumping scheme for efficient loading of a strontium magneto-optical trap," *Phys. Rev. A*, vol. 99, p. 033422, Mar 2019.

[112] I. H. Deutsch and P. S. Jessen, "Quantum control and measurement of atomic spins in polarization spectroscopy," *Optics Communications*, vol. 283, no. 5, pp. 681–694, 2010. Quo vadis Quantum Optics?

[113] E. Condon, E. Condon, and G. Shortley, *The Theory of Atomic Spectra*. Cambridge Univ.Pr.209, Cambridge University Press.

[114] Z. R. N, *Angular momentum : understanding spatial aspects in chemistry and physics*. A Wiley-Interscience publication, New York (N.Y.): J. Wiley, 1988.